Numerical modelling of the Arctic and North Atlantic exchanges with NEMO: Focus on freshwater and dynamics

by

Jonathan Grivault

A thesis submitted in partial fulfillment of the requirements for the degree of

Doctor of Philosophy

Department of Earth and Atmospheric Sciences

University of Alberta

Abstract

The Arctic is currently undergoing significant changes due to increasing anthropogenic greenhouse gases causing atmospheric warming. The impact of this warming is clearly visible in the Arctic: reduced sea-ice cover, enhanced land-ice melting, increased frequency of extreme weather, etc. Understanding the current dynamics of the Arctic Ocean and its exchange with the North Atlantic is the first step in understanding how it may change in the future. In this thesis, I focused on key regions where exchange between the Arctic Ocean and the North Atlantic occurs: Baffin Bay, the Canadian Arctic Archipelago, and the Arctic gateways. I used a numerical model with several domains, resolutions, atmospheric forcings, and runoff datasets to evaluate how Arctic outflow dynamics change or are impacted by the warming climate. I demonstrated (1) that enhanced Greenland melt significantly impacts the steric height in Baffin Bay, which changes the circulation in Baffin Bay, reducing the Arctic outflow through Baffin Bay. (2) The Canadian Arctic Archipelago throughflow is significantly impacted by sea-ice motion as sea-ice has a significant impact on the surface stress. In particular, I showed that more mobile ice enhanced the freshwater transport. (3) The main frequencies acting on the Arctic outflow variability are the seasonal cycle, and the 6-month, 3 year, 6 year, 8.5 year, and 21 year cycles. Variability on short timescales are associated with the atmospheric circulation via the Arctic Oscillation, while longer timescales are related to the variability of the sea surface height gradient between the Beaufort Gyre and Baffin Bay.

Preface

Chapter 3 has been published as:

Grivault, N., Hu, X., and Myers, P. G. (2017). *Evolution of Baffin Bay water masses and transports in a numerical sensitivity experiment under enhanced Greenland melt.* Atmosphere-Ocean, 55(3):169–194. doi: 10.1080/07055900.2017.1333950.

I was responsible for the data analysis and the writing of the manuscript. Xianmin Hu ran the experiments used and assisted with the analysis and writing. Paul G. Myers provided advice and manuscript edits.

Chapter 4 has been submitted for publication as:

Grivault, N., Hu, X., and Myers, P. G. (2018). *Impact of the surface stress on the volume and freshwater transport through the Canadian Arctic Archipelago from high resolution numerical modelling.* Journal of Geophysical Research: Oceans.

I was responsible for the data analysis and the writing of the manuscript. Xianmin Hu ran the experiments used and assisted with the analysis and writing. Paul G. Myers provided advice and manuscript edits.

Dedication

”You should be writing.
- I KNOW!!”

PhD Comics

This thesis is dedicated to Dominique.

Without you I might never have go to Canada in the first place and never had the opportunity to start a PhD. I'm looking back to my last 12 years as a student and, I think, I finally start to understand what your nickname means. *Tempus fugit...* yes, I wasted so much time doing nothing useful. I see it now. But whatever, the most important is truly what you said to me last: ”on se sera bien marré”. So true...

Thanks for everything, I won't forget you.

Cette thèse est dédiée à Dominique.

Sans toi je ne serais sans doute jamais allé au Canada et je n'aurais jamais eu l'opportinité de débuter un doctorat. Je regarde ces 12 dernières années de ma vie d'étudiant et je crois que je commence enfin à comprendre ce que ton pseudonyme signifiait. *Tempus fugit...* Oui, j'ai gâché tellement de temps à ne rien faire d'utile. Je m'en rend compte maintenant. Mais peut importe, le plus important est ce que tu m'as dit en dernier : ”on se sera bien marré”. Tellement vrai...

Merci pour tout, je ne t'oublierais pas.

Acknowledgements

My first thanks goes to my supervisor, Paul G. Myers, for his constant support and guidance during the four and a half years of my PhD. His help has been invaluable and this finished work is largely due to his support, and without him I would have jumped ship after my first candidacy exam.

I also want to thank my current and previous colleagues and friends: Xianmin Hu, Natasha Ridenour, Yarisbel Garcia Quintana, Laura Gillard, Laura Castro de la Guardia, Clark Pennelly, Juliana Marson, Charlène Feucher, Andrew Hamilton, Amanda Kahn, and Peggy Courtois. Your support was invaluable and my finished thesis today is also because of you. Special thanks to Natasha that had the difficult task to go through most of my draft to correct my dreadful English and to Xianmin and Clark for the hours of technical discussions about details that no one really cares about. I also apologize to everyone for being the annoying French guy who argued about these tiny technical details that I know you didn't care about.

Speaking of technical details, I also want to thanks Nicolas Dubois, Gilles "DJ_TBX" Maurer, Thibault Cherion, Phylos, pfoo, quetzal, Mickaël "lastmikoi" Falck, Tilou, bencoh, Kegeruneku, Aurélien Joga, and Starouille for their invaluable help when we had issues with our servers and storage arrays. Thanks to you guys I was able to look like I knew what I was doing in front of my colleagues. The Saviour Prize goes to Nicolas; without him we would have lost the data on this damned 11 TB storage array (and it would not have solved the underlying problem...).

My last thanks go to my family, in particular to my father and mother. Thank you dad, our Sunday meeting was always a fresh breath for me. Our discussions helped to sort out my thoughts and issues. Thank you mum, the time I was able to spend in France with you and the rest of the family significantly improved my moral after the long weeks of hard work. Thanks to my sisters and brothers, Myriam, Jennifer, Thomas, and Gary to care about my work. Big kisses to my grandmother Huguette. Kisses to my nephews and nieces. I am sad I had to go far away for this thesis and I did not see you as often as I wished.

Contents

List of Figures

List of Tables

Chapter 1

Introduction

The global mean atmospheric surface temperature increased by 0.85°C between 1880 and 2012, with most of the change occurring after 1970 (Hartmann et al., 2013). The leading explanations for this warming is the increase of anthropogenic greenhouse gases, in particular, carbon dioxide. During the industrial revolution, humankind began burning fossil fuels, increasing carbon dioxide concentration in the atmosphere by nearly 100 ppm ($\sim +30\%$) with respect to pre-industrial time. This amount is currently increasing at a rate of 2.13 ppm per year (data from NOAA ESRL-Station Mauna Loa: *http://www.esrl.noaa.gov*). Given the current increase rate, it is estimated by numerical models that Earth's mean temperature may increase 1 ± 0.5°C by 2050 (Kirtman et al., 2013). In the Arctic, the temperature increase is even more pronounced with an observed change of about 1.5°C, relative to 1951-1980, and a predicted warming of an additional $2-2.5$°C by 2050 (Kirtman et al., 2013).

The impacts of climate change are felt around the world. However, the Arctic is one of the regions the most sensitive to the changes (Kirtman et al., 2013). For example, it has been shown that the frequency of the extreme weather events (e.g., storms, extreme heat waves) over and near of the Arctic region are most likely going to increase in the future (Diffenbaugh et al., 2007; Mann and Emanuel, 2006). In addition, the sea surface rise due to land ice melt (e.g., Greenland Ice Sheet, and glaciers) will broadly impact the coastlines all over the world, flooding coastal infrastructures. The economic impacts of these changes will be astronomic, evaluated to cost several billions of CAD in total by the *Impacts, Adaptation and Vulnerability* group of the International Plant Protection Convention (IPPC) (Palut and Canziani, 2007) for both the prevention and the reorganization of the territories after changes occur.

1.1 Arctic geography

The Arctic Ocean is a Mediterranean type body of water surrounded by the North American continent and the Eurasian continent (see Figure 1.1). As shown in Figure 1.1, the largest island is Greenland, which is home to the largest ice sheet in the North Hemisphere. The Arctic Ocean covers around 14 million km^2 with an average depth of about 1038 m and a maximum depth of 5450 m. The Lomonosov Ridge divides the ocean, creating two basins: the Amerasian Basin and the Eurasian Basin. Both include smaller basins though that will be discussed in the subsequents chapters, when relevant.

Along the coast of Eurasia, the Eurasian continental shelves, often simply called Arctic Shelves, constitute three different shelves: the Chukchi Sea Shelf, Siberian Shelf, and Barents Shelf. Each is composed of at least one shallow sea, the Chukchi Sea for the first, the East Siberian, Laptev, and Kara Seas for the second, and the Barents Sea for the third.

Offshore of the North American coast, the land is occupied by the Canadian Arctic Archipelago (see Figure 1.2). This archipelago is composed of a tangle of small islands interconnected by shallow and narrow channels that connect the Amerasian Basin with Baffin Bay and the Hudson Bay Complex. The archipelago is composed of the Queen Elizabeth Islands (QEI, also known as the Sverdrup Basin) in the north, a region of relatively small islands and narrow channels, with only a few basins (see Figure 1.2). In the south, three main islands are present: Bank, Victoria and Prince of Wales Islands. This region is connected to the Arctic Ocean by the Amundsen Gulf. This part of the archipelago is separated by a relatively deep channel, Parry Channel, that is connected to the Arctic Ocean by the M'Clure Strait in the west and to Baffin Bay at Lancaster Sound. Additionally, between Greenland and Ellesmere Island, Nares Strait also connects the Arctic Ocean to Baffin Bay. Baffin Bay, is a deep body of water localized between Baffin Island and Greenland. South of Baffin Bay, lies the Labrador Sea between Canada and south-west Greenland. Lancaster Sound is also connected to the Gulf of Boothia, which is connected to the Hudson Bay Complex via Fury and Hecla Strait.

East of Greenland, the Nordic Seas are present between Greenland, Iceland, Norway, and Svalbard. They are separated from the North Atlantic by Denmark Strait between Greenland, and Iceland and the Iceland Scotland Ridge between Iceland and Scotland. In the north, the Barents Sea Opening separates the Nordic Seas and the Barents Sea while Fram Strait separates the Nordic Seas and the Arctic Ocean.

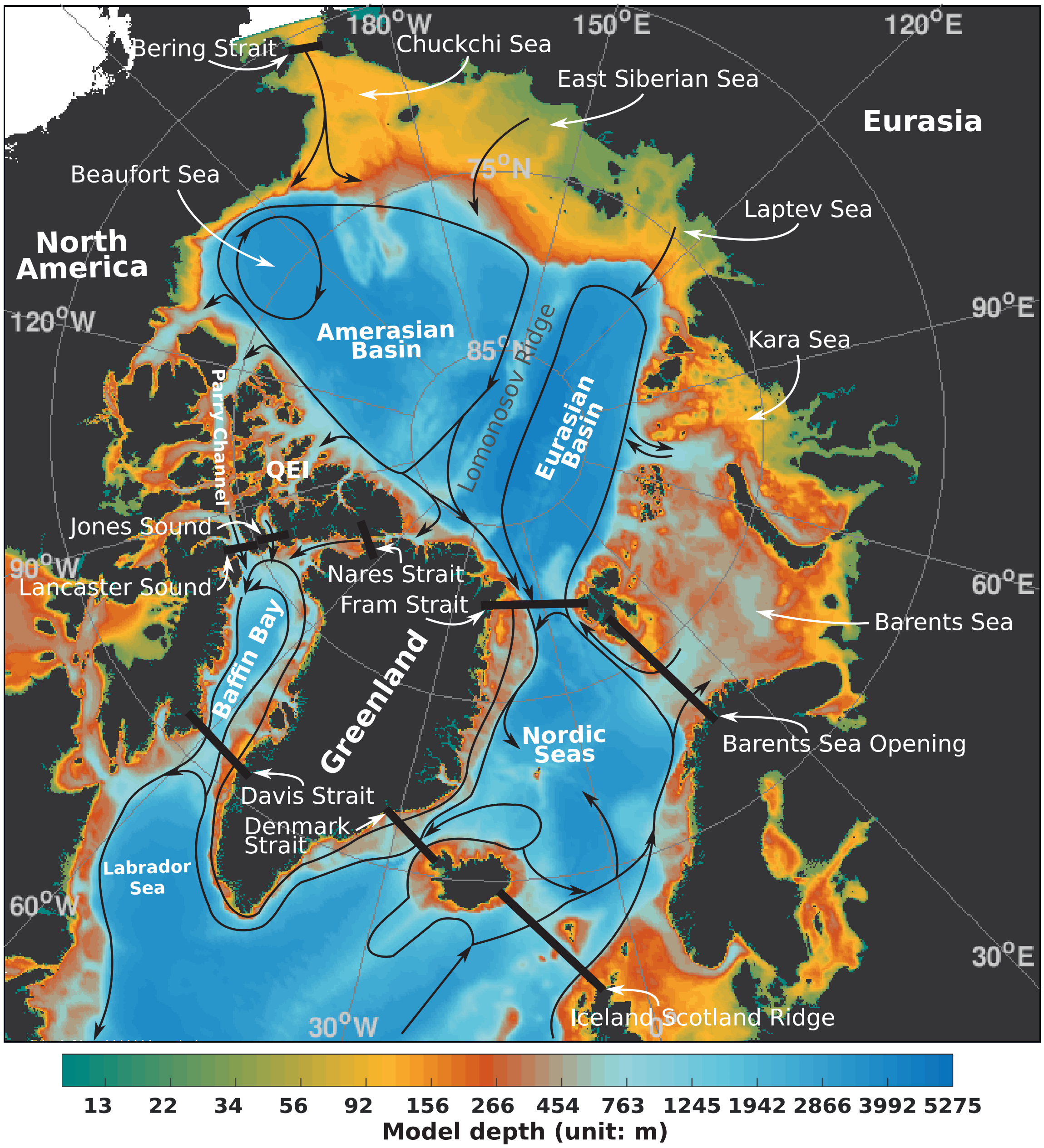

Figure 1.1: Map of the Arctic including the main geographical locations. A schematic of the upper ocean circulation is shown with black arrows. The black lines shows the main gates of the Arctic. The colormap indicates bathymetry used in this thesis work, in meters.

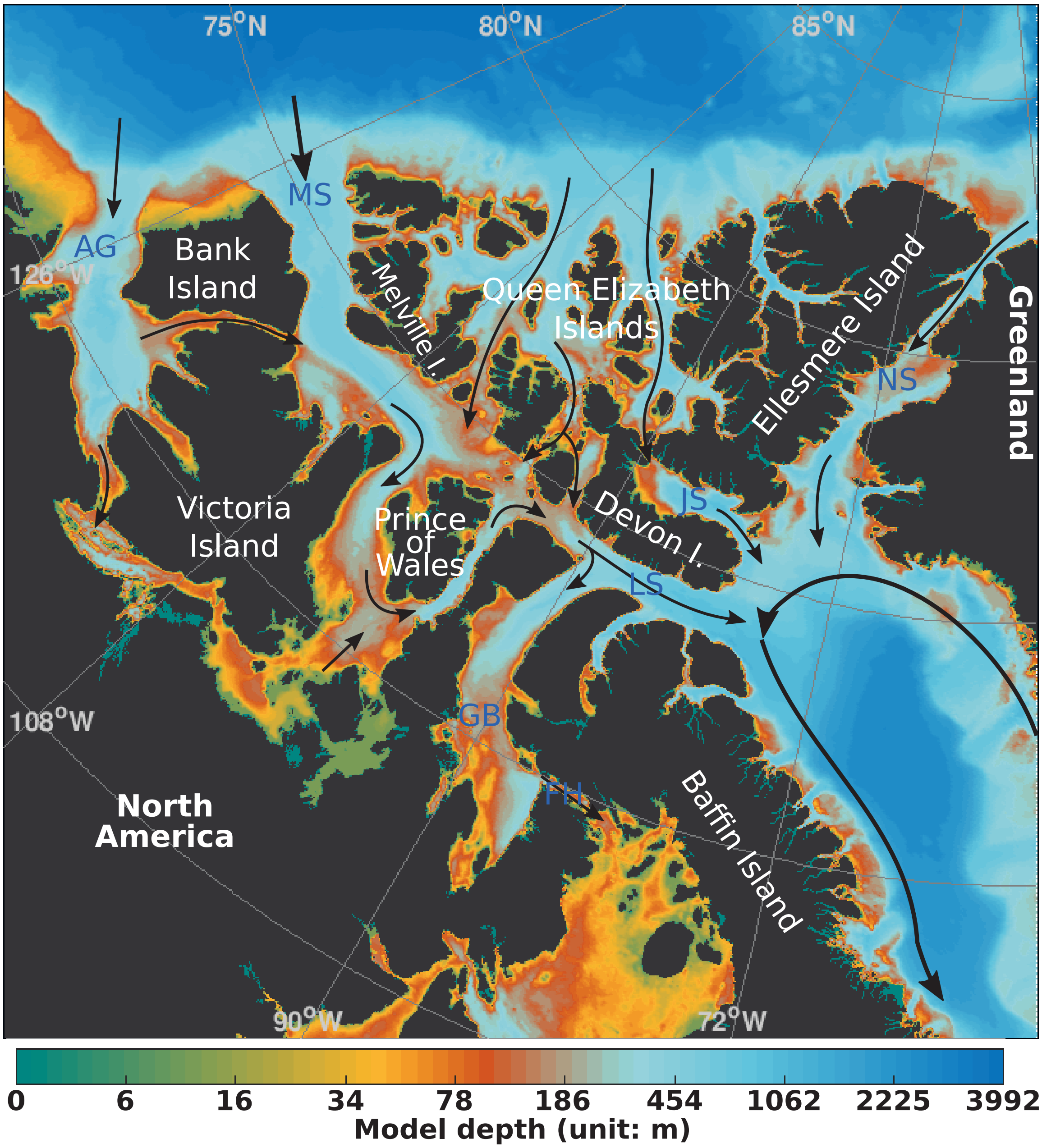

Figure 1.2: Map of the Canadian Arctic Archipelago. A schematic of the upper ocean circulation is shown with black arrows. AG: Amundsen Gulf, MS: M'Clure Strait, JS: Jones Sound, NS: Nares Strait, LS: Lancaster Sound, GB: Gulf of Boothia, FH: Fury and Hecla Strait. The colormap indicates bathymetry used in this thesis work, in meters.

1.2 Circulation in the Arctic

1.2.1 Pathways and structure

The Arctic Ocean receives cold and relatively fresh Pacific water from Bering Strait (Figure 1.1). The Pacific water inflow flows along the coast of North America and toward the Arctic Shelf (Talley et al., 2011). It will eventually leave the shallow shelves to reach the interior of the Arctic Ocean where it will mix with the cold and fresh Polar Mixed Water, or Arctic Water, a water mass (i.e., a volume of water with common salinity and temperature, as well as a common origin) created by the evaporation, precipitation, interaction with sea-ice melt and growth, as well as runoff (Rudels, 2001; Talley et al., 2011).

From the Atlantic Ocean, warm and salty Atlantic Water contained in the North Atlantic Current penetrates the Nordic Seas at the Iceland-Scotland Ridge (Talley et al., 2011). It follows the Norwegian shelf to the Barents Sea Opening where it can enter the Barents Sea to be further transformed before partially reentering the Nordic Seas via the Barents Sea Opening again (Talley et al., 2011). It will finally enter the Eurasian Basin via Fram Strait. The Barents Sea Opening is also directly connected to the Eurasian Basin (Talley et al., 2011).

The structure of the Arctic Ocean reflects the origin of each water mass that composes the water column. Under the Polar Mixed Water the salinity increases with depth, but not the temperature which stays close to the freezing point. This is the Arctic Ocean halocline which is formed due to the inflow of Pacific Water (Aagaard et al., 1981; Rudels, 2015; Talley et al., 2011). Under this layer, Atlantic Water, historically described as all the water above the 0°C isotherm, is present (Aagaard et al., 1981; Talley et al., 2011). Finally, the bottom layer is filled with the cold and salty Arctic Deep Water. We note that the halocline is different in the Eurasian and Amerasian Basins (Aagaard et al., 1981; Talley et al., 2011). The Pacific Water does not penetrate into the Eurasian Basin, so in this region the halocline is more strongly marked by the Atlantic Water and thus saltier (Aagaard et al., 1981; Coachman and Aagaard, 1974; Talley et al., 2011).

The deep circulation (i.e. more than 900 m depth) is nearly barotropic, rotating in a similar cyclonic way as the intermediate circulation (Talley et al., 2011). Each major basin (Eurasian and Amerasian) has its own circulation cell, with no transfer from one basin to the other due to the Locomonosov Ridge. The main pathway of the Arctic deep water in and out is through Fram Strait (Talley et al., 2011).

The intermediate circulation (i.e., 200 to 900 m depth) is largely cyclonic (Talley et al., 2011). Each major basin possesses its own cyclonic cell that is embedded into the large scale circulation, including the Beaufort Gyre where the surface anti-cyclonic circulation disappears. The major inflow of dense water is from brine rejected water from the continental shelves and the formation of deep water through deep convection in the Nordic Seas and Irminger Sea (Talley et al., 2011).

The upper layer circulation (i.e. 0 to 200 m depth) inside the Arctic Ocean is mainly anti-cyclonic in the Amerasian Basin and cyclonic in the Eurasian Basin (Rudels, 2001, 2015). These two basins are however joined by a current, called the Transpolar Drift, that leaves the Arctic Ocean at Fram Strait (Aagaard et al., 1985) to enter the Nordic Seas. The circulation in the Nordic Seas is cyclonic (Talley et al., 2011). It receives warm and salty water from the North Atlantic from the west (via Denmark Strait) and east of Iceland (via the Iceland Scotland Ridge). A strong southward flow is present east of Greenland, called the East Greenland Current (Timofeyev, 1962). This current splits south of Greenland into the Jan Mayen Current, most likely due to the topography. South of Greenland, this current bends to the west around Cape Farewell and becomes the West Greenland Current (Aagaard et al., 1985; Talley et al., 2011) going into Baffin Bay. Along the Norwegian coast, the North Atlantic Current becomes the Norwegian Atlantic Current that branches into the Barents Sea, following the coast. The second branch follows the Barents Sea Opening toward Fram Strait, where it eventually splits again, a part entering the Eurasian Basin while the remainder bends south, going back into the East Greenland Current and the Nordic Seas.

The second path for Arctic Water out of the Arctic is directly through the Canadian Arctic Archipelago, where it may enter via the Queen Elizabeth Islands, the Parry Channel, the Amundsen Gulf, or Nares Strait. The mean outflow is related to the baroclinic gradient (i.e., the pressure gradient, or sea surface height gradient) between the Beaufort Gyre and Northern Baffin Bay (e.g., Kliem and Greenberg (2003); Prinsenberg and Bennett (1987); Wang et al. (2017b); Wekerle et al. (2013)), as well as the atmospheric pattern over the Arctic that drives the short time scale variability of the outflow (e.g., Houssais and Herbaut (2011); Jahn et al. (2009); Peterson et al. (2012)). A weak southward flow goes through the Queen Elizabeth Islands (QEI) (Kliem and Greenberg, 2003; Lu et al., 2014; McGeehan and Maslowski, 2012; Wang et al., 2012; Wekerle et al., 2013; Zhang et al., 2016). The main flow goes through Parry Channel. The flow enters by M'Clure Strait in the west, then, due to the shallow sill at the end of the Viscount Melville Sound, the flow curves to the south into M'Clintock Channel, around Prince of Wales Island and north to Barrow Strait through Peel Sound (Wang et al., 2012). Finally, the Arctic outflow enters Baffin

Bay through Lancaster Sound, Jones Sound, and Nares Strait.

The circulation in Baffin Bay is mostly driven by a baroclinic gradient (Kliem and Greenberg, 2003; Myers and Ribergaard, 2013; Tang et al., 2004). The West Greenland Current brings warm and salty Irminger derived water. They import warm and salty water through the eastern part of Davis Strait (Cuny et al., 2005; Curry et al., 2014; Tang et al., 2004). They follow the continental shelf and slope in east Baffin Bay, with the West Greenland Current following the west coast of Greenland. In the north of Smith Sound, in northern Baffin Bay, this current curves to the west, following the east coast of Baffin Island toward the south. It is then called the Baffin Island Current (Münchow et al., 2015; Tang et al., 2004). The Polar outflow will mix in northern Baffin Bay with the water carried by the West Greenland Current before being exported to the Labrador Sea in the western part of Davis Strait. Finally, a cyclonic gyre exists in the center of Baffin Bay (Fissel et al., 1982; Tang et al., 2004).

1.2.2 Importance of atmospheric patterns

The atmospheric pattern over the Arctic reacts to the sea-level pressure that is usually low in the Barents Sea and high in the Eurasian Basin (Serreze and Barrett, 2011). The sea-level pressure variability (i.e., the amplitude) between the central and the Eurasian Arctic, and the Nordic Seas exceed the variability in the west Arctic (Morison et al., 2012). The Arctic Oscillation (Thompson and Wallace, 1998) describes the relative strength of each component, or, from a larger point of view, the strength of the polar vortex relative to the mid-latitude, translated into an index: the Arctic Oscillation Index.

The main atmospheric patterns in the Arctic as two polarities, namely, the positive and negative phase of the Arctic Oscillation. When the sea-level atmospheric pressure is high over the Beaufort Gyre and weak in the Eurasian Arctic, the winds are anticyclonic, increasing the strength of the gyre and the transpolar drift, and is defined as the negative phase. Conversely, during a positive phase, the weak Beaufort gyre permits the Pacific derived water to penetrate more into the Arctic, eventually being caught by a weaker transpolar drift to be exported through Fram Strait. They also leave through the Canadian Arctic Archipelago.

1.3 Freshwater in the Arctic

Commonly, in Arctic Oceanography we use the freshwater content of the water instead of the salt content. The freshwater is defined as the amount of pure fresh water needed to add (or remove) to a volume of water to bring it to a reference salinity. The reference salinity is usually set up as 34.8 in the Arctic to fit with the average salinity in the region (Aagaard and Carmack, 1989).

Recent estimates evaluate the Arctic Ocean freshwater content at about 93000 km^3 (Haine et al., 2015). The sources of freshwater in the Arctic are from runoff (38%), evaporation minus precipitation (E-P, 24%), and Bering Strait inflow (30%). Fram Strait and the Canadian Arctic Archipelago represent 51% (26% as liquid, 25% as solid) and 35% of the freshwater export, respectively (Serreze et al., 2006). Most of the storage in the Arctic is inside of the Beaufort Gyre (Proshutinsky et al., 2009; Serreze et al., 2006; Wang et al., 2016). The Arctic Oscillation plays an important role in the accumulation and release of the freshwater in the Beaufort Gyre, as well as in the freshwater export out of the Arctic. During the negative phase, the strong anticyclonic winds are pushing down the isopycnals leading to the accumulation of freshwater inside the Beaufort Gyre due to the convergence of Ekman transport (e.g., Manucharyan and Spall (2016); Manucharyan et al. (2016)). In addition, the anticyclonic winds increase the strength of the transpolar drift and make it fresher, due to more Pacific Water and runoff being trapped in the Beaufort Gyre. The opposite happens during the positive phase, when the winds are cyclonic, with weak freshwater storage in the Beaufort Gyre, and Pacific water is released to the transpolar drift. Moreover, the transport through the Canadian Arctic Archipelago is larger and the runoff from Eurasia can more freely penetrate into the Arctic Ocean during the positive phase. We note that the equilibrium of the Beaufort Gyre also depends on the mesoscale eddies that counteract the Ekman pumping (Manucharyan and Spall, 2016). Time scale of the Ekman pumping and the eddies however are not acting on the same timescale. A Beaufort Gyre that contains an important amount of freshwater will more easily release its freshwater during a switch in the Arctic Oscillation than an emptied Beaufort Gyre will refill (Manucharyan and Spall, 2016).

The location and motion of the freshwater inside and outside of the Arctic has an impact on the stability of the Arctic Ocean. The Arctic Ocean is a β-ocean (Carmack, 2007), meaning that the density is mainly a function of the water salinity. This implies that the stability of the water column is mainly controlled by the freshwater content. More freshwater contained in the water column, the less dense the water will be. A strong halocline, (i.e., a strong salinity gradient in the water column) will result in strong stratification and an reduction of vertical mixing.

Outside of the Arctic, the freshwater fluxes have a direct impact on the Earth's climate.

The most important examples in the recent past are related to the Great Salinity Anomalies of the 1970s and 1980s (Belkin et al., 1998; Dickson et al., 1988). These events correspond to the propagation over about a decade of a strong negative salinity anomaly (i.e., fresher than usual) from the Arctic Ocean to the North Atlantic and back to the Barents Sea (Belkin et al., 1998). The origin of these anomalies is the release of freshwater from the Beaufort Gyre (Belkin et al., 1998) that left the Arctic through Fram Strait in the 1970s and through the Canadian Arctic Archipelago route in the 1980s. These anomalies reached the Labrador Sea, where it has been reported to be the cause of the shut down of deep convection in the Labrador Sea (Gelderoos et al., 2012).

The deep convection is the result of breaking the stratification of the upper layer of the ocean due to strong heat loss at the surface, making the surface water sink in the deep ocean, thus trapping carbon dioxide in the deeper part of the ocean. It also controls the northern part of the Atlantic Meridional Overturning Circulation (AMOC), a part of the Conveyor Belt. The concept, originally described by Stommel (1961), explains that the Earth's atmosphere and ocean are not at an equilibrium state. Because of the tilting of the Earth, the equator region receives more energy than the pole. This excess of energy has somehow to be equilibrated and thus heat has to leave the equator towards the pole (e.g., Ganachaud and Wunsch (2001); Hall and Bryden (1982); Trenberth and Caron (2001)). The conveyor belt is one of the mechanics that helps to "fix" this imbalance. If the Labrador Sea receives more freshwater from the Arctic, the heat loss in winter can become insufficient to break the stratification (Gelderoos et al., 2012). If the stratification is broken only over a shallow depth, the surface water cannot reach the deeper part of the ocean and thus the amount of carbon dioxide trapped in the ocean will be reduced (e.g., Jahn and Holland (2013); Marshall and Schott (1999); Rhein et al. (2011)). This carbon dioxide will stay in the atmosphere and further contribute to global warming and the freshwater and heat will be differently redistributed around the planet. Recent estimates showed that the AMOC speed could be reduced by 15 to 20 % in the future (Rahmstorf et al., 2015). Vellinga and Wood (2002) showed that a major addition of freshwater in the upper part of the North Atlantic could lead to a collapse of the AMOC, which results in a cooling of the North Hemisphere by $1-2$ °C on average. Moreover, a warming of the southern hemisphere by 0.2°C on average and major modification on the atmospheric global precipitation pattern would occur. A modification of the mean temperature over the globe will impact significantly human activities. Locally the changes may be much stronger with a decrease up to 8 °C in the northern hemisphere and an increase up to 1°C in the southern hemisphere (Vellinga and Wood, 2002). We note that if the deep convection is important in the Labrador Sea, it is not the only location where deep convection occurs. It is also present in the Nordic Seas and Weddell Sea, close to Antarctica (e.g., Killworth (1983); Pickart et al. (2003).

1.4 Impact of Climate Change in the Arctic

In response to the surface temperature increases, the sea-ice coverage of the Arctic decreased significantly (Hartmann et al., 2013; Walsh, 2014) and faster than initially forecasted (Stroeve et al., 2007). Since 1979 the mean Arctic sea-ice extent decreased by 35000 ± 3900 km^{2}yr^{-1} ($-1.47 \pm 0.25\%$ decade^{-1}). This decrease is observed in every season and every month. September is impacted the most, with a trend of about $-2.2 \pm 0.4\%$ decade^{-1} (Parkinson, 2014). The sea-ice thickness also decreased by 1.7 m on average between 1980 and 2008. Recent years show an acceleration in the trend, with a thinning rate that increased from 0.08 m yr^{-1} in 1990 to 0.20 m yr^{-1} in the early 2000s (Kwok and Rothrock, 2009; Laxon et al., 2013).

The decreasing of the sea-ice cover has several impacts on the Arctic system. The most prominent is on the energy balance. With the opening of more ice free areas, more exchange between the newly open ocean and the atmosphere is possible, increasing the moisture supply to the atmosphere, the formation of clouds, and decreasing the global albedo (Screen and Simmonds, 2010). The consequences on the energy budget is complex. However, given the current state of knowledge, the resulting ice-temperature positive feedback leads to an increasing chance of further rapid warming and sea ice loss (Screen and Simmonds, 2010).

The Arctic Ocean is also impacted by global warming. The Atlantic water is becoming more predominant in the Arctic Ocean (Morison et al., 2012). This layer is also warming up, with an increase over 1°C over the Lomonosov Ridge in the late 1990s (Morison et al., 2000). The patterns of the storms is also modified in winter, which might eventually impact the Labrador Sea (Wang et al., 2017a) and eventually the whole Arctic Oscillation. The combination of a warmer ocean and atmosphere leads to an increase in the mass loss of the Greenland Ice Sheet, increasing the runoff from Greenland (Bamber et al., 2012; Howell et al., 2008; Myers and Ribergaard, 2013) and sea-ice melt (Steele et al., 2010). Moreover, the reduction of the sea-ice will increase the impact of winds on the oceanic transports, increasing the impact of atmospheric synoptic events all around the year (Chapter 4).

Finally, the increased sea-ice melt and runoff will increase the amount of freshwater in the upper layer of the ocean, which have the potential to impact the dynamics of the ocean. An increase in Greenland runoff, for example, can significantly change the circulation in

Baffin Bay (Castro de la Guardia et al., 2015; Grivault et al., 2017), increasing the warm water inflow from the Irminger Sea and reducing the freshwater throughflow. Increasing the runoff in the Arctic leads to similar results on the ocean, by increasing the stratification, and warming even more the Atlantic Water layer (e.g., Nummelin et al. (2016)). Moreover, the North Atlantic becomes colder and fresher (Nummelin et al., 2016), which leads to the impact on the AMOC and climate discussed previously.

1.5 Motivation and goals

For this thesis work, I will focus on the pathways out of the Arctic and, in particular, how the volume and freshwater fluxes can be modified along their way towards the North Atlantic. The understanding of these dynamics is key to determine what future changes may do to the North Atlantic, and the Labrador Sea in particular. This step is one of the many in understanding the dynamics of the Arctic outflow, how it may change in the future and how it might impact Earth's climate. I answer the following questions: (Q1) How the circulation in Baffin Bay will change in response to enhanced Greenland runoff and how it will impact the Arctic outflow towards the North Atlantic? (Q2) What is the impact of the surface stress on the volume and freshwater fluxes through the Canadian Arctic Archipelago? (Q3) What are the timescales associated with flux variability of the Arctic Ocean Gateways? These questions are answered with separate chapters organized with their own introduction, description of the method used, results, discussion, and conclusions for each question.

To answer these questions, I use a state-of-art ocean/sea-ice numerical framework, used with various configurations depending on each question. For Q1 I use two numerical experiments to compare the response of Baffin Bay dynamics to enhanced runoff from Greenland and the impacts on the freshwater fluxes leaving the Arctic at Davis Strait. Climatic forcing is used in order to push forwards in time and complete this study with insight on the future changes that may occur during the 21$^{\text{st}}$ century. For Q2, I use a high resolution (both temporal and spatial) atmospheric forcing coupled with a high resolution oceanic model to compute the surface stress during the fully ice covered and partially ice covered periods of the Canadian Arctic Archipelago and I analyze how the momentum exchange between the atmosphere and the sea-ice impact the volume and freshwater fluxes through the Archipelago and how it may change in the future with the sea-ice cover decline. Finally, for Q3, I use a climate product run over the last 4 decades to explain what is impacting the volume and freshwater variability outflow at the Arctic Ocean gateways.

This thesis is organized as the following. This introduction is Chapter 1. In Chapter 2 I describe the numerical framework used for this thesis (NEMO). This chapter contains only the details on the model that are shared by all the following chapters. Any specific configuration used to answer a question will be specified in the corresponding chapter. Chapter 3, Chapter 4, and Chapter 5 are written as independent chapters that answer to Q1, Q2, and Q3, respectively. Chapter 6 will summarize the main findings and highlight the scientific significance of our work.

Bibliography

Aagaard, K. and Carmack, E. C. (1989). The role of sea ice and other fresh water in the Arctic circulation. *Journal of Geophysical Research*, 94(C10):14485.

Aagaard, K., Coachman, L., and Carmack, E. (1981). On the halocline of the Arctic Ocean. *Deep Sea Research Part A. Oceanographic Research Papers*, 28(6):529–545.

Aagaard, K., Swift, J., and Carmack, E. (1985). Thermohaline circulation in the Arctic Mediterranean seas. *Journal of Geophysical Research: Oceans*, 90(C3):4833–4846.

Bamber, J., van den Broeke, M., Ettema, J., Lenaerts, J., and Rignot, E. (2012). Recent large increases in freshwater fluxes from greenland into the north atlantic. *Geophysical Research Letters*, 39(19):n/a–n/a.

Belkin, I. M., Levitus, S., Antonov, J., and Malmberg, S.-A. (1998). "great salinity anomalies" in the North Atlantic. *Progress in Oceanography*, 41(1):1–68.

Carmack, E. C. (2007). The alpha/beta ocean distinction: A perspective on freshwater fluxes, convection, nutrients and productivity in high-latitude seas. *Deep Sea Research Part II: Topical Studies in Oceanography*, 54(23-26):2578–2598.

Castro de la Guardia, L., Hu, X., and Myers, P. G. (2015). Potential positive feedback between greenland ice sheet melt and Baffin Bay heat content on the west Greenland shelf. *Geophysical Research Letters*, 42(12):4922–4930. 2015GL064626.

Coachman, L. K. and Aagaard, K. (1974). Physical oceanography of Arctic and subarctic seas. In *Marine geology and oceanography of the Arctic seas*, pages 1–72. Springer.

Cuny, J., Rhines, P. B., and Kwok, R. (2005). Davis Strait volume, freshwater and heat fluxes. *Deep Sea Research Part I: Oceanographic Research Papers*, 52(3):519–542.

Curry, B., Lee, C. M., Petrie, B., Moritz, R. E., and Kwok, R. (2014). Multiyear volume, liquid freshwater, and sea ice transports through Davis Strait, 2004–10*. *Journal of Physical Oceanography*, 44(4):1244–1266.

Dickson, R. R., Meincke, J., Malmberg, S.-A., and Lee, A. J. (1988). The "Great Salinity Anomaly" in the northern North Atlantic 1968–1982. *Progress in Oceanography*, 20(2):103–151.

Diffenbaugh, N. S., Pal, J. S., Giorgi, F., and Gao, X. (2007). Heat stress intensification in the Mediterranean climate change hotspot. *Geophysical Research Letters*, 34(11).

Fissel, D., Lemon, D., and Birch, J. (1982). Major features of the summer near-surface circulation of western Baffin Bay, 1978 and 1979. *ARCTIC*, 35(1):180–200.

Ganachaud, A. and Wunsch, C. (2001). correction: Improved estimates of global ocean circulation, heat transport and mixing from hydrographic data. *Nature*, 410(6825):240–240.

Gelderoos, R., Straneo, F., and Katsman, C. (2012). Mechanisms behind the temporary shutdown of deep convection in the labrador sea: Lessons from the Great Salinity Anomaly years 1968-71. *Journal of Climate*, 25:6743–6755.

Grivault, N., Hu, X., and Myers, P. G. (2017). Evolution of Baffin Bay water masses and transports in a numerical sensitivity experiment under enhanced greenland melt. *Atmosphere-Ocean*, 55(3):169–194.

Haine, T. W., Curry, B., Gerdes, R., Hansen, E., Karcher, M., Lee, C., Rudels, B., Spreen, G., de Steur, L., Stewart, K. D., and et al. (2015). Arctic freshwater export: Status, mechanisms, and prospects. *Global and Planetary Change*, 125:13–35.

Hall, M. M. and Bryden, H. L. (1982). Direct estimates and mechanisms of ocean heat transport. *Deep Sea Research Part A. Oceanographic Research Papers*, 29(3):339–359.

Hartmann, D. L., Tank, A. M. K., Rusticucci, M., Alexander, L. V., Brönnimann, S., Charabi, Y. A. R., Dentener, F. J., Dlugokencky, E. J., Easterling, D. R., Kaplan, A., et al. (2013). Observations: atmosphere and surface. In *Climate Change 2013 the Physical Science Basis: Working Group I Contribution to the Fifth Assessment Report of the Intergovernmental Panel on Climate Change*. Cambridge University Press.

Houssais, M.-N. and Herbaut, C. (2011). Atmospheric forcing on the Canadian Arctic Archipelago freshwater outflow and implications for the Labrador Sea variability. *Journal of Geophysical Research*, 116.

Howell, S. E., Tivy, A., Yackel, J. J., and McCourt, S. (2008). Multi-year sea-ice conditions in the western Canadian arctic archipelago region of the northwest passage: 1968–2006. *Atmosphere-Ocean*, 46(2):229–242.

Jahn, A. and Holland, M. M. (2013). Implications of Arctic sea ice changes for north atlantic deep convection and the meridional overturning circulation in CCSM4-CMIP5 simulations. *Geophysical Research Letters*, 40(6):1206–1211.

Jahn, A., Tremblay, B., Mysak, L. A., and Newton, R. (2009). Effect of the large-scale atmospheric circulation on the variability of the Arctic Ocean freshwater export. *Climate Dynamics*, 34(2-3):201–222.

Killworth, P. D. (1983). Deep convection in the world ocean. *Reviews of Geophysics*, 21(1):1–26.

Kirtman, B., Power, S., Adedoyin, J., Boer, G., Bojariu, R., Camilloni, I., Doblas-Reyes, F., Fiore, A., Kimoto, M., Meehl, G., Prather, M., Sarr, A., Schär, C., Sutton, R., van Oldenborgh, G., Vecchi, G., and Wang, H. (2013). *Near-term Climate Change: Projections and Predictability*, book section 11, pages 953–1028. Cambridge University Press, Cambridge, United Kingdom and New York, NY, USA.

Kliem, N. and Greenberg, D. A. (2003). Diagnostic simulations of the summer circulation in the Canadian arctic archipelago. *Atmosphere-Ocean*, 41(4):273–289.

Kwok, R. and Rothrock, D. A. (2009). Decline in Arctic sea ice thickness from submarine and ICESat records: 1958-2008. *Geophysical Research Letters*, 36(15):n/a–n/a.

Laxon, S. W., Giles, K. A., Ridout, A. L., Wingham, D. J., Willatt, R., Cullen, R., Kwok, R., Schweiger, A., Zhang, J., Haas, C., Hendricks, S., Krishfield, R., Kurtz, N., Farrell, S., and Davidson, M. (2013). CryoSat-2 estimates of arctic sea ice thickness and volume. *Geophysical Research Letters*, 40(4):732–737.

Lu, Y., Higginson, S., Nudds, S., Prinsenberg, S., and Garric, G. (2014). Model simulated volume fluxes through the Canadian Arctic Archipelago and Davis Strait: Linking monthly variations to forcing in different seasons. *Journal of Geophysical Research: Oceans*, 119(3):1927–1942.

Mann, M. E. and Emanuel, K. A. (2006). Atlantic hurricane trends linked to climate change. *Eos, Transactions American Geophysical Union*, 87(24):233.

Manucharyan, G. E. and Spall, M. A. (2016). Wind-driven freshwater buildup and release in the Beaufort Gyre constrained by mesoscale eddies. *Geophysical Research Letters*, 43(1):273–282.

Manucharyan, G. E., Spall, M. A., and Thompson, A. F. (2016). A theory of the wind-driven Beaufort Gyre variability. *Journal of Physical Oceanography*, 46(11):3263–3278.

Marshall, J. and Schott, F. (1999). Open-ocean convection: Observations, theory, and models. *Reviews of Geophysics*, 37(1):1–64.

McGeehan, T. and Maslowski, W. (2012). Evaluation and control mechanisms of volume and freshwater export through the Canadian Arctic Archipelago in a high-resolution pan-Arctic ice-ocean model. *Journal of Geophysical Research: Oceans*, 117(C8):n/a–n/a.

Morison, J., Aagaard, K., and Steele, M. (2000). Recent environmental changes in the Arctic: A review. *ARCTIC*, 53(4).

Morison, J., Kwok, R., Peralta-Ferriz, C., Alkire, M., Rigor, I., Andersen, R., and Steele, M. (2012). Changing Arctic Ocean freshwater pathways. *Nature*, 481(7379):66–70.

Münchow, A., Falkner, K. K., and Melling, H. (2015). Baffin Island and West Greenland Current systems in northern Baffin Bay. *Progress in Oceanography*, 132:305–317.

Myers, P. G. and Ribergaard, M. H. (2013). Warming of the Polar Water layer in Disko Bay and potential impact on Jakobshavn Isbrae. *Journal of Physical Oceanography*, 43(12):2629–2640.

Nummelin, A., Ilicak, M., Li, C., and Smedsrud, L. H. (2016). Consequences of future increased Arctic runoff on Arctic Ocean stratification, circulation, and sea ice cover. *Journal of Geophysical Research: Oceans*, 121(1):617–637.

Palut, M. P. J. and Canziani, O. F. (2007). *Contribution of working group II to the fourth assessment report of the intergovernmental panel on climate change*. Cambridge University Press.

Parkinson, C. L. (2014). Global sea ice coverage from satellite data: Annual cycle and 35-yr trends. *Journal of Climate*, 27(24):9377–9382.

Peterson, I., Hamilton, J., Prinsenberg, S., and Pettipas, R. (2012). Wind-forcing of volume transport through Lancaster Sound. *Journal of Geophysical Research: Oceans*, 117(C11):n/a–n/a.

Pickart, R. S., Spall, M. A., Ribergaard, M. H., Moore, G., and Milliff, R. F. (2003). Deep convection in the Irminger Sea forced by the Greenland tip jet. *Nature*, 424(6945):152.

Prinsenberg, S. and Bennett, E. (1987). Mixing and transports in Barrow Strait, the central part of the Northwest passage. *Continental Shelf Research*, 7(8):913–935.

Proshutinsky, A., Krishfield, R., Timmermans, M.-L., Toole, J., Carmack, E., McLaughlin, F., Williams, W. J., Zimmermann, S., Itoh, M., and Shimada, K. (2009). Beaufort Gyre freshwater reservoir: State and variability from observations. *Journal of Geophysical Research*, 114.

Rahmstorf, S., Box, J. E., Feulner, G., Mann, M. E., Robinson, A., Rutherford, S., and Schaffernicht, E. J. (2015). Exceptional twentieth-century slowdown in Atlantic Ocean overturning circulation. *Nature Climate Change*, 5:475.

Rhein, M., Kieke, D., Hüttl-Kabus, S., Roessler, A., Mertens, C., Meissner, R., Klein, B., Böning, C. W., and Yashayaev, I. (2011). Deep water formation, the subpolar gyre, and the meridional overturning circulation in the subpolar North Atlantic. *Deep Sea Research Part II: Topical Studies in Oceanography*, 58(17-18):1819–1832.

Rudels, B. (2001). Arctic Basin circulation. *Encyclopedia of Ocean Sciences*, pages 177–187.

Rudels, B. (2015). Arctic Ocean circulation, processes and water masses: A description of observations and ideas with focus on the period prior to the International Polar Year 2007–2009. *Progress in Oceanography*, 132:22–67.

Screen, J. A. and Simmonds, I. (2010). The central role of diminishing sea ice in recent Arctic temperature amplification. *Nature*, 464(7293):1334–1337.

Serreze, M. C. and Barrett, A. P. (2011). Characteristics of the Beaufort Sea High. *Journal of Climate*, 24(1):159–182.

Serreze, M. C., Barrett, A. P., Slater, A. G., Woodgate, R. A., Aagaard, K., Lammers, R. B., Steele, M., Moritz, R., Meredith, M., and Lee, C. M. (2006). The large-scale freshwater cycle of the Arctic. *Journal of Geophysical Research*, 111(C11).

Steele, M., Zhang, J., and Ermold, W. (2010). Mechanisms of summertime upper Arctic Ocean warming and the effect on sea ice melt. *Journal of Geophysical Research*, 115(C11).

Stommel, H. (1961). Thermohaline convection with two stable regimes of flow. *Tellus*, 13(2):224–230.

Stroeve, J., Holland, M. M., Meier, W., Scambos, T., and Serreze, M. (2007). Arctic sea ice decline: Faster than forecast. *Geophysical Research Letters*, 34(9).

Talley, L. D., Pickard, G. L., Emery, W. J., and Switft, J. H. (2011). Arctic Ocean and Nordic Seas.

Tang, C. C., Ross, C. K., Yao, T., Petrie, B., DeTracey, B. M., and Dunlap, E. (2004). The circulation, water masses and sea-ice of Baffin Bay. *Progress in Oceanography*, 63(4):183–228.

Thompson, D. W. J. and Wallace, J. M. (1998). The Arctic Oscillation signature in the wintertime geopotential height and temperature fields. *Geophysical Research Letters*, 25(9):1297–1300.

Timofeyev, V. (1962). The movement of Atlantic Water and heat into the Arctic basin. *Deep Sea Research and Oceanographic Abstracts*, 9(7-10):358–361.

Trenberth, K. E. and Caron, J. M. (2001). Estimates of meridional atmosphere and ocean heat transports. *Journal of Climate*, 14(16):3433–3443.

Vellinga, M. and Wood, R. A. (2002). Global climatic impacts of a collapse of the Atlantic thermohaline circulation. *Climatic Change*, 54(3):251–267.

Walsh, J. E. (2014). Intensified warming of the Arctic: Causes and impacts on middle latitudes. *Global and Planetary Change*, 117:52–63.

Wang, J., Kim, H.-M., and Chang, E. K. M. (2017a). Changes in Northern Hemisphere winter storm tracks under the background of Arctic Amplification. *Journal of Climate*, 30(10):3705–3724.

Wang, Q., Ilicak, M., Gerdes, R., Drange, H., Aksenov, Y., Bailey, D. A., Bentsen, M., Biastoch, A., Bozec, A., Böning, C., Cassou, C., Chassignet, E., Coward, A. C., Curry, B., Danabasoglu, G., Danilov, S., Fernandez, E., Fogli, P. G., Fujii, Y., Griffies, S. M., Iovino, D., Jahn, A., Jung, T., Large, W. G., Lee, C., Lique, C., Lu, J., Masina, S., Nurser, A. G., Rabe, B., Roth, C., y Mélia, D. S., Samuels, B. L., Spence, P., Tsujino, H., Valcke, S., Voldoire, A., Wang, X., and Yeager, S. G. (2016). An assessment of the Arctic Ocean in a suite of interannual CORE-II simulations. part II: Liquid freshwater. *Ocean Modelling*, 99:86–109.

Wang, Q., Myers, P. G., Hu, X., and Bush, A. B. (2012). Flow constraints on pathways through the Canadian Arctic Archipelago. *Atmosphere-Ocean*, 50(3):373–385.

Wang, Z., Hamilton, J., and Su, J. (2017b). Variations in freshwater pathways from the Arctic Ocean into the North Atlantic Ocean. *Progress in Oceanography*, 155:54–73.

Wekerle, C., Wang, Q., Danilov, S., Jung, T., and Schröter, J. (2013). The Canadian Arctic Archipelago throughflow in a multiresolution global model: Model assessment and the driving mechanism of interannual variability. *Journal of Geophysical Research: Oceans*, 118(9):4525–4541.

Zhang, Y., Chen, C., Beardsley, R. C., Gao, G., Lai, Z., Curry, B., Lee, C. M., Lin, H., Qi, J., and Xu, Q. (2016). Studies of the Canadian Arctic Archipelago water transport and its relationship to basin-local forcings: Results from AO-FVCOM. *Journal of Geophysical Research: Oceans*, 121(6):4392–4415.

Chapter 2

Numerical Frameworks: Nucleus for European Modelling of the Ocean (NEMO)

The Nucleus for European Modelling of the Ocean (NEMO) is a state-of-art numerical framework developed to be a robust solution for numerical oceanography research, operational oceanography, seasonal forecasting and climate studies. The framework is composed of 5 components, each managing a component of the ocean system:

- The blue ocean (ocean dynamics, NEMO-OPA)
- The white ocean (sea-ice, NEMO-LIM)
- The green ocean (biogeochemistry, NEMO-TOP)
- The assimilation component (NEMO-TAM)
- The adaptive mesh refinement software (AGRIF)

Each component is usable individually, but NEMO provides its full strength when the modules are used together. Each component is independently parameterizable and possesses several numerical approaches to study of the ocean system. For instance, multiple coordinate systems, parametrization choices of the turbulence or multiple treatment of the surface boundary layer are available. In this chapter, I will provide details about the components used in my studies: The blue (ocean) and white (sea-ice) and their configurations. The full documentation, the official updates and announcements are published on the official NEMO website: *http://www.nemo-ocean.eu*.

This chapter is organized as the following: the model approximations are going to be discussed in section 2.1. A description of the ocean component is provided (section 2.2).

Section 2.3 describes the grid on which the physics is resolved. Section 2.4 describes how the unresolvable physics is parametrized. Section 2.5 explains how the surface boundary layer is treated. Finally, Section 2.6 describes the sea-ice model used.

2.1 Model assumption

NEMO uses the following set of mathematical approximations:

(1) Spherical earth approximation:

The Earth is considered to be a sphere instead of an ellipsoid. Consequently, the geopotential surfaces are assumed to be spheres, so that acceleration of gravity is, at every point, aligned with the earth's radius.

(2) Thin-shell approximation:

The ocean depth is neglected compared to the Earth's radius. Even the deepest part of the ocean (i.e., Marianas Trench, 10994 m depth) is shallow with respect to the 6371 10^3 m of the Earth's radius.

(3) Hydrostatic hypothesis:

The vertical momentum equation is reduced to a balance between the vertical pressure gradient and the buoyancy force. This statement removes the explicit resolution of the convective processes from the Navier-Stokes equations, which are instead parametrized.

(4) Boussinesq approximation:

Density differences are neglected except if they are associated with the acceleration due to gravity, such as the buoyancy force. This means that the difference in inertia is negligible but gravity is strong enough to make the specific weight (i.e., the weight per volume unit) appreciably different when the fluid properties changes (e.g., layers with two different density).

(5) Incompressibility hypothesis:

At an infinitesimal scale, the flow density (ρ) is constant when following the flow motion ($\frac{D\rho}{Dt} = 0$). Combined with the continuity equation ($\frac{\partial\rho}{\partial t} + \rho\nabla\cdot\mathbf{U} = 0$), the three-dimensional divergence of the velocity vector ($\mathbf{U}$) is assumed to be zero ($\nabla\cdot\mathbf{U} = 0$).

(6) Turbulent closure hypothesis:

The turbulent fluxes (the small scale processes) are expressed in terms of large scale-

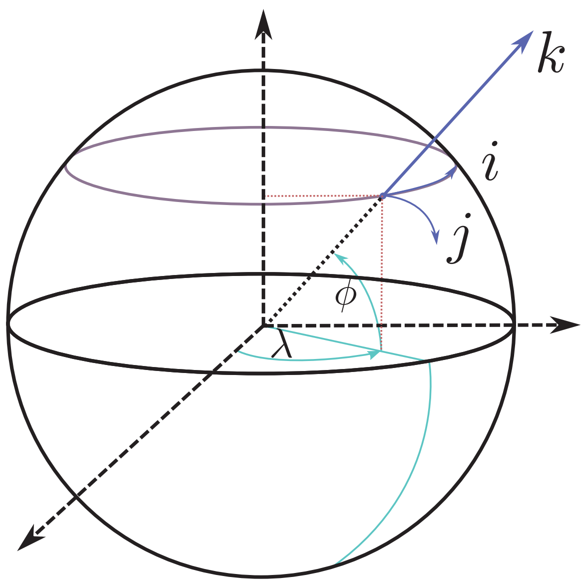

Figure 2.1: Spherical coordinate system used by NEMO.

features. This approximation is according to Reynolds (1895). A fluid can be decomposed between the time mean flow and the variation from the mean (turbulent flow). The application of the Reynolds decomposition to the Navier-Stokes equations leads to the appearance of unknown turbulent fluxes terms. The system is closed by the parameterization of these unknown terms by a closure scheme (see section 2.4).

2.2 Ocean component

2.2.1 Coordinate system

I use a curvilinear z-coordinate system (the vertical levels are fixed at given depths). Based on the spherical and thin layer approximations, the local upward vector $\mathbf{k}$ is defined as the z-axis, and the horizontal plane is chosen with the unit vectors ($\mathbf{i}$, $\mathbf{j}$) orthogonal to $\mathbf{k}$ (Figure 2.1). The horizontal plane can be defined in any possible way. The $\mathbf{i}$ and $\mathbf{j}$ origin are set up at the bottom left boundary of the domain, with indexes increasing going eastwards and northwards, respectively. At the convergence of the meridians in the standard geographical latitude-longitude grid system a singularity appears (Madec and Imbard, 1996). To avoid the above issue, a tri-polar grid transformation is applied. This consists of a grid rotated and re-projected to displace the singularity to land instead of at the poles, such as proposed by Murray (1996) and Madec and Imbard (1996). Consequently, the $\mathbf{i}$-axis and $\mathbf{j}$-axis are not aligned with lines of longitude and latitude, respectively.

2.2.2 Primitive equations

The physics of the oceans is well described by the fluid dynamic primitive equations (i.e., the Navier-Stokes equations) along with a non linear equation of state which couples the two active tracers, namely the temperature and salinity of the fluid, to the fluid velocity. With the above six model assumptions, a set of seven primitive equations to govern the model ocean physics are used:

$$\frac{\partial \mathbf{U_h}}{\partial t} = \underbrace{(\nabla \times \mathbf{U_h}) \times \mathbf{U_h} + \frac{1}{2}\nabla \mathbf{U_h}^2}_{\text{Inertia force}} - \underbrace{f\mathbf{k} \times \mathbf{U_h}}_{\text{Coriolis force}} - \underbrace{\frac{1}{\rho_0}\nabla_h p}_{\text{Pressure gradient force}} + \underbrace{\mathbf{D^U} + \mathbf{F^U}}_{\text{Subgrid parameterization + surface forces}} \tag{2.1a}$$

$$\frac{\partial p}{\partial z} = \underbrace{-\rho g}_{Hydrostatic} \tag{2.1b}$$

$$\nabla \cdot \mathbf{U} = \underbrace{0}_{\text{Incompressibility}} \tag{2.1c}$$

$$\rho = \underbrace{\rho(T, S, p)}_{\text{Water density function}} \tag{2.1d}$$

$$\frac{\partial T}{\partial t} = \underbrace{-\nabla \cdot (T\mathbf{U})}_{\text{Heat divergence}} + \underbrace{\mathbf{D^T} + \mathbf{F^T}}_{\text{Subgrid parameterization + surface forces}} \tag{2.1e}$$

$$\frac{\partial S}{\partial t} = \underbrace{-\nabla \cdot (S\mathbf{U})}_{\text{Salt divergence}} + \underbrace{\mathbf{D^S} + \mathbf{F^S}}_{\text{Subgrid parameterization + surface forces}} \tag{2.1f}$$

where the 3D velocity is defined by $\mathbf{U} = \mathbf{U_h} + w\mathbf{k}$, with $\mathbf{U_h}$ is the horizontal velocity defined on the plane $(\mathbf{i}, \mathbf{j})$, w is the vertical velocity, T is the potential temperature, S is the salinity, ρ the in-situ density, ρ_0 is the reference density, p is the pressure, g is the gravitational acceleration and $f = 2\Omega\ \sin\phi$ is the Coriolis parameter (Ω is the Earth's angular velocity and ϕ the latitude). $\mathbf{D^U}$, $\mathbf{D^T}$ and $\mathbf{D^S}$ are the parameterization of subgrid scale diffusion for, respectively, momentum, potential temperature and salinity (see section 2.4) and $\mathbf{F^U}$, $\mathbf{F^T}$ and $\mathbf{F^S}$ are the surface forcing term for, respectively, momentum, potential temperature and salinity (see section 2.5). A list of all physical parameters used in NEMO is provided in Table 2.1.

The model has two boundaries located at the air-ocean or ice-ocean interfaces for the upper boundary ($z = \eta(i, j, k, t)$; see Figure 2.2) and at the contact with the topography ($z = -H(i, j)$). η is the representation of the sea surface height ($k = 1$) and H is the bottom of

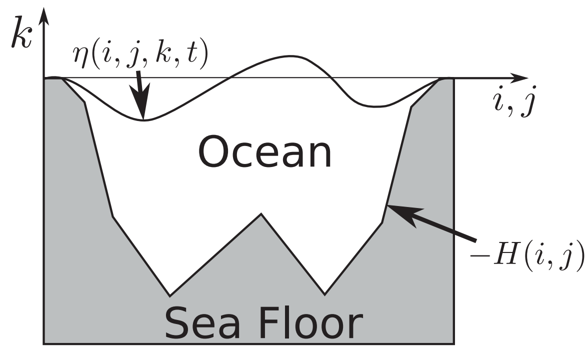

Figure 2.2: Schematic of the surface and bottom boundaries.

the ocean. The lateral boundaries follow the complex coastlines. In the configurations used for my studies, the boundaries are built from a smoothed version of the 1 arc-minute global relief model of the Earth's surface ETOPO1 (Amante and Eakins, 2009). The smoothing process was made in order to adapt the high resolution of ETOPO1 to the coarser resolution of our configurations.

At the solid earth-ocean interface, heat and salt fluxes through the sea floor are small (Huang, 1999), except in limited areas (e.g., rifts, hot spots). These fluxes are not taken into consideration in our experiments, and thus are set to zero. For the momentum transfer, no flow can cross the solid earth boundaries boundaries and thus the normal velocity has to be zero. The kinematic boundary condition can be expressed as:

$$w|_{z=-H} = -\mathbf{U_h} \cdot \nabla H \tag{2.2}$$

A region with small exchange due to friction is present at the contact with the topography. The vertical resolution of the model does not permit to explicitly resolve this boundary layer and this is parametrized in the sub-scale processes described in section 2.4.

At the atmosphere-ocean interface, the heat and freshwater fluxes are forced by the atmosphere and thus are not negligible. The fluid is also free to move in response to dynamical processes if no ice is present on the top of the ocean. Considering the mass balance, the kinematic condition is given as:

$$w|_{z=\eta} = \frac{\partial \eta}{\partial t} + \mathbf{U_h}|_{z=\eta} \cdot \nabla_h \eta + (P - E + R) \tag{2.3}$$

Where P is precipitation flux, E is evaporation flux and R is runoff flux. The dynamical boundary condition, neglecting the surface tension leads to the continuity of pressure across the boundary.

Under the free slip condition, using the continuity equation (2.1c), the previous equation becomes:

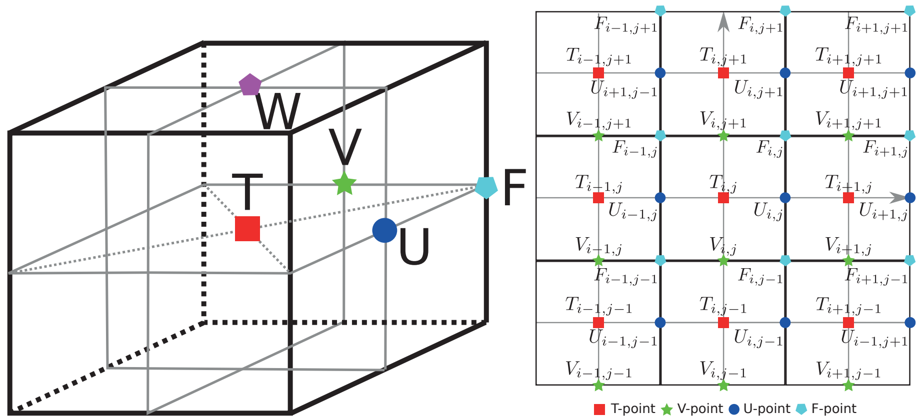

Figure 2.3: 3D (left) and 2D over the horizontal plane (right) representation of a C-grid cell with the position where each quantity is computed.

$$\frac{\partial \eta}{\partial t} = (P - E + R + I) - \nabla \cdot \left[(H + \eta) \, \overline{\mathbf{U}}_{\mathbf{h}} \right] \tag{2.4}$$

Where I is the ice melt and $\overline{\mathbf{U}}_{\mathbf{h}} = \frac{1}{H+\eta} \int_{-H}^{\eta} \mathbf{U}_{\mathbf{h}} dz$ is the vertical average velocity. The atmospheric and ocean also exchange horizontal momentum (i.e. wind stress) and heat as a forcing term. The processes to transform the atmospheric inputs from the given height to the ocean surface is described in section 2.5.

By default, the small scale processes coming from the external gravity waves (e.g., from tides) are considered as noise and thus not included in the model. Consequently, in order to improve the stability of the system as well as decrease the computational time, a linear filter is applied at the surface. The filter consists of the introduction of a damping term in the momentum equation 2.1a:

$$\frac{\partial \mathbf{U}_{\mathbf{h}}}{\partial t} = M - g \nabla \widetilde{\rho} \eta - g T_c \nabla \left(\widetilde{\rho} \frac{\partial \eta}{\partial t} \right) \tag{2.5}$$

where T_c is a parameter characterizing the force homogeneous to a time such as $T_c > \Delta t$, $\widetilde{\rho} = \frac{\rho}{\rho_0}$ is the reduced density and M the collected contributions of the Coriolis, hydrostatic pressure gradient, non linear and viscous terms in 2.1a.

2.3 Domain Discretization

The numerical equations previously shown are solved by the finite difference method. This method involves the creation of a numerical grid where each quantity will be discretized. The numerical solver will then resolve the equations at each point of this grid. In the model we use an Arakawa C grid (Mesinger and Arakawa, 1976), with scalar points (T, S, p, ρ)

are computed at the middle and vector points (U, V, W) at the center of the corresponding face (Figure 2.3). The relative and planetary vorticity, ζ and f, and the barotropic stream function, ψ are defined on the center of each vertical edge (F point on figure 2.3). The dimensions of each grid cell are defined by two horizontal scale factors (e_1 and e_2, related to the **i**-axis and **j**-axis, respectively) and one vertical scale factor (e_3, related to the k-axis). Because of the tri-polar grid described previously, the grid size is a function of the relative position of the grid element in respect with the location of the virtual pole and of the resolution of the numerical grid (namely, 1/4° and 1/12° in our studies). In this coordinate system, these three scale factors are defined as:

$$e_1 = R\left[\left(\frac{\partial\lambda}{\partial i}\cos\phi\right)^2 + \left(\frac{\partial\phi}{\partial i}\right)\right]^{1/2} \tag{2.6a}$$

$$e_2 = R\left[\left(\frac{\partial\lambda}{\partial j}\cos\phi\right)^2 + \left(\frac{\partial\phi}{\partial j}\right)\right]^{1/2} \tag{2.6b}$$

$$e_3 = \left(\frac{\partial z}{\partial k}\right) \tag{2.6c}$$

where λ, ϕ, and R are the longitude, latitude and the Earth's radius, respectively. Based on this coordinate system, the discrete version of the usual mathematical operators become:

$$\nabla q = \frac{1}{e_1}\frac{\partial q}{\partial i}\,\mathbf{i} + \frac{1}{e_2}\frac{\partial q}{\partial j}\,\mathbf{j} + \frac{1}{e_3}\frac{\partial q}{\partial k}\,\mathbf{k} \tag{2.7a}$$

$$\nabla\cdot\mathbf{A} = \frac{1}{e_1 e_2}\left[\frac{\partial(e_2 a_1)}{\partial i} + \frac{\partial(e_1 a_2)}{\partial j}\right] + \frac{1}{e_3}\left[\frac{\partial a_3}{\partial k}\right] \tag{2.7b}$$

$$\nabla\times\mathbf{A} = \left[\frac{1}{e_2}\frac{\partial a_3}{\partial j} - \frac{1}{e_3}\frac{\partial a_2}{\partial k}\right]\mathbf{i} + \left[\frac{1}{e_3}\frac{\partial a_1}{\partial k} - \frac{1}{e_1}\frac{\partial a_3}{\partial i}\right]\mathbf{j} + \frac{1}{e_1 e_2}\left[\frac{\partial e_2 a_2}{\partial j} - \frac{\partial a_2}{\partial j}\right]\mathbf{k} \tag{2.7c}$$

$$\Delta q = \nabla\cdot\nabla q \tag{2.7d}$$

$$\Delta\mathbf{A} = \nabla\left(\nabla\cdot\mathbf{A}\right) - \nabla\times\left(\nabla\times\mathbf{A}\right) \tag{2.7e}$$

The resolution of the discretized partial differential equations described previously is performed by a centered second order finite difference approximation. The thickness of each layer in the z-coordinate system is by default fixed everywhere, except at the contact with the topography. At this location, a partial step is used (Adcroft et al., 1997; Barnier et al., 2006). This consists of reducing the thickness of the layer in contact with the topography to be closer to the average depth of the topography in the considered cell (Figure 2.4) and thus improve the simulation of the bottom boundary layer (Adcroft et al., 1997; Barnier et al., 2006). The thickness of the bottom cells is automatically computed by the model based on the bathymetry data.

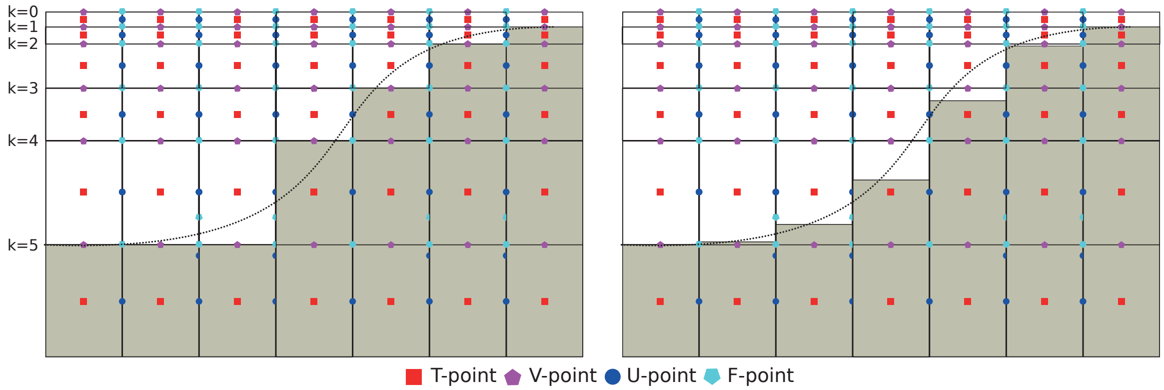

Figure 2.4: Vertical coordinate system without partial step (left) and with partial step (right)

2.3.1 Time discretization

When the model is resolved the equations in the space domain (**i**, **j** and **k**), the model computes the result for the next time step. The value (in seconds) of the time step has to be set to ensure that, in one time step, the velocity of the fluid cannot move a virtual particle for more than one grid cell. This condition, called Courant-Friedrichs-Lewy (CFL) condition, is expressed as:

$$C = \frac{u\Delta t}{e_1} + \frac{v\Delta t}{e_2} < C_{\max} \tag{2.8}$$

where, u and v are the largest velocities in the **i** and **j** direction. This criterion has to be less than $C_{\max} = 1$. As the time step is directly related to the resolution of the spatial discretization, it is set up $\Delta t = 1080$s and 180s for our $1/4°$ and $1/12°$ horizontal resolution, respectively.

We use a three level scheme time stepping that can be represented as:

$$x^{t+\Delta t} = x^{t-\Delta t} + 2\Delta t \mathrm{RHS}_x^{t-\Delta t, t, t+\Delta t} \tag{2.9}$$

where x stands for u, v, T or S, the RHS is the Right-Hand-Side of the corresponding time evolution equation, Δt is the time step; and the superscripts indicates the time level at which the variable is evaluated.

To ensure stability and efficiency, the integration method differs for the non diffusive and diffusive equations. The non diffusive equations (momentum and tracers advection and Coriolis term) use a Leap-Frog integration scheme (Mesinger and Arakawa, 1976). This method achieves second-order accuracy with just one RHS evaluation per time step. However, the differencing decouples odd and even grid points at any given time step (the

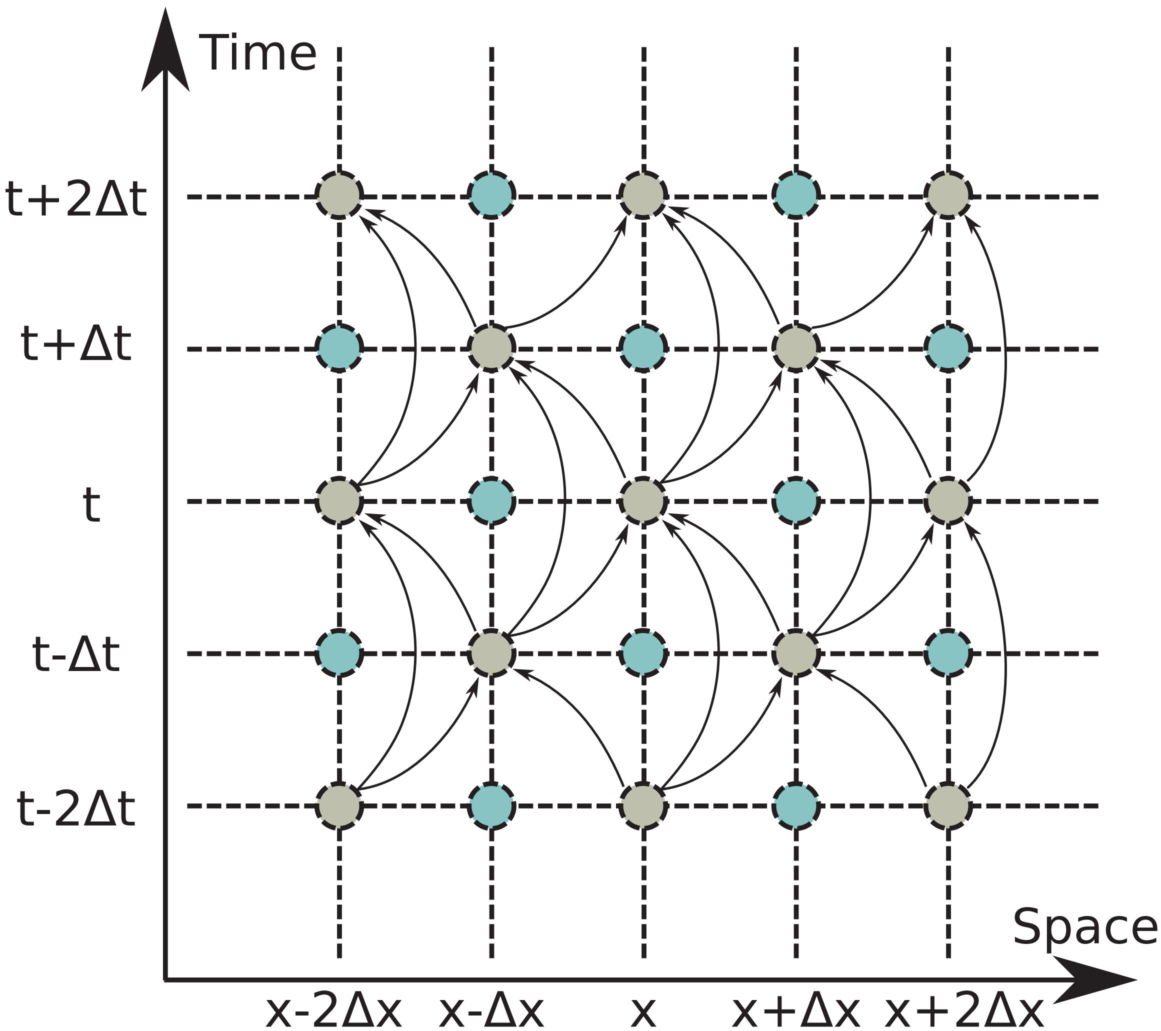

Figure 2.5: Temporal and spatial pattern of the time stepping in the Leapfrog scheme.

grey points on figure 2.5) leading to numerical instability. To prevent the divergence, a Robert-Asselin filter is applied. The filter is similar to a Laplacian diffusion in time that mixes odd and even time steps:

$$x_F^t = x^t + \gamma \left[x_F^{t-\Delta t} - 2x^t + x^{t+\Delta t} \right] \tag{2.10}$$

where the subscript F denotes filtered values and $\gamma = 0.1$ is the Asselin coefficient.

The Leap-frog scheme cannot be used for the diffusive equations because all the coefficients of even derivative terms are zero. Instead, we use a Forward scheme. The horizontal diffusion and tracer restoring terms use a forward time discretization scheme:

$$x^{t+\Delta t} = x^{t-\Delta t} + 2\Delta t D_x^{t-\Delta t} \tag{2.11}$$

where D_x represents the diffusive term. This scheme is only conditionally stable. For the stability of fourth and second order diffusion schemes, the following conditions are required:

$$A^h > \begin{cases} \frac{e^2}{8\Delta t} & \text{Laplacian diffusion} \\ \frac{e^4}{64\Delta t} & \text{bilaplacian diffusion} \end{cases} \tag{2.12}$$

where e is the smallest grid size in the two horizontal directions and A^h is the mixing coefficient. In our study laplacian and bilaplacian diffusion are used for horizontal tracer and momentum diffusion, respectively.

For the vertical diffusion, a Backward scheme is used:

$$x^{t+\Delta t} = x^{t-\Delta t} + 2\Delta t \mathrm{RHS}_x^{t+\Delta t} \tag{2.13}$$

which is unconditionally stable.

2.4 Sub-scale physics

2.4.1 Turbulence

Despite the progress of computational power over the last few decades, the spatial and temporal resolution is always insufficient to resolve various physical mechanisms such as the small scale turbulent motions coming from the advective terms in the Navier-Stokes equation, or molecular diffusion. However, these components are important for the larger scale dynamics and thermodynamics of the ocean. The implementation of the sub-scale physics in the model, as well as the closure systems in the turbulent schemes, involves the parameterization of the physics. This parameterization is included in the terms $\mathbf{D^U}$, $\mathbf{D^T}$ and $\mathbf{D^S}$ in the primitive equations (2.1a, 2.1e and 2.1f) and are divided into their horizontal and vertical components.

The model uses a Total Variance Dissipation (TVD) scheme to resolve advection. In this formulation, the tracer at a velocity point is evaluated using a combination of an upstream and a centered scheme. For example, in the **i**-direction:

$$\begin{aligned} \tau_u^{ups} &= \begin{cases} \tau_{i+1} & \text{if } u_{i+1/2} < 0 \\ \tau_i & \text{if } u_{i+1/2} \geq 0 \end{cases} \\ \tau_u^{tvd} &= \tau_u^{ups} + c_u(\tau_u^{cen2} - \tau_u^{ups}) \end{aligned} \tag{2.14}$$

where c_u is a flux limiter function taking values between 0 and 1, each corresponding to a different total variance decreasing scheme. The value chosen in NEMO is described in Zalesak (1979). τ_u^{cen2} corresponds to the classical 2nd order formulation that, in order to evaluate the tracer at the velocity point uses the two neighbor points ($\tau_u^{cen2} = \overline{T}^{i+1/2}$).

For the lateral diffusivity, a bilaplacian operator is used for tracers. It involves applying the Laplacian operator twice, namely:

$$D_l^T = \Delta(A_l^T \mathfrak{M} \Delta T) \text{ with } \mathfrak{M} = \begin{pmatrix} 1 & 0 & -r_1 \\ 0 & 1 & -r_2 \\ -r_1 & -r_2 & r_1^2 + r_2^2 \end{pmatrix} \tag{2.15}$$

where r_1 and r_2 represent the slope between the surface along which the diffusive operator acts and the model vertical layer. For an iso-neutral diffusion in the z-coordinate, the lateral momentum diffusion operator is rotated along a geo-potential. The diffusion operator is then defined simply as the divergence of the down gradient momentum fluxes on each momentum component. The resulting discrete representation is:

$$\begin{aligned} D_u^{l\mathbf{U}} = & \frac{1}{e_{1u}e_{2u}e_{3u}} \Bigg\{ \\ & \delta_{\mathbf{i}+1/2} \left[A_T^{lm} \left(\frac{e_{2t}e_{3t}}{e_{1t}} \delta_{\mathbf{i}}[\mathbf{u}] - e_{2t} r_{1t} \overline{\overline{\delta_{k+1/2}[\mathbf{u}]}}^{\mathbf{i},\mathbf{k}} \right) \right] \\ & \delta_{\mathbf{j}} \quad \left[A_f^{lm} \left(\frac{e_{1f}e_{3f}}{e_{2f}} \delta_{\mathbf{j}+1/2}[\mathbf{u}] - e_1 f r_{2f} \overline{\overline{\delta_{k+1/2}[\mathbf{u}]}}^{\mathbf{j}+1/2,\mathbf{k}} \right) \right] \\ & \delta_{\mathbf{k}} \quad \Bigg[A_{uw}^{lm} \Bigg(- e_{2u} r_{1uw} \overline{\overline{\delta_{\mathbf{i}+1/2}[\mathbf{u}]}}^{\mathbf{i}+1/2,\mathbf{k}+1/2} \\ & \qquad - e_{1u} r_{2uw} \overline{\overline{\delta_{\mathbf{j}+1/2}[\mathbf{u}]}}^{\mathbf{j}+1/2,\mathbf{k}+1/2} \\ & \qquad + \frac{e_{1u}e_{2u}}{e_{3uw}} (r_{1uw}^2 + r_{2uw}^2) \Bigg) \delta_{\mathbf{k}+1/2}[\mathbf{u}]) \Bigg] \Bigg\} \end{aligned} \tag{2.16}$$

$$
\begin{aligned}
D_v^{l\mathbf{V}} = & \frac{1}{e_{1v}e_{2v}e_{3v}} \Bigg\{ \\
& \delta_{\mathbf{i}+1/2} \left[A_T^{lm} \left(\frac{e_{2t}e_{3t}}{e_{1t}} \delta_{\mathbf{i}}[\mathbf{v}] - e_{2t} r_{1t} \overline{\overline{\delta_{k+1/2}[\mathbf{v}]}}^{\,\mathbf{i},\mathbf{k}} \right) \right] \\
& \delta_{\mathbf{j}} \quad \left[A_f^{lm} \left(\frac{e_{1f}e_{3f}}{e_{2f}} \delta_{\mathbf{j}+1/2}[\mathbf{v}] - e_1 f r_{2f} \overline{\overline{\delta_{k+1/2}[\mathbf{v}]}}^{\,\mathbf{j}+1/2,\mathbf{k}} \right) \right] \\
& \delta_{\mathbf{k}} \quad \Bigg[A_{vw}^{lm} \Bigg(- e_{2v} r_{1vw} \overline{\overline{\delta_{\mathbf{i}+1/2}[\mathbf{v}]}}^{\,\mathbf{i}+1/2,\mathbf{k}+1/2} \\
& \qquad - e_{1v} r_{2vw} \overline{\overline{\delta_{\mathbf{j}+1/2}[\mathbf{v}]}}^{\,\mathbf{j}+1/2,\mathbf{k}+1/2} \\
& \qquad + \frac{e_{1v}e_{2v}}{e_{3vw}} (r_{1vw}^2 + r_{2vw}^2) \Bigg) \delta_{\mathbf{k}+1/2}[\mathbf{v}]) \Bigg] \Bigg\}
\end{aligned} \tag{2.17}
$$

where r_1 and r_2 are the slope between the surface along which the diffusion operator acts and the z-surface.

The vertical diffusion is based on the laplacian operator. This assumes that the turbulent fluxes are linearly dependent on the gradients of large-scale quantities (cf., model assumption n°6). In NEMO, the vertical advection and tracer diffusion are expressed as follows:

$$\mathbf{D}_v^{\mathbf{U}} = \frac{\partial}{\partial z} \left(A_v^m \frac{\partial \mathbf{U_h}}{\partial z} \right) \tag{2.18a}$$

$$\mathbf{D}_v^{T} = \frac{\partial}{\partial z} \left(A_v^T \frac{\partial T}{\partial z} \right) \tag{2.18b}$$

$$\mathbf{D}_v^{S} = \frac{\partial}{\partial z} \left(A_v^T \frac{\partial S}{\partial z} \right) \tag{2.18c}$$

where A_v^m and A_v^T are, respectively, the vertical eddy viscosity and diffusivity coefficients.

Initial values of viscosity and diffusivity are provided, however these value are going to change as a function of the propagation of eddies due to turbulence. In order to compute the changes in the values, we use a classical Turbulent Kinetic Energy (TKE) closure system. This scheme is based on the Reynold's decomposition of the velocity fields, separating the flow as a mean flow and a turbulent fluctuation from the mean ($\mathbf{u}(i,j,k) = \overline{\mathbf{u}(i,j,k)} + \mathbf{u}'(i,j,k)$) and the addition of a prognostic equation of turbulent kinetic energy ($\overline{\epsilon}$) defined as:

$$\bar{\epsilon} = \underbrace{\frac{1}{2}(\overline{u'^2} + \overline{v'^2} + \overline{w'^2})}_{\text{Turbulent kinetic energy}} \tag{2.19a}$$

$$\frac{\partial \bar{\epsilon}}{\partial t} = \underbrace{\frac{A_v^m}{e_3}\left[\left(\frac{\partial u}{\partial k}\right)^2 + \left(\frac{\partial v}{\partial k}\right)^2\right]}_{\text{Vertical shear}} - \underbrace{A_v^T N^2}_{\text{Stratification}} + \underbrace{\frac{1}{e_3}\frac{\partial}{\partial k}\left(\frac{A_v^m}{e_3}\frac{\partial \bar{\epsilon}}{\partial k}\right)}_{\text{Vertical diffusion}} - \underbrace{c_\epsilon \frac{\epsilon^{\frac{3}{2}}}{l_\epsilon}}_{\text{Kolmogorov dissipation}} \tag{2.19b}$$

$$A_v^m = \underbrace{c_k l_k \sqrt{\bar{\epsilon}}}_{\text{Vertical eddy viscosity}} \tag{2.19c}$$

$$A_T^m = \underbrace{\frac{A_v^m}{P_{rt}}}_{\text{Vertical eddy diffusivity}} \tag{2.19d}$$

where N is the local Brunt-Väisälä frequency, $c_\epsilon = \sqrt{2}/2$ and $c_k = 0.1$, P_{rt} is the Prandtl number, l_ϵ and l_k are the dissipation and mixing length scales, estimated as:

$$l_k = l_\epsilon = \sqrt{2\bar{\epsilon}}/N \tag{2.20a}$$

$$\frac{1}{e_3}\left|\frac{\partial l}{\partial k}\right| \leq \text{with } l_k = l_\epsilon \tag{2.20b}$$

2.4.2 Top and bottom vertical shear

At the surface and at the contact with the topography, a boundary layer not resolved by the Navier-Stokes equations is present and thus is included into the Total Kinetic Energy scheme described earlier. The resolution of this part of the turbulent scheme is resolved by a non-linear bottom friction parametrization that assumes the bottom friction to be quadratic, defined as:

$$F_h^{\mathbf{U}} = \frac{A_v^m}{e_3}\left[\left(\frac{\partial u}{\partial k}\right)^2 + \left(\frac{\partial v}{\partial k}\right)^2\right] = C_D\sqrt{u_b^2 + v_b^2 + e_b}\,\mathbf{U}_h^b \tag{2.21}$$

where C_D is a drag coefficient, and e_b a fixed bottom turbulent kinetic energy due to internal waves, breaking and other short time scale currents. The trend of the momentum due to the boundary layer is then added to the general momentum trend, as:

$$C_b^u = -C_D\left[u^2 + (\overline{\overline{v}}^{i+1,j})^2 + e_b\right]^{1/2} \tag{2.22}$$

$$C_b^v = -C_D\left[(\overline{\overline{u}}^{i,j+1})^2 + v^2 + e_b\right]^{1/2} \tag{2.23}$$

2.5 Surface boundary

In order to have correct forcing at the surface boundary of the ocean, the heat fluxes and surface stress are needed by the ocean module. We do not couple NEMO with an atmospheric model. Instead, we use several products that are either from atmospheric reanalysis (e.g., CORE2, Large and Yeager (2009)) or climate models (e.g., MIROC-ESM, Watanabe et al. (2011)). These products provide the variables needed by NEMO to compute the sensible heat flux (Q_s), latent heat flux (Q_l), short wave radiation (Q_{sw}), long wave radiation (Q_{lw}) and wind stress (u and v).

We use the bulk formulation from Large and Yeager (2009) as follows:

$$Q_l = \rho_a L_e C_e (q - q_s)\, |\mathbf{u}_a - \mathbf{u}_o| \tag{2.24a}$$

$$Q_s = \rho_a c_p C_h (T_a - T_o)\, |\mathbf{u}_a - \mathbf{u}_o| \tag{2.24b}$$

$$Q_{sw} = (1 - i_0)(1 - \alpha) Q_{ds} \tag{2.24c}$$

$$Q_{lw} = \epsilon (Q_{dl} - \sigma T_o^4) \tag{2.24d}$$

$$\tau_{ao} = \rho C_d\, (\mathbf{u}_a - \mathbf{u}_o)\, |\mathbf{u}_a - \mathbf{u}_o| \tag{2.24e}$$

where L_e is the latent heat of vaporization of water, C_e and C_h are the transfer coefficients of sensible and latent heat, respectively, q and T_a are the near surface atmospheric temperature and specific humidity, q_s and T_o are the saturated specific humidity (that depends on the sea surface temperature) and the sea surface temperature, $\mathbf{u}_a$ and $\mathbf{u}_o$ are the wind speed and the ocean surface speed, i_0 is fraction of the net shortwave radiation that penetrates the snow/ice, α is the albedo of the snow/ice, ϵ is the emissivity, σ is the Stefan-Boltzmann constant and τ_{ao} is the surface stress at the surface of the ocean. All transfer coefficients are defined based to be either between a fixed value, set up to ensure stability (e.g., 0.25 for C_d), or a value computed based on the log-layer model applied at the surface (for more details, see Large (2006)). In order to ensure numerical stability, the model decides which value should be used based on which is the larger.

We note that in the presence of ice, all the above equations are applied at the surface of the sea-ice, taking in consideration sea-ice variables instead of the ocean's. Under the ice, these equations are applied again, but using the sea-ice and ocean variables. In this second case, because of the small range in velocity variation, C_d is not computed anymore for each grid cell but is fixed to be 0.005.

2.6 Sea ice

The sea-ice component in NEMO is managed by LIM (Louvain-la-Neuve sea-Ice model) version 2. This model including both dynamic and thermodynamic effects for the behavior of the sea ice. A elastic-viscous-plastic (EVP) rheology is used to compute internal stress (Hunke and Dukowicz, 1997). This model is designed based on momentum balance formulation from Hibler (1979).

A full description of the model is available in Fichefet and Maqueda (1997). The following sections are an overview of the main features.

2.6.1 Sea-ice dynamics

The model dynamics is based on three categories: two ice categories of equal size (consolidated ice plus leads) and a layer of snow at the top. This is treated as a two-dimensional fluid driven by winds and oceanic currents. The resistance to deformation increases monotonically with ice thickness and concentration. The final output for each grid is a layer of ice with an uniformed mean thickness of ice covering a variable part of the grid cell.

The conservation of linear momentum is expressed as:

$$m\frac{\partial \mathbf{u}}{\partial t} = \underbrace{A\left(\tau_a + \tau_w\right)}_{\text{Atmospheric forcing}} - \underbrace{mf\mathbf{k}\times\mathbf{u}}_{\text{Coriolis}} - \underbrace{mg\nabla\eta}_{\text{Pressure}} + \underbrace{\nabla\cdot\sigma}_{\text{Internal stress}} \tag{2.25}$$

where m is the mass of snow and ice per unit area, A is the ice concentration, τ_a and τ_w are the atmosphere-ice and water-ice interfacial stresses, f, g, η and $\mathbf{k}$ are the Coriolis parameter, the acceleration of gravity, sea surface elevation and vertical upwards unit vector, respectively, and $\nabla\cdot\sigma$ is the internal stress tensor. The air and water stress terms ($\boldsymbol{\tau}_a+\boldsymbol{\tau}_w$) are computed as described previously. We note that, Thorndike (1986) shows that when the model is run over large time scale (more than 30 minutes), the advective momentum term can be ignored. This approximation is used by the sea-ice model.

The internal horizontal stress tensor is defined as:

$$\nabla_h \cdot \sigma = \left(\frac{\partial \sigma_1}{\partial i}, \frac{\partial \sigma_2}{\partial i}\right) \tag{2.26}$$

where σ_1 and σ_2 are the principal direction of the internal stress, defined as:

$$\sigma_1 = \sigma_{11} + \sigma_{22} \tag{2.27a}$$

$$\sigma_2 = \sigma_{11} - \sigma_{22} \tag{2.27b}$$

The sea-ice divergence (D_D), horizontal tension (D_T) and shear (D_S) strain rates are given by:

$$D_D = \frac{1}{e_1 e_2}\left(\frac{\partial(e_2 u)}{\partial i} + \frac{\partial(e_1 v)}{\partial j}\right) = \dot{\epsilon}_{11} + \dot{\epsilon}_{22} \tag{2.28a}$$

$$D_T = \frac{1}{e_1 e_2}\left(e_2^2\frac{\partial(u/e_2)}{\partial i} - e_1^2\frac{\partial(v/e_1)}{\partial j}\right) = \dot{\epsilon}_{11} - \dot{\epsilon}_{22} \tag{2.28b}$$

$$D_S = \frac{1}{e_1 e_2}\left(e_1^2\frac{\partial(u/e_1)}{\partial i} + e_2^2\frac{\partial(v/e_2)}{\partial j}\right) = 2\dot{\epsilon}_{12} \tag{2.28c}$$

where $\dot{\epsilon}_{11}$, $\dot{\epsilon}_{22}$ and $\dot{\epsilon}_{12}$ are the classical formulation for the strain rate in the solid mechanics convention of the principal and shear strain rate. On short time scales, the elastic response of the sea-ice become preponderant. The internal stress tensor becomes:

$$\frac{1}{E}\dot{\sigma}_1 = D_D - \frac{\sigma_1\Delta}{P} - \Delta \tag{2.29a}$$

$$\frac{1}{E}\dot{\sigma}_2 = D_T - \frac{\sigma_2\Delta}{P} \tag{2.29b}$$

$$\frac{1}{E}\dot{\sigma}_{12} = \frac{1}{2}D_S - \frac{\sigma_{12}e^2\Delta}{P} \tag{2.29c}$$

$$\Delta = \sqrt{D_D^2 + \frac{1}{e^2}\left(D_T^2 + D_S^2\right)} \tag{2.29d}$$

where E is the Young's modulus (i.e., modulus of elasticity for a given material), e is the eccentricity of the sea-ice elliptical curve, P is ice strength, which is a function of mean ice thickness (h) and concentration (A) defined as:

$$P = P^* h \exp\left[-C_{reh}(1-A)\right] \tag{2.30}$$

where P^*, C_{reh} are constant. We note if we take the equations 2.29a to 2.29c at a steady state (i.e., with a long enough time scale), we obtain the equations for the visco-plastic behaviour described earlier.

2.6.2 Sea-ice thermodynamics

The thermodynamic part of the sea-ice describes how the heat flux goes through the ice. The thermodynamic part of LIM2 uses the three layer model for the vertical heat conduction within snow and ice. It includes the storage of latent heat in brine pockets. Sea ice growth and decay rates are computed from the ice energy budget.

Internal temperature of snow and ice are governed by the one dimension heat diffusion equation:

$$\rho c_p \frac{\partial T}{\partial t} = Gk\frac{\partial^2 T}{\partial z^2} \tag{2.31}$$

where ρ, c_p and k and the density, specific heat and thermal conductivity of the material (snow or ice), respectively. T is the temperature. G is a correction factor that accounts for the fact that the unresolved ice floes of varying thickness contribute differently to the average heat conduction.

At the surface of the sea ice, the heat flux balance (B_{su}, which depends on the surface temperature, T_{su}) is the sum of five components: the conductive heat (Q_c), the latent heat flux (Q_l), the sensible heat flux (Q_s), the shortwave solar radiation (Q_{sw}) and the longwave radiation (Q_{lw}).

$$B_{su}(T_{su}) = Q_c + Q_l + Q_s + Q_{sw} + Q_{lw} \tag{2.32}$$

The last four terms are computed from bulk formula given by Large and Yeager (2009) as described in the section 2.5.

If the sea surface temperature is above the melting point, the excess of energy will be used for snow/ice melting:

$$\frac{\partial h_*}{\partial t} = \frac{B_{si}}{L_*} \tag{2.33}$$

where L is the volumetric latent heat of fusion, the subscript $*$ represents the snow (s subscript) if existing or the ice otherwise (i subscript).

At the contact between the oceanic surface and the sea ice, any imbalance between the conductive heat flux (Q_c) and the heat flux from the ocean (Q_{oi}) is used to generate or remove ice:

$$\frac{\partial h_i}{\partial t} = \frac{Q_c - Q_{oi}}{L_i} \tag{2.34}$$

The lateral growth and decay is associated with the sea ice concentration (A), which is defined as a fraction of the grid cell area covered by ice. Its evolution depends on the heat budget of the open water area (B_l):

$$\frac{\partial A}{\partial t} = \sqrt{1 - A^2}\frac{(1 - A)B_l}{L_i h_0} \tag{2.35}$$

where h_0 is the ice thickness of the ice formed in a lead. When $B_l > 0$, all the heat gained in a lead is used for melting from below through Q_{oi} in equation 2.34.

2.6.3 Ocean - Sea ice coupling

The sea ice affects the upper ocean temperature, salt and momentum fluxes. As an example, the shortwave radiation at the ocean surface (Q_{swoc}) can now be expressed as:

$$Q_{swoc} = AQ_{str} + (1 - A)(A - \alpha)Q_{ds} \tag{2.36a}$$

$$Q_{str} = i_0(1 - \alpha)Q_{ds} \exp(-1.5(h_i) - 0.1) \tag{2.36b}$$

where α is the open water albedo and Q_{str} is the shortwave radiation reaching the bottom of an ice slab.

The snow and ice melting will release freshwater at the oceanic surface while freezing will release salt. Melt from the surface of the ice, evaporation and precipitation will also impact the salt flux as the surface:

$$\begin{aligned} Q_{salt} =& \underbrace{S_m \frac{\partial m_s}{\partial t}}_{\text{snow melt}} + \underbrace{(S_m - S_i)\frac{\partial m_i}{\partial t}}_{\text{ice melt}} + \underbrace{(S_m - S_i)\left(\frac{\partial m_s}{\partial t} + \frac{\partial m_i}{\partial t}\right)}_{\text{brine rejection}} \\ &+ \underbrace{S_i \frac{\partial m_s}{\partial t}}_{\text{artificial meteoric ice}} + \underbrace{S_m(AE - P)}_{evaporation-precipitation} \end{aligned} \tag{2.37}$$

where m_s is the snow mass per unit of area, m_i and S_i are the mass and salinity of ice, respectively, E is the evaporation rate over the leads and P is the freshwater change from precipitation. The artificial meteoric ice term corresponds to the meltwater flux from the snow melt that reaches the ocean by infiltration through the ice.

Finally, in ice-covered regions, the sensible heat flux from the ocean to the ice (Q_{oi}) and the heat balance of the leads (B_l) are equilibrated with the heat gained inside of the sub-surface region where the temperature and salinity are homogeneous due to the oceanic mixing (i.e., the mixed layer):

$$Q_{oi} = (1 - i_w|_{z=-h_m})Q_{str} + \Gamma\left[\frac{(1-A)B_l}{A}\right] + Q_{ent} + Q_{dif} + Q_{ovT}|_{-h_m} + Q_{fus} \tag{2.38}$$

where h_m is the mixed layer depth, i_w is the fraction of net shortwave radiation penetrating the ocean (function of z), Γ is the Heaviside unit function and Q_{ent}, Q_{dif}, $Q_{ovT}|_{-h_m}$ and Q_{fus} are the heat flux due to entrainment, diffusion, overturning and changes in salinity which are handled by the ocean mixed layer model and provided back to the sea-ice module to close the heat budget.

2.7 List of constants

Bibliography

Adcroft, A., Hill, C., and Marshall, J. (1997). Representation of topography by Shaved Cells in a Height Coordinate Ocean Model. *Monthly Weather Review*, 125(9):2293–2315.

Amante, C. and Eakins, B. (2009). ETOPO1 1 arc-minute global relief model: Procedures, data sources and analysis. *NOAA Technical Memorandum NESDIS NGDC-24*.

Barnier, B., Madec, G., Penduff, T., Molines, J.-M., Treguier, A.-M., Sommer, J. L., Beckmann, A., Biastoch, A., Böning, C., Dengg, J., Derval, C., Durand, E., Gulev, S., Remy, E., Talandier, C., Theetten, S., Maltrud, M., McClean, J., and Cuevas, B. D. (2006). Impact of partial steps and momentum advection schemes in a global ocean circulation model at eddy-permitting resolution. *Ocean Dynamics*, 56(5-6):543–567.

Fichefet, T. and Maqueda, M. A. M. (1997). Sensitivity of a global sea ice model to the treatment of ice thermodynamics and dynamics. *Journal of Geophysical Research: Oceans*, 102(C6):12609–12646.

Hibler, W. D. (1979). A dynamic thermodynamic sea ice model. *Journal of Physical Oceanography*, 9(4):815–846.

Huang, R. X. (1999). Mixing and energetics of the oceanic thermohaline circulation*. *Journal of Physical Oceanography*, 29(4):727–746.

Hunke, E. C. and Dukowicz, J. K. (1997). An Elastic–Viscous–Plastic model for sea ice dynamics. *Journal of Physical Oceanography*, 27(9):1849–1867.

Large, W. B. (2006). *Surface Fluxes for Practitioners of Global Ocean Data Assimilation*. Springer.

Large, W. G. and Yeager, S. G. (2009). The global climatology of an interannually varying air–sea flux data set. *Climate Dynamics*, 33(2):341–364.

Madec, G. and Imbard, M. (1996). A global ocean mesh to overcome the North Pole singularity. *Climate Dynamics*, 12(6):381–388.

Mesinger, F. and Arakawa, A. (1976). Numerical methods used in atmospheric models. -1.

Murray, R. J. (1996). Explicit generation of orthogonal grids for ocean models. *Journal of Computational Physics*, 126(2):251–273.

Reynolds, O. (1895). On the dynamical theory of incompressible viscous fluids and the determination of the criterion. *Philosophical Transactions of the Royal Society of London A: Mathematical, Physical and Engineering Sciences*, 186:123–164.

Thorndike, A. S. (1986). Kinematics of sea ice. *The Geophysics of Sea Ice*, pages 489–549.

Watanabe, S., Hajima, T., Sudo, K., Nagashima, T., Takemura, T., Okajima, H., Nozawa, T., Kawase, H., Abe, M., Yokohata, T., and et al. (2011). MIROC-ESM 2010: model description and basic results of CMIP5-20C3M experiments. *Geoscientific Model Development*, 4(4):845–872.

Zalesak, S. T. (1979). Fully multidimensional flux-corrected transport algorithms for fluids. *Journal of Computational Physics*, 31(3):335–362.

Variable	Value	Units	Description
$\pi =$	3.141592653589793		Pi
$\Omega =$	7.292116×10^{-5}	s^{-1}	Earth rotation parameter
$R =$	6371229	m	Earth radius
$g =$	9.80665	$m\ s^{-2}$	Gravity
$\rho_0 =$	1026	$kg\ m^{-3}$	Reference mass volumetric
$\rho_{cp} =$	3991.86795711963	$J\ K^{-1}$	Heat capacity of water
$L_e =$	2.5×10^6	J	Latent heat of evaporation
$\kappa =$	0.4		Von Karman constant
$\sigma =$	5.67×10^{-8}	$W\ m^{-2}\ K^{-1}$	Stefan-Boltzmann constant
$T_{tp} =$	273.16		Temperature of the triple point
$T_f =$	273.15		Freezing point of fresh water
$S_i =$	6		Ice salinity
$T_i =$	273.05		Melting point of ice
$I_i =$	1.8837×10^6	$J\ m{-}3\ K^{-1}$	Volumetric specific heat for ice
$\rho_i =$	900	$kg\ m^{-3}$	Ice volumic mass
$k_i =$	2.034396	$W\ m^{-1}\ K^{-1}$	Ice conductivity
$L_i =$	330.33×10^6	$J\ m3$	Ice Volumetric latent heat fusion
$T_s =$	273.15		Melting point of snow
$\rho_s =$	330	$kg\ m^{-3}$	Volumic mass of snow
$I_s =$	6.9096×10^5	$J\ m{-}3\ K^{-1}$	Volumetric specific heat for snow
$k_s =$	0.22	$W\ m^{-1}\ K^{-1}$	Snow conductivity
$L_s =$	110.121×10^6	$J\ m3$	Snow Volumetric latent heat fusion
E_{is}	0.97		Ice/snow emissivity
$G =$	0.3×10^3		Ice diffusion constant
$A^h =$	1.17×10^4	$\mathrm{m^2 s^{-1}}$	Laplacian diffusion (ANHA4)
$A^h =$	1.56×10^{11}	$\mathrm{m^4 s^{-1}}$	Bilaplacian diffusion (ANHA4)
$C_D =$	1×10^{-3}		Bottom drag coefficient
$e_b =$	2.5×10^{-3}	$\mathrm{m^3 s^{-2}}$	Bottom turbulent kinetic energy background
$P^* =$	5000	Nm^{-2}	Ice strength factor
$C_{reh} =$	20		Ice strength spatial factor

Table 2.1: List of the constants used by NEMO

Chapter 3

Evolution of Baffin Bay water masses and transports in a numerical sensitivity experiment under enhanced Greenland melt

Published in Atmosphere - Oceans (July 2017). doi: 10.1080/07055900.2017.1333950

Nathan Grivault, Xianmin Hu and Paul G. Myers

Abstract

We used a numerical model forced with three different scenarios to analyze Baffin Bay circulation sensitivity to runoff around Baffin Bay, especially the Greenland runoff, for the past (1970-2010) and future (2010-2099). We observed an overall decrease in transport from the Arctic to the North Atlantic for the volume, heat, and freshwater over the time period as well as an augmentation of the freshwater and heat in Baffin Bay. In the early 1990s, the increase in heat in Baffin Bay was consistent with an increase in the West Greenland Irminger Water (WGIW) inflow at Davis Strait while later on the West Greenland Shelf Water played an important role in the heat import, sustaining the idea that the West Greenland Current might have an impact on the melt of West Greenland tidewater glaciers. The increase in freshwater and later in heat in Baffin Bay leads to changes in the steric height inside Baffin Bay, which leads to changes in the circulation. After 1978, the WGIW reaches the North Water polynya and recirculates into the Baffin Bay gyre where it accumulates over time. In the future experiment, the dynamic changes in Baffin Bay are mainly related to the accumulation of heat inside the gyre.

3.1 Introduction

The Arctic Ocean is an enclosed basin surrounded by North America, the Canadian Arctic Archipelago, Greenland, and Eurasia. The relative isolation of the Arctic Oceans from other oceans limits exchanges with the Pacific Ocean to Bering Strait, where relatively warm and freshwater is imported. The Arctic Ocean's cold and fresh upper layer is exported to southern latitudes. This outflow may take two different pathways: in the East Greenland Current through Fram Strait or through the Canadian Arctic Archipelago (CAA). Previous studies have shown that the CAA is a major pathway for liquid freshwater export from the Arctic to the North Atlantic. The freshwater transport through the CAA is evaluated as being between 36 and 63 mSv (1 mSv = 10^3 m^3s^{-1}), with a reference salinity of 34.8 (Dickson et al., 2007; McGeehan and Maslowski, 2012; Serreze et al., 2006) while the liquid freshwater export through Fram Strait is evaluated as being 100 ± 23 mSv, with a slightly different reference salinity of 34.9 (Rabe et al., 2013). Once in the CAA, the outflow can leave through Baffin Bay (Aksenov et al., 2010; Wang et al., 2012) or through Foxe Basin to Hudson Strait.

Baffin Bay is a small and relatively deep body of water between the CAA and Greenland (Figure 3.1a). It is surrounded by Greenland to the east, Ellesmere and Devon Islands to the north and Baffin Island to the west. It is about 1400 km long by 550 km wide, with a large abyssal plain in its central area having a depth greater than 2300 m. The continental shelf on the Baffin Island side is narrower than on the Greenland side. The connection to the Labrador Sea takes place in Davis Strait, which has a sill depth of about 650 m and a width of about 170 km. In the north, Baffin Bay is connected to the Arctic Ocean through three different passages. The deepest, Nares Strait located between Greenland and Ellesmere Island, is about 26 km wide at its narrowest point, with a sill about 250 m deep in the centre of the strait. The shallower Lancaster and Jones Sounds are located between Baffin and Devon Islands and Devon and Ellesmere Islands, respectively. The first has a width of about 55 km and a sill about 125 m deep, while the second is no wider than 30 km with a 190 m deep sill (Melling et al., 2008; Tang et al., 2004). Baffin Bay is mostly ice free in the summer and has near complete ice cover between December and April (Tang et al., 2004).

The oceanic circulation in Baffin Bay is mostly driven by a baroclinic gradient (Kliem and Greenberg, 2003; Myers and Ribergaard, 2013; Tang et al., 2004). The West Greenland Slope Current transports the shallow West Greenland Shelf Water (WGSW) while fur-

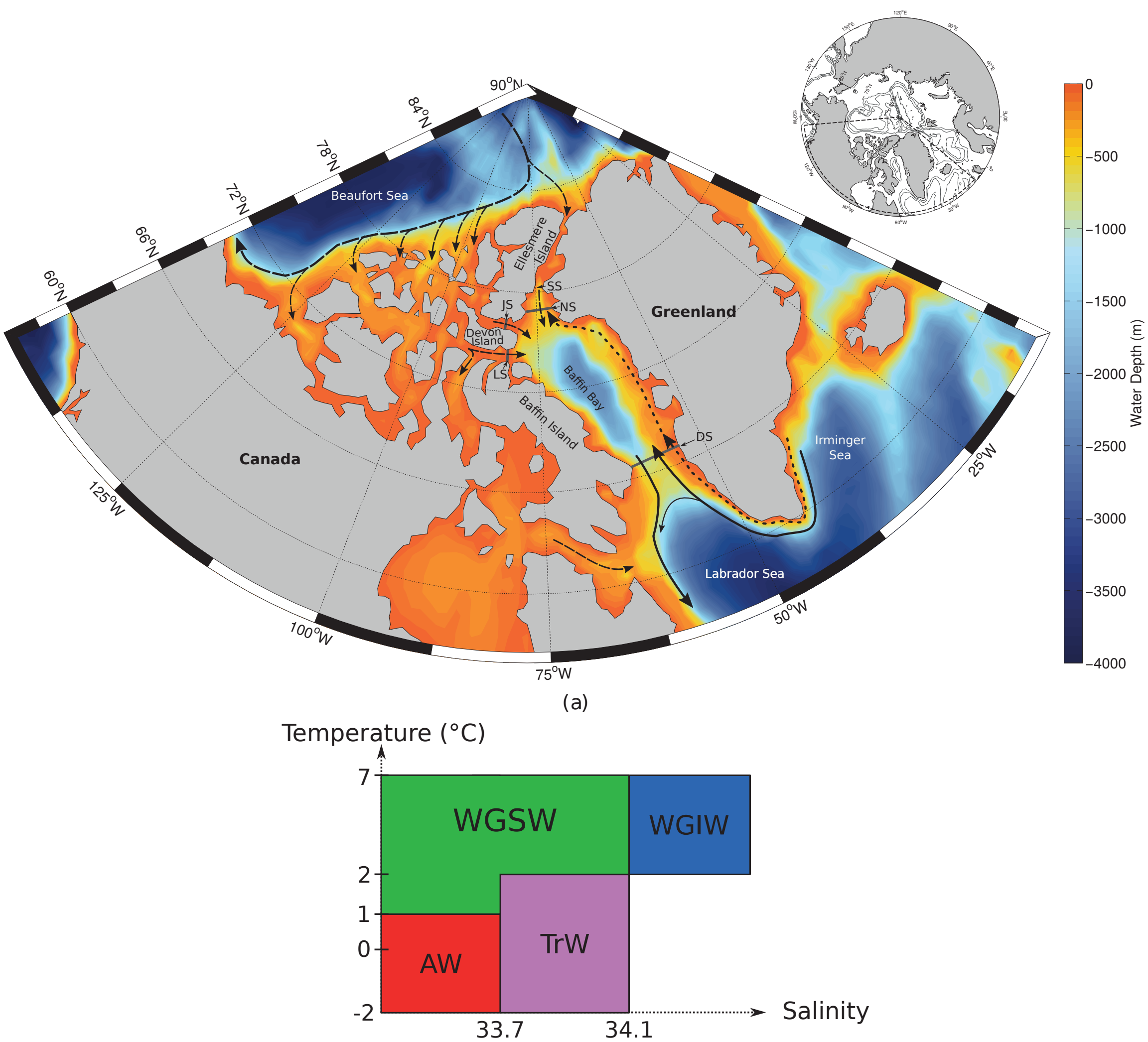

(b)

Figure 3.1: (a) represents Baffin Bay and the Canadian Arctic Archipelago (NS: Nares Strait; JS: Jones Sound; LS: Lancaster Sound; DS: Davis Strait, SS: Smith Sound, FS: Fram Strait) with its localization in the Arctic (upper right). The black arrows represent the travel of different water masses (solid line: West Greenland Water; dotted line: West Greenland Shelf Water; dashed lines: Arctic Water). The gray lines are our domain boundaries used in our calculations. (b) represents the definition of the water masses used in this paper.

ther offshore the West Greenland Current (WGC) carries West Greenland Irminger Water (WGIW). These waters, mostly originating in the Irminger Sea, are Atlantic Waters. They import warm and salty water through the eastern part of Davis Strait (Cuny et al., 2005; Curry et al., 2014; Tang et al., 2004). They follow the continental shelf and slope in east Baffin Bay, with the WGC following the west coast of Greenland. In the north of Smith Sound, in northern Baffin Bay, this current curves to the west, following the east coast of Baffin Island toward the south. It is then called the Baffin Island Current (Münchow et al., 2015). Export to the Labrador Sea occurs in the western part of Davis Strait. Moreover, in northern Baffin Bay, the WGC is modified by the addition of shallow cold and fresh polar outflow, or Arctic Water (AW), that enters Baffin Bay through Nares Strait and Jones and Lancaster Sounds. Finally, a cyclonic gyre exists in the centre of Baffin Bay (Fissel et al., 1982; Tang et al., 2004). Under the previously mentioned water masses a fourth water mass fills the bottom of Baffin Bay: this is the Transitional Water (TrW).

Each of these water masses will have, due to its origin, different temperatures and salinity. In the current paper, we use the same definitions for the water masses as Curry et al. (2014): WGIW is warm (T $>$ 2°C) and salty (S $>$ 34.1), WGSW has a larger temperature range (T $<$ 7°C) and is fresher (S $<$ 34.1), AW is cold (T $<$ 1°C) and fresh (S $<$ 33.7) and TrW lies between the AW and the WGSW (T $<$ 2°C, S $>$ 33.7). Figure 3.1b summaries the water masses definition.

Between 1916 and 2003, Baffin Bay underwent major changes, becoming warmer and fresher (Zweng and Münchow, 2006). The extended warming took place in several parts of the water column. Firstly, a warming in the deep areas in Baffin Bay (between the 300 and 2400 m isobaths) occurred with an increase in temperature of about 0.23 ± 0.13 °C/decade around 300 m. Secondly, significant warming also happened in the 600 to 1000 m range with a temperature increase of about 0.15 ± 0.08°C/decade in the WGC (0.17 ± 0.05°C/decade at 900 m depth, Zweng and Münchow (2006)). Below, the warming is vertically uniform (0.11 °C/decade). It is suspected that this increase in temperature is related to changes that bring warmer water into Baffin Bay, as proposed by Holland et al. (2008a) and Andresen et al. (2011).

The freshening might be a consequence of the observed warming. It has been shown that ice shelf basal melting is sensitive to heat increase in the ocean (Holland et al., 2008a; Myers and Ribergaard, 2013). In particular, Holland et al. (2008b) and Andresen et al. (2011) showed respectively, that the enhanced melting of the Jakobshavn and Helheim Glaciers over the past decades is not only related to milder atmospheric conditions but also to warmer sub-surface water.

The possible impact of the surface temperature increase goes further: if tidewater glaciers are melting, runoff will increase, inputting more freshwater to the ocean surface. Castro de la Guardia et al. (2015) showed from their numerical experiments that this runoff could lead to the lifting of the sea surface height (SSH) in Baffin Bay due to steric effects, changing the baroclinic circulation and reducing the flow through the CAA. The inflow from the WGC will increase, leading to warmer and shallower WGIW that can more easily reach fjords on the Greenland coast and accelerate their melt. Consequently they identified the possibility of a positive feedback between Greenland Ice Sheet melt and Baffin Bay heat content on the eastern Baffin Bay shelf.

The relative impact of the evolution of the temperature and salinity to linear steric height trends in the high latitude ocean was studied by Steele and Ermold (2007) who found that the steric height increase in the North Pacific Subpolar Gyre and Nordic Seas is mostly from freshening. They found freshening in the North Atlantic between 1950 and 2000, but a compensating cooling limited the steric height change. They identified a possible slowdown in the circulation over the North Atlantic and the Arctic Oceans from 1965 to 1990 due to a decrease in steric height, leading to a change in the baroclinic balance. However, their study did not include Baffin Bay.

The long-term evolution of the heat and liquid freshwater going into and out of Baffin Bay is mainly unknown. Observations at Davis Strait and Lancaster Sound show an important variability in the incoming freshwater (heat) flux, with inflow values between 72 and 130 mSv (18 and 20 TW) at Davis Strait (Cuny et al., 2005; Curry et al., 2011; Dickson et al., 2007). At Lancaster Sound, the freshwater and heat inflow are 48 ± 36 mSv and 4.1 ± 1.3 TW, respectively (Melling et al., 2008; Peterson et al., 2012). Only freshwater inflow data are available at Nares Strait (between 25 and 54 mSv, Melling et al. (2008); Münchow (2016)) and Jones Sound (10 mSv, Melling et al. (2008)). Numerical studies focused on Baffin Bay and the CAA improved our understanding of the fluxes through Baffin Bay by providing numerical evaluation of the unknown fluxes. The simulated net outflow is usually lower than observed at Davis Strait but within the variability range at the northern passages (Aksenov et al., 2010; Kliem and Greenberg, 2003; McGeehan and Maslowski, 2012).

From numerical experiments, the relative importance of each northern passage on heat import has been evaluated. Kliem and Greenberg (2003) found that the same amount of heat crosses Barrow Strait (which feeds Lancaster Sound) and Nares Strait (about 38% each), followed by Jones Sound (23%). However their simulation is based only on summer conditions. Numerical experiments over multiple decades from Aksenov et al. (2010) showed that Lancaster Sound had a higher relative importance in the heat transport into Baffin Bay between 1989 and 2006 than the other northern passages (80% of the heat carried, with a reference temperature of $-0.1°$C). The liquid freshwater transport is 69% through Lancaster Sound, 21% through Nares Strait and 10% through Jones Sound (Aksenov et al., 2010; McGeehan and Maslowski, 2012).

The evolution of individual water masses inside Baffin Bay has been observed in order to understand the origin of the variability and the changes that happened in Baffin Bay. Myers and Ribergaard (2013) showed that the temperature of the polar water layer in Disko Bay has increased by 1-2°C since the mid-90s. An acceleration of this warming occurs after 1997. They also noticed an increase in WGIW heat by a factor of two. From the mooring array at Davis Strait, Curry et al. (2014) observed a decrease in the cold and fresh AW transport between 1987-1990 and 2004-2010 (from -2.2 to -1.7 Sv) and an increase in the warm and salty WGIW inflow (from 0.1 to 0.7 Sv). The consequences for Baffin Bay is a reduction in the freshwater outflow and an increase in the heat and salt inflow.

A future projection of the Canadian Arctic based on the Special Report on Emissions Scenarios (SRES) A1B scenario shows a lifting of the SSH of Baffin Bay (Hu and Myers, 2014). This leads to a decrease in the SSH gradient between the Arctic and North Atlantic Oceans. Consequently, the current velocity in Baffin Bay may be modified in response to the lower baroclinic gradient. In addition, the projection predicts a decrease in sea-ice cover in the CAA, which will increase the freshwater available in the ocean because of sea-ice melt. The increased surface and duration of open water will lead to enhanced penetration of precipitation and runoff into the ocean. Finally, the absence of sea-ice will increase the area where heat exchange occurs between the ocean and atmosphere, enhancing air-sea exchange. All of these processes might significantly impact the freshwater and heat supply to the North Atlantic, in particular the Labrador Sea.

The aim of this study is to analyze how the dynamics of Baffin Bay will be modified by the runoff around Baffin Bay, especially from Greenland. In order to do so, we analyzed the evolution of the water masses in Baffin Bay and the transports into and out of the Bay in two sensitivity experiments: one with a constant and the other with an interannual runoff from Greenland. The impact of these changes on the steric height in Baffin Bay for the past (1958-2010) and future (2010-2099) is discussed, as well as the consequences on Baffin Bay circulation and mixing. We present the domain considered, the numerical experiments, their setup, and the numerical tools used for this study in Section 3.2. The evolution of the volume, heat and freshwater transport of the entire water column, as well as an evaluation of the model's ability to reproduce realistic variability for the past will be discussed (Section 3.3). Then, we break down the results by individual water mass and present the evolution in terms of the volume, heat, and freshwater transport (Section 3.4) as well as the evolution inside Baffin Bay (Section 3.5). The same analysis will then be discussed for simulation under an Intergovernmental Panel on Climate Change (IPCC) projection for the future (Section 3.6). We discuss the significance of the results by showing their relation with Baffin Bay steric height (Section 3.7) and present conclusions in the final section (Section 3.8).

3.2 Method

3.2.1 Numerical models

In this study we used a pan-Arctic configuration based on the Nucleus for European Modelling of the Ocean (NEMO) numerical framework, version 3.1 (Madec, 2008). This coupled ocean and sea-ice model includes a three-dimensional, free surface, hydrostatic, primitive-equation ocean component and a dynamic-thermodynamic sea-ice model. The sea-ice module is from the Louvain-la-Neuve sea-ice model (LIM2) (Fichefet and Maqueda, 1997) with a modified elastic-viscous-plastic (EVP) ice rheology (Hunke, 2001; Hunke and Dukowicz, 1997). No-slip and free-slip boundary conditions were applied for sea-ice and the ocean, respectively.

Our model domain starts from the North Atlantic north of 45°N and covers the Arctic seas and the northern Bering Sea with a variable horizontal resolution ranging from approximately 11 km within the central CAA region to approximately 15 km in the Arctic Ocean (Hu and Myers, 2014). In order to overcome the coordinate singularity at the North Pole in standard spherical grids, an orthogonal transformation method (Murray, 1996) was used. In the vertical, 46 z-levels were used with layer thickness varying smoothly from approximately 6 m at the surface to approximately 240 m at the bottom. The bathymetry data were derived from the 1 arcminute global relief model (ETOPO1, Amante and Eakins (2009)) provided by the US National Geophysical Data Center (NGDC).

The model was spun up for 18 years with initial ocean temperature and salinity from the Polar Science Center Hydrographic Climatology (PHC 3.0; Steele et al. (2001)) using normal year atmospheric forcing (6-hourly 10 m surface wind, 10 m air temperature and specific humidity, daily downward longwave and shortwave radiation and monthly total precipitation and snowfall) from the Coordinate Ocean-ice Reference Experiments-phase II (CORE-II) (Large and Yeager, 2009). No temperature or salinity restoring is active except the buffer zones close to the open boundaries and in Foxe Basin. More details can be found in Hu and Myers (2013).

After the spin up we have three different experiments: an interannual hindcast experiment (HINDCAST), forced with atmospheric forcing (1970-2007) from the interannual

CORE-II dataset (Large and Yeager, 2009), a climatic experiment (CLIMATIC), forced by an interannual (1970-2010) hindcast of rescaled monthly atmospheric output from the twentieth century climate experiment (20C3M) of the UK Met Office Hadley Centre Coupled Model, version 3 (HadCM3) (Gordon et al., 2000) (horizontal resolution of 3.75°× 2.5°) and a future scenario simulation (2010-2099; FUTURE). HINDCAST atmospheric variables used the same frequency of the CORE-II normal year forcing. For CLIMATIC and FUTURE, the experiment was forced with monthly rescaled atmospheric output from HadCM3 run under SRES A1B scenario (Nakicenovic et al., 2000) (horizontal resolution of 3.75°× 2.5°).

The low resolution of the atmospheric model fields could affect the high-resolution ocean simulation because of local bias (e.g., due to a too coarse coastline in the atmospheric model). Thus, following an approach similar to that of Dumas et al. (2006) reconstructing atmospheric dataset by applying the variations in the original fields onto relatively higher resolution climatological fields might help avoid part of the bias. This approach allowed us to study the responses of the sea-ice and ocean to changes in the original fields, meanwhile, guaranteeing a reasonable seasonal cycle by taking advantage of the climatology dataset as the base. The preprocess is documented in Hu and Myers (2014). A brief summary is described here.

The precipitation, snowfall and specific humidity are corrected by multiplying the climatology by a ratio between the original numerical output and the climatological mean (CORE-II normal year data):

$$X_{\text{new}}(t) = \overline{C}_{\text{core}} \times (X_{ori}(t)/\overline{C}_{\text{1970-1999}}) \tag{3.1}$$

where X_{new} is the new value; $\overline{C}_{\text{core}}$ is the CORE-II normal year value; X_{ori} is the output from HadCM3; $\overline{C}_{\text{1970-1999}}$ is the average of the output from HadCM3 for 1970 to 1999, and t is time. The surface air temperature and downward radiation are modified by adding the mathematical difference from the mean to climatology data:

$$X_{\text{new}}(t) = X_{ori}(t) + (\overline{C}_{\text{core}} - \overline{C}_{\text{1970-1999}}) \tag{3.2}$$

Runoff and winds ($u-$ and $v-$ winds) are left unmodified.

Monthly eastern and western open boundary fields are taken from a global numerical simulation (ORCA025-KAB001; Barnier et al. (2006)) for HINDCAST; CLIMATIC and FUTURE are taken from the corresponding runs of the Canadian Centre for Climate Modelling and Analysis (CCCma) Third Generation Coupled Global Climate Model CGCM3.1 (Gordon et al., 2000).

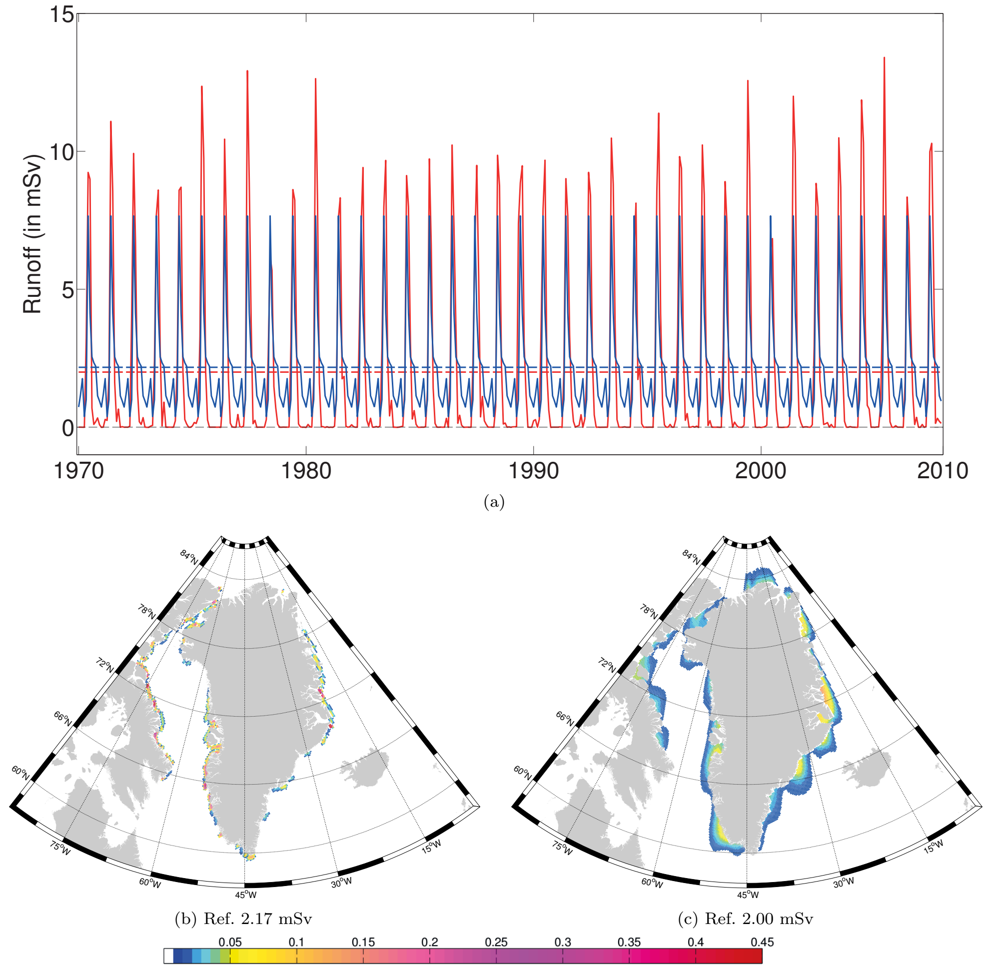

(a)

(b) Ref. 2.17 mSv

(c) Ref. 2.00 mSv

Figure 3.2: (a) represents the temporal evolution of summed monthly runoff over the area shown in (b) and (c). HINDCAST is in blue while CLIMATIC is in red. (b) and (c) represent the spatial distribution of the runoff around Baffin Bay and Greenland for (b) HINDCAST and (c) CLIMATIC, the color map represents the mean fraction of runoff at each grid point averaged over the mean runoff from 1970 to 2010 for each considered forcing.

The runoff after the spin up phase is different in the experiments. The HINDCAST simulation uses fixed monthly Dai and Trenberth (2002) climatology runoff data repeated every year, whereas CLIMATIC and FUTURE use unmodified interannual runoff from HadCM3 output. Both seasonal and interannual cycles are different. Around Baffin Bay, on average, between 1970 and 2010, the HINDCAST simulation has more runoff into Baffin Bay (2.17 mSv) than CLIMATIC simulation (2.00 mSv) (Figure 3.2a). However, the interannual seasonal runoff has a more realistic seasonal cycle, with more runoff in summer and almost no runoff during winter and with interannual varibility (Figure 3.2a). Moreover, the spatial distribution is different. The HINDCAST simulated runoff is located close to the coast leading to locally high values of freshwater (Figure 3.2b), while the interannual runoff has a smoother distribution of freshwater along the continental shelf, which includes freshwater from rivers, glaciers and fjords (Figure 3.2b), as well as the coarse resolution of the HadCM3 model. We note that the simulated sea surface temperature is applied as river's temperature in the experiments.

3.2.2 Transport and storage

We define Baffin Bay as the area located between Davis Strait in the south and Lancaster Sound, Jones Sound and Nares Strait in the north (gray lines in Figure 3.1a). The criteria to define each water masses are based on the water masses crossing Davis Strait, similar to those used by Curry et al. (2011) as described in section 3.1.

To characterize the evolution of Baffin Bay water masses we examine the relation between the heat and freshwater contained in Baffin Bay and the evolution of the transport of volume, heat, and freshwater at the boundaries of the domain, including the ocean-air (sea-ice) boundary.

Transport calculations

The annual averaged volume, liquid freshwater, and heat transports were computed for each grid-cell face, summed over the grid cells defining each boundary and time averaged to compute the annual transport. Volume transport across a grid cell of a given section is calculated by multiplying the normal velocity field belonging to a grid cell by the corresponding area of the same grid cell. To obtain the total transport across a section we then sum up the transport of each individual grid cell belonging to the cross-section considered. Heat and liquid freshwater (eq. 3.3a) and heat (eq. 3.3b) transports are calculated as:

$$\mathrm{T}_{\mathrm{Heat}} = \rho_{\mathrm{ref}} C_p \sum v_i (T_{\mathrm{ref}} - T_i) A_i \tag{3.3a}$$

$$\mathrm{T}_{\mathrm{FW}} = \sum v_i \frac{S_{\mathrm{ref}} - S_i}{S_{\mathrm{ref}}} A_i \tag{3.3b}$$

where v_i, S_i, T_i, C_p and A_i are the normal velocity, the salinity, the temperature, the heat capacity ($C_p = 4218$ J °C^{-1} kg^{-1}), and area associated with a given grid cell. The reference salinity ($S_{\mathrm{ref}} = 34.8$) considers the average Arctic Ocean salinity (Aagaard and Carmack, 1989) and the reference temperature ($T_{\mathrm{ref}} = -2.0$ °C) corresponds to the freezing point at the highest salinity possible in this area. The temperature reference was chosen to avoid a negative value for heat that would be wrongly summed during the discrete integration process. The transport sign is defined as positive when entering Baffin Bay and negative when exiting Baffin Bay. Solid transports were not examined, considering their minor contribution (Sou and Flato, 2009). If not specified, the freshwater transport discussed later in the paper will consider only the liquid part.

Domain storage calculations

The volume storage is defined by computing the volume of each grid cell within the domain. Heat and freshwater storage are computed from the 5- or 30-day average ocean temperature and salinity:

$$\mathrm{T}_{\mathrm{Heat}} = \rho_{\mathrm{ref}} C_p \sum (T_{\mathrm{ref}} - T_i) V_i \tag{3.4a}$$

$$\mathrm{T}_{\mathrm{FW}} = \sum \frac{S_{\mathrm{ref}} - S_i}{S_{\mathrm{ref}}} V_i \tag{3.4b}$$

where S_i, T_i and V_i are, respectively, the salinity, the temperature and the volume associated with a given grid cell.

3.2.3 Steric height

The steric height corresponds to the vertically integrated departure of density ρ at a given salinity, temperature and pressure, S, T and p, respectively, from a standard reference ρ_{ref} multiplied the layer thickness z_i summed from the surface to a given depth H, computed from the 5- or 30-day average model output as:

$$\mathrm{SH} = \sum_{\mathrm{Surface}}^{\mathrm{H}} \left(\frac{\rho_{\mathrm{ref}} - \rho_{i,T,S,p}}{\rho_{\mathrm{ref}}} \right) z_i \tag{3.5}$$

In order to be certain that we captured all the changes in the deeper part of Baffin Bay the integration was carried out over the top 1000 m.

The total steric height can also be separated into the contribution from temperature (thermosteric height, SHt) and salinity (halosteric height, SHs) alone, that is:

$$\mathrm{SH} = \mathrm{SHt} + \mathrm{SHs} \tag{3.6a}$$

$$\mathrm{SH} = \sum_{\mathrm{Surface}}^{\mathrm{H}} \left(\frac{\rho_{\mathrm{ref}} - \rho_{i,T_{\mathrm{ref}},S,p}}{\rho_{\mathrm{ref}}} \right) z_i + \sum_{\mathrm{Surface}}^{\mathrm{H}} \left(\frac{\rho_{\mathrm{ref}} - \rho_{i,T,S_{\mathrm{ref}},p}}{\rho_{\mathrm{ref}}} \right) z_i \tag{3.6b}$$

Non-linear terms in the equation of state are generally less than 1% and were neglected (Landerer et al., 2007). Non-Boussinesq effects are negligible in our region of interest and thus were not taken in consideration by the model, which uses the Boussinesq approximation

(Griffies and Greatbatch, 2012). Moreover, the thermosteric (halosteric) height can be related to the vertically integrated heat content and freshwater content for small departures of temperature (salinity) from their reference value, that is,

$$\mathrm{SHt} = \left\langle \frac{1}{\rho_{\mathrm{ref}}^2 c_p} \left(\frac{\Delta\rho}{\Delta T}\right)_{T,S_{\mathrm{ref}}} \right\rangle \sum_{\mathrm{Surface}}^{H} \rho_{\mathrm{ref}} c_p \left(T_{\mathrm{ref}} - T_{\mathrm{i}}\right) z_i \tag{3.7a}$$

$$\mathrm{SHs} = \left\langle \frac{S_{\mathrm{ref}}}{\rho_{\mathrm{ref}}} \left(\frac{\Delta\rho}{\Delta S}\right)_{T_{\mathrm{ref}},S} \right\rangle \sum_{\mathrm{Surface}}^{H} \frac{\left(S_{\mathrm{ref}} - S_{\mathrm{i}}\right)}{S_{\mathrm{ref}}} z_i \tag{3.7b}$$

where heat capacity is considered constant over the temperature range and angle brackets $\langle\rangle$ denote the vertical average.

3.3 Transports

3.3.1 Volume

The net long term-model outflow transport through Davis Strait is larger (-2.5 versus -0.9 Sv, 1 Sv $= 10^6 \mathrm{m}^3\mathrm{s}^{-1}$) in the HINDCAST simulation than in the CLIMATIC one (Figure 3.3a). This is comparable to observational estimates between -2.0 and -2.6 Sv (Cuny et al., 2005; Curry et al., 2011; Melling et al., 2008). Values from HINDCAST are closer to these estimates than previous modelling experiments, such as McGeehan and Maslowski (2012) who obtained -1.6 ± 0.3 Sv between 1979 and 2004. Both the CLIMATIC and HINDCAST simulations have local transport peaks in the early 1980s and 1990s. Transports between the two experiments are not correlated. Higher frequency variability is seen in HINDCAST.

The inflow component of the Davis Strait transport (i.e., WGC inflow) is comparable between the two runs (1.4 versus 1.8 Sv). Thus, the difference in the net transport between the two experiments is a function of the southward transport in the Baffin Island Current being significantly larger (-2.3 versus -4.3 Sv) in HINDCAST. Years with enhanced outflow transport are generally those with larger net transport.

The volume transport is larger in HINDCAST for each of the northern passages. Lancaster Sound is the main source of inflow (73 % in HINDCAST and 56 % in CLIMATIC) into Baffin Bay, followed by Nares Strait (32 % and 17 %) and Jones Sound (12 % and 9%). Compared to previous studies focused on the northern transport CLIMATIC is closer to the observational breakdown, evaluated at approximatively 52% at Lancaster Sound, 25% at Nares Strait and 23% at Jones Sound (Melling et al., 2008; Münchow et al., 2007; Münchow and Melling, 2008; Peterson et al., 2012).

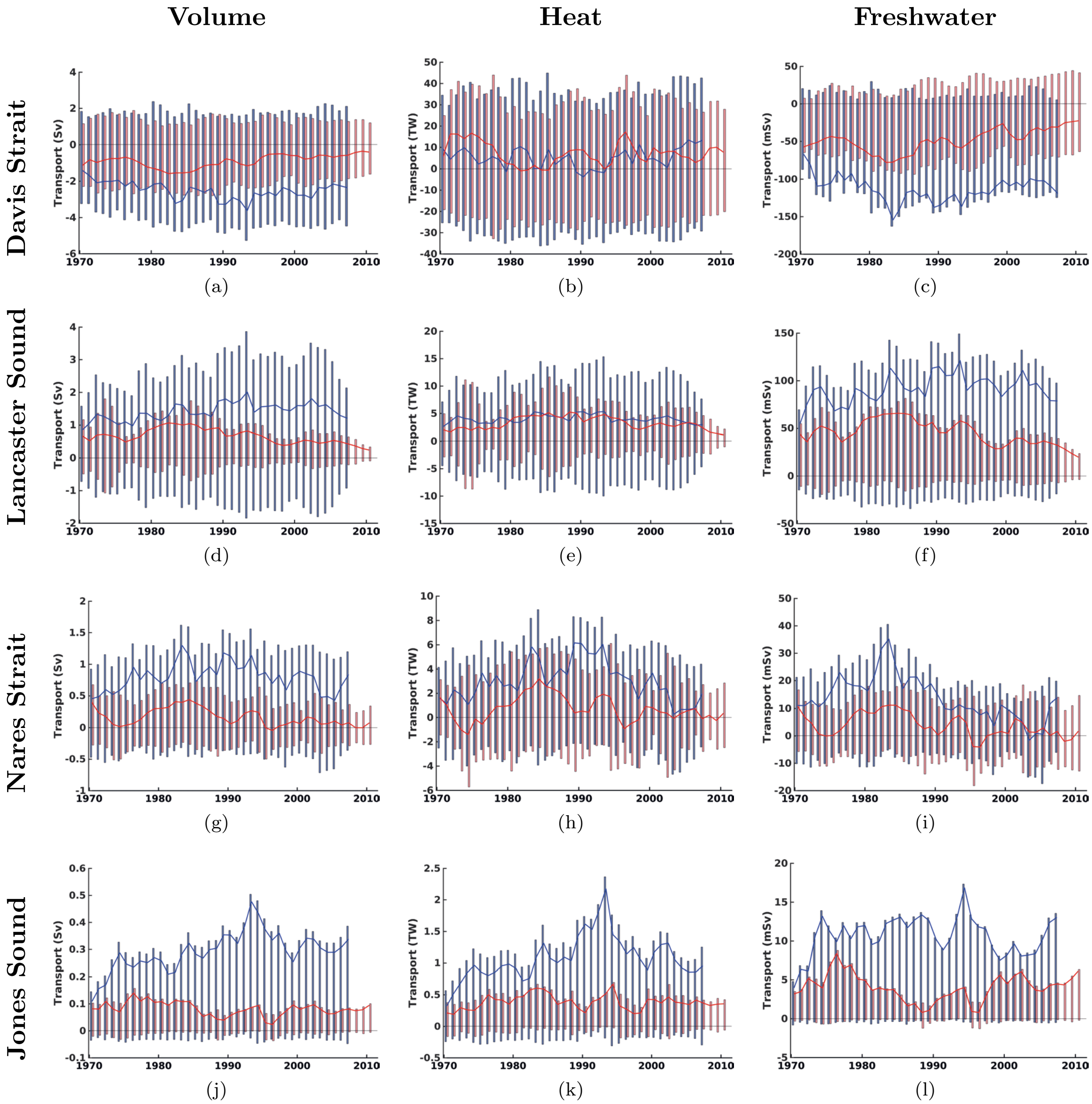

Figure 3.3: Total volume (left column), heat (middle column) and freshwater (right column) transport for: Davis Strait Transport (a, b and c), Lancaster Sound (d, e and f), Nares Strait (g, h and i) and Jones Sound (j, k and l) . The bars are for the inflow (positive) or outflow (negative) component of the transport only. The thick lines corresponds to the net transport. The blue color is for HINDCAST while CLIMATIC is in red.

At Lancaster Sound, CLIMATIC shows a decreasing trend in the net transport after 1984 from 1.3 Sv to 0.20 Sv (Figure 3.3d), because of a 80% reduction of the inflow (from 1.0 to 0.2 Sv) and a reduction of 33% of the outflow (from -0.9 Sv to -0.2 Sv). This evolution is not present in HINDCAST where the variability hides any clear trend.

Nares Strait outflow stays stable in both experiments, with an average of 0.4 ± 0.05 Sv (Figure 3.3g). The inflow component has more variability and controls the net transport.

The transport in HINDCAST increases between 1970 and 1985 from 0.5 Sv to 1.2 Sv (increase of 58%) and decreases after 1985 back to its initial value. Only the second period is present in CLIMATIC (decrease of 90%), but is initiated 5 years later, in 1990.

The net transport at Jones Sound in the HINDCAST simulation increases from 0.1 Sv to 0.3 Sv with a spike of about ~ 0.5 Sv in 1992 (Figure 3.3j) because of higher inflow. The net transport in CLIMATIC increases slightly from 0.1 Sv to 0.05 Sv after 1984 (decrease of about 50%).

3.3.2 Heat

The net heat transport at Davis Strait is slightly higher in the CLIMATIC simulation (7.1 versus 5.1 TW, Figure 3.3b). The inflow component only (i.e., the heat carried by the WGC) is also higher in this experiment (36.8 versus 31.8 TW). The relatively low value of the net transport in HINDCAST is related to a higher outflow (-31.6 TW versus -24.8 TW). This is comparable to the observational estimates of about 27.0 ± 15 TW (inflow) and -15.5 ± 8 TW (outflow) (Cuny et al., 2005). We note that Cuny et al. (2005) do not include the West Greenland shelf, and they use a different reference temperature of about 0 °C instead of our -2 °C. From numerical modelling experiments, Aksenov et al. (2010) showed a smaller value for net heat transport of about 15.0 ± 7 TW, with a reference temperature of -0.1 °C.

Both experiments present strong interannual variability that is very likely to be controlled by the strength of the WGC. This is consistent with the high correlation coefficient between the total net transport and the inflow ($r = 0.90$ in CLIMATIC and $r = 0.80$ in HINDCAST). We note the large increase in heat associated with a higher inflow between 1994 and 1996 in both experiments.

The net heat transport at the northern passages presents a net inflow in both experiments at Lancaster Sound (4.0 versus 3.2 TW, correlated at $r = 0.48$) (Figure 3.3e). HINDCAST net transport is higher for both Nares Strait (3.0 versus 0.7 TW, Figure 3.3h) and Jones Sound (1.1 versus 0.4 TW, Figure 3.3k). This compares well with the previous numerical modelling study of Aksenov et al. (2010) that evaluated Lancaster Sound heat inflow at about 5.0 ± 1 TW, Nares Strait at about 2.0 ± 1 TW, and an outflow at about -1.0 ± 1 TW happens at Jones Sound.

The net heat transport through Lancaster Sound stays close to its average over the time period for both experiments (4.0 ± 0.5 and 3.2 ± 1.3 TW). In both experiments, the heat transport is highly correlated to the net transport ($r > 0.75$). After 1988 the correlation coefficient increases to 0.98 for CLIMATIC and 0.89 for HINDCAST.

Nares Strait heat transport is highly correlated to the volume transport for Davis Strait ($r > 0.73$) in both experiments. The heat outflow at Nares Strait is related to the warm inflow pulse that follows west coast of Greenland and pushes north inside a deep trough present at Smith Sound, before shifting toward the west and returning.

At Jones Sound, the volume and heat transports are highly correlated in HINDCAST (correlation coefficient of about 0.90), while in CLIMATIC the correlation coefficient decreases to $r = 0.50$.

3.3.3 Freshwater

At Davis Strait, the evolution of the net liquid freshwater transport is highly correlated to the volume transport (HINDCAST: $r = 0.95$, CLIMATIC: $r = 0.81$) (Figure 3.3c). The net freshwater transport is higher in HINDCAST (-113.2 versus -48.5 mSv). This is comparable to the observations and other model results that are between -70.0 mSv (model; McGeehan and Maslowski (2012)) and -130.0 mSv (observation; (Curry et al., 2011)).

At the northern passages, the correlation coefficient between the volume transport and the liquid freshwater transport is the highest at Lancaster Sound with a correlation coefficient greater than 0.95 for both experiments (Figure 3.3f). Regarding the other passages, CLIMATIC has a higher correlation coefficient for Nares Strait ($r = 0.96$ versus $r = 0.63$, Figure 3.3i), and Jones Sound ($r = 0.86$ versus $r = 0.62$, Figure 3.3l). The net freshwater transport is still lower in CLIMATIC (Lancaster Sound: 45.2 versus 91.3 mSv, Jones Sound: 4.0 versus 10.7 mSv, and Nares Strait: 3.8 versus 13.2 mSv). This is comparable with observations that evaluated the freshwater transport between 31.0 to 48.0 mSv for Lancaster Sound, 10.0 mSv at Jones Sound and 10.4 to 25.0 mSv at Nares Strait (McGeehan and Maslowski, 2012; Melling et al., 2008; Münchow et al., 2007; Wekerle et al., 2013). From a numerical study, Aksenov et al. (2010) evaluated the liquid transport between 1989 and 2005 to 64.0 ± 11 mSv at Lancaster Sound, 20.0 ± 6 mSv at Nares Strait, and 9.0 ± 2 mSv at Jones Sound.

3.4 Transport of the water masses

3.4.1 Arctic Water

At Davis Strait, the AW transport is mainly southward (i.e., outflow) in both experiments (Figure 3.4a). The net transport is higher in HINDCAST (-1.4 versus -0.9 Sv), but

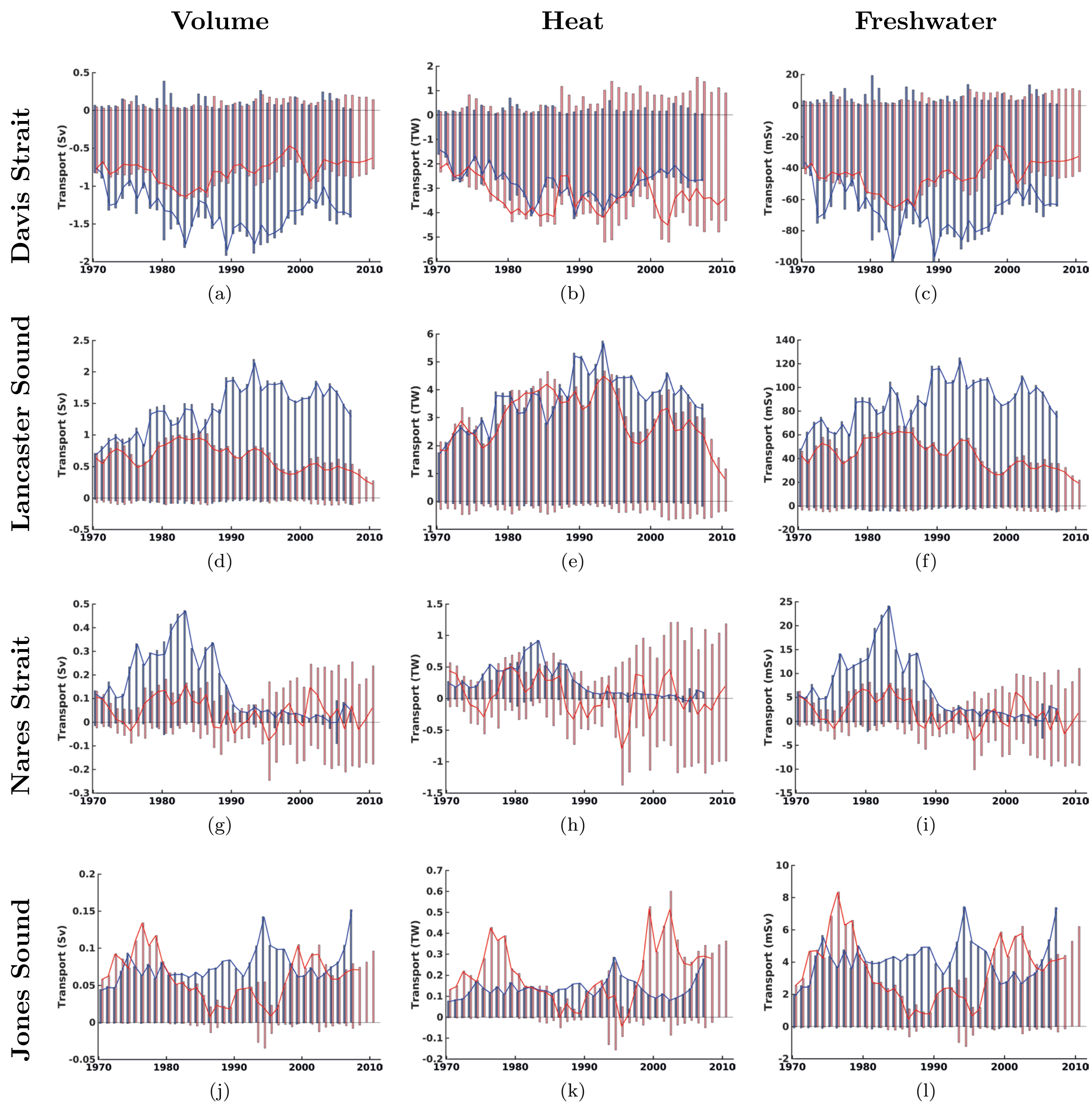

Figure 3.4: Arctic Water volume (left column), heat (middle column) and freshwater (right column) transport for: Davis Strait Transport (a, b and c), Lancaster Sound (d, e and f), Nares Strait (g, h and i) and Jones Sound (j, k and l) . The bars are for the inflow (positive) or outflow (negative) component of the transport only. The thick lines corresponds to the net transport. The blue color is for HINDCAST while CLIMATIC is in red.

its proportion of the total outflow is smaller (33% versus 39%). The AW outflow increases by 20% in the 2000s in both experiment to reach an average transport of about −0.4 Sv (CLIMATIC) and −1.5 Sv (HINDCAST). This is comparable to measurements from Curry et al. (2014) over the 2002 and 2010 period. They evaluated the AW mean outflow at −1.8 Sv (all future measurements reported from this paper will be for the mean over the same time period). Davis Strait outflow variability is more closely related to the AW variability in HINDCAST (correlation coefficient of about 0.75 versus 0.65).

The correlation coefficient between the total AW transport and the heat and freshwater transport are high in both experiments (heat: $r > 0.70$; freshwater: $r > 0.95$) (Figure 3.4b and Figure 3.4c). The AW is only a marginal source of heat through Davis Strait in both experiments (< 15%). CLIMATIC AW carries approximatively 30% more heat than HINDCAST. This conveys a similar amount of heat, given the lower volume transport, implying that AW is warmer in this experiment.

In both experiments AW is the main source of freshwater outflow. Despite the lower transport in CLIMATIC, its importance in the freshwater outflow is higher (65 versus 57% of the total freshwater exported at Davis Strait). The corresponding outflow is higher in HINDCAST (−66.7 versus −44.4 mSv). This compares well with the approximately 70 mSv averaged between 2002 and 2010 noted by Curry et al. (2014).

In the north, Lancaster Sound is the main source of AW with a higher inflow in HINDCAST (0.6 versus 1.4 Sv) (Figure 3.4d). The AW represents more than 95% of the total transport through the strait in both experiments. The AW variability is the main source of the total volume variability at Lancaster Sound, especially in HINDCAST (correlation coefficient of about 0.81 versus 0.93).

In CLIMATIC, after 1985 the correlation coefficient between AW inflow at Lancaster Sound and AW outflow at Davis Strait decreases by 0.20, showing that these straits start to be less important. The AW inflow across Nares Strait and Jones Sound is higher in HINDCAST (0.1 versus 0.2 Sv and 0.1 versus 0.1 Sv, respectively) (Figure 3.4g and 3.4j). At Jones Sound, the AW represents the same amount of the inflow but is relatively more important in CLIMATIC ($r = 0.70$ versus $r = 0.24$) (Figure 3.4j). This is the main source of variability in the total transport in CLIMATIC only (correlation coefficient between AW and the net inflow: 0.85 versus 0.67).

The heat transport through northern passages carried by the AW is higher in the HINDCAST simulation because of the higher transport (Lancaster Sound: 2.9 versus 3.7 TW, Nares Strait: 0.1 versus 0.3 TW, Jones Sound: 0.2 versus 0.1 TW; Figure 3.4e, 3.4e, h and 3.4k, respectively). The net inflow however, is small in both simulations. At Lancaster Sound, AW is warmer in CLIMATIC and carries about 91% of the total heat in both experiments. This could be the reason for the higher heat in the outflow at Davis Strait in this experiment.

The main source of AW freshwater is Lancaster Sound with higher transport overall in the HINDCAST simulation because of the higher volume transport (43.3 versus 87.1 mSv;

Figure 3.4f). Nares Strait and Jones Sound transport about the same amount of freshwater (Nares Strait: 1.9 versus 6.9 mSv, Jones Sound: 3.5 versus 4.2 mSv; Figure 3.4i and 3.4j). At Nares Strait, the AW proportion is higher in CLIMATIC but is not the main inflow water mass (27 versus 19%), and its variability only has a moderate impact on the total transport, particularly in HINDCAST (correlation coefficient of about 0.27 versus 0.62).

We note at Nares Strait, in the CLIMATIC simulation, an increase in the interannual variability in the volume inflow and outflow after 1995. This variability does not significantly affect the freshwater net transport (correlation coefficient: 0.99); however, there is a decrease in the correlation coefficient between the volume and heat transport ($r = 0.87$). It indicates a warming of AW after 1995 in this experiment.

This is also observed in the same experiment at Jones Sound where two periods of important inflow appear in 1975-1976 and 1999-2002. The second spike brings about 40% more heat into Baffin Bay than the first one, despite a smaller volume transport (-25%).

3.4.2 West Greenland Irminger and Shelf Waters

At Davis Strait, the mean WGIW inflow over the time period is larger in the HINDCAST simulation (1.3 versus 0.8 Sv; Figure 3.5a). This explains 59 and 74% of the total inflow. The outflow is also much higher in HINDCAST (-0.3 versus -1.6 Sv) for 15% and 37% of the total outflow. The higher outflow in HINDCAST leads to a negative net transport of WGIW through Davis Strait (i.e., net export) with a total mean net transport over the time period of about -0.3 Sv.

The temporal evolution of the WGIW transport does not show any significant variation in the HINDCAST simulation, while in CLIMATIC, the reduction of the northward component after 1975 leads to a reduction of about 50% in the net transport, reaching an average of 0.6 Sv between 2004 and 2010. This compares with previous measurements of the WGIW inflow of between 0.4 and 1.2 Sv (Curry et al., 2014); no outflow of WGIW at Davis Strait was found by the authors.

In the CLIMATIC simulation, the higher WGIW inflow around 1975 is also associated with a pulse of WGSW inflow of about 0.2 Sv. After 1985 this water mass becomes more important in this experiment with much higher inflow of about 0.3 Sv, representing 21% of the total inflow. This is not balanced by any outflow before 1995 when the changing outflow leads to a reduction of the net transport of 30%. This evolution is not present in HINDCAST, in which the WGSW inflow is very small (3% of the total inflow). The outflow is, however, more important (-0.5 Sv versus -0.1 Sv) leading to an export of WGSW. This is comparable to previous measurement by Curry et al. (2014) that evaluated the WGSW inflow to be about 0.7 Sv. They did not observe WGSW outflow at Davis Strait.

In both experiments, these two water masses carried more than 80% of the total heat inflow through Davis Strait (Figure 3.5b and 3.6b). In the HINDCAST simulation, almost all the heat is carried by the WGIW alone, whereas in CLIMATIC this amount is shared (WGIW: 62%, WGSW: 12%). The net transport of heat is higher in CLIMATIC (7.1 versus 5.1 TW).

The evolution of the total heat flux in the HINDCAST simulation can be explained by the evolution of the WGIW, with a correlation coefficient between the total heat transport and the WGIW transport of about 0.98. In CLIMATIC, the total evolution is shared with the WGIW and WGSW (correlation coefficient of about 0.78 and 0.50, respectively).

At Davis Strait, the WGIW and WGSW inflows are sources of freshwater (Figure 3.5c and 3.6c). The proportion of freshwater carried by these water masses is higher in CLIMATIC than in HINDCAST (WGIW: 30% versus 15%; WGSW: 39% versus 32%). The greater outflow of WGIW and WGSW in HINDCAST leads, however, to a net export of freshwater in this simulation. This export is also present in CLIMATIC but only after 1998, showing that the outflow is fresher than the inflow.

The mean net freshwater transport during the entire time series for both water masses is higher in the HINDCAST simulation (-7.6 versus -3.3 mSv and -25.4 versus -4.7 mSv). This is comparable to previous measurement of about -2.0 to -5.0 mSv for the WGIW transport and -17.0 mSv for the WGSW (Curry et al., 2014).

In the north, both WGIW and WGSW transport, across our boundaries are almost negligible and not seen every year. However, we note, a similar evolution of the northward and southward transports in HINDCAST that suggests that the WGIW is recirculating through the boundary: everything that comes from the east side of the cross-section crosses to the west side of the section in the same year (not shown). We note a particularly strong inflow pulse of WGIW between 1989 and 1991 of about 0.4 Sv (3.0 TW and 2.0 mSv).

3.4.3 Transitional Water

The inflow of TrW at Davis Strait is higher in the CLIMATIC simulation but still small (0.2 versus 0.1 Sv; Figure 3.7a). The TrW outflow is also higher in CLIMATIC (41% versus 14% of the total outflow). The net outflow average over the entire time period is higher in CLIMATIC (-0.8 Sv versus -0.5 Sv). This is comparable with previous measurements of about -0.2 Sv (Curry et al., 2014).

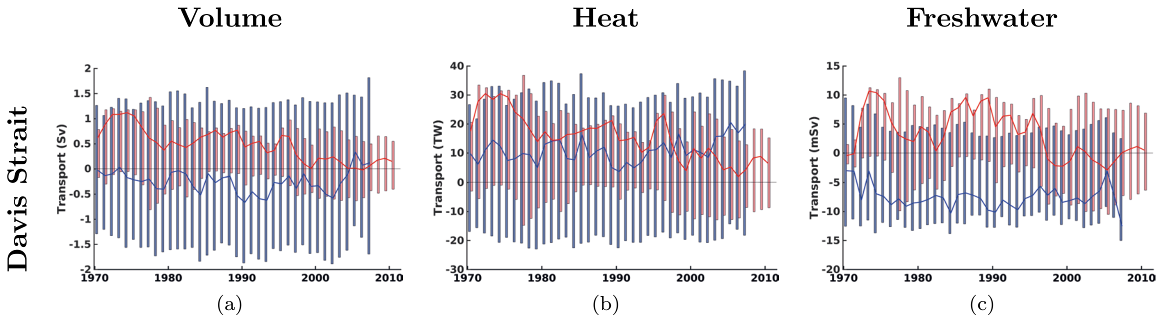

Figure 3.5: West Greenland Irminger Water volume (left column), heat (middle column) and freshwater (right column) transport for: Davis Strait Transport (a, b and c). The bars are for the inflow (positive) or outflow (negative) component of the transport only. The thick lines corresponds to the net transport. The blue color is for HINDCAST while CLIMATIC is in red.

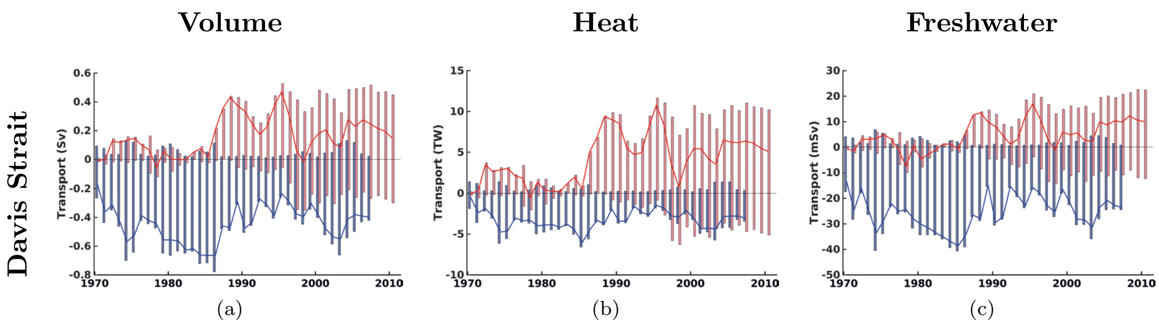

Figure 3.6: West Greenland Shelf Water volume (left column), heat (middle column) and freshwater (right column) transport for: Davis Strait Transport (a, b and c). The bars are for the inflow (positive) or outflow (negative) component of the transport only. The thick lines corresponds to the net transport. The blue color is for HINDCAST while CLIMATIC is in red.

In the HINDCAST simulation, the outflow increases slowly by 15% over the whole time period. CLIMATIC presents a clear decrease in the transport resulting from a lower outflow between 1975 and 1980 (drop of 30%) and after 1990 (drop of 66%).

The transport of heat and freshwater at Davis Strait is strongly related to the volume transport in both experiments with a correlation coefficient greater than 0.90 (Figure 3.7b and 3.7c). The heat outflow is higher in CLIMATIC (-9.8 versus -2.7 TW). However, the freshwater outflow is similar in both experiments (-12.8 versus -12.6 mSv), despite the higher outflow in CLIMATIC. This indicates that the TrW outflow in CLIMATIC is warmer and fresher than in HINDCAST. This is comparable to a measurement of TrW freshwater outflow of about -19.0 mSv by Curry et al. (2014).

At the northern passages, TrW inflow is only significant in the HINDCAST simulation in which it comes from Lancaster Sound and Nares Strait (0.5 and 0.7 Sv, respectively).

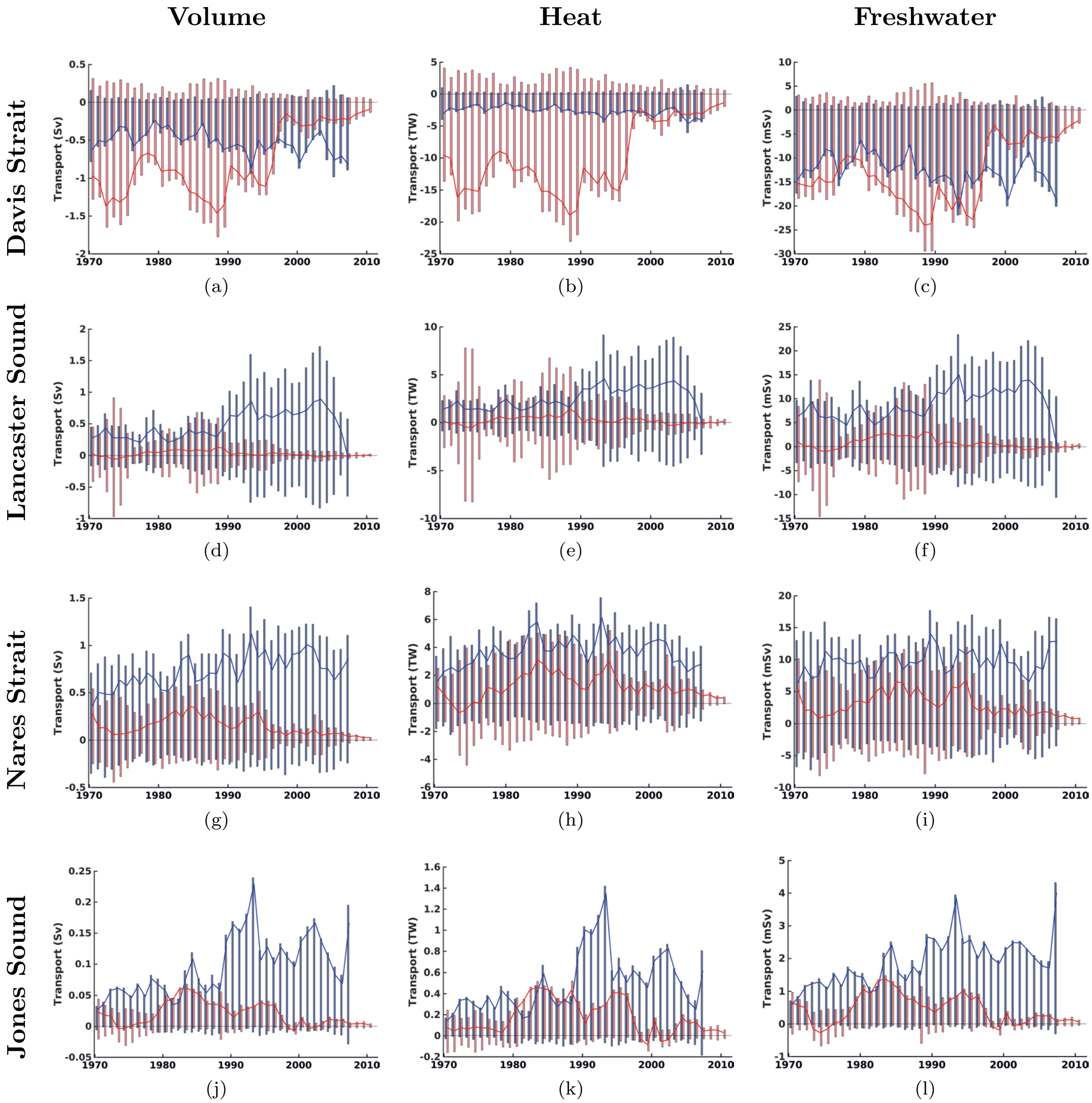

Figure 3.7: Transitional Water volume (left column), heat (middle column) and freshwater (right column) transport for: Davis Strait Transport (a, b and c), Lancaster Sound (d, e and f), Nares Strait (g, h and i) and Jones Sound (j, k and l) . The bars are for the inflow (positive) or outflow (negative) component of the transport only. The thick lines corresponds to the net transport. The blue color is for HINDCAST while CLIMATIC is in red.

The inflow from Jones Sound is smaller (0.1 Sv). Only Nares Strait inflow is significant in CLIMATIC with an inflow of about 0.2 Sv. The net inflow from Lancaster Sound and Jones Sound is close to zero; the transport across Lancaster Sound is mainly recirculation around the section (not shown).

The correlation coefficient between the heat and freshwater inflow is higher than 0.95 in both experiments, which gives negligible TrW heat and freshwater inflow, consistent with the low volume inflow. The TrW heat inflow is greater in the HINDCAST simulation at each strait (Lancaster Sound: 2.5 versus 0.2 TW; Nares Strait: 3.7 versus 1.2 TW; Jones Sound: 3.7 versus 1.2 TW) as well as the freshwater transport (Lancaster Sound: 8.7 versus 0.7 mSv; Nares Strait: 9.6 versus 3.0 mSv; Jones Sound: 1.9 versus 0.5 mSv).

3.5 Evolution of the water masses in Baffin Bay

The evolution of the volume of each water mass shows no major changes in time in the HINDCAST simulation (Figure 3.8a), which is not the case in CLIMATIC (Figure 3.8d). The only observable change in HINDCAST concerns the AW which increases in importance between 1970 and 1981 and then slowly decreases. The TrW is the dominant water mass (92%), followed by the AW (5%) and the WGIW (2%). The WGSW is almost absent in Baffin Bay (< 1%).

Sharing the same initial conditions, CLIMATIC starts with similar proportions as HINDCAST. However, during the run the TrW loses its dominance in the total volume to reach only 52% of the total. For later analysis we define 1970-1978 as Period I, 1979-1988 as Period II, 1989-1994 as Period III and 1995-2010 as Period IV. In Period I, the importance of WGIW reaches 20%. Its importance decreases to 10% by 1988. In Period II the importance of WGSW starts to grow, reaching 3% in 1994. In Period III the increase of the WGSW is

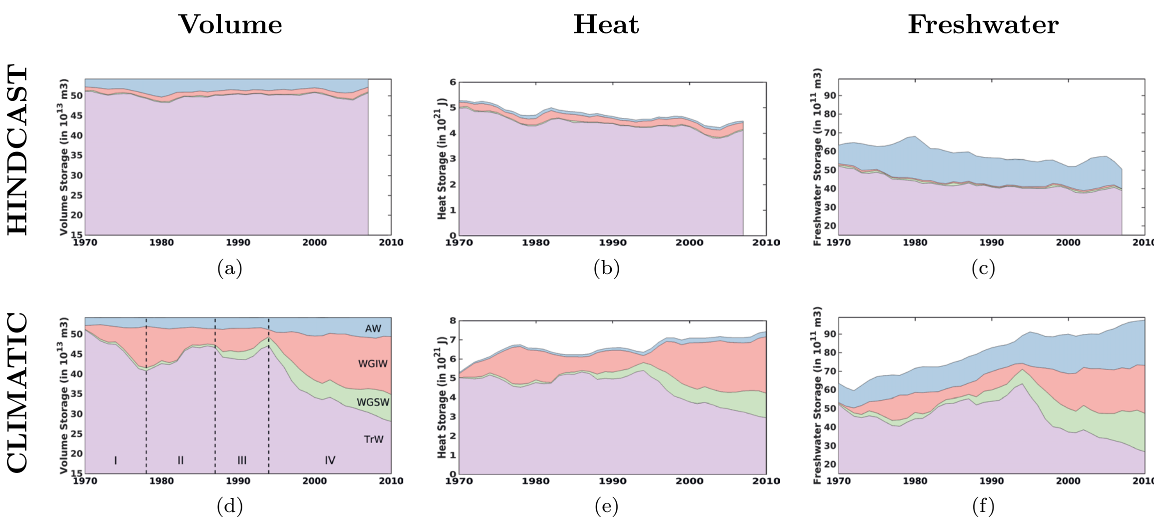

Figure 3.8: Volume (left panels), heat (middle panels) and freshwater (right panels) storage for each water mass in Baffin Bay. The first line is for HINDCAST while the second line is for CLIMATIC. Transitional Water is in purple, West Greenland Shelf Water in green, West Greenland Irminger Water in red and Arctic Water in blue.

associated with a decrease in WGIW, reaching a minimum of 3% in 1994, and an increase in the TrW. In Period IV, the importance of the WGIW grows to 26% and the WGSW increases to 21%. The relative importance of AW remains almost steady during the first decade. It starts to increase after 1994 to reach a maximum of 26% in 2008.

Three possibilities could explain the evolution of each individual water mass: a larger input of heat or freshwater at the surface, an imbalance in the transport going through Baffin Bay, or internal changes inside the domain. The increase in the AW proportion in Baffin Bay in the HINDCAST simulation around 1980 and 2005 can be explained by the increase in the AW inflow that is not immediately balanced by an increase in the outflow, leading to a greater importance of the AW. Meanwhile, in CLIMATIC, the slow increase in AW with time is related to the transformation being more important in this experiment. The AW is located at the surface and is thus more easily affected by runoff. The greater spreading of the runoff in this simulation and the enhanced runoff in summer when Baffin Bay is mostly ice free leads to easier freshening of the water column (Figure 3.2b). Consequently, more AW is generated from saltier water during the journey through Baffin Bay because of interaction with the other water mass. We note that in our simulation we do not consider the temperature of the runoff. Thus, the enhanced runoff can only lead to the creation of fresher water masses.

The evolution of the other water masses in the CLIMATIC simulation can be explained by a combination of transport imbalance and internal changes, depending on the time period. During Period I the large WGIW inflow from the WGC replaces the TrW in Baffin Bay. During Period II the WGIW is trapped in the northern trough and canyons of Baffin Bay and then mixes with the underlying TrW, leading to the formation of more TrW. During Period III, the WGSW inflow increases from the WGC, replacing the WGIW. After 1996, the WGIW curves to the inside of the gyre and gets trapped. The WGIW builds up inside the gyre during Period IV, mixing with the TrW and leading to the formation of more WGIW. The WGSW pathway follows a different route. It stays on the shelves and circulates around Baffin Bay. It avoids central Baffin Bay, preventing this water mass from being trapped by the gyre. This prevents any mixing between the WGSW and the other water masses in the interior, which leads to no noticeable change in the proportion of WGSW in Baffin Bay.

Under the influence of the WGSW and WGIW the TrW becomes warmer and fresher due to the increase in the surface exchange, which enhances mixing between the three water masses. We note in the CLIMATIC simulation a transformation of about 80% of the AW to the WGSW in central Baffin Bay during the summer due to air-sea interaction (i.e., surface heating). The cooling in winter reverses the process. The process is also present over the east Baffin Island Current with a smaller magnitude (about 20%). None of the interactions discussed previously are present in HINDCAST; thus, the water masses proportions do not evolve beyond what is due to the transport imbalance, which is less than 1%.

3.5.1 Heat Storage Evolution

In the HINDCAST simulation the heat available in Baffin Bay decreases by 15% during the time period (Figure 3.8e). The decrease is steady at 2 ZJ/decade (1 ZJ = 10^{21} J), with the exception of the periods when the importance of TrW decreases, leading to a rapid reduction if the total heat in Baffin Bay. The heat contained by the other water masses does not change significantly.

In the CLIMATIC simulation, the heat inside Baffin Bay increases by 40%. The heat evolution is closely related to the evolution of the individual water mass (correlation coefficient between the heat and volume content evolution > 0.97 for every water mass). From 1970 to 1978 the heat increases by 20%. From 1978 to 1995, after a decrease of about 8%, the heat content stays relatively stable. From 1995 and 1998 the heat increases abruptly by 10%. After 1998 the heat increases only slowly until the end of the simulation.

The change in Period I is driven by the increase in the heat contained in the WGIW which is directly related to the higher proportion of this water mass in Baffin Bay (i.e., related to the WGIW inflow). During Periods II and III, the importance of WGIW decreases in favour of cooler TrW (i.e., the WGIW inflow is replaced by the cooler TrW inflow). The 1995 heat increase is also related to an increase in the WGIW importance during this period.

We also note a steady increase of 74% in the heat contained by the AW despite the low increase in this water mass volume (Figure 3.8d and 3.8e). This indicates warming of this water mass with time. This evolution is only present in the AW. The WGIW heat and WGSW heat have large interannual variability but no clear long-term trend. However, we note an increase in the WGIW heat beginning between 1992 and 1995 (21%) related to the warmer WGIW inflow at Davis Strait. The TrW heat content stays relatively constant with a small increase between 1970 and 1975 (11%) and a slow decrease after 1995 (9%).

3.5.2 Freshwater Storage Evolution

In the HINDCAST simulation, the freshwater decreases by 20% during the same period of the experiment (Figure 3.8b). The decrease is the same for all water masses; thus, is more likely due to a model drift that increases the salinity over time. This decrease is not related to the evolution of the water masses.

In the CLIMATIC simulation, the freshwater content increases by 53% from 1970 to 2010 (Figure 3.8e). This freshening is almost constant with time and closely related to the evolution of the volume of each water mass ($r > 0.98$). From 1970 to 1995 the AW, WGIW and, after 1978, the TrW freshwater content increases by 47%, 675% and 290%, respectively. We note that the WGSW freshwater content starts to grow after 1985 (72%). Finally, after 1995 the total freshwater increases more slowly.

This evolution is mainly due to the augmentation of the proportion of the high freshwater content water masses but also to a freshening of Baffin Bay (Figure 3.8d and 3.8f). The WGIW water mass freshens the most (60%). The TrW freshwater content per cubic metre does not change significantly. The WGSW experiences a significant drop in its freshwater content per cubic metre between 1984 and 1987 (26%), related to an increase in its salinity, but otherwise stays relatively constant with time. The AW slowly loses freshwater between 1970 and 2000 (9%) before increasing again to its initial state.

3.6 Twenty-first century transport

3.6.1 Volume

The volume transport at Davis Strait stays relatively constant until 2020, then decreases from -0.3 Sv (i.e., southward flow) to almost zero by 2040 (Figure 3.9a). This decrease is the result of the outflow decreasing by 22% because of the decrease in the AW outflow by 80% between 2010 and 2050 (correlation coefficient of about 0.98 between net volume transport and AW outflow decrease). The proportion of AW does not significantly change after this decrease (35% of the total outflow; Figure 3.10a). The WGIW increases (27%; Figure 3.11a), while the WGSW increases (37%; Figure 3.12a). The TrW outflow becomes marginal (1%; Figure 3.13a).

The total inflow stays relatively constant over the entire time period. The relative proportion of each water mass stays constant over the twenty-first century with the WGSW becoming the dominant water mass (47%), followed by the WGIW (35%), the AW (16%) and the TrW (2%). After 2040, the net transport is 0.1 ± 0.2 Sv. We note that the TrW net transport becomes close to zero after 2040. Finally, after 2060, the variability increases in both inflow and outflow, without any noticeable impact on the net transport. This higher variability is due to the AW and WGSW variability across the strait during the same period

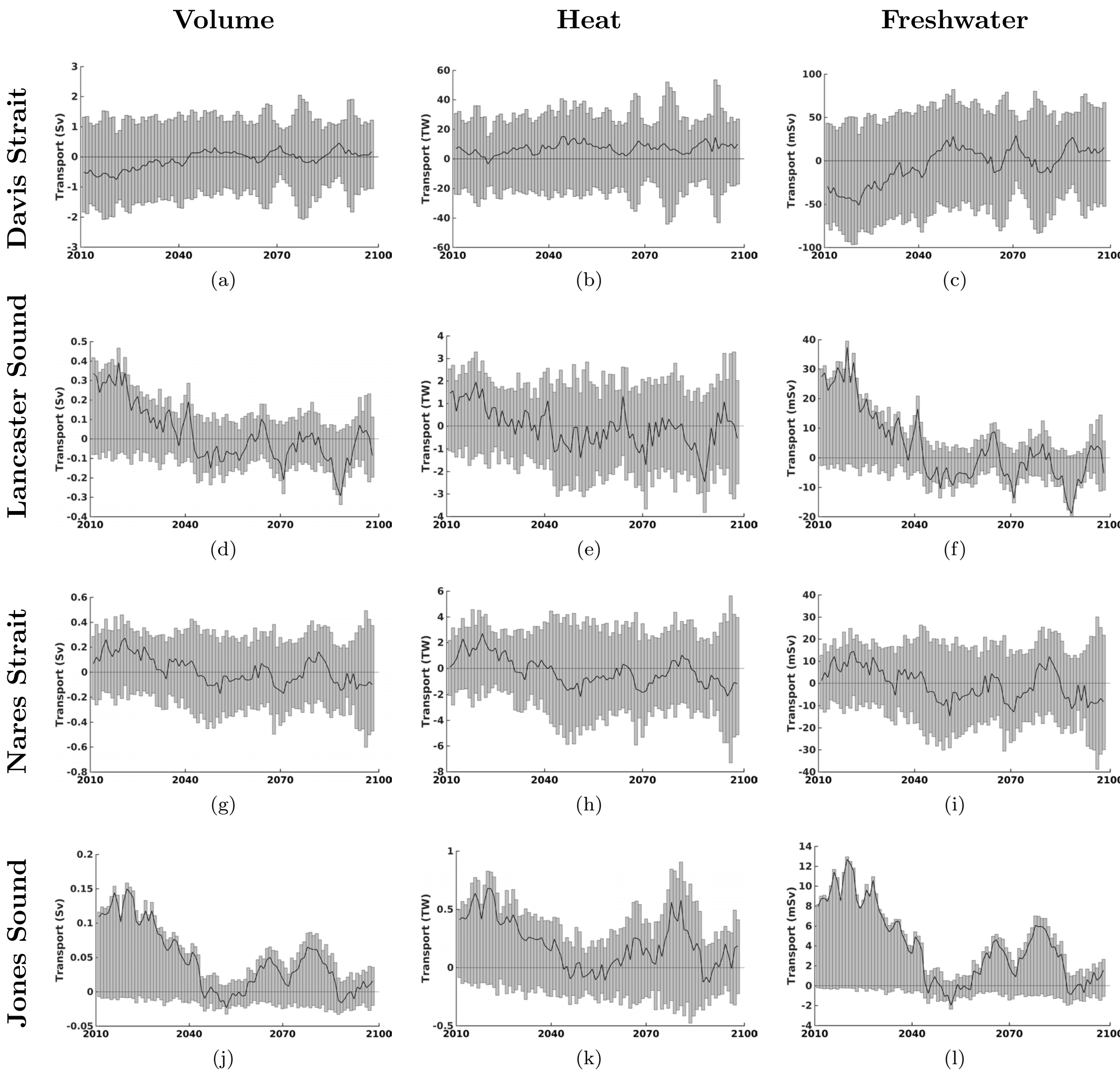

Figure 3.9: Total volume (left column), heat (middle column) and freshwater (right column) transport for: Davis Strait (a, b and c), Lancaster Sound (d, e and f), Jones Sound (g, h and i) and Nares Strait (j, k and l) for FUTURE. The bars are for the inflow (positive) and outflow (negative) component only. The thick line corresponds to the net transport.

($r = 0.94$ and $r = 0.73$).

The net transport decreases at each of the northern passages until 2040, when high interannual variability obscures any clear trend (Figure 3.9j, 3.9g and 3.9d). The decrease is explained by a decrease in the inflow component of the transport at Lancaster Sound (75%) and Jones Sound (70%). At Nares Strait, no clear trend is seen over this period. The decrease in the inflow is led by a decrease in the AW ($r > 0.97$ for each strait). No other water mass seems to be significantly involved in the inflow decrease ($r < 0.40$ for each water masses and passage).

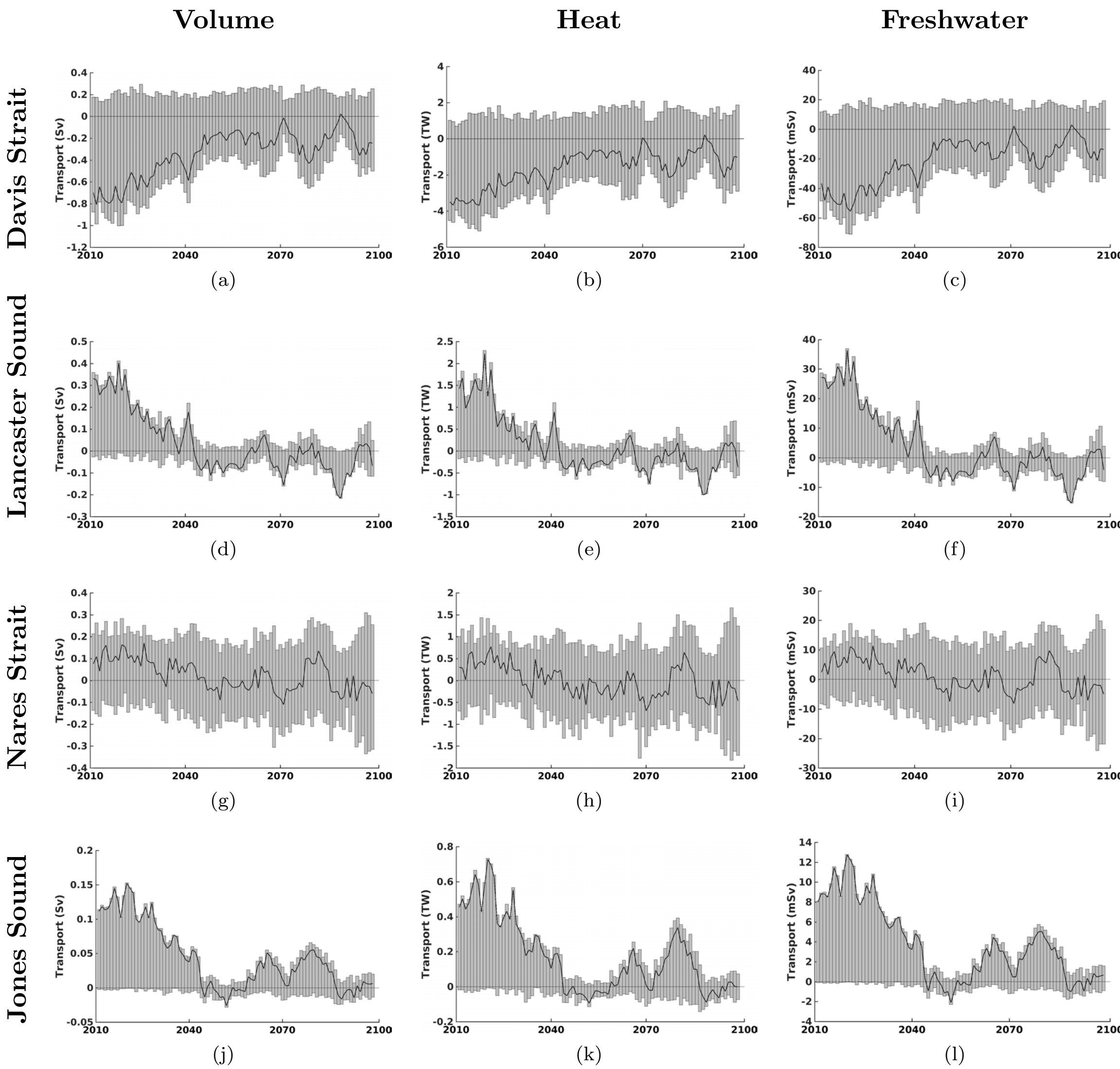

Figure 3.10: Arctic Water volume (left column), heat (middle column) and freshwater (right column) transport for: Davis Strait (a, b and c), Lancaster Sound (d, e and f), Jones Sound (g, h and i) and Nares Strait (j, k and l) for FUTURE. The bars are for the inflow (positive) and outflow (negative) component only. The thick line corresponds to the net transport.

At Lancaster Sound, the transport reaches 0.1 ± 0.1 Sv after 2040, with the transport at Nares Strait and Jones Sound being 0.0 ± 0.1 Sv. This decrease does not significantly impact the relative importance of the transport in each passage, decreasing only the importance of Jones Sound (from 24% to 15%) in favour of Nares Strait (from 27% to 33%).

We observe a negative net transport (i.e., outflow) through all the passages in 2045-2065 period and, for Lancaster Sound and Nares Strait only, around 2070 and 2090. These outflows are associated with higher inflow from Davis Strait. The net transport at the northern passages is highly correlated with Davis Strait transport ($r > 0.92$ for each passage). The

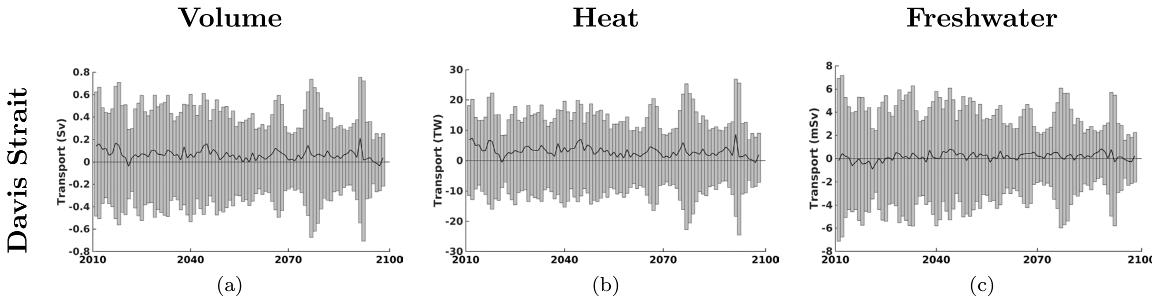

Figure 3.11: West Greenland Irminger Water volume (left column), heat (middle column) and freshwater (right column) transport for Davis Strait (a, b and c). The bars are for the inflow (positive) and outflow (negative) component only. The thick line corresponds to the net transport.

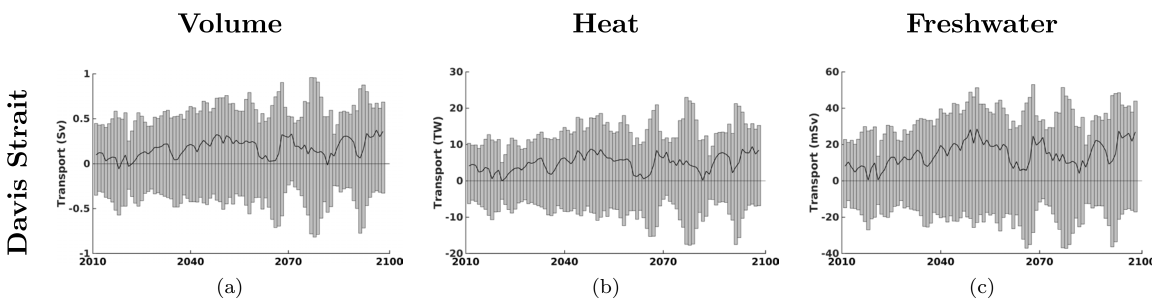

Figure 3.12: West Greenland Shelf Water volume (left column), heat (middle column) and freshwater (right column) transport for: Davis Strait (a, b and c). The bars are for the inflow (positive) and outflow (negative) component only. The thick line corresponds to the net transport.

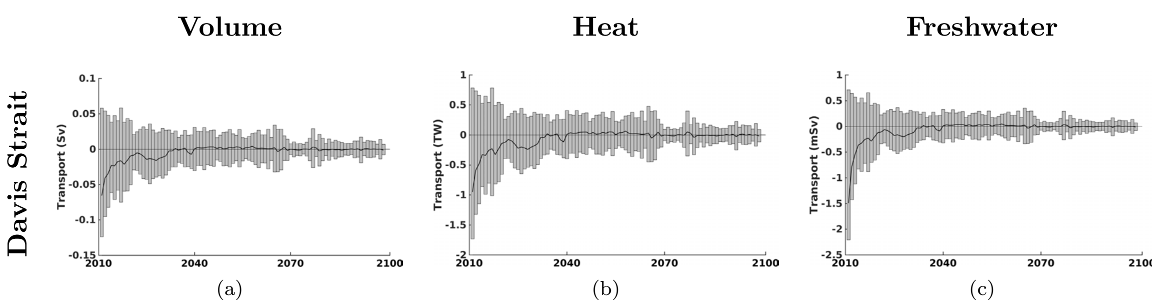

Figure 3.13: Transitional Water volume (left column), heat (middle column) and freshwater (right column) transport for: Davis Strait (a, b and c). The bars are for the inflow (positive) and outflow (negative) component only. The thick line corresponds to the net transport.

relative importance of each water mass crossing the northern passages does not significantly change during the twenty-first century with more than 95% of the transport being composed of AW.

3.6.2 Heat

The heat transport at Davis Strait does not significantly decrease between 2010 and 2040 (Figure 3.9b), showing that the WGC inflow is not affected by the reduction in the outflow. The interannual variability is correlated at 0.75 with the volume transport. The average transport of heat over this time period is 6.2 ± 4.1 TW. The interannual variability is more pronounced after 2060, as is the volume transport.

The WGSW has a greater importance in the heat inflow at Davis Strait, carrying about the same amount of heat as the WGIW (44% and 47%; Figure 3.11a and 3.12a). The interannual variability in the heat transport is mainly led by the WGSW (correlation coefficient of about 0.85). The WGIW has lower importance in the heat transport variability (correlation coefficient of about 0.40).

At the northern passages, the heat transport is strongly related to the volume transport ($r > 0.92$ for each strait; Figure 3.9e, 3.9h and 3.9k). Consequently, low volume transport leads to a small amount of heat transport (mean over the period for Lancaster Strait: 0.7 TW, for Nares Strait: 1.1 TW, for Jones Sound: 0.2 TW). We note that heat is also exported when the net volume transport is negative.

At Lancaster and Jones Sounds, the AW inflow between 2010 and 2040 decreases by 75% (correlation coefficient between the volume and heat transport > 0.98 for both straits; Figure 3.10d). At Nares Strait, the main source of heat transport variability is the WGIW (correlation coefficient of about 0.97), followed by the AW (correlation coefficient of about 0.86) (not shown).

After 2040, the importance of AW to the heat transport at the northern passages decreases significantly with only 10% of the heat carried at Lancaster Sound, 28% at Nares Strait and 32% at Jones Sound. At Lancaster Sound, the main source of heat becomes the WGIW (56%; WGSW is 34%). At Nares Strait the WGSW is more important (45%; WGIW is 25%). At Jones Sound, both WGIW and WGSW share about the same importance (30% and 37%, respectively).

3.6.3 Freshwater

At Davis Strait, the freshwater transport is correlated at 0.99 with the volume transport. Consequently, after 2040 the WGC carries more freshwater into Baffin Bay than the Arctic outflow removes (Figure 3.9c).

The AW proportion of the Davis Strait outflow decreases from 67% to 54% between 2010 and 2040, and after 2040 the net export is -12.0 ± 7.0 mSv (Figure 3.10c). The

WGSW increases from 25% to 38% (Figure 3.12c). This is associated with an increase in the WGSW freshwater inflow (300%) between 2010 and 2040 because of the higher volume inflow of this water mass (correlation coefficient between WGSW volume and freshwater transport: 0.96). The net WGIW freshwater transport at Davis Strait is close to zero, the inflow and outflow being of the same order of magnitude (net transport: 0.2 ± 0.3 mSv; Figure 3.11c). We note that the TrW volume transport is not large enough to have any effect on the freshwater transport (Figure 3.13c).

At the northern passages, between 2010 and 2040, the average freshwater transport decreases for each passage by the same proportion as the volume transport (correlation coefficient between the volume and freshwater transport > 0.98 for each passage). The dynamics of the freshwater transport into Baffin Bay are modified, with an export of freshwater toward the CAA at Lancaster Sound (average transport between 2040 and 2099: -3.4 ± 6.1 mSv). At Nares Strait, the transport can be either direction, depending on the year. High interannual variability hides any clear trend (average: 3.5 ± 6.2 mSv). Jones Sound remains, on average, a source of freshwater to Baffin Bay (average: 1.9 ± 2.2 mSv). More than 95% of this freshwater is carried by the AW (Figure 3.10f, the other water masses are not shown).

3.6.4 Future evolution of the water masses in Baffin Bay

The relative importance of the TrW to the total volume steadily decreases over the twenty-first century (26%) replaced by the WGIW (45%) and the WGSW (19%) (Figure 3.14a) because of the build-up in these two water masses inside the gyre and in its periphery. The amount of AW stays constant with little interannual variability. In 2040, the TrW represents 42% of the total water in Baffin Bay, followed by the WGIW (37%), the WGSW (15%) and the AW (6%). By 2099, the proportion is TrW (39%), WGIW (39%), WGSW (16%) and AW (6%).

During the twenty-first century, the heat content available in Baffin Bay increases by 37% (Figure 3.14b). This increase occurs mainly between 2040 and 2060 (22%). This increase is partially the result of a higher proportion of the WGIW in Baffin Bay but also due to a significant warming of the water mass itself (40% for the amount of heat contained by the same volume of WGIW between 2010 and 2099). The decrease in the TrW heat is related to the decrease in its importance, while the WGSW and the AW heat content do not change significantly.

The evolution of the water masses can be explained by a warming of Baffin Bay that transforms some of the TrW into the warmer WGIW and WGSW. This transformation is driven by the input of additional heat into Baffin Bay. The total freshwater content does not change significantly during the twenty-first century (Figure 3.14c).

3.7 Discussion

The differences between our two experiments come from the atmospheric forcing and the seasonality and total amount of runoff, especially from Greenland. The corresponding additional freshwater that remains in the upper layer of the ocean increases the buoyancy of the top surface layer, increasing the stratification. It will also increases the sea surface height, due to steric effects. The global evolution of the steric height (SH) over the whole bay, for the period between 1970 and 2010 is a net increase (2.5 cm, 83%) in the CLIMATIC simulation (Figure 3.15a).

The additional freshwater is not the only cause of the change in the SH. The total increase can be separated into the contribution from the freshwater component only (halosteric height, SHs) and heat component only (thermosteric height, SHt). A larger contribution to the total SH in Baffin Bay is made by SHs than the SHt. Between 1970 and 2010, the absolute increase in SHs is larger than the increase in SHt (1.6 cm, 60% versus 0.9 cm, 110%); however, both of them have the same relative importance in the total SH evolution (correlation between SH and SHs is 0.80 and between SH and SHt is 0.78). We note the larger relative increase in SHt.

At the beginning of the experiment, SH is higher in the interior of Baffin Bay and along the Baffin Island Current (Figure 3.16a) because of the accumulation of the warm TrW over the top 1000 m in the centre of Baffin Bay that increases SHt (Figure 3.16b). The

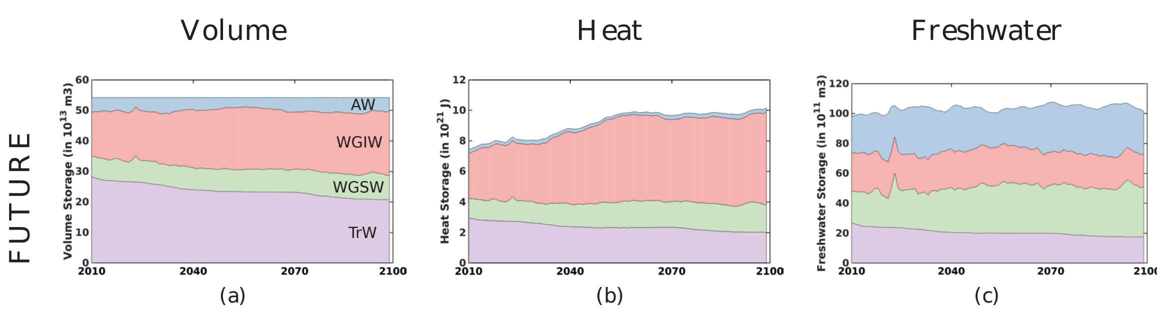

Figure 3.14: Volume (left panels), heat (middle panels) and freshwater (right panels) storage for each water masses in Baffin Bay for FUTURE. Transitional Water is in purple, West Greenland Shelf Water in green, West Greenland Irminger Water in red, Arctic Water in blue.

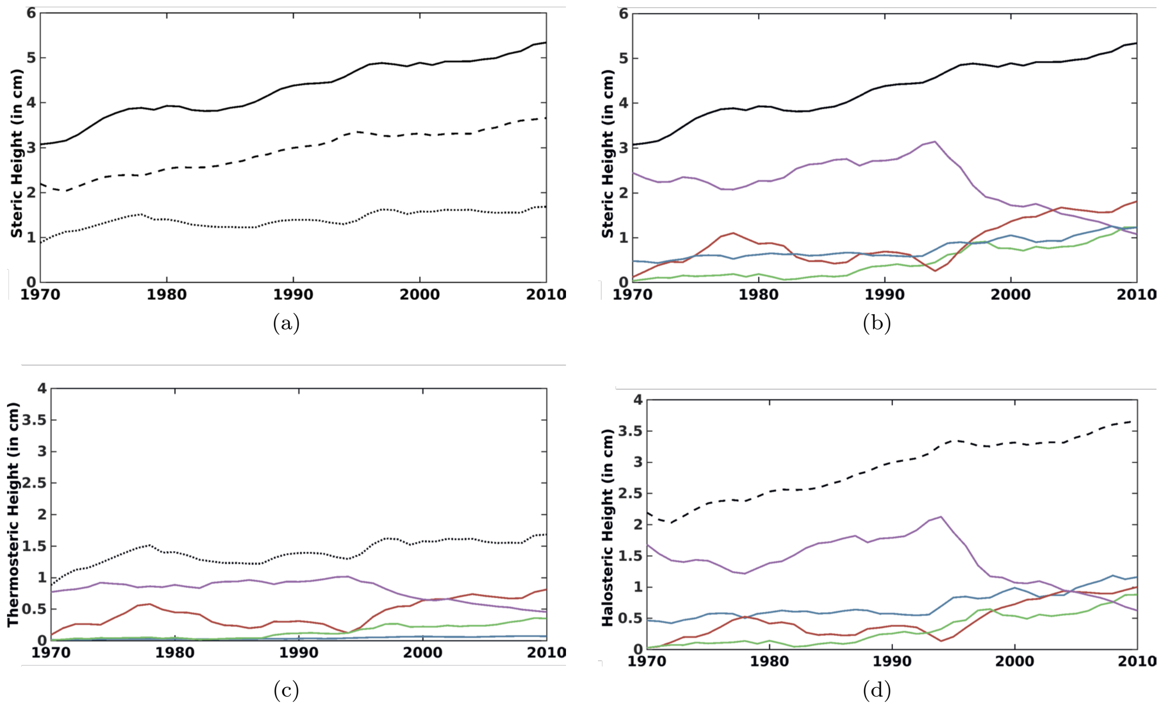

(a) (b) (c) (d)

Figure 3.15: Top right panel: evolution of steric height in Baffin Bay, thick line is for the total steric height, dashed line is for the halosteric component only and dotted line is for the thermosteric component only. Others panels: evolution of the total steric height separated by water masses for (b) the total steric height, (c) the thermosteric component only and (d) the halosteric component only. Transitional Water is in purple, West Greenland Shelf Water in green, West Greenland Irminger Water in red and Arctic Water in blue. Total is in black

high proportion of fresh AW in western Baffin Bay increases the SHs (Figure 3.16c). In the eastern part of Baffin Bay, SHt increases over the shelf break and inside the troughs on the continental shelf. This is a consequence of the presence of incoming WGIW from Davis Strait.

We acknowledge that the SH in 1970 does not appear to be consistent with the SSH leading to a cyclonic circulation (Figure 3.16a and 3.17a). This occurs because of a topography effect in the SH (i.e., deeper regions will contain more water and thus more heat and freshwater). The integration over the deeper part of Baffin Bay is necessary to capture the evolution of the intermediate water masses (i.e., WGIW, WGSW and TrW). With a shallow integration depth (e.g., 100 m) we miss most of the change on the SH over the twentieth century (Figure 3.17b, 3.17e and 3.17h) and over the twenty-first century (not shown). Removing the region shallower than the reference from our calculation misses the interesting features that occur over the shelf and especially in the troughs (e.g., with an integration depth of about 1000 m; Figure 3.17c, 3.17f and 3.17i).

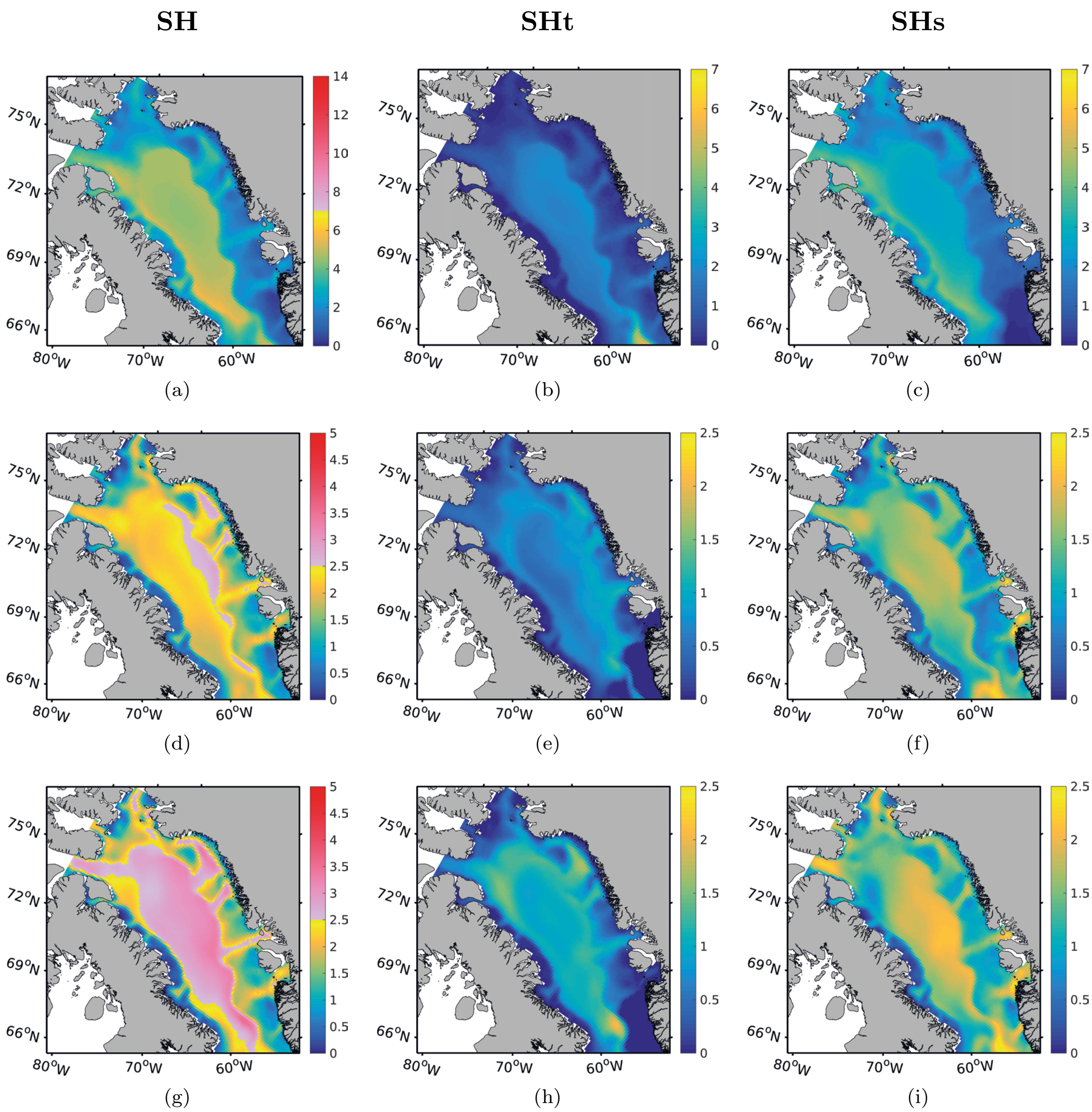

Figure 3.16: Yearly averaged total steric height (left column), thermosteric component only (central column) and halosteric component only (right column) in Baffin Bay for 1970 (first line) and the difference between 1970 and 1995 (second line) and between 1970 and 2007 (third line). The colorscale is in cm.

By 1995, the central region of Baffin Bay has been lifted significantly, particularly along the WGC and in the troughs that are draining various Greenland tidewater glaciers (up to 2.3 cm in the WGC) (Figure 3.16d). This lifting is the result of WGIW inflow that increases the SHt (Figure 3.16f) along the WGC pathway and the increase in freshwater from the Greenland runoff that accumulates in the troughs, the WGC, and inside the gyre. This additional freshwater is contained inside all the water masses (Figure 3.15b and 3.15d) that are freshened in eastern Baffin Bay in response to the larger runoff from Greenland.

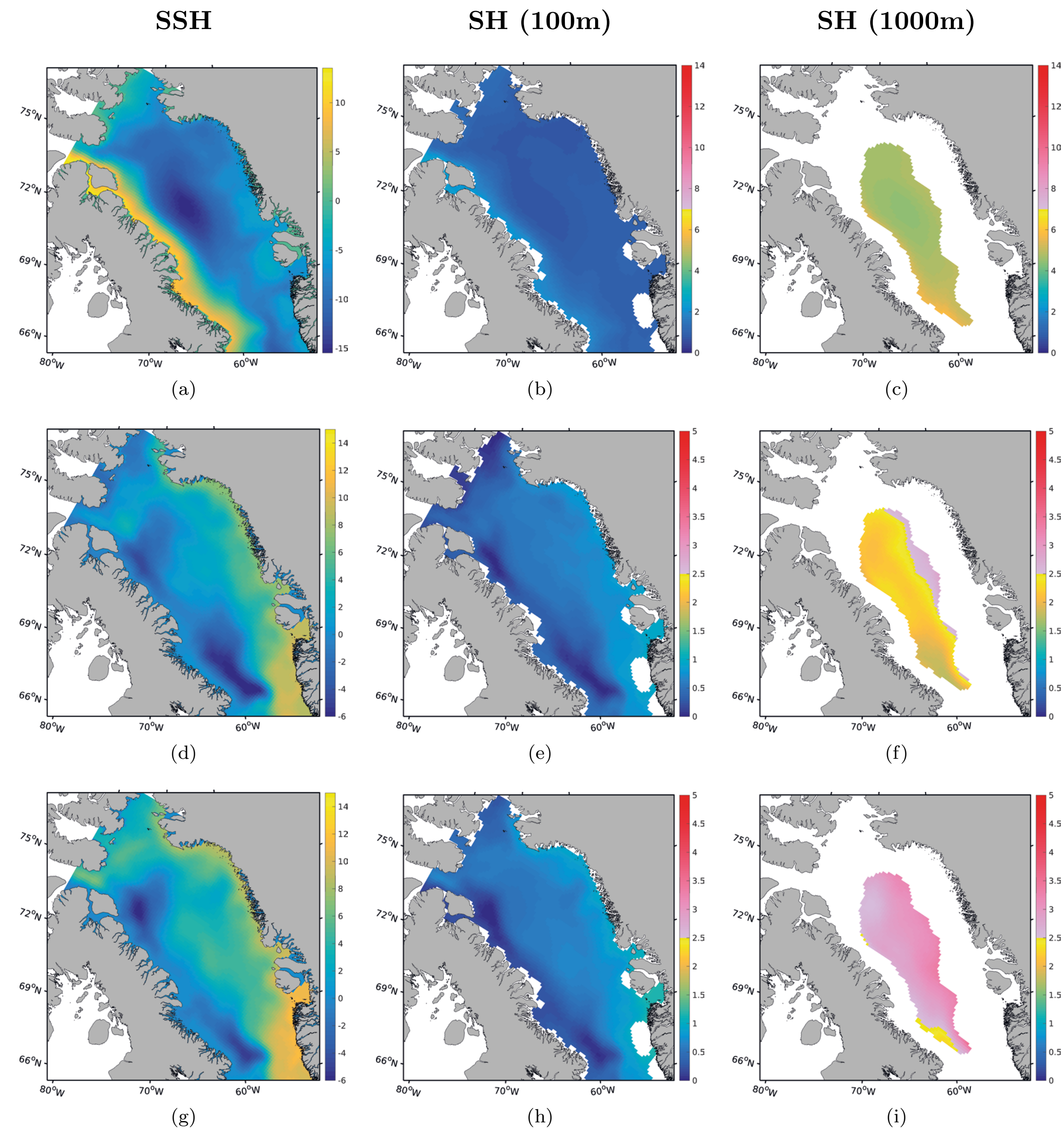

Figure 3.17: Yearly averaged total sea surface height (left column), total steric height over the first 100m only (central column) and steric height over the first 1000m only (right column) in Baffin Bay for 1970 (first line) and the difference between 1970 and 1995 (second line) and between 1970 and 2007 (third line). The colorscale is in cm.

The SH increase between 1995 and 2007 is less pronounced, with an augmentation smaller than 1 cm, on average, over central Baffin Bay (Figure 3.16g). The main increase is due to the heat from the WGIW. The WGC transports the WGIW to the northern part of Baffin Bay. When the current curves to the west, the WGIW is caught in the Baffin Bay gyre and accumulates inside it, progressively filling the interior of the gyre.

Because of its location over the continental shelf, the WGSW is not trapped by the gyre. Instead it continues its path toward the western part of Baffin Bay and follows the Baffin Island Current. As a consequence, it takes the place of the cold AW and thus increases the heat available in northern Baffin Bay and inside the Baffin Island Current, increasing the SHt (Figure 3.16h).

We note that the WGSW inflow at Davis Strait in the early 2000s is not larger than the WGIW inflow, as observed by Curry et al. (2014). It might arise from a mismatch between the WGIW and the WGSW: the WGIW observed by Curry et al. (2014) is simulated as WGSW in our experiment. The runoff inputs occurs over a large region away from the Greenland coastline in the CLIMATIC simulation (Figure 3.2c). Consequently, the WGC freshens over a larger area, including the region close to the shelf break, where WGIW is located. This could lead to the formation of the fresher WGSW where the WGIW should be present.

The freshening of the WGC and Baffin Island Current plays an important role in the increase of the overall SH, increasing SHs (Figure 3.16i). This evolution is due to the increased freshwater contained by most of the water masses (Figure 3.15d). Between 1970 and 1995, the WGIW mean salinity decreases by 0.39 ± 0.07, the WGSW by 0.12 ± 0.39 and the TrW by 0.10 ± 0.02. The AW mean salinity does not change significantly, with the increase in freshwater from this water mass thus related to its larger proportion in Baffin Bay. Between 1995 and 2007 no significant change in the salinity of AW can be seen. Overall, the mean salinity of Baffin Bay drops by 0.50 ± 0.06 from 1970 to 2007 (0.125 per decade), which is a larger freshening than the 0.032 ± 0.021 per decade observed by Zweng and Münchow (2006).

The modification of the baroclinic gradient resulting from runoff from Greenland is not present in the HINDCAST simulation. The freshening of the Baffin Island Current and the strengthening of the WGC is consistent with the results of Castro de la Guardia et al. (2015). The modification of the SH gradient also leads to a greater spreading of the WGIW and WGSW in Baffin Bay. This increases the surface contact between the WGIW, the WGSW, and the underlying water mass (i.e., the TrW). Between 1970 and 1995, the resulting enhanced mixing increases the mean temperature of the AW by 0.63 ± 0.04 °C, the WGIW by 0.37 ± 0.06 °C, the WGSW by 0.51 ± 0.14 °C and the TrW by 1.27 ± 0.07 °C. Between 1995 and 2007 the increase flattens and only the WGIW and WGSW show a significant change in temperature with a decrease of 0.48 ± 0.07 °C and -0.30 ± 0.12 °C, respectively.

Overall, Baffin Bay mean temperature increases in the CLIMATIC simulation by 0.79 °C between 1970 and 2007, with an increase between 1970 and 1995 (0.85 ± 0.18 °C) and a decrease between 1995 and 2007 (0.24 ± 0.15 °C). The temperature change is slightly larger than has been observed from 1916 to 2003 by Zweng and Münchow (2006) and they do not observe any cooling after 1995.

The increase in SHt from the mid-1990s onward is related to the increase in heat contained inside the WGIW. The increase is due to a higher proportion of this water mass instead of a higher mean temperature (Figure 3.8d, 3.16e and 3.16h). The increase is consistent with previous studies (Andresen et al., 2011; Curry et al., 2014; Holland et al., 2008b; Myers and Ribergaard, 2013). This increase is associated with a pulse of WGIW inflow and also of the WGSW inflow (Figure 3.8d). We note that the two pulses start in the same year (1992, two years earlier than observations), with the WGIW pulse continuing for two further years (until 1997).

In eastern Baffin Bay, the heat increase over the continental shelf and close to the west coast of Greenland is consistent with the enhanced melt of the tidewater glaciers along the west coast of Greenland from the 1990s onwards, as has been discussed previously (Andresen et al., 2011; Holland et al., 2008b; Zweng and Münchow, 2006).

In the North Water Polynya (i.e., near Lancaster Sound, Jones Sound, Smith Sound and east to Devon Island) the SHt between 1995 and 2007 (Figure 3.16b and 3.16h) associated with a higher proportion of the warm WGIW and WGSW at this location might help to explain the reduced ice thickness over the polynya. It could also explain the increase in size and number of completely open water regions inside the polynya, which leads to an overall increase in polynya size. This could have a significant impact on local species (e.g., narwhals, white whales, and more generally sea birds; Stirling (1980)). The detailed impact of oceanic dynamics changes on biology is, however, out of the scope of this paper.

The evolution of the transport at the boundaries of Baffin Bay is consistent with the evolution of the SH. The baroclinic gradient between the CAA and northern Baffin Bay is modified by the flows of WGIW and WGSW that increase the SHt, as well as the increase in freshwater and its effect on SHs. Between 1976 and 1985, the freshening of the Baffin Island Current increases the SHs and consequently increases outflow through Davis Strait (Figure 3.16c, 3.16f). In the north, the western part of Lancaster Sound becomes fresher, increasing the SHs and thus the baroclinic gradient, leading to a higher inflow. A similar freshening occurs in Smith Sound that explains the higher volume transport through Nares Strait. We note that Jones Sound transport is not significantly affected by the SH changes

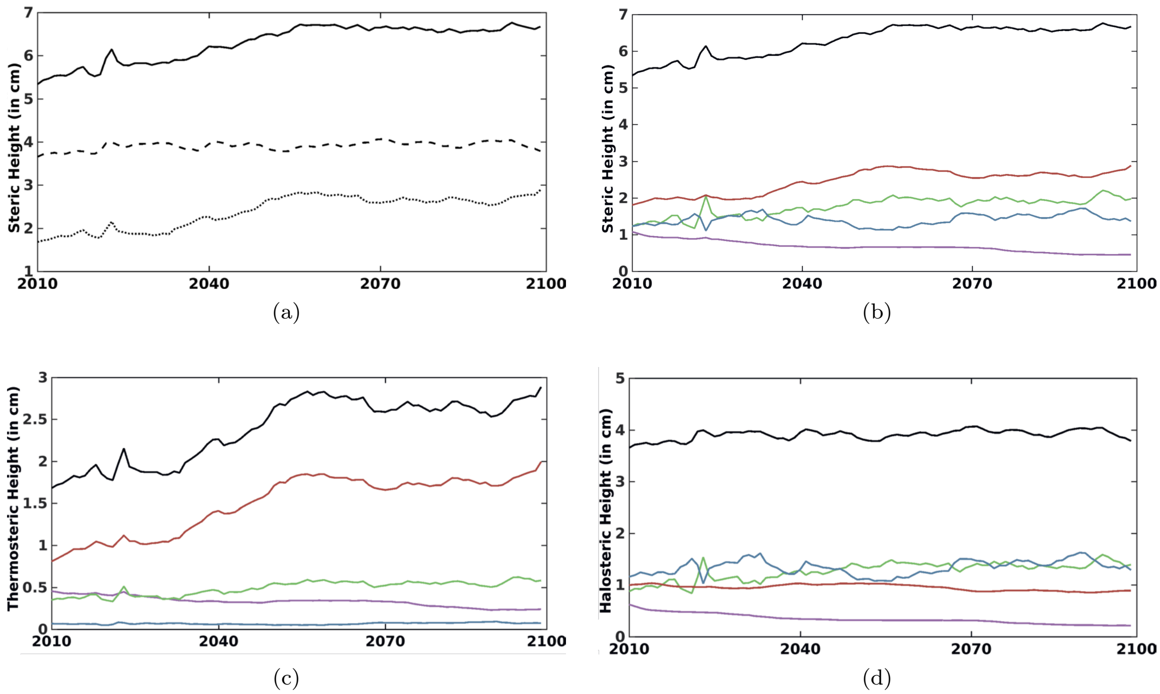

Figure 3.18: Top right panel: evolution of steric height in Baffin Bay, thick line is for the total steric height, dashed line is for the halosteric component only and dotted line is for the thermosteric component only. Others panels: evolution of the total steric height separated by water masses for (a) the total steric height, (c) the thermosteric component only and (d) the halosteric component only. Transitional Water is in purple, West Greenland Shelf Water in green, West Greenland Irminger Water in red and Arctic Water in blue. Total is in black.

in Baffin Bay.

After 1985, a shift in the baroclinic balance in Baffin Bay occurs, when eastern Baffin Bay SH becomes higher than in western Baffin Bay (Figure 3.16i). In consequence, the gyre strength is reduced and the transport of water through Baffin Bay decreases. The inflow from the northern boundary decreases accordingly, as well as the outflow at Davis Strait. Overall, the lift in Baffin Bay reduces the baroclinic gradient between the CAA and the North Atlantic, thus reducing the overall transport to the North Atlantic.

We note that the features shown in the evolution of SH (e.g., lifting of the eastern and central Baffin Bay, lifting in the eastern troughs) are also present in the evolution of SSH (Figure 3.17a, 3.17d and 3.17g) and shallow integration SH evolution (Figure 3.17b, 3.17e and 3.17h).

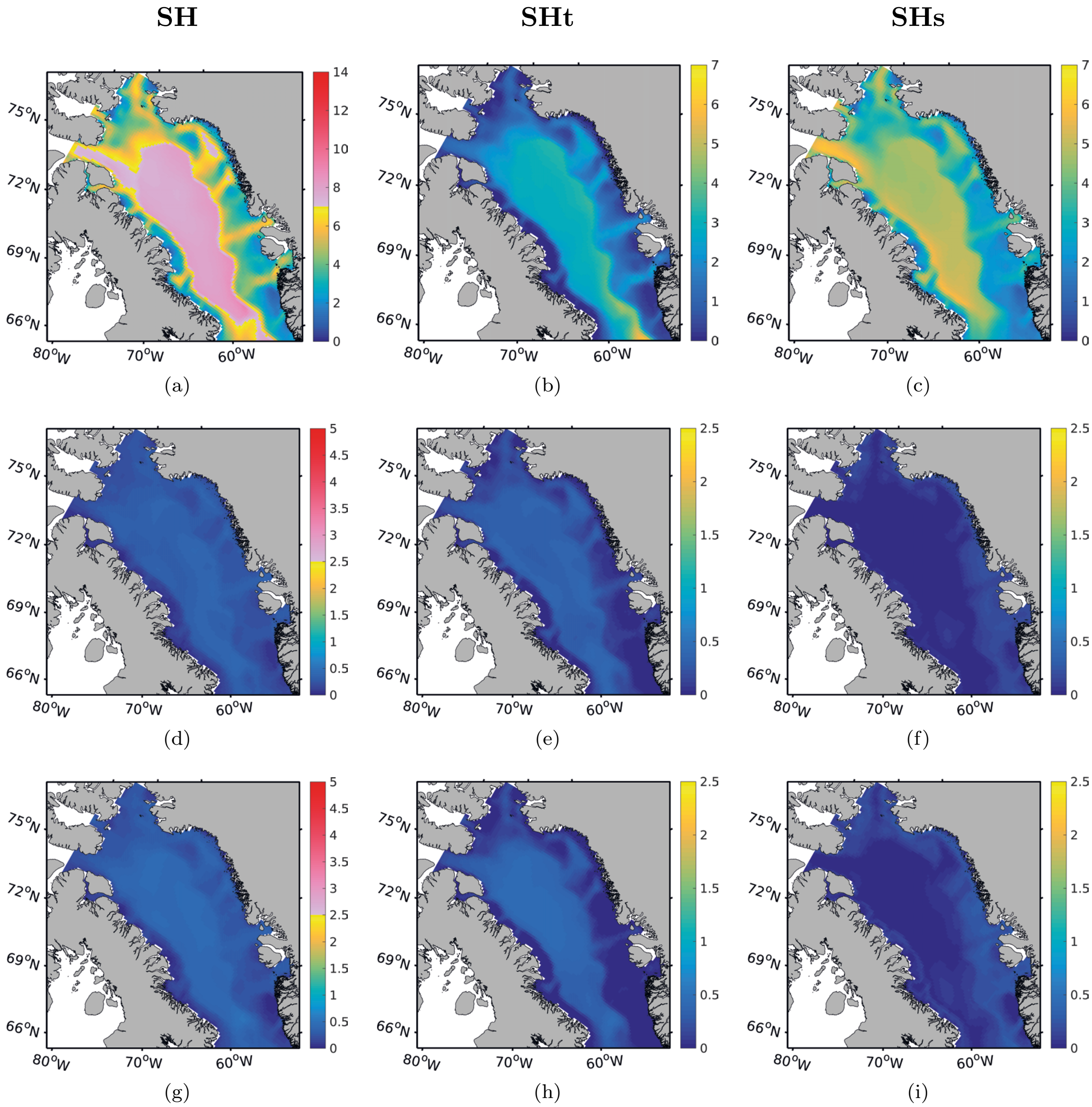

Figure 3.19: Yearly averaged total steric height (left column), thermosteric component only (central column) and halosteric component only (right column) in Baffin Bay for 2010 (first line) and the difference between 2010 and 2050 (second line) and between 2010 and 2099 (third line). The colorscale is in cm.

3.7.1 Future evolution of Baffin Bay

In the FUTURE simulation, the mean SHs in Baffin Bay increases from 3.7 cm to 4.0 cm (8%) between 2010 and 2023 (Figure 3.18a). After that, there is no clear trend (mean SHs: 3.9 ± 0.1 cm). The SHt increases significantly between 2010 and 2055 (from 1.6 cm to 2.8 cm; 75%) and stabilizes afterward (mean between 2055 and 2099: 2.7 ± 0.1 cm). As a result, total SH increases between 2010 and 2055 (from 5.4 cm to 6.7 cm; 34%) and then stabilizes thereafter.

The spatial distribution of the SH shows that the interior of Baffin Bay will be the region that undergoes the larger SH increase (Figure 3.19). This evolution occurs mainly during the first half of the twenty-first century, with a significant warming (1.00 ± 0.20°C on average, for the entire bay) due to the accumulation of the WGIW inside of the gyre and in the troughs, increasing the SHt (Figure 3.19b, 3.18c). In the second half of the twenty-first century, the mean temperature of the Bay decreases (-0.33 ± 0.22°C). Overall, from 2010 to 2099, the mean temperature of most of the water masses increases (average temperature at the end of the twenty-first century: AW: -0.17 ± 0.05°C, WGIW: 2.41 ± 0.20°C, WGSW: -0.68 ± 0.14°C). The only exception is the TrW that has its mean temperature decreasing (average temperature at the end of the twenty century: -0.36 ± 0.01°C) showing a transfer of heat from the deep Baffin Bay to shallower layers.

The mean salinity in Baffin Bay decreases slightly over the first part of the twenty-first century (0.38 ± 0.07), but there is no significant change over the second part of the century. Over the entire century the AW and the WGSW mean salinity decrease by 0.49 ± 0.03 and 0.55 ± 0.07, respectively, while the WGIW and TrW mean salinity increase by 0.17 ± 0.01 and 0.34 ± 0.01, respectively. The consequence on the SHs is that the SHs increases only over the shelf in the eastern part of Baffin Bay for this period and most of the change happens over the first part of the century (Figure 3.19c, 3.19f and 3.19i).

Baffin Bay lifting is consistent with previous studies (Hu and Myers, 2014; Sou and Flato, 2009). The consequence of this lifting is a reduction of the overall transport due to the lower baroclinic gradient, as discussed for the past. However, the leading component of the SH change in the FUTURE simulation is the SHt, not SHs. This can be explained by the changes in the circulation in Baffin Bay. The new baroclinic gradient inside Baffin Bay reduces the AW inflow and thus the inflow of freshwater, while the WGC carries warmer water. Moreover, under the future projection experiment conditions, the sources of freshwater from runoff decrease because of the heavy melt that occurred during the first half of the twenty-first century (e.g., the south of the CAA is eventually ice free during winter; Hu and Myers (2014)), reducing the ongoing sources of freshwater.

From a more general point of view, we can infer that the changes in the circulation in Baffin Bay and the resultant changes in the AW outflow are a consequence of the interplay of heat and freshwater. The increase in heat coming from the WGC in the early 1990s is associated with enhanced runoff from Greenland. The additional heat creates a positive feedback on the runoff, increasing the tidewater glacier melt. The additional freshwater increases the SH in the eastern part of Baffin Bay, leading to more mixing of the water masses, increasing the temperature, and decreasing the salinity of most of the water masses.

In the twentieth century, freshwater plays a greater role in changes in the dynamics of Baffin Bay, but the situation changes in the twenty-first century when the SH gradient in Baffin Bay inverts (i.e., the east is higher than the west) with the circulation leading to an accumulation of WGIW in Baffin Bay, significantly increasing the temperature of Baffin Bay because of mixing processes. After this point, the freshwater does not significantly change the total SH. However, the accumulation of heat due to higher temperatures continues the process of lifting in eastern and central Baffin Bay. The threshold point is reached in the 2050s. These results are consistent with the sensitivity experiments realized by Castro de la Guardia et al. (2015).

3.8 Conclusion

The purpose of this paper is to evaluate the sensitivity of the throughflow into and out of Baffin Bay and dynamics responses of Baffin Bay to Greenland runoff. We set up two numerical experiments for the past: HINDCAST and CLIMATIC with different runoffs. The CLIMATIC experiment was also extended into the twenty-first century (FUTURE). The CLIMATIC and FUTURE simulations have an enhanced Greenland runoff from the 1990s and during the twenty-first century; the atmospheric forcing also differs. The HINDCAST and CLIMATIC simulation start from the same initial conditions after a 18-year normal-year forcing spin-up phase.

Over time, Baffin Bay becomes fresher and warmer in CLIMATIC, whereas in HINDCAST Baffin Bay becomes saltier and cooler. Consequently, due to Steric Height, Baffin Bay lifts in CLIMATIC and lowers in HINDCAST. In both cases, the evolution of the SH is mainly controlled by the variation of the Halosteric Height which is associated with the evolution of freshwater in Baffin Bay.

The lifting of Baffin Bay due to steric effects in the CLIMATIC simulation reduces the baroclinic gradient between the fresh and cold Arctic and the warm and salty North Atlantic, reducing the transport from the northern passages. This reduction leads to a reduced transport of freshwater entering Baffin Bay. The modification of the baroclinic gradient in Baffin Bay also strengthens the WGC inflow. It brings more heat because of enhanced northward transport of the warm WGIW and WGSW through Davis Strait. The second consequence is an increase of the surface of contact between the water carried by the WGC and the underlying TrW, which increases mixing in Baffin Bay, and thus the transformation of one water mass to another. This behaviour is not present in HINDCAST in which the SH is mainly driven by the numerical salt drift common to many regional models. We thus suggest that the additional Greenland runoff explains the difference between the two experiments.

For the twenty-first century, the FUTURE simulation shows that the transport across the Bay is reduced to a fraction of what it was during the twentieth century. This affects all water mass transport with the greatest effect being on the AW outflow. The flow of AW from the Arctic Ocean is reduced to a very small amount. AW is even exported back through the northern passages in some years. The freshwater storage in Baffin Bay stays relatively stable.

Despite this smaller inflow and outflow, the heat available in the Bay increases as the result of an increase in the relative proportion of the WGIW, as well as a warming of this water mass. This warming is not associated with an increase in the transport of this water mass at the boundaries nor with surface heating and, thus, is probably controlled by internal processes that are warming Baffin Bay.

Most of the features seen in the CLIMATIC simulation have been observed previously. The warming of Baffin Bay is similar to observations by Zweng and Münchow (2006). The increase in heat in Baffin Bay is also consistent with the temperature increase in Disko Bay found by Myers and Ribergaard (2013), as well as the acceleration of the heat increase in Baffin Bay since 1997 because of an increase in the available heat in the WGIW.

The origin of these changes are consistent with the proposal of both Andresen et al. (2011) and Holland et al. (2008a): a change in the baroclinic gradient inside Baffin Bay triggered by freshwater inflow coming from enhanced runoff from Greenland enhances WGC inflow.

However, we did not find a similar increase in the WGIW heat content. Instead, we found that the increase in heat in the WGC was associated with an increase in heat in the WGSW. This mismatch in the water masses might be a consequence of the increased runoff in Baffin Bay that freshens the WGC. It should also be noted that the runoff we input does not change the temperature of the grid cell where it is input, only the salinity.

We did not detect a strengthening of the southward export of AW, as found by Münchow et al. (2015). However, we did detect a freshening of Baffin Bay due to the freshening of both the AW and the WGSW. The consequent SH increases in Baffin Bay are consistent with those proposed by Antonov et al. (2002) and Steele and Ermold (2007).

Finally, further improvements in this experiment may need to be considered. The first would be the implementation of the temperature of the runoff water in order to determine whether it has an effect on the heat available in Baffin Bay. The second would be to obtain a more realistic freshwater discharge from Greenland. The effect of these changes on the freshwater supply in the Labrador Sea is beyond the scope of this paper.

Acknowledgments

This work was founded by NSERC through a Discovery Grant Award (RGPIN 04357), as well as the Canadian Arctic Geotraces Program (433848-2012). We are grateful to Westgrid and Compute Canada for computional resources. We thank C. Boening and A. Biastoch for providing us model output that was used for open boundary forcing. We also thank two anonymous reviewers for their useful comments and suggestions.

Bibliography

Aagaard, K. and Carmack, E. C. (1989). The role of sea ice and other fresh water in the Arctic circulation. *Journal of Geophysical Research*, 94(C10):14485.

Aksenov, Y., Bacon, S., Coward, A. C., and Holliday, N. P. (2010). Polar outflow from the Arctic Ocean: A high resolution model study. *Journal of Marine Systems*, 83(1-2):14–37.

Amante, C. and Eakins, B. (2009). ETOPO1 1 arc-minute global relief model: Procedures, data sources and analysis. *NOAA Technical Memorandum NESDIS NGDC-24*.

Andresen, C. S., Straneo, F., Ribergaard, M. H., Bjørk, A. A., Andersen, T. J., Kuijpers, A., Nørgaard-Pedersen, N., Kjær, K. H., Schjøth, F., Weckström, K., and et al. (2011). Rapid response of Helheim Glacier in Greenland to climate variability over the past century. *Nature Geoscience*, 5(1):37–41.

Antonov, J. I., Levitus, S., and Boyer, T. P. (2002). Steric sea level variations during 1957-1994: Importance of salinity. *Journal of Geophysical Research: Oceans*, 107(C12):SRF 14–1–SRF 14–8.

Barnier, B., Madec, G., Penduff, T., Molines, J.-M., Treguier, A.-M., Sommer, J. L., Beckmann, A., Biastoch, A., Böning, C., Dengg, J., Derval, C., Durand, E., Gulev, S., Remy, E., Talandier, C., Theetten, S., Maltrud, M., McClean, J., and Cuevas, B. D. (2006). Impact of partial steps and momentum advection schemes in a global ocean circulation model at eddy-permitting resolution. *Ocean Dynamics*, 56(5-6):543–567.

Castro de la Guardia, L., Hu, X., and Myers, P. G. (2015). Potential positive feedback between greenland ice sheet melt and Baffin Bay heat content on the west Greenland shelf. *Geophysical Research Letters*, 42(12):4922–4930. 2015GL064626.

Cuny, J., Rhines, P. B., and Kwok, R. (2005). Davis Strait volume, freshwater and heat fluxes. *Deep Sea Research Part I: Oceanographic Research Papers*, 52(3):519–542.

Curry, B., Lee, C. M., and Petrie, B. (2011). Volume, freshwater, and heat fluxes through Davis Strait, 2004–05*. *Journal of Physical Oceanography*, 41(3):429–436.

Curry, B., Lee, C. M., Petrie, B., Moritz, R. E., and Kwok, R. (2014). Multiyear volume, liquid freshwater, and sea ice transports through Davis Strait, 2004–10*. *Journal of Physical Oceanography*, 44(4):1244–1266.

Dai, A. and Trenberth, K. E. (2002). Estimates of freshwater discharge from continents: Latitudinal and seasonal variations. *Journal of Hydrometeorology*, 3(6):660–687.

Dickson, R., Rudels, B., Dye, S., Karcher, M., Meincke, J., and Yashayaev, I. (2007). Current estimates of freshwater flux through Arctic and subarctic seas. *Progress in Oceanography*, 73(3-4):210–230.

Dumas, J. A., Flato, G. M., and Brown, R. D. (2006). Future projections of landfast ice thickness and duration in the Canadian Arctic. *Journal of Climate*, 19(20):5175–5189.

Fichefet, T. and Maqueda, M. A. M. (1997). Sensitivity of a global sea ice model to the treatment of ice thermodynamics and dynamics. *Journal of Geophysical Research: Oceans*, 102(C6):12609–12646.

Fissel, D., Lemon, D., and Birch, J. (1982). Major features of the summer near-surface circulation of western Baffin Bay, 1978 and 1979. *ARCTIC*, 35(1):180–200.

Gordon, C., Cooper, C., Senior, C. A., Banks, H., Gregory, J. M., Johns, T. C., Mitchell, J. F. B., and Wood, R. A. (2000). The simulation of SST, sea ice extents and ocean heat transports in a version of the Hadley Centre coupled model without flux adjustments. *Climate Dynamics*, 16(2-3):147–168.

Griffies, S. M. and Greatbatch, R. J. (2012). Physical processes that impact the evolution of global mean sea level in ocean climate models. *Ocean Modelling*, 51:37–72.

Holland, D. M., Thomas, R. H., de Young, B., Ribergaard, M. H., and Lyberth, B. (2008a). Acceleration of Jakobshavn Isbræ triggered by warm subsurface ocean waters. *Nature Geoscience*, 1(10):659–664.

Holland, P. R., Jenkins, A., and Holland, D. M. (2008b). The response of ice shelf basal melting to variations in ocean temperature. *Journal of Climate*, 21(11):2558–2572.

Hu, X. and Myers, P. G. (2013). A Lagrangian view of Pacific water inflow pathways in the Arctic Ocean during model spin-up. *Ocean Modelling*, 71:66–80.

Hu, X. and Myers, P. G. (2014). Changes to the Canadian Arctic Archipelago sea ice and freshwater fluxes in the twenty-first century under the Intergovernmental Panel on Climate Change A1B climate scenario. *Atmosphere-Ocean*, 52(4):331–350.

Hunke, E. C. (2001). Viscous–plastic sea ice dynamics with the EVP model: Linearization issues. *Journal of Computational Physics*, 170(1):18–38.

Hunke, E. C. and Dukowicz, J. K. (1997). An Elastic–Viscous–Plastic model for sea ice dynamics. *Journal of Physical Oceanography*, 27(9):1849–1867.

Kliem, N. and Greenberg, D. A. (2003). Diagnostic simulations of the summer circulation in the Canadian arctic archipelago. *Atmosphere-Ocean*, 41(4):273–289.

Landerer, F. W., Jungclaus, J. H., and Marotzke, J. (2007). Regional dynamic and steric sea level change in response to the IPCC-A1B scenario. *Journal of Physical Oceanography*, 37(2):296–312.

Large, W. G. and Yeager, S. G. (2009). The global climatology of an interannually varying air–sea flux data set. *Climate Dynamics*, 33(2):341–364.

Madec, G. (2008). Nemo ocean engine. *Note du Pole de modelisation*, 27:1288–1619.

McGeehan, T. and Maslowski, W. (2012). Evaluation and control mechanisms of volume and freshwater export through the Canadian Arctic Archipelago in a high-resolution pan-Arctic ice-ocean model. *Journal of Geophysical Research: Oceans*, 117(C8):n/a–n/a.

Melling, H., Agnew, T. A., Falkner, K. K., Greenberg, D. A., Lee, C. M., Münchow, A., Petrie, B., Prinsenberg, S. J., Samelson, R. M., and Woodgate, R. A. (2008). *Fresh-Water Fluxes via Pacific and Arctic Outflows Across the Canadian Polar Shelf*, pages 193–247. Springer Netherlands.

Münchow, A. (2016). Volume and freshwater flux observations from Nares Strait to the west of Greenland at daily time scales from 2003 to 2009. *Journal of Physical Oceanography*, 46(1):141–157.

Münchow, A., Falkner, K. K., and Melling, H. (2007). Spatial continuity of measured seawater and tracer fluxes through Nares Strait, a dynamically wide channel bordering the Canadian Archipelago. *Journal of Marine Research*, 65(6):759–788.

Münchow, A., Falkner, K. K., and Melling, H. (2015). Baffin Island and West Greenland Current systems in northern Baffin Bay. *Progress in Oceanography*, 132:305–317.

Münchow, A. and Melling, H. (2008). Ocean current observations from Nares Strait to the west of Greenland: Interannual to tidal variability and forcing. *Journal of Marine Research*, 66(6):801–833.

Murray, R. J. (1996). Explicit generation of orthogonal grids for ocean models. *Journal of Computational Physics*, 126(2):251–273.

Myers, P. G. and Ribergaard, M. H. (2013). Warming of the Polar Water layer in Disko Bay and potential impact on Jakobshavn Isbrae. *Journal of Physical Oceanography*, 43(12):2629–2640.

Nakicenovic, N., Alcamo, J., Grubler, A., Riahi, K., Roehrl, R., Rogner, H.-H., and Victor, N. (2000). *Special report on emissions scenarios (SRES), a special report of Working Group III of the intergovernmental panel on climate change*. Cambridge University Press.

Peterson, I., Hamilton, J., Prinsenberg, S., and Pettipas, R. (2012). Wind-forcing of volume transport through Lancaster Sound. *Journal of Geophysical Research: Oceans*, 117(C11):n/a–n/a.

Rabe, B., Dodd, P. A., Hansen, E., Falck, E., Schauer, U., Mackensen, A., Beszczynska-Möller, A., Kattner, G., Rohling, E. J., and Cox, K. (2013). Liquid export of Arctic freshwater components through the Fram Strait 1998–2011. *Ocean Science*, 9(1):91–109.

Serreze, M. C., Barrett, A. P., Slater, A. G., Woodgate, R. A., Aagaard, K., Lammers, R. B., Steele, M., Moritz, R., Meredith, M., and Lee, C. M. (2006). The large-scale freshwater cycle of the Arctic. *Journal of Geophysical Research*, 111(C11).

Sou, T. and Flato, G. (2009). Sea ice in the Canadian Arctic Archipelago: Modeling the past (1950–2004) and the future (2041–60). *Journal of Climate*, 22(8):2181–2198.

Steele, M. and Ermold, W. (2007). Steric sea level change in the Northern Seas. *Journal of Climate*, 20(3):403–417.

Steele, M., Morley, R., and Ermold, W. (2001). PHC: A global ocean hydrography with a high-quality Arctic Ocean. *Journal of Climate*, 14(9):2079–2087.

Stirling, I. (1980). The biological importance of polynyas in the Canadian Arctic. *ARCTIC*, 33(2).

Tang, C. C., Ross, C. K., Yao, T., Petrie, B., DeTracey, B. M., and Dunlap, E. (2004). The circulation, water masses and sea-ice of Baffin Bay. *Progress in Oceanography*, 63(4):183–228.

Wang, Q., Myers, P. G., Hu, X., and Bush, A. B. (2012). Flow constraints on pathways through the Canadian Arctic Archipelago. *Atmosphere-Ocean*, 50(3):373–385.

Wekerle, C., Wang, Q., Danilov, S., Jung, T., and Schröter, J. (2013). The Canadian Arctic Archipelago throughflow in a multiresolution global model: Model assessment and the driving mechanism of interannual variability. *Journal of Geophysical Research: Oceans*, 118(9):4525–4541.

Zweng, M. M. and Münchow, A. (2006). Warming and freshening of Baffin Bay, 1916–2003. *Journal of Geophysical Research: Oceans*, 111(C7):n/a–n/a. C07016.

Chapter 4

Impact of the surface stress on the volume and freshwater transport through the Canadian Arctic Archipelago from high resolution numerical modelling

Submitted for publication to Journal of Geophysical Research: Oceans (June 2018).

Nathan Grivault, Xianmin Hu, Paul G. Myers

Abstract

We use a numerical model forced with high temporal and spatial resolution atmospheric forcing to evaluate the volume and freshwater transport through the Canadian Arctic Archipelago (CAA). On average, the simulated inflow through the Queen Elizabeth Islands (QEI) represents 40% of the transport entering the CAA through M'Clure Strait. The transport through Admunsden Gulf represents less than 10% of the total inflow. The impact sea-ice and winds on the volume and freshwater transports into and through this region is also investigated. At Nares Strait and West Lancaster Sound, the transport is overestimated due to too mobile sea-ice but different physical processes related to surface stress, ice driving larger ocean flow in the first case while ice causing less flow reduction in the second case. While the transport through the QEI responds to the changes in surface stress over the Beaufort Gyre and northern Baffin Bay, local surface stress opposed to the mean flow over the straits tends to reduce the throughflow transport. In Parry Channel and the southern CAA, the surface stress tends to enhance the transport and have a greater impact locally. Finally, the surface stress related to sea-ice motion can significantly change

the transport in the CAA during the winter months.

4.1 Introduction

The Canadian Arctic Archipelago (CAA) is a tangle of shallow basins and narrow straits that connect the Arctic Ocean to Baffin Bay and then the Northern Atlantic. It is composed of two main regions. The Queen Elizabeth Islands (or Sverdrup Basin) in the north, which is an area with relatively small islands surrounded by the larger Ellesmere, Devon, Cornwallis, Bathurst, Melville and Prince Patrick islands (Figure 4.1). The other one is the southern CAA, which is composed of larger islands (Bank, Victoria and Prince of Wales Islands). Between the two regions, Parry Channel directly connects the Beaufort Sea to Baffin Bay.

Due to the harsh weather and thick sea-ice that covers the archipelago most of the year, it is difficult to access the northern part of the CAA, even in summer. Therefore, very few long term mooring based observations are available in the CAA. Based on numerical studies (Kliem and Greenberg, 2003; Lu et al., 2014; McGeehan and Maslowski, 2012; Wang et al., 2012; Wekerle et al., 2013; Zhang et al., 2016), it is known that a weak inflow occurs through the Queen Elizabeth Islands (QEI), while the main flow is through the relatively wide passage, i.e., Parry Channel, present between the QEI and the southern CAA. The main flow enters Parry Channel from the west M'Clure Strait (90 km wide, sill at $\sim$ 350 m). It continues to the east until reaches the shallow sill at the end of the Viscount Melville Sound (110 km wide). Then, the flow curves to the south into M'Clintock Channel, around Prince of Wales Island, and turns north back to Parry Channel at Barrow Strait (60 km wide, sill at $\sim$ 150 m) through Peel Sound (Wang et al., 2012). This flow enters Baffin Bay via Lancaster Sound at the east end of Parry Channel. The Arctic ouflow enters Baffin Bay also through Jones Sound and Nares Strait.

The CAA (via Lancaster Sound, Nares Strait and Jones Sound) is the main pathway of liquid freshwater from the Arctic Ocean to the Northern Atlantic with an annual mean flux of about 100 mSv (1 mSv = 10^3 m^{3}s^{-1}; reference salinity: 34.8) (Melling et al., 2008; Münchow, 2016; Prinsenberg et al., 2009). Relatively, solid freshwater export through the CAA is small (6 mSv; Tang et al. (2004)). This freshwater can affect local circulation within Baffin Bay (e.g., Castro de la Guardia et al. (2015); Grivault et al. (2017)). Combined with other freshwater sources (e.g., Greenland meltwater), the freshwater leaving Baffin Bay to the south through Davis Strait is 72 to 130 mSv based on mooring observations (Cuny et al., 2005; Curry et al., 2011, 2014). Eventually, it will arrive in the Labrador Sea, where Labrador Sea Water forms. Consequently, it may impact the large scale oceanic circulation

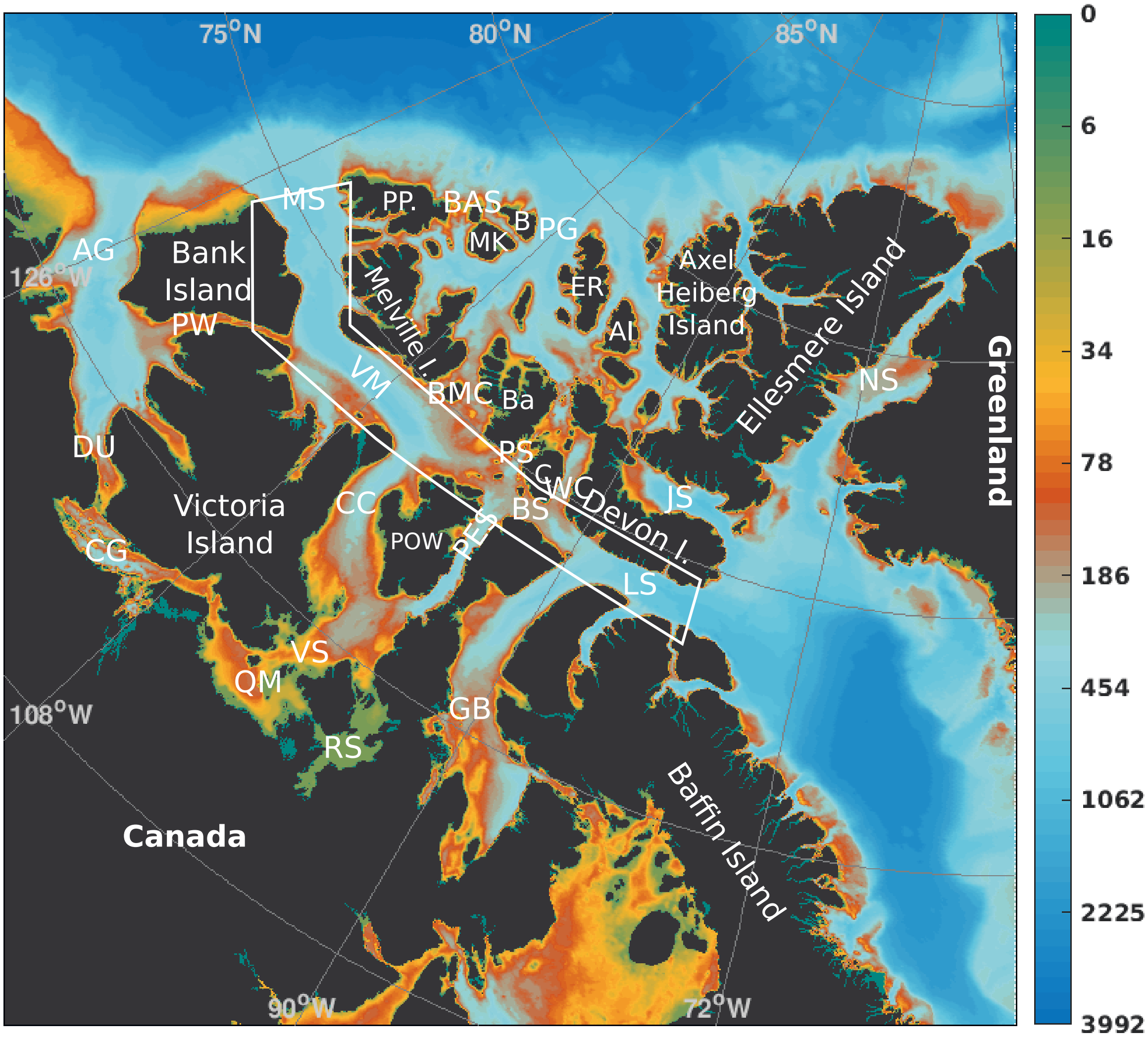

Figure 4.1: Map of the Canadian Arctic Archipelago. AG: Amundsen Gulf, MS: M'Clure Strait, BAS: Ballantyne Strait, PG: Prince Gustaf Adolf Strait, BMC: Byam Martin Channel, PS: Penny Strait, WC: Wellington Channel, DU: Dolphin Union Strait, VM: Viscount Melville Strait, CC: M'Clintock Channel, PES: Peel Sound, VS: Victoria Strait, RS: Rae Strait, QM: Queen Maud Strait, JS: Jones Sound, NS: Nares Strait, LS: Lancaster Sound, BS: Barrow Strait, GB: Gulf of Boothia, CG: Coronation Gulf, B: Baden Island, MK: Mackenzie King Island, PP: Prince Patrick Island, Ba: Bathurst Island, C: Cornwallis Island, AI: Amund Ringnes Island, POW: Prince of Wales Island. The colormap indicates the model domain bathymetry in meters. The white square corresponds to the Parry Channel.

by affecting the upper limit of the Atlantic Meridional Overturning Circulation (AMOC) (Yang et al., 2016). In addition to the Arctic outflow, the river discharge from the main islands contribute about 6 mSv from May to October (i.e., when not covered by ice), based on a study by Spence and Burke (2008).

The current consensus on the CAA dynamics is that the mean flow is controlled by the baroclinic gradient between the Beaufort Gyre and northern Baffin Bay (e.g., Kliem and Greenberg (2003); Prinsenberg and Bennett (1987); Wang et al. (2017); Wekerle et al. (2013)) while the high frequency variability is driven by wind (e.g., Peterson et al. (2012)). Jahn et al. (2009) and Houssais and Herbaut (2011) also found a correlation between large scale atmospheric pattern (i.e., North Atlantic Oscillation) and the transport through the CAA. Linking the CAA throughflow to large scale atmospheric circulation is consistent with a recent study done by Manucharyan et al. (2016), which proposed that the large scale wind forcing over the Beaufort Gyre leads to accumulation or release of freshwater, based on the direction of the winds.

As an important freshwater outflow from the Arctic Ocean to the Northern Atlantic, however, its exact amount of volume and freshwater export through the CAA is still an open question. A summary of previous studies is present in Table 4.1. Mooring data are available at West Lancaster Sound from 1998 to 2010 (Peterson et al., 2012; Prinsenberg et al., 2009) and Nares Strait from 2004 to 2006 and from 2007 to 2009 (Münchow, 2016; Münchow and Melling, 2008). These observations measured a mean volume (freshwater) flow of about 0.46 Sv (32 mSv) at Lancaster Sound (Peterson et al., 2012)). At Nares Strait, the transports are about 0.67 Sv (29.6 mSv) and 1.03 Sv (49 mSv) for 2004-2006 and 2007-2009, respectively (Münchow, 2016). Numerical models for the same sections show various amount of transport, usually larger than the observations, with volume (freshwater) transports between 0.46 and 1.15 Sv (32 to 55 mSv) at Lancaster Sound and between 0.81 and 1.4 Sv (25 to 70 mSv) at Nares Strait (Lu et al., 2014; McGeehan and Maslowski, 2012; Shroyer et al., 2015; Wang et al., 2017; Wekerle et al., 2013; Zhang et al., 2016). We note that the impact of tides is not included in the previously given transports. The tidal current will impact the short time scale transport as well as the overall mixing in the CAA, which is significant for the representation of the Polynyas in the region (e.g., Hannah et al. (2009)).

Another important hydrographic process within the CAA is sea-ice. The maximum sea-ice extent occurs in May, while the minimum occurs in October (Parkinson and Cavalieri, 2008). Landfast ice (i.e., no-motion, fully ice covered) is present in the QEI region between October-November and late July. In the western QEI landfast ice is observed even during summer (Galley et al., 2012; Melling, 2002). In the central CAA, most of the sea-ice is landfast by the end of January, while M'Clure Strait, Amundsen Gulf, and eastern Parry Channel have mobile ice in some years (Galley et al., 2012). The break up of landfast ice starts from June in the southern CAA, and then moves towards the central CAA from the periphery until the end of the summer (Galley et al., 2012). During this period, sea-ice extent varies inter-annually. While sea-ice extends across Parry Channel to the southern part of the CAA, a fully open Parry Channel is already observed during the lowest sea-ice extent years, such as 2007 and 2012 (Parkinson and Cavalieri, 2008; Stroeve et al., 2007).

The thickness of the sea-ice in the CAA is also an open question. Based on drill-hole measurements conducted in the 1970s winters, the average ice thickness over the northern CAA is estimated to be about 3 m (Melling, 2002). The ice is often classified by its age, with first-year ice (FYI) having a thickness up to 2.2 m while the multi-year ice is thicker. The Northwest CAA is one of the last bastion of thick MYI in the Arctic, with a thickness of up to 5.5 meters in winter (Melling, 2002). Most MYI present in the CAA is located in the QEI while the southern CAA is mainly covered with first year ice. The transition between MYI and FYI occurs in Viscount Melville Strait and M'Clintock Channel (Howell et al., 2009; Melling, 2002). Recent observation from Nares Strait showed a median ice draft of about 0.8 m with a significant inter-annual variability, while MYI of more than 5 m are present (Ryan and Münchow, 2017).

Sea-ice area and thickness have decreased dramatically over the last decades (e.g., Comiso (2012); Kwok and Rothrock (2009); Parkinson and Cavalieri (2008); Parkinson and Comiso (2013); Stroeve et al. (2007)). In the CAA, the sea-ice area is decreasing at a rate of about 8.7% decade^{-1} (Howell et al., 2009) and the concentration at a rate of about 2% decade^{-1} (Comiso et al., 2017). The sea-ice melt period has increased by 7 days decade^{-1} (Howell et al., 2009). MYI volume has decreased at the rate of 6.4% decade^{-1} (Comiso, 2012), while record sea-ice thickness decreases have been observed, at Cambridge Bay (-4.31 ± 1.4 cm decade^{-1}), Eureka (-4.65 ± 1.7 cm decade^{-1}), and Alert (-4.44 ± 1.6 cm decade^{-1}) (Howell et al., 2016). These changes did not impact Nares Strait during the last decade (Ryan and Münchow, 2017). Changes in CAA sea-ice could impact the overall freshwater fluxes towards the Northern Atlantic.

In the present paper, we pursue two main goals: 1) to evaluate modeled volume and freshwater transports through the CAA, and 2) to understand the impact of the sea-ice and wind on modeled volume and freshwater transports through the CAA. To achieve these goals, a high resolution eddy permitting regional simulation is conducted, based on a structured ocean-sea-ice coupled model. The simulation is also driven by high temporal and spatial resolution atmospheric forcing.

This paper is structured as follows. Section 4.2 describes the model configuration and the observations used in this study. Section 4.3 presents the model evaluation over the CAA. The impact of sea-ice on the transport is investigated in section 4.4. Finally, conclusions are given in section 4.5.

4.2 Method

4.2.1 Numerical model

IIn this study we use the Nucleus for European Modeling of the Ocean (NEMO) numerical framework, version 3.4. This coupled ocean and sea-ice model includes a three-dimensional, free surface, hydrostatic, primitive-equation ocean component, and a dynamic-thermodynamic sea-ice model (Madec, 2008). The sea-ice model is from the Louvain-la-Neuve sea-ice model (LIM2) (Vancoppenolle et al., 2009) with a modified elastic-viscous-plastic (EVP) ice rheology (Hunke, 2001). The vertical diffusivity and viscosity coefficients are computed by a turbulent closure scheme based on the prognostic equation for the turbulent kinetic energy (Blanke and Delecluse, 1993) modified by Madec et al. (1998). Horizontal tracer diffusivity and viscosity use a Laplacian operator ($A^t \Delta T$, where $A^t = 300$ m^2 s^{-1} is the tracer mixing coefficient) while a bi-Laplacian operator is used for the momentum ($A^{\mathbf{u}} \Delta^2 \mathbf{u}$, where $A^{\mathbf{u}} = -1.5 \times 10^{11}$ m^4 s^{-1} is the maximum velocity mixing coefficient). The bottom friction is based on a non-linear relationship dependent on the bottom velocity with a drag coefficient of 1.0×10^{-3}. The fast frequency variation of the free surface has been filtered out. The model time step is 180 seconds. Note that the experiment does not include tides.

Our domain, called Atlantic and Northern Hemisphere Atlantic (ANHA), is a subdomain of the global ORCA12 domain. It covers the Arctic and the Northern Atlantic Oceans with a resolution of 1/12° (about 3.5 km in the CAA). In vertical, there are 50 levels with layer thickness increasing with depth from 1 m for the first level to 146 m at the 31st level (at a depth of 453 m). The bathymetry in the Arctic is derived from the 1 minute-arc global relief model of Earth's surface ETOPO1 (Amante and Eakins, 2009). Two open boundaries are present in the Bering Sea and at 20°S in the Atlantic Ocean, respectively. Open boundary conditions (temperature, salinity, horizontal velocities) are obtained from the GLobal Ocean ReanalYSis 2 version 3 (GLORYS2v3; Masina et al. (2015)). Surface forcing, i.e., 10 m winds, 2 m temperature and specific humidity, as well as surface downwelling short and long wave radiative fluxes are taken from the high temporal and spatial resolution atmospheric forcing from the Canadian Meteorological Centre's (CMC) Global Deterministic Prediction System (GDPS) ReForcasts (CGRF) (Smith et al., 2014). The initial conditions (ocean temperature, salinity, horizontal velocities and sea surface height) are taken from GLORYS2v3.

Runoff is based on the inter-annual monthly 1°× 1° river discharge data from Dai et al.

(2009), as well as Greenland meltwater (5 km $\times$ 5 km) provided by Bamber et al. (2012). The source runoff is carefully (volume conserved) remapped onto the model grid. The river runoff dataset ends in 2007 while the Greenland runoff goes up to 2010. After each date, the data from the last year is repeated until the end of the simulation.

Our numerical experiment starts from January 2002 and is integrated to the end of December 2016. If not stated otherwise, the results presented in this paper start from November 2003. This is done to consider model adjustment from the initial conditions. We define the winter months as the period from November to April of the following year, and the summer months as the period from May to October. The sign convention for transport is defined as a positive value means towards the North Atlantic (i.e., Arctic outflow) while a negative value means into the Arctic Ocean. The reference salinity is chose to 34.8 in freshwater flux calculation.

4.2.2 Observations

Satellite data

Sea-ice concentration observations are based on the data from the Special Sensor Microwave/Imager (SSM/I) sensors on the Defense Meteorological Satellite Program's (DMSP) -F8, -F11 and -F13 and the Scanning Multichannel Microwave Radiometer (SMMR) on the Nimbus-7 satellite. Measurements from the Special Sensor Microwave Imager/Sounder (SSMIS) aboard DMSP-F17 are also included. The dataset has been generated by using the Advanced Microwave Scanning Radiometer - Earth Observing System (AMSR-E) Bootstrap Algorithm with daily varying tie-points (Comiso, 2015). We used the daily data averaged over the winter period from 2003 to 2016. The data are gridded on the SSM/I polar stereographic grid (25 $\times$ 25 km).

Sea-ice thickness data are combined from the ICESat1-G (2003-2008) and CryoSat-AWI (2011-2017) dataset extracted from the Unified Sea-Ice Thickness Climate Data Record (Lindsay and Schweiger, 2017). ICESat1-G data are derived from measurements made by from the Ice, Cloud, and land Elevation Satellite (ICESat) Geoscience Laser Altimeter System (GLAS) instrument, the Special Sensor Microwave/Imager (SSM/I), and climatologies of snow and ice drift. CryoSat-AWI thickness is derived from Radar Altimeter freeboard measurements. Due to the irregularity in the position of each data point between the dataset and within the years in the same dataset, we averaged all data over 1-degree bins first, then over the winter period from 2003 to 2016. The years with no data available (2009-2010) have been ignored in the averaging, as well as during summer.

Mooring data

Two locations with moorings are available in the study region: at Nares Strait and West Lancaster Sound. At Nares Strait, observation are available for two periods, from August 2004 to August 2006, and from August 2007 to August 2009, respectively (Münchow, 2016). The daily average of detided data is used here. More in depth description of the moorings is available in Münchow and Melling (2008). At West Lancaster Sound, observations are available from August 1998 to August 2010. Both monthly and 6-hourly detided data are used in this study. More details of the mooring data are available in Prinsenberg et al. (2009) and Peterson et al. (2012). In order to compute the correlation between model and observation, high frequency observations (either daily or 6-hourly) are averaged every 5 days (same frequency as model output).

4.3 Evaluation

4.3.1 Sea-ice

In summer (Figure 4.2a), ice concentration is 70% to 80% in the western and central Parry Channel, and decreases gradually to 50% at the mount of Lancaster Sound. Spatial variation in ice concentration also exists in Peel Sound, high ($\sim$ 80%) on the west side and lower ($\sim$ 70%) on the east side. The Amundsen Gulf is almost ice free (less than 30%). Within Baffin Bay, the ice concentration is low on the Greenland side because of the intrusion of warm water carried by West Greenland Current at depth. In winter (Figure 4.2b), the CAA is fully covered by the sea ice, with the exception of the North Water Polynya where the sea ice concentration decreases slightly ($\sim$ 80%). The sea ice edge is located at the eastern part of Davis Strait over the Greenland continental shelf.

In summer, sea-ice thickness is up to 5.5 meters around the Prince Patrick, Baden and Ellef Ringnes Islands (Figure 4.2a). Ice thickness within the QEI is around 5 m while it is less than 1 m in Parry Channel and Amundsen Gulf. In winter (Figure 4.2b), ice thickness withing Amudsen Gulf increases up to 2 m. The maximum sea-ice thickness stays around 5.5 m. Sea-ice distribution and thickness over the other regions of the CAA does not change significantly. We note that the model forms in the QEI thicker sea-ice in summer than winter, as well as in Nares Strait. This is due to the summer and winter periods definition here. It is also evidenced in Hu et al. (2018) with a different definition (figure 4a and b in their paper).

Overall, sea-ice concentration in winter in the model compares well with the available

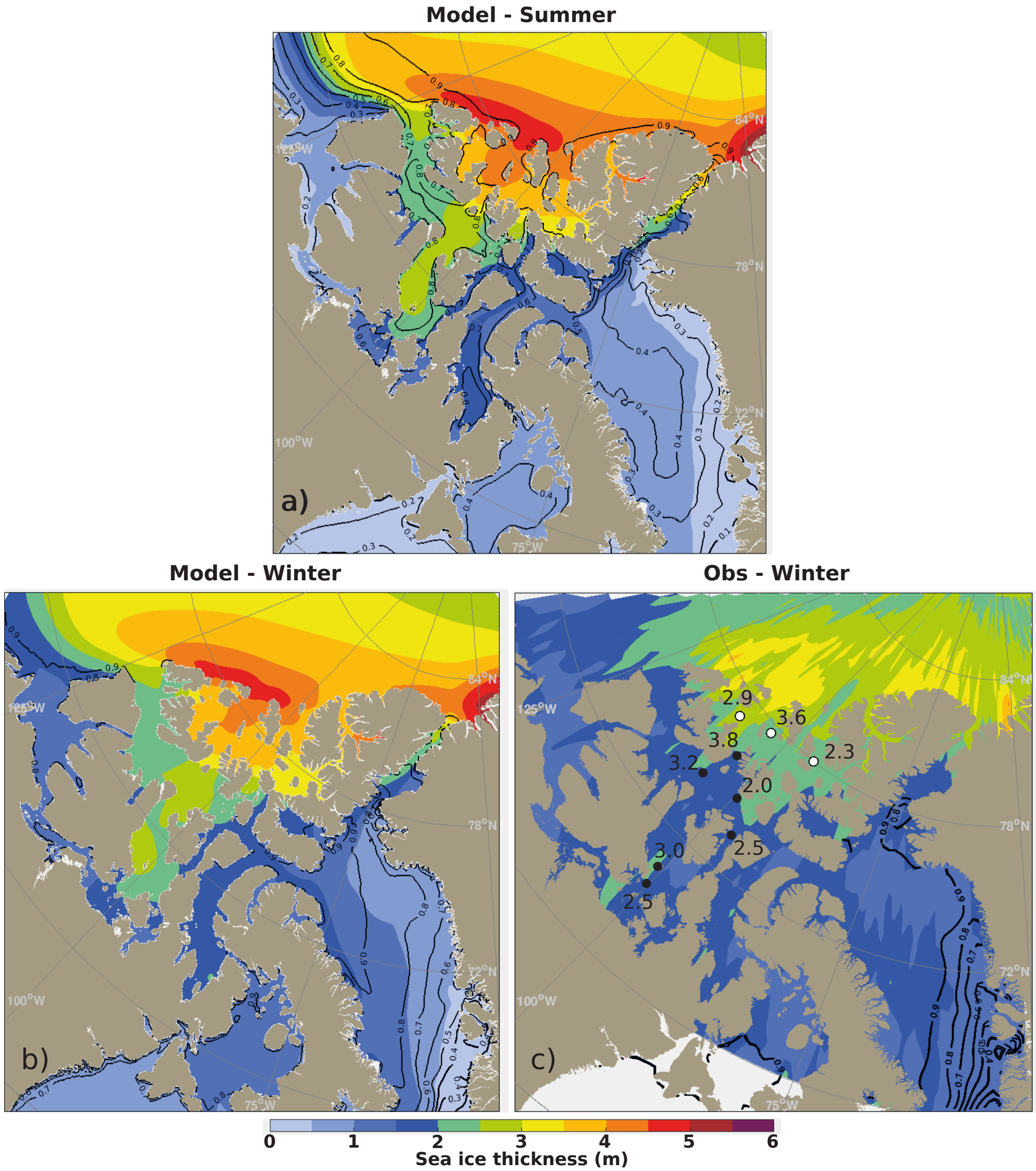

Figure 4.2: Sea ice thickness (shading) and concentration (contour lines) for summer (a) and winter (b) and observations for the winter period (c). Observations south of 66°N are masked. The black points are airborne electromagnetic measurements from Haas and Howell (2015) from late winter 2011 and 2015. White dots are drill hole measurements from Melling (2002) from late winter in the 1970s. Both are in meters.

observations for the same period (Figure 4.2c). The main difference is the 90% sea-ice concentration contour of the observation occurs further south. But it does not impact the analysis in this study. The overall spatial pattern of the sea-ice thickness in the model matches the observations. The main difference is that the simulated sea-ice is thicker than in the satellite data, especially in the QEI where the difference is about 1.5 m. Compared to the drill hole measurements in the late winter of 1970s (Melling, 2002), the simulated sea-ice thickness is still thicker but with a smaller difference. In the Northwest Passage, simulated sea ice thickness, however, is very close (only $\sim$ 0.5 m thicker) to observations from the airbone electromagnetic survey performed in late 2011 and 2015 (Haas and Howell, 2015). At Nares Strait, the simulated sea-ice thickness is about 2 m, which agrees the winter observations from 2002 to 2012 that the median daily ice draft is from 1.5 m to 3 m (Ryan and Münchow, 2017).

A more complete analysis of sea ice thickness changes and dynamic-vs-thermodynamic contributions could be found in another study based on the same numerical experiment by Hu et al. (2018).

4.3.2 Transports via Nares Strait

The modelled volume transport at Nares Strait over the whole time period of 2002-2016 is 0.92 ± 0.44 Sv (Figure 4.3a, b). The inter-annual variability is relatively small or insignificant except in 2010. In 2010, the transport decreased significantly, even switched the direction in November (i.e., back to the Arctic Ocean). In the first common period (2004-2006), the modelled volume (freshwater) transport is 0.92 ± 0.36 Sv (32 ± 14 mSv), which compares well with the observed 0.67 ± 0.44 Sv (30 ± 21 mSv). The correlation between the observation and the model is $r = 0.62$ ($r = 0.59$). During the second common period (2007-2009), the simulated transport is 0.99 ± 0.37 Sv (freshwater transport: 44 ± 21 mSv), which compares well with the observed 1.03 ± 0.35 Sv (49 ± 22 mSv). The correlation between the model and observation is $r = 0.80$ ($r = 0.75$), which is higher than that in the first common period. We note that the correlation between volume and freshwater transports is greater than 0.95, which is consistent with observations (Münchow, 2016)

The seasonal cycle of the volume and freshwater transport is shown in Figure 4.4a. The seasonal cycle for the observations are computed from all available data, while the seasonal cycle for the model is computed from winter 2003 to summer 2016. It shows that the model has too much volume transport between March and June (i.e., during the end of winter) and not enough in November and December. The seasonal cycle for the freshwater transport is similar, except in December. In December, the model underestimates the freshwater transport more than what it does for the volume transport (Figure 4.4a) ($\sim$ 10 mSv less than observations).

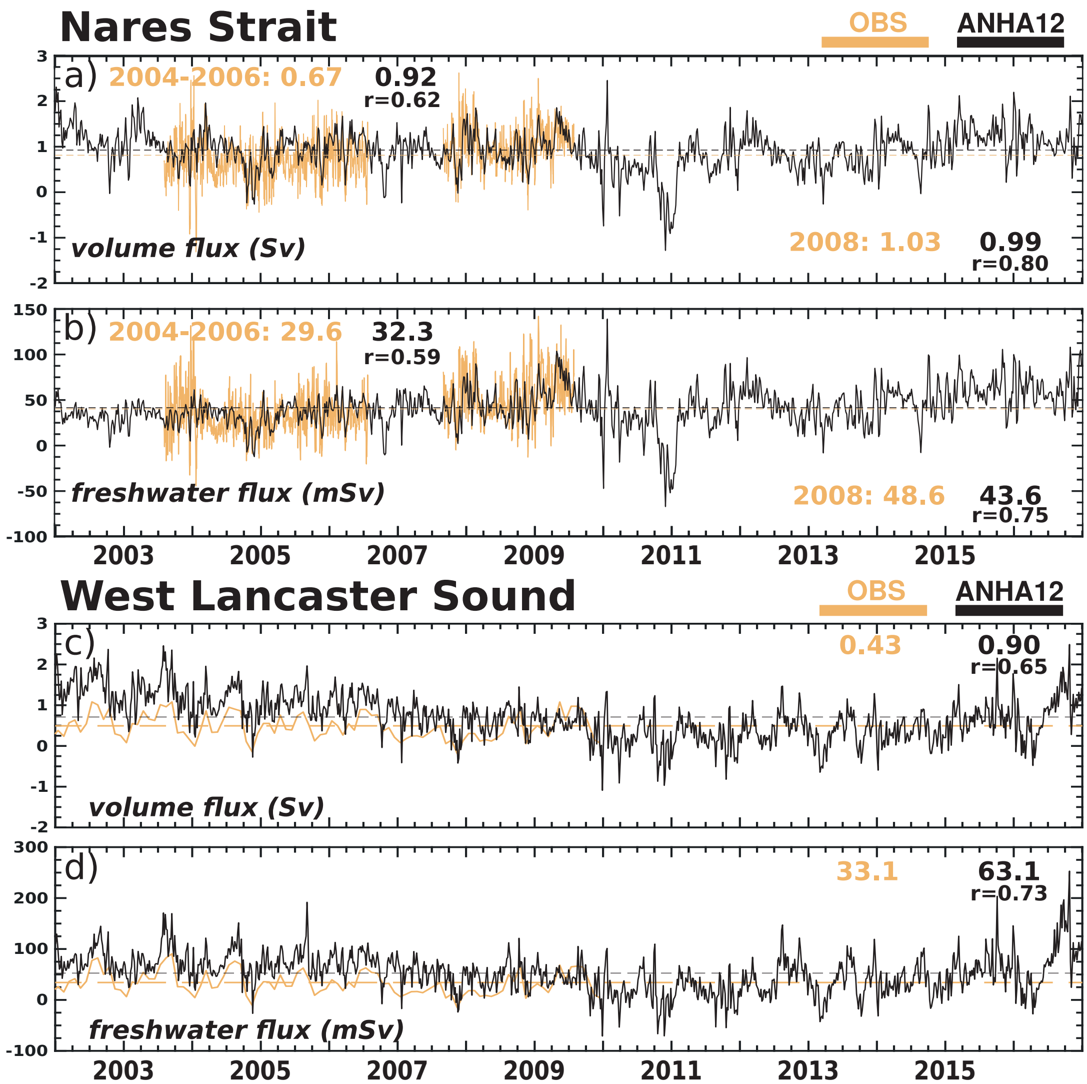

Figure 4.3: Observed (orange line) and simulated (black line) volume and freshwater transports for Nares Strait (a and b) and West Lancaster Sound (c and d). The average transports and correlations are computed over the common period of time between observations and model outputs. The dashed lines correspond to the average over the whole period for each dataset.

4.3.3 Transport via West Lancaster Sound

At West Lancaster Sound, the average modelled volume (freshwater) transport for the whole time period is 0.71 ± 0.55 Sv (53 ± 38 mSv). Over the common period (2002 to 2010), it is even larger, 0.95 ± 0.52 Sv (63 ± 33 mSv), compared with observations, 0.46 ± 0.56 Sv (32 ± 24 mSv) (Figure 4.3b, d). The correlation between the model and observations is $r = 0.65$ ($r = 0.73$). The seasonal cycles shows that the transport in the summer months in the model is close to observations (Figure 4.4b). However, the volume transport during the

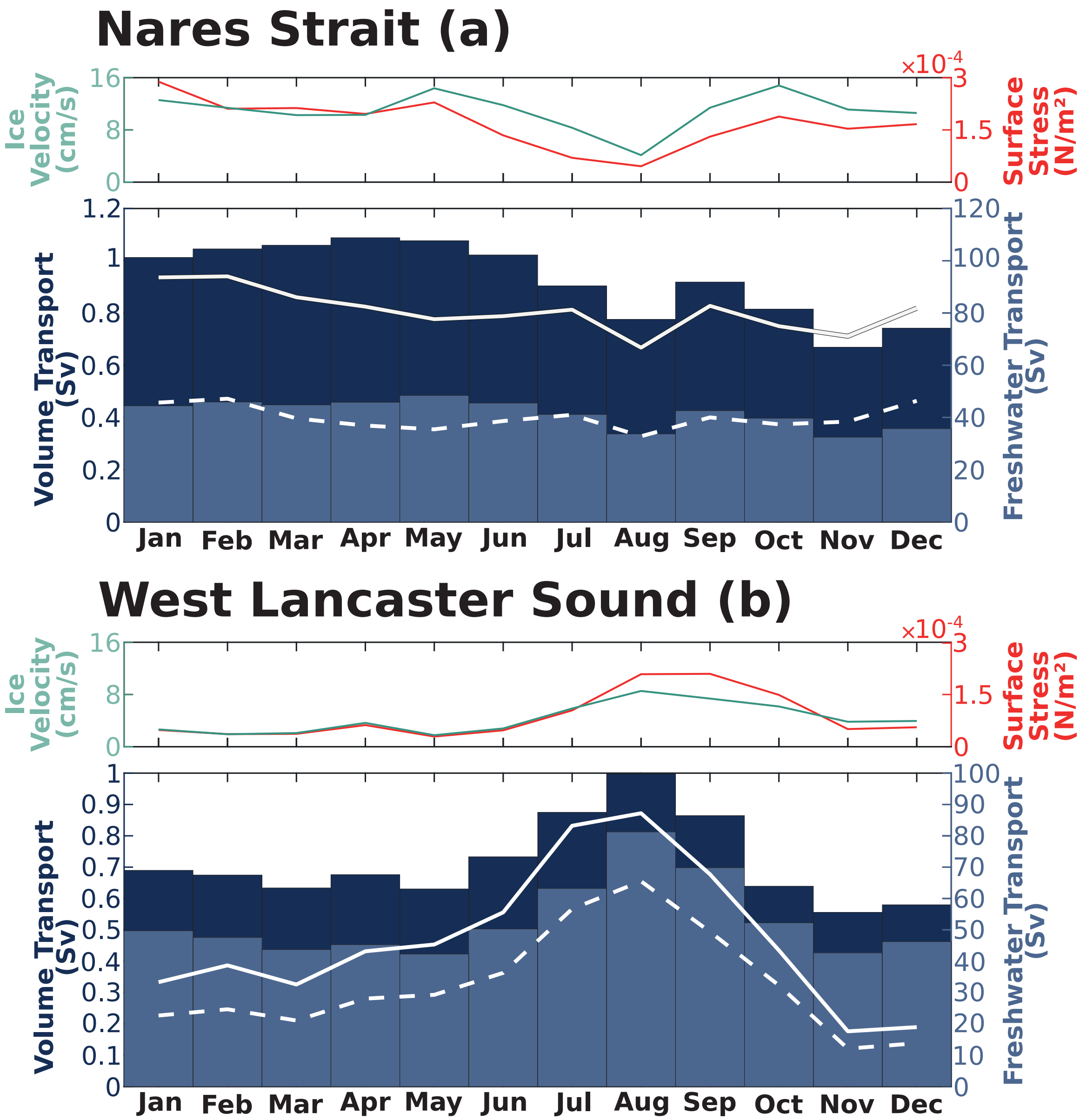

Figure 4.4: Nares Strait (a) and West Lancaster Sound (b) volume and freshwater transport seasonal cycles (bars). Volume (freshwater) transport is shown in dark blue (light blue) bar. White solid (dashed) line is the volume (freshwater) transport seasonal cycle from observations. Volume (freshwater) transport is associated with the left (right) axis. Each upper panel shows the ice velocity (green line, left axis) and surface stress (red line, right axis) directly above the section. Note different scales are used for left hand and righ hand y-axis in each panel.

winter is 75% higher than observations (about 0.7 Sv instead of 0.4 Sv). The modelled freshwater transport is slightly better, only 55% higher than the observation ($\sim$ 45 mSv vs 20 mSv).

Using high resolution observations, we expand the fluxes analysis for each sub-section

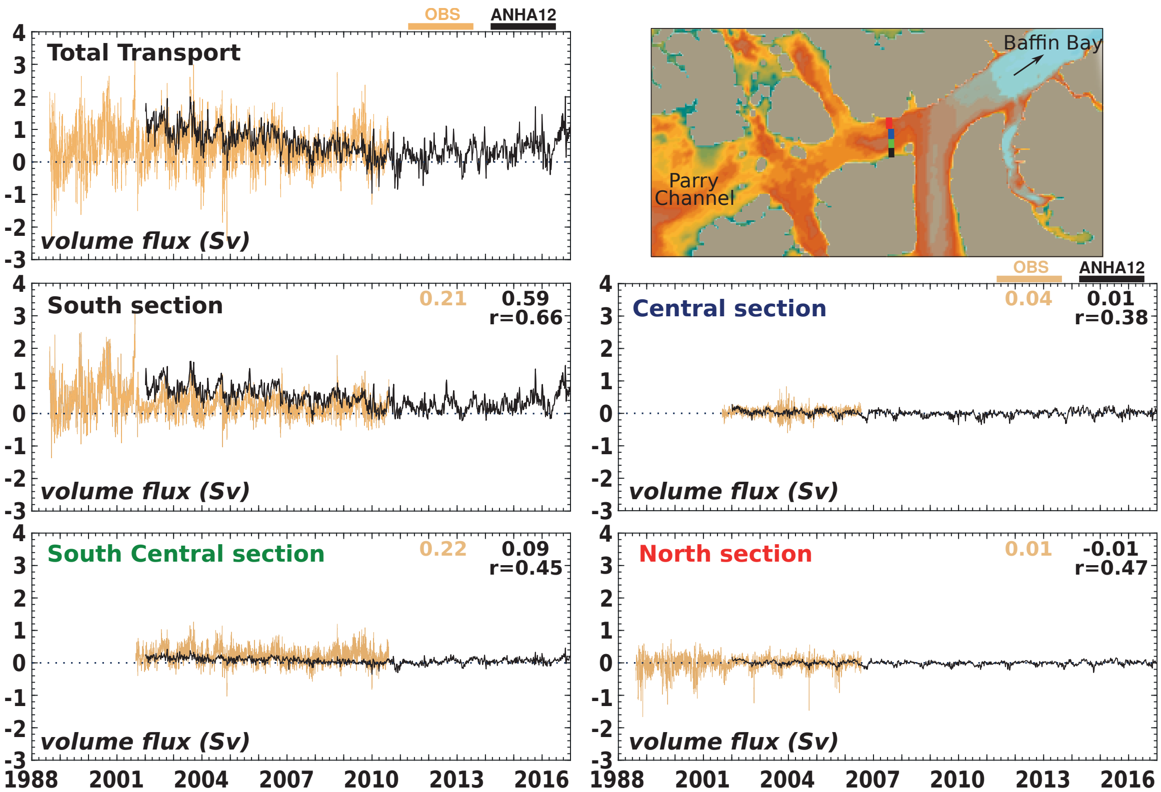

Figure 4.5: Detailed transport break down at Barrow Strait observations (orange line) vs model (black line). The total transport is shown in the top left panel. Location of each sub-section is shown in the top right panel. The other panels represent the transport per sub-section. The line colours of each sub-section in the top right panel correspond to the colour in the name of each sub-section in the transport panels.

across the West Lancaster Sound (Figure 4.5). For the details about how the observations are computed per sub-section, please sea Peterson et al. (2012) and Prinsenberg et al. (2009)). The model mean transport is slightly higher than observations between 2002 and 2009 in the southern part but close to the observations in the other parts and after 2009. The transport through the south section decreases progressively, being more comparable with the observations.. The variability is satisfyingly represented by the model for each sub-section (Figure 4.5). Several cells are used in the model to compute the transports, while only one mooring is available for each subsection, thus, uncertainty in observation is not yet considered here.

Overall, the model represents the observed transport relatively well. The model overestimates both volume and freshwater transport for each section for the early years, but becomes close to observation both in mean value and correlation in later years. The reasons behind the overestimates on the transports is discussed in section 4.4.1. More evaluation

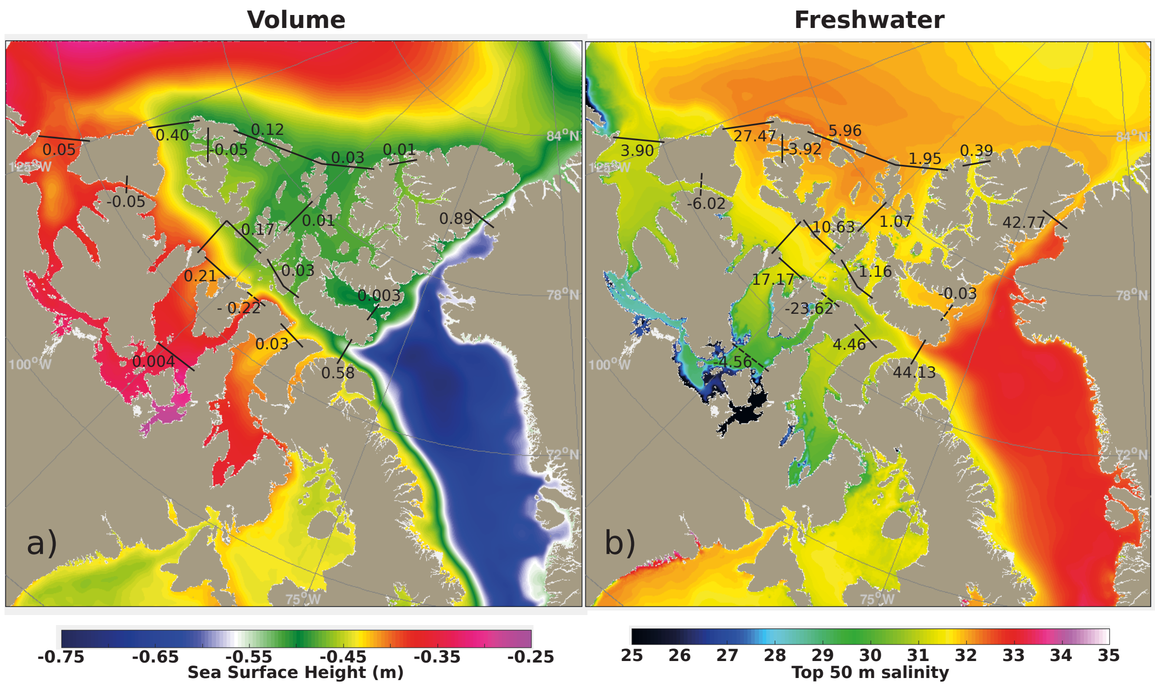

Figure 4.6: Sea surface height (a) and top 50 m salinity (b) in the Canadian Arctic Archipelago. The numbers represent the volume (a) transport (unit: Sv) and the freshwater (b) transport (unit: mSv) through the Canadian Arctic Archipelago averaged from November 2003 to December 2016. Transport is positive when going towards the Northern Atlantic and negative when going towards the Arctic Ocean.

on the transport through the CAA, including current velocity and surface density, and mixing processes in this region is described by Hughes et al. (2017) for a similar experiment. Additionally, Dmitrenko et al. [in prep] compares the along-slope current velocity in our experiment with mooring in the Beaufort Sea.

4.3.4 Transport via the other major gates in the Canadian Arctic Archipelago

An overall picture of the oceanic transports through the CAA are shown in Figure 4.6a and Figure 4.6b for volume and freshwater transport, respectively. A summary is shown in Table 4.1 as well as values from other studies. We note that the transports values from the 1980s and earlier are computed based on only a few observations. The modelled volume (freshwater) transport going into the QEI from the Arctic Ocean is about 0.16 Sv (8 mSv), which is about 40% (30%) of the incoming transport through M'Clure Strait (0.40 Sv; 27 mSv). Part of the inflow through M'Clure Strait could enter the QEI via the strait between Prince Patrick Island and Melville Island. It is 0.05 Sv (4 mSv) in our simulation. However, whether it is a realistic case or a bias due to model resolution needs

Panel	Section Name	Volume Transport	Freshwater Transport	Source
(**a**)	Ballantyne + Prince Gustaf Adolf Straits	0.12	5.96	This study
(**b**)	Ellef Ringnes – Axel Heiberg Island Strait	0.03	1.95	This study
(**c**)	Central QEI	0.01	1.07	This study
(**d**)	Prince Patrick Island – Melville Island Strait	-0.05	3.92	This study
(**e**)	Byam Martin Channel	0.17	10.63	This study
	1958-2007	0.27	22	Wekerle et al. (2013)
	1982-1984	**0.12**		Fissel (1988)
(**f**)	Penny Strait + Wellington Channel	0.03	1.16	This study
	1958-2007	0.09*	7*	Wekerle et al. (2013)
	1982-1984	**0.29**		Fissel (1988)
(**g**)	Lancaster Sound	0.58	44.13	This study
	1988-2007	1.15	55	Lu et al. (2014)
	1958-2007	0.86	71	Wekerle et al. (2013)
	1978-2013	0.71		Zhang et al. (2016)
	1998-2010	**0.46**	**32**	Peterson et al. (2012)
	1982-1984	**0.45**		Fissel (1988)
	1928	**0.65**		Kiilerich (1939)
	1954	**1.50**		Bailey (1957)
	1954	**1.00**		Collin (1962)
	1966	**0.45**		Palfrey and Day (1968)
(**h**)	M'Clure Strait	0.40	27.47	This study
	1958-2007	0.45	40	Wekerle et al. (2013)
	1982-1984	**0.05**		Fissel (1988)
(**I**)	Prince of Wales Strait	-0.05	-6.02	This study
	1958-2007	0.01	2	Wekerle et al. (2013)
	1982-1984	**0.05**		Fissel (1988)
(**j**)	Mc Clintock Channel	0.21	17.17	This study
	1958-2007	0.27	24	Wekerle et al. (2013)
	1982-1984	**0.06**		Fissel (1988)
(**k**)	Peel Sound	-0.22	-23.62	This study
	1958-2007	-0.29	-26	Wekerle et al. (2013)
(**l**)	Gulf of Boothia	0.03	4.46	This study
(**m**)	Amundsen Gulf	0.05	3.90	This study
(**n**)	Victoria Strait	0.00	-4.56	This study
(**o**)	Jones Sound	0.00	-0.03	This study
	1978-2013	0.31		Zhang et al. (2016)
	1928	**0.30**		Kiilerich (1939)
	1954	**-0.40**		Bailey (1957)
	1954	**0.25**		Collin (1962)
	1966	**0.30**		Palfrey and Day (1968)
(**p**)	Nares Strait	0.89	42.77	This study
	1988-2007	1.14	25	Lu et al. (2014)
	1958-2004	1.40	77	Wang et al (2017)
	1978-2007	0.91	48	Wekerle et al. (2013)
	1978-2013	0.81		Zhang et al. (2016)
	1998-2010	0.16		Peterson et al. (2012)
	2003-2009	**0.85**	**39**	Münchow (2016)

Table 4.1: Summary of the volume (in Sv) and freshwater (in mSv) transport averaged from November 2003 to December 2016 at the main gates and through the CAA. The panel letters correspond to the straits shown in Figure 4.9. Bold numbers are from observations.
* Only includes Penny Strait
♣ Data from Smith Sound

further investigation.

This suggests, this region is important in terms of the exchange through the CAA. 80% of the QEI inflow inflow enters Parry Channel via Byam Martin Channel (0.17 Sv for modelled volume and 0.03 mSv for modelled freshwater transport), and 15% via Penny Strait and Wellington Channel (0.03 Sv for modelled volume and 1 mSv for modelled freshwater transport). Jones Sound has a negligible effect on the volume and freshwater outflow out of the QEI in the simulation. These values compare well with a previous numerical experiment from Wekerle et al. (2013) who obtained modelled volume (freshwater) transports of 0.45 Sv (40 mSv), 0.27 Sv (22 mSv) and 0.09 Sv (7 mSv) through M'Clure Strait, Byam Martin Channel, and Penny Strait, respectively. Only the modelled freshwater flow via M'Clure Strait is significantly higher in our experiment. We also note that the simulated flow through Jones Sound is significantly lower than the one obtained by Zhang et al. (2016) in their numerical experiment, which also has a significantly higher simulated flow at Lancaster Sound compared with observations. The modelled volume transport is stronger in the western part of the QEI ($\sim$ 80% of the transport follows this route), and a weak eastern simulated flow is present inside of the QEI between the western and eastern part (0.01 Sv; 1 mSv).

Amundsen Gulf receives about 0.05 Sv (4 mSv) from the Arctic Ocean. This inflow later enters Parry Channel via Prince of Wales Strait due to the high sea surface height (SSH) in Coronation Gulf. Compared to a previous numerical study by Wekerle et al. (2013), the volume flux through this pathway is 5 times larger in our simulation. The difference could be due to difference in model resolution in this region. We also note that the direction of freshwater transport in our simulation is different than in Wekerle et al. (2013).

The simulated flow in the central Parry Channel goes around the Prince of Wales Island via the M'Clintock Channel and Peel Sound, which agrees with previous studies (Wang et al., 2012; Wekerle et al., 2013; Zhang et al., 2016). The modelled transport through M'Clintock Channel and Peel Sound is 0.21 Sv (17 mSv) and 0.22 Sv (24 mSv), respectively. These numbers compare well with Wekerle et al. (2013), 0.27 Sv (24 mSv) and 0.29 Sv (26 mSv), respectively.

The increase in transport through Peel Sound is from Victoria Strait ($\sim$ 0.01 Sv). Due to the low salinity (< 20) in its upstream region, the freshwater transport can be as large as 5 mSv, which represents about 1/5 of the freshwater flow through Peel Sound. This indicates a non negligible freshwater source into Parry Channel.

4.4 Surface stress and ice velocity

4.4.1 West Lancaster Sound and Nares Strait

The difference in quality of the simulated volume and freshwater transports at West Lancaster Sound and Nares Strait can be explained by the different impact of the ice velocity on the transport.

It is found the simulated volume transport is high correlated to surface stress both at West Lancaster Sound ($r = 0.75$) and Nares Strait ($r = 0.53$). The variation of surface stress at West Lancaster Sound is mainly controlled by ice velocity with a correlation of 0.96, which indicates the variation of the transport here is mainly due to ice motion. At Nares Strait, the correlation between surface stress and ice velocity is lower ($r = 0.72$), suggesting a bigger role from the wind. Similarly, difference in surface stress sources may also play a role in the freshwater transport. The modelled freshwater transport is highly correlated to the surface stress at West Lancaster Sound ($r = 0.90$) while $r = 0.55$ only at Nares Strait.

The timing of the overestimated transport through the two straits is found to be correlated to the too mobile ice in the simulation. Figure 4.4b shows larger discrepancies between observation and simulated volume transport occur in the winter months, i.e, November to May in the following year. During this period, the simulated mean ice velocity is as large as 3 cm s^{-1}, leading to too big downstream flow. Similarly at Nares Strait, the fast ice motion (up to 14 cm s^{-1} in May) in April-June results in most overestimated volume transport here in our simulation. At Nares Strait, Ryan and Münchow (2017) showed the landfast ice exists in May of most years between 2003 and 2012 based on observations. The sea-ice jam is also an important physical process that controls the sea ice dynamics at Nares Strait. However, the model utilized here does not resolve landfast ice physics, e.g., using the parameterization from (Lemieux et al., 2016). Therefore, the modelled sea-ice velocity is usually high compared to the real word. The ice-bridge is not resolved either, however, the accumulation of ice in the narrow channel plays a similar role to reduce the ice velocity (see Figure 4d in Hu et al. (2018)). It explains why the transport overestimation at Nares Strait happens later than that at West Lancaster Sound in our simulation.

Although too mobile sea-ice leads to overestimated transport through both West Lancaster Sound and Nares Strait, the role of sea-ice is different. At West Lancaster Sound, the surface stress (same for the ice stress, not shown here) is in opposite direction of the surface flow (Figure 4.7b), thus, the ice works as a drag reducing the ocean flow. As the

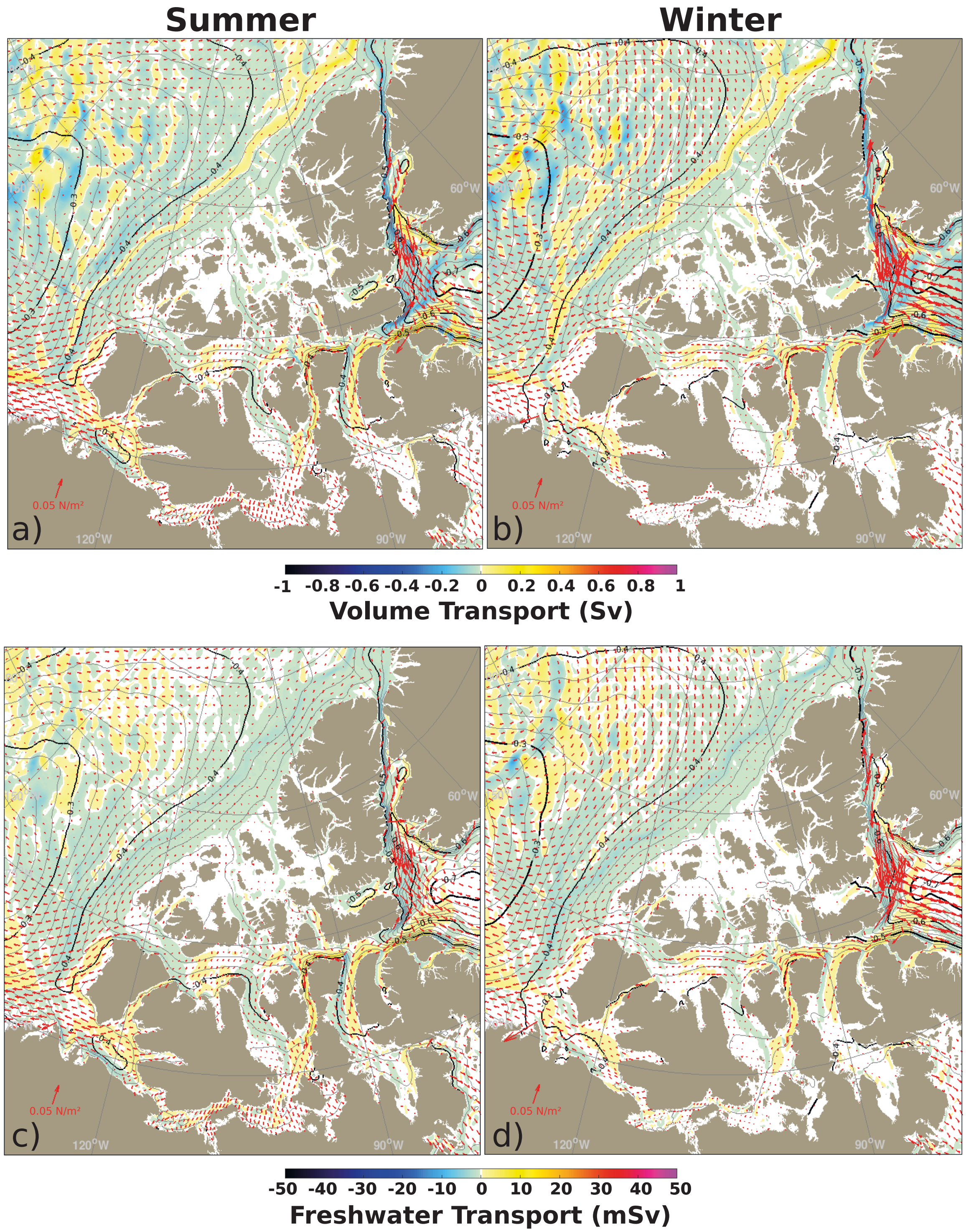

Figure 4.7: Maps showing the volume (a and b) and freshwater (c and d) transports at each point of domain (background colour) with the surface stress (red arrows) and sea surface height (black contour lines) averaged over all summers from 2004 to 2016 (a and c) and all winter from 2003 to 2016 (b and d).

ice is too mobile, the reduction of ocean flow due to surface stress is not enough, resulting larger volume transport to downstream. However, at Narest Strait, the ice is drifting faster (not shown) than the ocean surface flow, thus, the surface stress is in the same direction as the ocean flow (Figure 4.7b). Therefore, sea-ice there does drive a faster surface ocean current. Different ice-ocean interactions is likely due to much stronger along channel wind at Nares Strait. More discussion about the dependence of Nares Strait oceanic transport on the sea-ice motion available in Shroyer et al. (2015).

4.4.2 Other straits over the Canadian Arctic Archipelago

In summer (Figure 4.8a), sea-ice velocity in the numerical experiment is small in most of the CAA with a velocity less than 1 cm s^{-1} in the QEI, except in the main channels where the velocity can be up to 3 cm s^{-1}. In the southern CAA, this velocity increases up to 7 cm s^{-1}. High sea ice velocity (up to 16 cm s^{-1}) can be found at Barrow Strait, at the mouth of Lancaster Sound, in Nares Strait, and in the area of the North Water polynya. In winter (Figure 4.8b), despite not having real landfast ice in the model, the ice velocity is less than 1 cm s^{-1} over most of the CAA. High velocity (up to 10 cm s^{-1}) can be found in the Amundsen Gulf and in Lancaster Sound in the numerical experiment. Much larger (more than 25 cm s^{-1} locally) ice velocity is seen along the path from Nares Strait to eastern Baffin Island coast. Observations Ryan and Münchow (2017) also shows large velocity in this region but with a lower winter average velocity due to the presence of ice-bridge. We note that these modelled velocities are close to the observed ice speed in this period but higher than the average velocity over the winter, considering the presence of the ice-bridge . The dependence of Nares Strait oceanic transport to the sea-ice motion is more fully discussed in Shroyer et al. (2015).

Another way to quantify the impact of surface stress on the ocean flow is Ekamn depth and Ekman transport (Appendix C). Figure 4.8c, and 4.8d) show the summer and winter Ekman depth (colours) and transport (arrows) in the CAA region based on model simulation. It clearly shows Ekman depth is deeper in summer (Figure 4.8c) in most region of the CAA CAA (QEI, Amundsen Gulf and south CAA). The Ekman depth shallowing is associated with a 50% decrease of surface stress in these regions in winter (Figure 4.8d), indicating weaker transport there. However, it is a different case in the eastern part of the CAA and Baffin Bay. At Nares Strait, the Ekman depth is deeper in winter by up to 70% due to an increase of the surface stress over the strait. In the following section, we will focus on how and from where the transport through the CAA is affected by the surface stress.

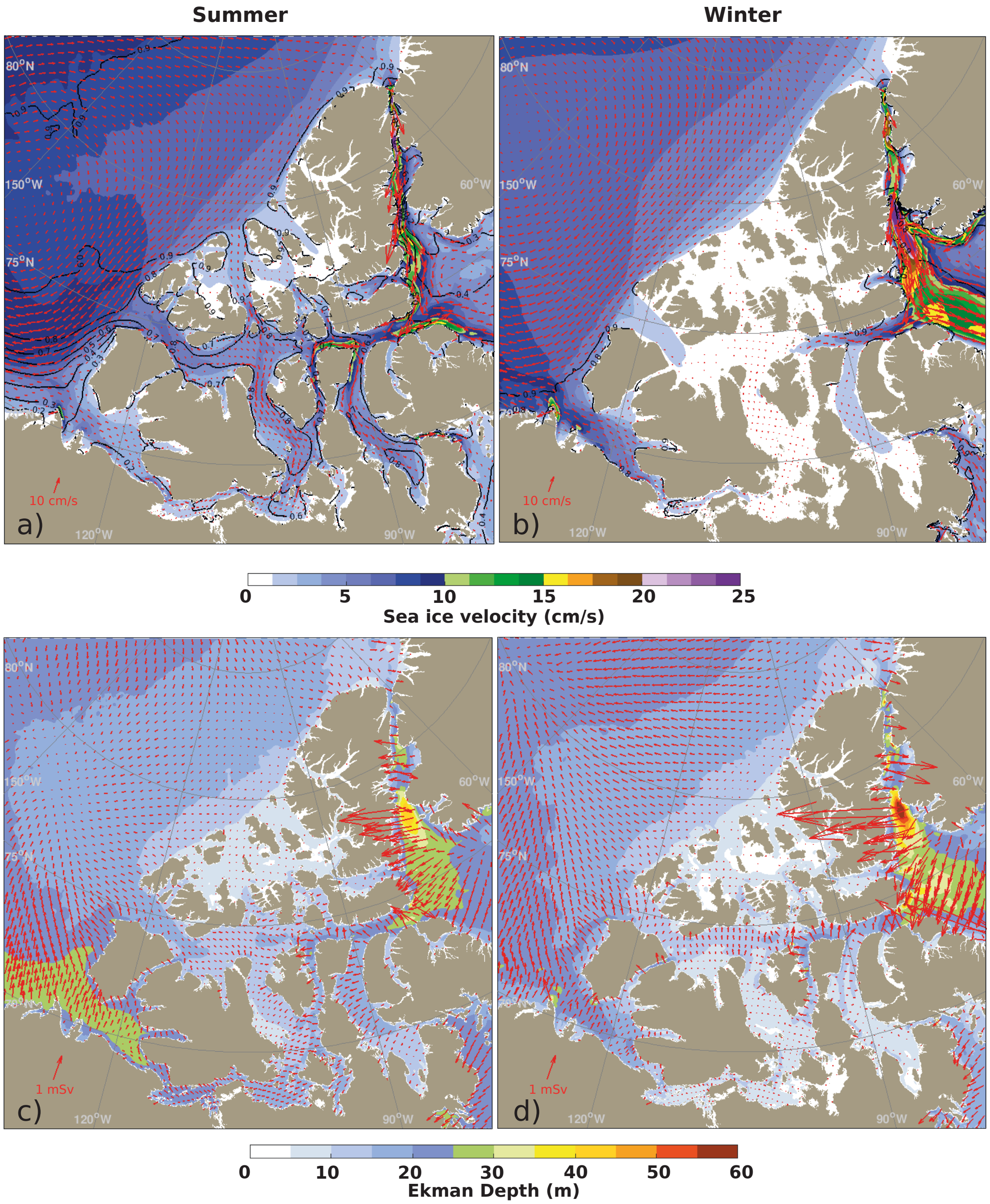

Figure 4.8: The top panels show the sea-ice velocity (shading) and direction (arrows) for summer (a) and winter (b). The bottom panels show the Ekman Depth (shading) and Ekman Transport (arrows) for summer (c) and winter (d).

4.4.3 Correlation between volume transport through main gateways and surface stress in space

To better understand the the impact of surface stress on ocean transports, we correlated the transport (volume and freshwater respectively) time series via main gateways in the CAA with surface stress time series on each model individual point. To remove the linear adjustment of the model, both time series are linearly detrended (more information on how and why the correlation is computed this way is provided in Appendix D). The correlation is performed for summer and winter periods separately. A positive correlation means that a stronger surface stress enhances the mean transport, while a negative correlation means a stronger surface stress weakens the mean transport. The spatial distribution of correlation can be interpreted in two aspects. A significant correlation close to the section means that the variability in the transport can be explained by local changes, or changes over the immediate upstream or downstream region, in the surface stress forcing (i.e., the atmospheric forcing or the sea-ice motion, depending on the sea-ice cover) while a significant correlation farther away from the section shows how much of the variability can be explained by remote changes in the surface stress. In the second case, we define two regions

Panel	Section Name	Summer		Winter	
		Local	Large	Local	Large
(**a**)	Ballantyne + Price Gustaf Adolf Strait	Weak^{+}	None	Weak$^{-/+}$	Weak$^{-/+}$
(**b**)	Ellef Ringnes – Axel Heiberg Island Strait	Weak$^{\varnothing/-}$	Strong$^{-/-}$	Weak^{-}	Weak$^{-/\varnothing}$
(**c**)	Central QEI	Weak$^{+/-}$	Weak$^{-/-}$	Weak^{-}	None
(**d**)	Prince Patrick Island – Melville Island Strait	Weak^{-}	Weak$^{+/+}$	Strong^{-}	Weak$^{+/-}$
(**e**)	Byam Martin Channel	Weak^{+}	Weak$^{-/\varnothing}$	Strong^{+}	None
(**f**)	Penny Strait + Wellington Channel	Weak^{-}	Strong$^{-/\varnothing}$	Strong$^{-/+}$	Weak$^{-/-}$
(**g**)	Lancaster Sound	Weak$^{+/-}$	Strong$^{-/\varnothing}$	Strong^{+}	Weak$^{-/\varnothing}$
(**h**)	M'Clure Strait	Weak$^{-/\varnothing}$	Weak$^{-/\varnothing}$	Weak$^{+/-}$	Weak$^{-/\varnothing}$
(**I**)	Prince of Wales Strait	Weak$^{+/-}$	Strong$^{+/\varnothing}$	Strong^{-}	Weak$^{+/\varnothing}$
(**j**)	Mc Clintock Channel	Weak^{+}	Weak$^{-/\varnothing}$	Strong^{+}	Weak$^{-/\varnothing}$
(**k**)	Peel Sound	Weak^{-}	Weak$^{+/\varnothing}$	Strong^{-}	Weak$^{+/\varnothing}$
(**l**)	Gulf of Boothia	Weak^{+}	Weak$^{\varnothing/+}$	Weak^{+}	Weak$^{\varnothing/+}$
(**m**)	Amundsen Gulf	Strong^{-}	Strong$^{-/-}$	Strong^{-}	Strong$^{-/\varnothing}$
(**n**)	Victoria Strait	Weak^{-}	Strong$^{-/-}$	Weak^{+}	Weak$^{-/\varnothing}$
(**o**)	Jones Sound	Weak^{-}	Strong$^{-/-}$	None	Weak$^{-/-}$
(**p**)	Nares Strait	Weak^{+}	Weak$^{\varnothing/+}$	Strong^{+}	Weak$^{\varnothing/+}$

Table 4.2: Relative strength of the local and large scale correlation for each strait shown in Figure 4.9 (summer) and 4.10 (winter). The superscript in the Local columns indicates the direction of the correlation ($^{+}$: positive correlation; $^{-}$: negative correlation; both means that both correlations are present). The superscript in the Large columns indicates the correlation over the Beaufort Gyre (first superscript) and over the northern Baffin Bay (second superscript). The subscript $\varnothing$ indicates when there is no significant correlation over the considered region.

Figure 4.9: Correlation between the surface stress and the volume transport in summer for the sections defined by the thick black line in each panel. All values with a degree of confidence lower than 0.05 have been masked out. The black boxes in the top left figure (a) show the boxes used to define the remote correlations in tab 4.2.

of interest: over the Beaufort Gyre and in northern Baffin Bay, shown in Figure 4.9a. The strength of the correlation is classified as "none" ($r \leq 0.1$ or not significant at a significant level of 0.05), "weak" ($0.5 < r < 0.1$) and "strong" ($r \geq 0.5$). A summary of the relative strength of each aspect for each section is shown in Table 4.2. All further discussion will only be about the transport and surface stress modelled by the model.

Overall, in summer (Figure 4.9a, b, and c), it shows a local negative correlation between the surface stress and the transport in the QEI, indicating that the surface stress tends to reduce the transport across the CAA and from the west to the east of the QEI. The exceptions are the Ballantyne and Prince Gustaf Adolf straits where the correlation is mainly positive downstream and upstream in the northern part of the strait only. A local negative correlation is also present west of Baden Island.

The flow towards Parry Channel (Figure 4.9e, i, j, l) and Nares Strait (Figure 4.9p) have a positive correlation, with the exception of M'Clure Strait (Figure 4.9h), Prince Patrick Island - Melville Island Strait (Figure 4.9d), Peel Sound (Figure 4.9k), and Penny Strait (Figure 4.9f). M'Clure Strait presents only a negative correlation upstream and no correlation downstream. Penny Strait has a negative correlation along the strait, while Wellington Channel has no correlation at all. Inside Parry Channel, at West Lancaster Sound (Figure 4.9g), the correlation is positive upstream and negative downstream. Finally, in the south, the correlation at both Amundsen Gulf (Figure 4.9m) and Victoria Strait is negative (Figure 4.9n).

The local negative correlation in the northern QEI, in the southern CAA and at M'Clure Strait can be explained by the direction of the mean surface stress over the CAA (Figure 4.7a). The mean surface stress over the northern QEI is westward because the sea-ice inside of the CAA is packed and has limited mobility. Consequently, the sea ice flows southwards following the mean current. The Ekman transport associated with this motion is directed outside of the CAA (Figure 4.8). This is well shown in the central QEI (Figure 4.9c). The baroclinic gradient however is in the opposite direction, pushing the water into the CAA, such as shown by the volume transport (Figure 4.6a). The surface stress is then directed in the opposed direction to the mean flow. A reduction of the stress will thus increase the flow through the section (less Ekman transport in the opposite direction), hence the negative correlation.

For Parry Channel, the correlations can be explained by the sea-ice concentration (Figure 4.6a) and motion (Figure 4.6c). The straits towards Parry Channel have relatively lower sea-ice concentration and the sea-ice motion is relatively high (~ 5 cm s^{-1}) compared with the other straits in the CAA. The ice is thus flowing southwards toward Parry Channel, leading to the mean flow and Ekman Transport to be almost in the same direction. Thus, the surface stress tends to accelerate the flow. At M'Clure strait, the mean ice motion is along the edge of the CAA coastline. An increase in the surface stress tends to move the ice outside of Parry Channel and pushes the Ekman Transport outside of the CAA. Inside of Parry Channel, the geometry of the straits then controls how ice motion will impact the Ekman transport. At Byam Martin Channel, the opening is relatively large, letting the ice flow to the south. An increase of stress drives more ice and more transport. At Penny Strait and Wellington Channel, an increase of surface stress jams the ice inside of Parry Channel and thus reduces the transport.

West Lancaster Sound is a peculiar case because the flows through this strait are not unidirectional in summer, as shown previously. Consequently, surface stress acting upstream will accelerate the flow due to the Ekman Transport while downstream, it will accelerate the northward flow (i.e., positive correlation), which reduces the mean southward transport as the stress increases (i.e., negative correlation). A similar bi-directional correlation can be found at the Prince of Wales Strait.

On the large scale, changes over the Beaufort Gyre and Northern Baffin Bay are opposed to the changes in the transports over the QEI, with a strong negative correlation at the gates of the QEI from the Arctic Ocean and Lancaster Sound directly towards Baffin Bay. The changes in the surface stress over the northern Baffin Bay do not significantly impact the transport. Over the Beaufort Gyre, the sign of the correlation can be explained by the dynamic of the Beaufort Gyre. The sea surface height of the Beaufort Gyre depends on the accumulation of water due to Ekman Transport. By decreasing the surface stress in this region, we will change the Beaufort Gyre height and thus the baroclinic gradient between the Gyre and Baffin Bay, which will increase the transport through the strait (e.g., Manucharyan and Spall (2016); Manucharyan et al. (2016)).

A positive correlation with the Beaufort Gyre is present in the Prince of Wales Strait (Figure 4.9i) and between Prince Patrick and Melville Islands (Figure 4.9d) with no impact from Baffin Bay. This is explained by the the sign of the transport that is negative towards M'Clure Strait that also changes the sign of the correlation. We note that changes over Baffin Bay are related to the transport only for the strait between Prince Patrick and Melville Islands.

Two exceptions are the Bellantyne and Prince Gustaf Adolf Straits (Figure 4.9a) where only local correlation impact the transport. At Nares Strait (Figure 4.9p) and the Gulf of

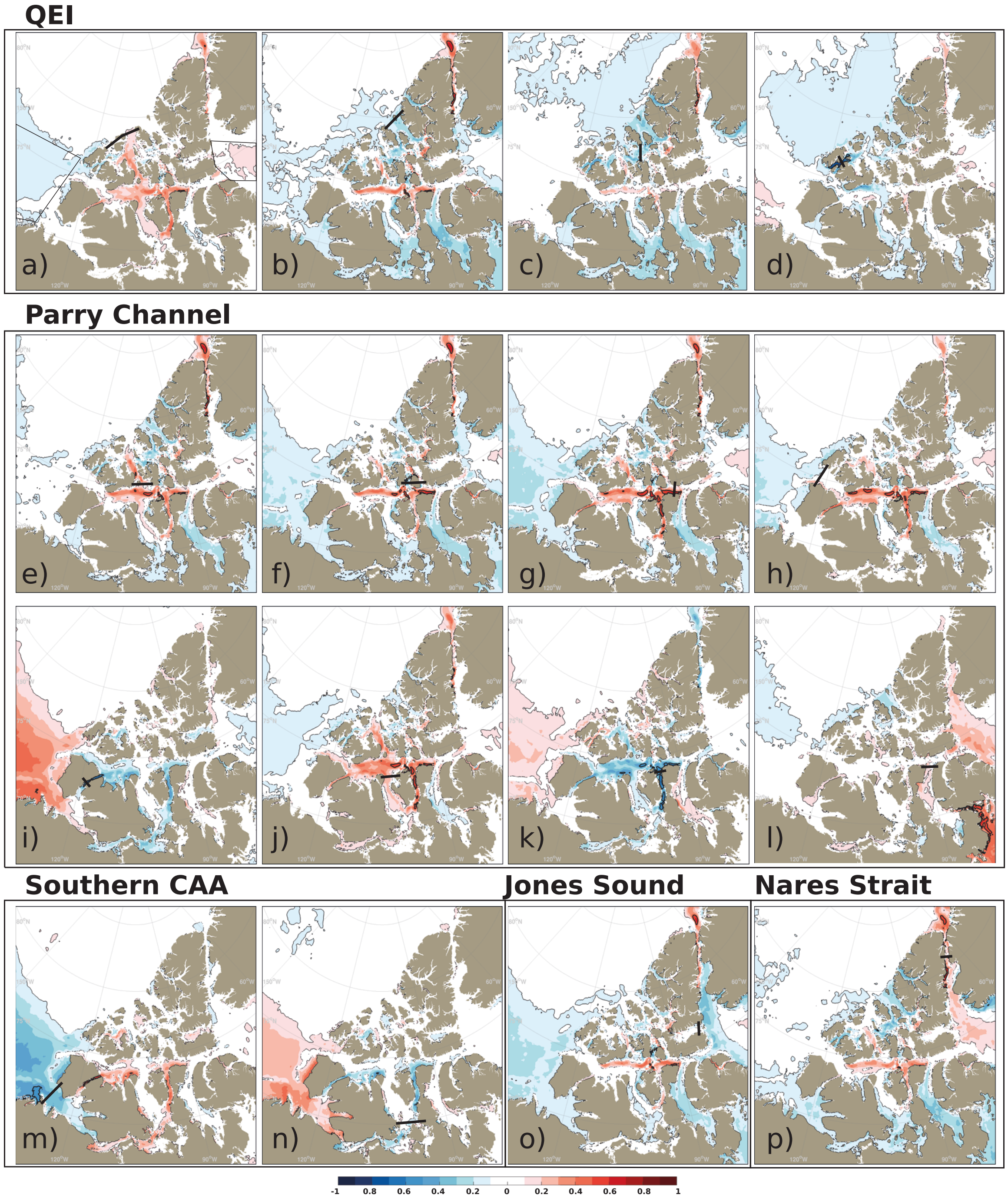

Figure 4.10: Same as figure 4.9 but averaged over winters from 2003 to 2016.

Boothia (Figure 4.9l) only local correlation and correlation over Baffin Bay show a positive correlation with the transport.

In winter (Figure 4.10), the transport is impacted by the surface stress over a larger area for most of the straits. This can be explained by a more compact ice concentration moving more uniformly. Moreover, the correlation is usually stronger showing that the surface stress has a greater importance on the total volume transport in winter (e.g., Nares Strait, M'Clintock Channel, around Peel Sound). This suggests that sea-ice concentration plays a stronger role in the control of transport variability than the wind in summer, which is consistent with a larger transport. We note that, for Nares Strait, these results are consistent with Münchow (2016) who also noticed a larger yearly volume transport when the sea ice is mobile throughout the year and lower when a sea-ice bridge is formed in winter.

The dynamics are modified by the sea ice motion in several straits. At Prince of Wales Strait (Figure 4.10i) the correlation becomes strongly negative, showing that sea-ice decreases the volume transport. This can be explained by the fact that the sea-ice motion decreases along the strait, nearing zero in Parry Channel.

At Byam Martin Channel (Figure 4.10e) the correlation is now strongly positive showing that, in winter, sea-ice motion increases the volume transport. At Penny Channel (Figure 4.10f), the correlation is still negative while it becomes positive at Wellington Channel (Figure 4.10f). The increase in sea-ice velocity east of Barrow Strait permits the sea-ice to flow more freely out of the QEI, thus leading to an increase in the transport.

At Jones Sound (Figure 4.10o), sea-ice cover tends to remove the correlation just at the strait, but the correlation increases in Norwegian Bay. This shows that the dynamics of Jones Sound in winter is not only related to the flow in northern Baffin Bay but is also related to the inflow from the QEI. At M'Clure Strait (Figure 4.10h) the correlation is still negative upstream, but becomes positive over the western part of the strait, showing that sea-ice motion over this region increases the incoming transport in Parry Channel but only in winter. At the entrance of the Gulf of Boothia (Figure 4.10l), the correlation becomes very localized showing that sea-ice does not significantly impact the volume transport in winter. At West Lancaster Sound (Figure 4.10g), the absence of a bi-directional flow modifies the correlation to be only strongly positive: the flow is only impacted by sea-ice motion upstream. Finally, at Victoria Strait the correlation is the opposite compared to summer showing that sea-ice is increasing the volume transport.

4.4.4 Impacts on the seasonal freshwater transport

The freshwater transport and surface stress correlations over most of the straits remain similar to the volume transport for the summer (Figure 4.11) and winter (Figure 4.12). The main difference is that the correlation coefficient increases as well as the area with a significant correlation for most of the sections. This is due to the majority of freshwater

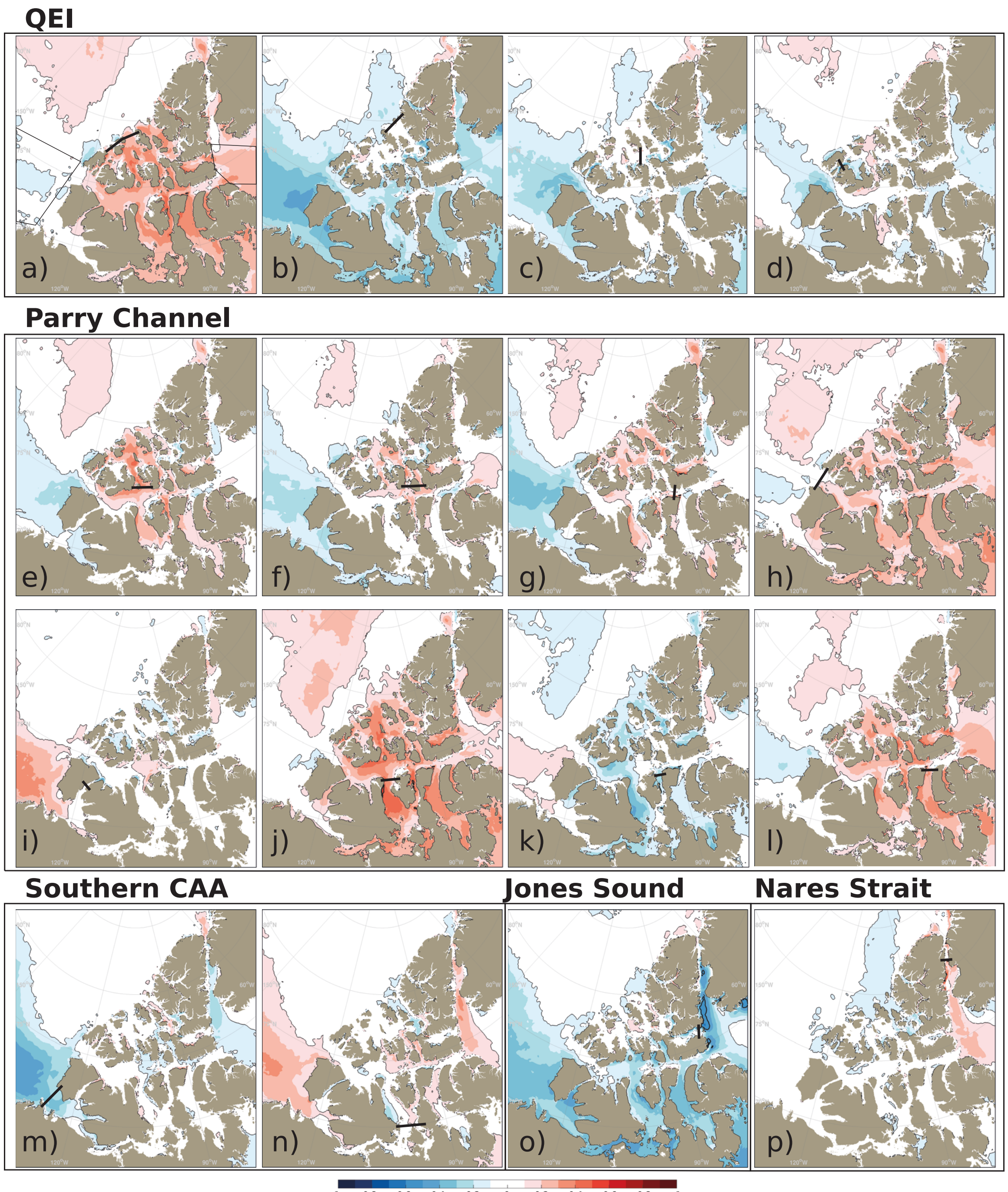

Figure 4.11: Same as figure 4.9 but for freshwater transport.

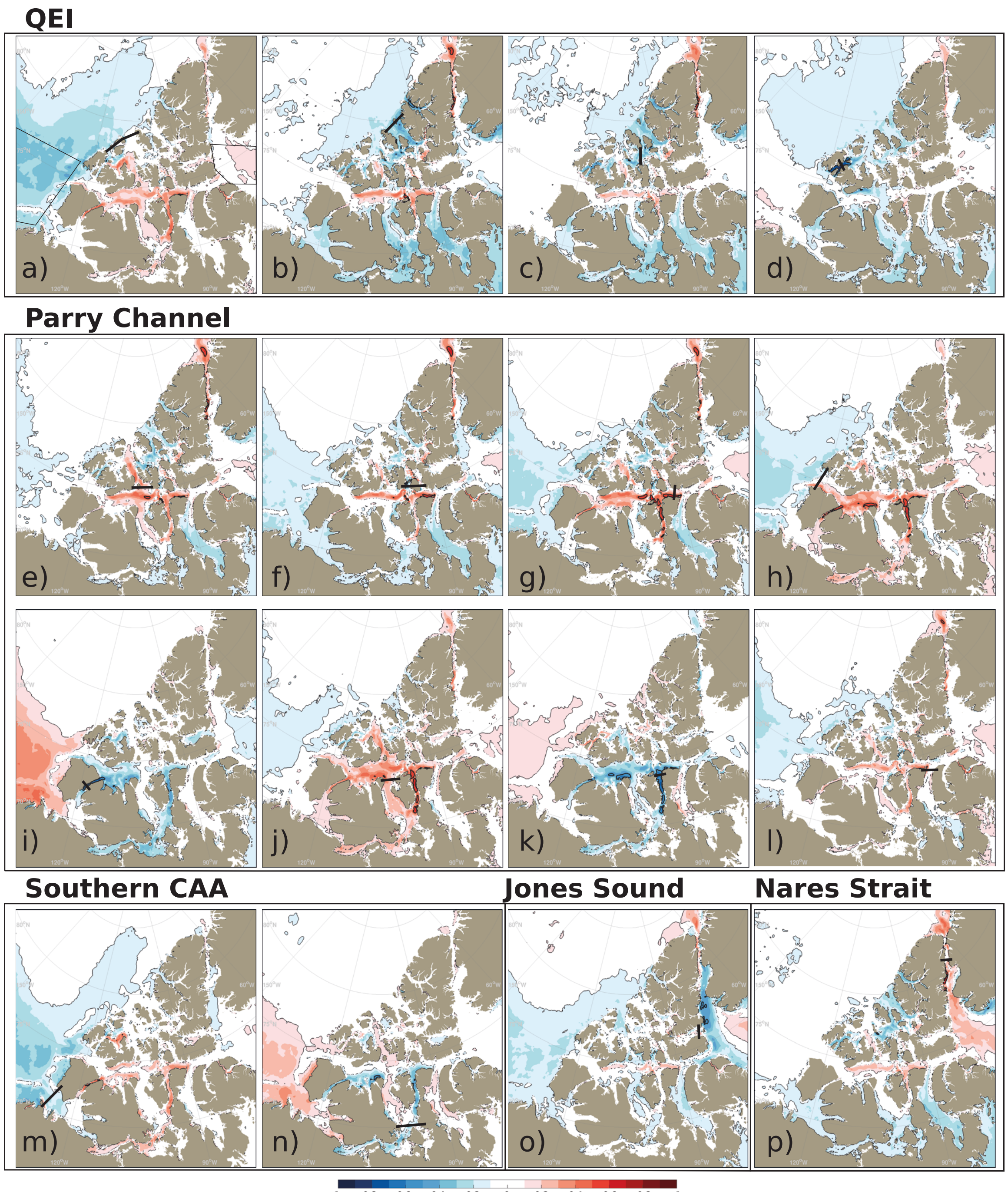

Figure 4.12: Same as figure 4.10 but for freshwater transport.

transport being contained in the upper layer, which makes it proportionally more influenced by the Ekman transport.

However, the dynamics of some straits have changed. In summer, the correlations at Penny Strait and Wellington Channel become positive (Figure 4.11f), while at M'Clure Strait the correlation becomes positive only in the western part of the strait (Figure 4.11h). At Nares Strait, the positive correlation becomes more significant along the strait (Figure 4.11p). This shows that a weak variation in the surface stress might not impact the total transport but the freshwater transport will respond. This is true for the straits where the volume transport is relatively low, compared to the freshwater transport.

In winter, we observe fewer differences in the correlation between the volume and freshwater. The main difference is present at Jones Sound where the correlation is now locally positive (Figure 4.12o). This suggests that sea-ice motion impacts the freshwater transport at Jones Sound in a similar way to what we observe at West Lancaster Sound and Nares Strait.

The positive correlation in western M'Clure Strait is also significantly stronger for the freshwater transport (Figure 4.10h) than for the volume transport (Figure 4.12h). This shows that the sea-ice motion at the entrance of Parry Channel could directly impact the freshwater inflow to the CAA even if the volume transport does not significantly change.

4.5 Conclusion

We analyzed the relative importance of each gate in the CAA for the volume and freshwater transport based upon a high resolution numerical model. The transport across the QEI is about 40% of the transport going through Parry Channel at M'Clure Strait. The main pathway is through the western part of the QEI. The transports going through Amundsen Gulf represents less than 10 % of the total inflow. We also showed the importance of Victoria Strait in the freshwater inflow into Peel Sound.

Detailed comparison with observations have been carried out. At West Lancaster Sound we compared the observations from Peterson et al. (2012) with the model. The model overestimates the transport in winter while the transports in summer are close to observations. At Nares Strait, we compared the model with observations from Münchow (2016). The model represents the transport during the winter and in summer well but is too large during the melting and freezing seasons. In both cases this is due to too mobile sea-ice in the model that drives too much transport. We observe a similar pattern in the freshwater transports with larger overestimations due to the fact that sea ice transport impacts the freshwater transport more than the total volume transport as the surface water contains the lowest salinity.

We then explored the importance of the surface stress on the volume and freshwater transports at the main straits of the CAA in summer and winter. We show the different impacts on the transport: in the QEI the surface stress tends to act in the opposite direction of the transport while in Parry Channel and in the southern part of the CAA the surface stress tends to enhance the oceanic transport. We demonstrate that large scale changes in the surface stress impacts each strait differently, with the QEI being more sensitive to changes over the Beaufort Gyre and northern Baffin Bay than the straits towards Parry Channel and the southern CAA. We also observe the importance of sea ice motion in the transport with a high correlation between the transport and the surface stress in most of the CAA straits. When covered by ice, the local stress becomes more dominant in the transport, mainly over the regions with moving ice. For a few straits (e.g., Barrow Strait, Prince of Wales Strait, M'Clure Strait) the presence of sea ice changes the correlation to enhance the transport instead of being opposed to it.

As a consequence of these findings, the question of what the future transport will be through the CAA arises. If the current downward trend in the ice over the CAA continues (e.g., Howell et al. (2009, 2013); Melling (2002); Sou and Flato (2009); Stroeve et al. (2007)) the CAA should be almost ice free by 2050 (Hu and Myers, 2014). The transition will be slow, with more mobile sea-ice in winter, especially in the QEI. The dynamic shown during the summer months in the current paper will last over a longer time period and the surface stress will increase in winter, due to an increase in sea-ice mobility, leading to more transport, even in winter. Consequently, the variability of the transport will be larger and will depend more on the year round atmospheric circulation.

4.6 Acknowledgments

Processing of the CryoSat-2 is funded by the German Ministry of Economics Affairs and Energy (grant: 50EE1008) and data from 2011 to 2017 obtained from http://www.meereisportal.de (grant: REKLIM-2013-04). The Barrow Strait data from provided by Simon Prinsenberg and the Nares Strait data by Andreas Münchow. This work was funded by NSERC through a Discovery Grant Award [RGPIN 04357], an ENGAGE Grant [EGP 514588-17], as well as the Canadian Arctic Geotraces Program [433848-2012]. The experiments have been ran on a Jasper, a Compute Canada computational cluster. We thank the two anonymous reviewers for their input and the discussion that improved the quality of this paper.

Appendix 4.A: Transports

The volume and freshwater transports are computed from 5-day averaged output from the numerical model as the following:

$$T_{\mathrm{Vol}} = \int_H^0 v \; dAdz \tag{4.1}$$

$$T_{\mathrm{FW}} = \int_H^0 v \left(\frac{S_{\mathrm{ref}} - S}{S_{\mathrm{ref}}} \right) \; dAdz \tag{4.2}$$

where H, v, dA, S_{ref} and S are depth of the water column, the velocity normal to the section, the area of the section, the reference salinity ($S\mathrm{ref} = 34.8$), and the salinity, respectively.

Appendix 4.B: Surface Stress

The total surface stress is defined as :

$$\tau = (1 - i_c)\tau_{\mathrm{wo}} + i_c\tau_{\mathrm{io}} \tag{4.3}$$

where i_c, τ_{io}, and τ_{wo} are the ice concentration, surface stress due to the ice and surface stress due to the wind respectively. Surface stresses are computed with the bulk formulae:

$$\tau_{\mathrm{wo}} = \rho_{\mathrm{a}} C_D \|u_w - u_o\|(u_w - u_o) \tag{4.4}$$

$$\tau_{\mathrm{io}} = \rho_{\mathrm{o}} C_D \|u_i - u_o\|(u_i - u_o) \tag{4.5}$$

where ρ_{a}, C_D, u_w, u_o, ρ_{o}, and u_i are the reference density of the air, a roughtness coefficient, the 10 m wind velocity, the first layer ocean velocity, the reference density of the ocean and the sea-ice velocity acccordingly. The surface stress is computed individually for the u and v component of the velocity (τ_x and τ_y, respectively). We note that C_D is computed by the model for the wind-ocean stress and set to $C_D = 5 \times 10^{-3}$ for the ice-ocean interaction.

Appendix 4.C: Ekman Depth and Ekman Transport

The Ekman Depth, i.e. the depth where the Ekman Transport will be effective is defined as:

$$Ek_{\mathrm{d}} = 0.70 * \left(\frac{1}{f} \sqrt{\frac{\overline{\tau_m}}{\rho}} \right) \tag{4.6}$$

where 0.70 is a transfer function given by (Large et al., 1994), f is the Coriolis parameter, $\overline{\tau_m}$ is the magnitude of the surface stress (see Appendix D) and $\rho = 1035$ kg m^3 is the reference density used in the numerical model for this experiment.

The Ekman Transport is defined as:

$$T^x_{\mathrm{Ek}} = \frac{1}{\rho f}\tau_y dy \tag{4.7}$$

$$T^y_{\mathrm{Ek}} = -\frac{1}{\rho f}\tau_x dx \tag{4.8}$$

where $\tau_{surface}$ is the surface stress, dy the grid size in the y direction, and dx the grid size in the x direction. The superscripts x and y denote the direction of the transport and the stress.

Appendix 4.D: Correlation between the surface stress and the transport

The correlation is computed from the magnitude of the surface stress and the integrated volume (freshwater) transport at each point of the domain. The magnitude of the surface stress is defined as:

$$\overline{\tau_m} = \sqrt{\tau_x^2 + \tau_y^2} \tag{4.9}$$

where τ_x and τ_y are the total surface stress in the x and y direction, respectively, as described in Appendix B.

The correlation coefficient is thus computed as:

$$r(\tau_m, T) = \frac{1}{N-1}\sum_{N=1}^{N}\left(\frac{\overline{\tau_{mi} - \mu_{\tau m}}}{\sigma_{\tau m}}\right)\left(\frac{\overline{T_i - \mu_T}}{\sigma_T}\right) \tag{4.10}$$

where τ_m is the linearly detrended surface stress magnitude, T the linearly detendred transport. μ and σ are the mean and standard deviation of τ_m and T, respectively. This is performed at each grid point individually.

Both the magnitude of the surface stress and the integrated transport are detrended to remove all influence of the slow drift that is common to most regional numerical models. The purpose of this study is to analyze how the sea-ice dynamics impacts the transport. Consequently, using the magnitude of the stress instead of the individual direction gives a more direct indication by showing if the surface stress increase or decrease the integrated transport through each considered gate. No other modification on the signals has been performed to ensure that the correlation captures the fast variability in both the transport and magnitude of the surface stress.

Bibliography

Amante, C. and Eakins, B. (2009). ETOPO1 1 arc-minute global relief model: Procedures, data sources and analysis. *NOAA Technical Memorandum NESDIS NGDC-24*.

Bamber, J., van den Broeke, M., Ettema, J., Lenaerts, J., and Rignot, E. (2012). Recent large increases in freshwater fluxes from greenland into the north atlantic. *Geophysical Research Letters*, 39(19):n/a–n/a.

Blanke, B. and Delecluse, P. (1993). Variability of the Tropical Atlantic Ocean simulated by a general circulation model with two different mixed-layer physics. *Journal of Physical Oceanography*, 23(7):1363–1388.

Castro de la Guardia, L., Hu, X., and Myers, P. G. (2015). Potential positive feedback between greenland ice sheet melt and Baffin Bay heat content on the west Greenland shelf. *Geophysical Research Letters*, 42(12):4922–4930. 2015GL064626.

Comiso, J. C. (2000, updated 2015). Bootstrap sea ice concentration from Nimbus-7 SMMR and DMSP SSM/I, version 2 [2002 - 2016]. *NASA DAAC at National Snow and Ice Data Centre, Boulder, CO.*

Comiso, J. C. (2012). Large decadal decline of the Arctic multiyear ice cover. *Journal of Climate*, 25(4):1176–1193.

Comiso, J. C., Meier, W. N., and Gersten, R. (2017). Variability and trends in the Arctic sea ice cover: Results from different techniques. *Journal of Geophysical Research: Oceans*, 122(8):6883–6900.

Cuny, J., Rhines, P. B., and Kwok, R. (2005). Davis Strait volume, freshwater and heat fluxes. *Deep Sea Research Part I: Oceanographic Research Papers*, 52(3):519–542.

Curry, B., Lee, C. M., and Petrie, B. (2011). Volume, freshwater, and heat fluxes through Davis Strait, 2004–05*. *Journal of Physical Oceanography*, 41(3):429–436.

Curry, B., Lee, C. M., Petrie, B., Moritz, R. E., and Kwok, R. (2014). Multiyear volume, liquid freshwater, and sea ice transports through Davis Strait, 2004–10*. *Journal of Physical Oceanography*, 44(4):1244–1266.

Dai, A., Qian, T., Trenberth, K. E., and Milliman, J. D. (2009). Changes in continental freshwater discharge from 1948 to 2004. *Journal of Climate*, 22(10):2773–2792.

Galley, R. J., Else, B. G., Howell, S. E., Lukovich, J. V., and Barber, D. G. (2012). Landfast sea ice conditions in the Canadian Arctic: 1983 – 2009. *ARCTIC*, 65(2).

Grivault, N., Hu, X., and Myers, P. G. (2017). Evolution of Baffin Bay water masses and transports in a numerical sensitivity experiment under enhanced greenland melt. *Atmosphere-Ocean*, 55(3):169–194.

Haas, C. and Howell, S. E. L. (2015). Ice thickness in the Northwest Passage. *Geophysical Research Letters*, 42(18):7673–7680.

Hannah, C. G., Dupont, F., and Dunphy, M. (2009). Polynyas and tidal currents in the Canadian Arctic Archipelago. *ARCTIC*, 62(1).

Houssais, M.-N. and Herbaut, C. (2011). Atmospheric forcing on the Canadian Arctic Archipelago freshwater outflow and implications for the Labrador Sea variability. *Journal of Geophysical Research*, 116.

Howell, S. E. L., Duguay, C. R., and Markus, T. (2009). Sea ice conditions and melt season duration variability within the Canadian Arctic Archipelago: 1979–2008. *Geophysical Research Letters*, 36(10).

Howell, S. E. L., Laliberté, F., Kwok, R., Derksen, C., and King, J. (2016). Landfast ice thickness in the Canadian Arctic Archipelago from observations and models. *The Cryosphere*, 10(4):1463–1475.

Howell, S. E. L., Wohlleben, T., Dabboor, M., Derksen, C., Komarov, A., and Pizzolato, L. (2013). Recent changes in the exchange of sea ice between the Arctic Ocean and the Canadian Arctic Archipelago. *Journal of Geophysical Research: Oceans*, 118(7):3595–3607.

Hu, X. and Myers, P. G. (2014). Changes to the Canadian Arctic Archipelago sea ice and freshwater fluxes in the twenty-first century under the Intergovernmental Panel on Climate Change A1B climate scenario. *Atmosphere-Ocean*, 52(4):331–350.

Hu, X., Sun, J., Chan, T. O., and Myers, P. G. (2018). Thermodynamic and dynamic ice thickness contributions in the Canadian Arctic Archipelago in NEMO-LIM2 numerical simulations. *The Cryosphere*, 12(4):1233–1247.

Hughes, K. G., Klymak, J. M., Hu, X., and Myers, P. G. (2017). Water mass modification and mixing rates in a 1/12° simulation of the canadian arctic archipelago. *Journal of Geophysical Research: Oceans*, 122(2):803–820.

Hunke, E. C. (2001). Viscous–plastic sea ice dynamics with the EVP model: Linearization issues. *Journal of Computational Physics*, 170(1):18–38.

Jahn, A., Tremblay, B., Mysak, L. A., and Newton, R. (2009). Effect of the large-scale atmospheric circulation on the variability of the Arctic Ocean freshwater export. *Climate Dynamics*, 34(2-3):201–222.

Kliem, N. and Greenberg, D. A. (2003). Diagnostic simulations of the summer circulation in the Canadian arctic archipelago. *Atmosphere-Ocean*, 41(4):273–289.

Kwok, R. and Rothrock, D. A. (2009). Decline in Arctic sea ice thickness from submarine and ICESat records: 1958-2008. *Geophysical Research Letters*, 36(15):n/a–n/a.

Large, W. G., McWilliams, J. C., and Doney, S. C. (1994). Oceanic vertical mixing: A review and a model with a nonlocal boundary layer parameterization. *Reviews of Geophysics*, 32(4):363.

Lemieux, J.-F., Dupont, F., Blain, P., Roy, F., Smith, G. C., and Flato, G. M. (2016). Improving the simulation of landfast ice by combining tensile strength and a parameterization for grounded ridges. *Journal of Geophysical Research: Oceans*, 121(10):7354–7368.

Lindsay, R. and Schweiger, A. J. (2013, updated 2017). Unified sea ice thickness climate data record, 1947 onward, version 1. [ICESat1-G and CryoSat-AWI]. *Boulder, Colorado USA. NSIDC: National Snow and Ice Data Center.*

Lu, Y., Higginson, S., Nudds, S., Prinsenberg, S., and Garric, G. (2014). Model simulated volume fluxes through the Canadian Arctic Archipelago and Davis Strait: Linking monthly variations to forcing in different seasons. *Journal of Geophysical Research: Oceans*, 119(3):1927–1942.

Madec, G. (2008). Nemo ocean engine. *Note du Pole de modelisation*, 27:1288–1619.

Madec, G., Delecluse, P., Imbard, M., and Levy, C. (1998). OPA 8 ocean general circulation model - reference manual. Technical report, LODYC/IPSL Note 11.

Manucharyan, G. E. and Spall, M. A. (2016). Wind-driven freshwater buildup and release in the Beaufort Gyre constrained by mesoscale eddies. *Geophysical Research Letters*, 43(1):273–282.

Manucharyan, G. E., Spall, M. A., and Thompson, A. F. (2016). A theory of the wind-driven Beaufort Gyre variability. *Journal of Physical Oceanography*, 46(11):3263–3278.

Masina, S., Storto, A., Ferry, N., Valdivieso, M., Haines, K., Balmaseda, M., Zuo, H., Drevillon, M., and Parent, L. (2015). An ensemble of eddy-permitting global ocean reanalyses from the MyOcean project. *Climate Dynamics*, pages 1–29.

McGeehan, T. and Maslowski, W. (2012). Evaluation and control mechanisms of volume and freshwater export through the Canadian Arctic Archipelago in a high-resolution pan-Arctic ice-ocean model. *Journal of Geophysical Research: Oceans*, 117(C8):n/a–n/a.

Melling, H. (2002). Sea ice of the northern Canadian Arctic Archipelago. *Journal of Geophysical Research*, 107(C11).

Melling, H., Agnew, T. A., Falkner, K. K., Greenberg, D. A., Lee, C. M., Münchow, A., Petrie, B., Prinsenberg, S. J., Samelson, R. M., and Woodgate, R. A. (2008). *Fresh-Water Fluxes via Pacific and Arctic Outflows Across the Canadian Polar Shelf*, pages 193–247. Springer Netherlands.

Münchow, A. (2016). Volume and freshwater flux observations from Nares Strait to the west of Greenland at daily time scales from 2003 to 2009. *Journal of Physical Oceanography*, 46(1):141–157.

Münchow, A. and Melling, H. (2008). Ocean current observations from Nares Strait to the west of Greenland: Interannual to tidal variability and forcing. *Journal of Marine Research*, 66(6):801–833.

Parkinson, C. L. and Cavalieri, D. J. (2008). Arctic sea ice variability and trends, 1979–2006. *Journal of Geophysical Research: Oceans*, 113(C7):n/a–n/a. C07003.

Parkinson, C. L. and Comiso, J. C. (2013). On the 2012 record low Arctic sea ice cover: Combined impact of preconditioning and an august storm. *Geophysical Research Letters*, 40(7):1356–1361.

Peterson, I., Hamilton, J., Prinsenberg, S., and Pettipas, R. (2012). Wind-forcing of volume transport through Lancaster Sound. *Journal of Geophysical Research: Oceans*, 117(C11):n/a–n/a.

Prinsenberg, S. and Bennett, E. (1987). Mixing and transports in Barrow Strait, the central part of the Northwest passage. *Continental Shelf Research*, 7(8):913–935.

Prinsenberg, S., Hamilton, J., Peterson, I., and Pettipas, R. (2009). Observing and interpreting the seasonal variability of the oceanographic fluxes passing through Lancaster Sound of the Canadian Arctic Archipelago. In *Influence of Climate Change on the Changing Arctic and Sub-Arctic Conditions*, pages 125–143. Springer Netherlands.

Ryan, P. A. and Münchow, A. (2017). Sea ice draft observations in Nares Strait from 2003 to 2012. *Journal of Geophysical Research: Oceans*, 122(4):3057–3080.

Shroyer, E. L., Samelson, R. M., Padman, L., and Münchow, A. (2015). Modeled ocean circulation in Nares Strait and its dependence on landfast-ice cover. *Journal of Geophysical Research: Oceans*, 120(12):7934–7959.

Smith, G. C., Roy, F., Mann, P., Dupont, F., Brasnett, B., Lemieux, J.-F., Laroche, S., and Bélair, S. (2014). A new atmospheric dataset for forcing ice-ocean models: Evaluation of reforecasts using the Canadian global deterministic prediction system. *Quarterly Journal of the Royal Meteorological Society*, 140(680):881–894.

Sou, T. and Flato, G. (2009). Sea ice in the Canadian Arctic Archipelago: Modeling the past (1950–2004) and the future (2041–60). *Journal of Climate*, 22(8):2181–2198.

Spence, C. and Burke, A. (2008). Estimates of Canadian Arctic Archipelago runoff from observed hydrometric data. *Journal of Hydrology*, 362(3-4):247–259.

Stroeve, J., Holland, M. M., Meier, W., Scambos, T., and Serreze, M. (2007). Arctic sea ice decline: Faster than forecast. *Geophysical Research Letters*, 34(9).

Tang, C. C., Ross, C. K., Yao, T., Petrie, B., DeTracey, B. M., and Dunlap, E. (2004). The circulation, water masses and sea-ice of Baffin Bay. *Progress in Oceanography*, 63(4):183–228.

Vancoppenolle, M., Fichefet, T., Goosse, H., Bouillon, S., Madec, G., and Maqueda, M. A. M. (2009). Simulating the mass balance and salinity of Arctic and Antarctic sea ice. 1. model description and validation. *Ocean Modelling*, 27(1–2):33–53.

Wang, Q., Myers, P. G., Hu, X., and Bush, A. B. (2012). Flow constraints on pathways through the Canadian Arctic Archipelago. *Atmosphere-Ocean*, 50(3):373–385.

Wang, Z., Hamilton, J., and Su, J. (2017). Variations in freshwater pathways from the Arctic Ocean into the North Atlantic Ocean. *Progress in Oceanography*, 155:54–73.

Wekerle, C., Wang, Q., Danilov, S., Jung, T., and Schröter, J. (2013). The Canadian Arctic Archipelago throughflow in a multiresolution global model: Model assessment and the driving mechanism of interannual variability. *Journal of Geophysical Research: Oceans*, 118(9):4525–4541.

Yang, Q., Dixon, T. H., Myers, P. G., Bonin, J., Chambers, D., and van den Broeke, M. R. (2016). Recent increases in Arctic freshwater flux affects Labrador Sea convection and Atlantic overturning circulation. *Nature Communications*, 7:10525.

Zhang, Y., Chen, C., Beardsley, R. C., Gao, G., Lai, Z., Curry, B., Lee, C. M., Lin, H., Qi, J., and Xu, Q. (2016). Studies of the Canadian Arctic Archipelago water transport and its relationship to basin-local forcings: Results from AO-FVCOM. *Journal of Geophysical Research: Oceans*, 121(6):4392–4415.

Chapter 5

Timescales associated with flux variability of the Arctic Ocean Gateways

5.1 Introduction

The Arctic Ocean is one of the main oceanic reservoirs of freshwater. Early estimates evaluated the Arctic freshwater content (FWC) between 1979 and 2001 at about 80000 km^3, relative to a salinity of 34.8. The majority of this FWC is contained inside the Beaufort Gyre (Proshutinsky et al., 2009; Serreze et al., 2006; Wang et al., 2016). More recent estimates, evaluated this amount to be 93000 km^3, while including the Canadian Arctic Archipelago (CAA) and Baffin Bay (Haine et al., 2015). Since the 2000s, the FWC in the Arctic increased by about 10%, with an acceleration after 2005 and a stabilization after 2009 (Carmack et al., 2016; Haine et al., 2015; McPhee et al., 2009).

The origin of this freshwater has been evaluated over the period 1979-2001 (Serreze et al., 2006). It is split between runoff (38%), evaporation minus precipitation (E-P, 24%) and Bering Strait inflow (30%). Export to the North Atlantic is mainly driven by ocean transports through Fram Strait (26% in liquid, 25% in solid) and through the Canadian Arctic Archipelago (35% mainly liquid). During the first decade of the 2000s, Carmack et al. (2016) noticed significant changes in the freshwater budget, with an increase of 30% of the runoff, 10% of the E-P, 6% of Bering Strait inflow and 4% of the flux at Fram Strait (liquid part only). In return, the Fram Strait sea-ice export reduced by 17%.

The freshwater in the Arctic is mainly localized in the upper layer of the ocean. Consequently, it makes it sensitive to changes in the wind-driven circulation. The atmospheric pattern over the Arctic reacts to the sea-level pressure that is usually low in the Barents Sea and high in the Eurasian Basin (Serreze and Barrett, 2011). The sea-level pressure variability (i.e., the amplitude) between the central and the Eurasian Arctic, and the Nordic Seas exceeds the variability in the west Arctic (Morison et al., 2012). The Arctic Oscillation (Thompson and Wallace, 1998) describes the relative strength of each component, or, from a larger point of view, the strength of the polar vortex relative to the mid-latitude, translated into an index: the Arctic Oscillation Index.

Two main atmospheric patterns are present in the Arctic, namely, the positive and negative phase of the Arctic Oscillation. When the sea-level atmospheric pressure is high over the Beaufort Gyre and weak in the Eurasian Arctic, the winds are anticyclonic, increasing the strength of the gyre and the transpolar drift, and is defined as the negative phase. Conversely, during a positive phase, the weak Beaufort permits the Pacific derived water to penetrate more in the Arctic, eventually being caught by a weaker transpolar drift. Pacific water is also now observed to leave through the Canadian Arctic Archipelago (Hu and Myers, 2013).

The Arctic Oscillation plays an important role in the freshwater content of the Beaufort Gyre. The strong anticyclonic winds over the Beaufort Gyre that occur during the positive phase lead to a strong convergence of Ekman pumping, increasing the freshwater storage in the gyre (Manucharyan et al., 2016; Proshutinsky et al., 2002; Yang, 2009), increasing the strength of the transpolar drift and making it fresher, due to more Pacific water being trapped in the Beaufort Gyre. The opposite happens during the positive phase, with weak freshwater storage in the Beaufort Gyre, and Pacific water is released to the transpolar drift (Proshutinsky et al., 2002). Moreover, the transport through the Canadian Arctic Archipelago is larger and the runoff from Eurasia can more freely penetrate into the Arctic Ocean during the positive phase (Proshutinsky et al., 2002).

The redistribution, accumulation and residence time of the freshwater in the Arctic is a key component of the climate system. Indeed, the freshwater leaving the Arctic will eventually reach the Labrador Sea, a region where deep convection occurs. This process consists of the subduction of the upper layer into the deep ocean, trapping at the same time carbon dioxide as well as mixing nutrients and oxygen. One of the prerequisites for deep convection is to have strong heat loss from the surface in order to increase the density of the surface water (Straneo, 2006). The lateral fluxes, i.e. eddies shed from the West Greenland Currents and the Arctic outflow, also play a role in the stability of the Labrador Sea and the strength of the winter subduction (Straneo, 2006). It has been shown in the past that increasing the freshwater content of the Labrador Sea has the potential to impact the deep water formation (e.g., Jahn and Holland (2013); Yang et al. (2016)). The most dramatic examples occur after the Great Salinity Anomaly. This phenomenon, which occurred several time over the last few decades, consists of an abnormal export of freshwater out of the Arctic Ocean (Belkin et al., 1998), which has been reported to be the cause of the shut down of deep convection in the Labrador Sea in the past (Gelderoos et al., 2012).

Only a few long term flux measurements are available for the Arctic gateways. On the Canadian side of the Arctic, moorings are available at Nares Strait from 2003 to 2006 and from 2007 to 2009 (Münchow, 2016; Münchow and Melling, 2008). The initial estimates (2003-2006) evaluated the volume flux through this strait at 0.57 ± 0.09 Sv, noticing an increase of 20 ± 10 % below 30 m (Münchow and Melling, 2008). These numbers have been reevaluated to range from 0.71 ± 0.09 to 1.03 ± 0.11 Sv after the dataset was expanded to 2009. A similar reevaluation of the mean transport has been done at West Lancaster Sound and Davis Strait. At West Lancaster Sound, the mean transport from 1998 to 2006 was evaluated to 0.70 ± 0.30 Sv by Prinsenberg et al. (2009) and then reduced to 0.46 ± 0.09 Sv after the mooring record was extended to 2010 (Peterson et al., 2012). We note that this later number is closer to an initial measurement performed in the late 80s of 0.51 Sv (Prinsenberg and Bennett, 1989). All these numbers are within the variability of the instantaneous transport; 0 to 1.3 Sv based on the season (Prinsenberg et al., 2009). At Davis Strait, the initial estimate from 2004 to 2005 measured a mean outflow of about 2.3 ± 0.7 Sv (Curry et al., 2011), which was reduced to 1.6 ± 0.5 Sv based on extended data covering 2004 to 2010 (Curry et al., 2014). A similar pattern of reevaluation is shown at Fram Strait, however the major modification of the arrays between each measurement period prevent us to separate what part of these changes is related to changes in the outflow and what is related to the modification in the measurement array (Rabe et al., 2013).

This constant reevaluation of the flows at the gates of the Arctic based on different time periods clearly shows that long term measurements are primordial in order to quantify Arctic outflows and their variability. Previous studies also pinpointed the large variations in the outflow estimates from observations and models (e.g., Carmack et al. (2016); Haine et al. (2015); Jahn and Holland (2013); Lique et al. (2016); Wang et al. (2016)). It is thus crucial that observations are in place for a long enough time period to ensure that they capture all relevant timescales associated with the gateways, and the budget of the Arctic Ocean. Correlations between the AO and each component of the freshwater budget in the Arctic has been made, but at this time it is not clear what are the frequencies of the events leaving the Arctic. In the present paper, we propose to use a state-of-the-art numerical model to perform this frequency analysis and identify what are the time scales of the variability of the volume and freshwater outflow leaving the Arctic.

5.2 Method

We use the Nucleus for European Modeling of the Ocean (NEMO) numerical framework, version 3.4. This framework couples a three-dimensional, free surface, hydraostatic, primitive equation component ocean model and a dynamic-thermodynamic sea-ice model (Madec, 2008). The sea-ice model is the Louvain-la-Neuve sea ice model (LIM2) (Vancoppenolle et al., 2009) with a modified elastic-viscous-plastic (EVP) ice rheology (Hunke, 2001). The TKE closure system is used to parametrize turbulence (Blanke and Delecluse, 1993; Madec et al., 1998). The model time step is 1080 seconds. The model does not include the effect of tides.

We use a 1/12°(ANHA12) and 1/4°(ANHA4) configuration of the Arctic and Northern Hemisphere Atlantic model. The experiment using ANHA12 is called HIGH RESOLUTION, while the experiment using ANHA4 is called MIROC. The boundaries are in

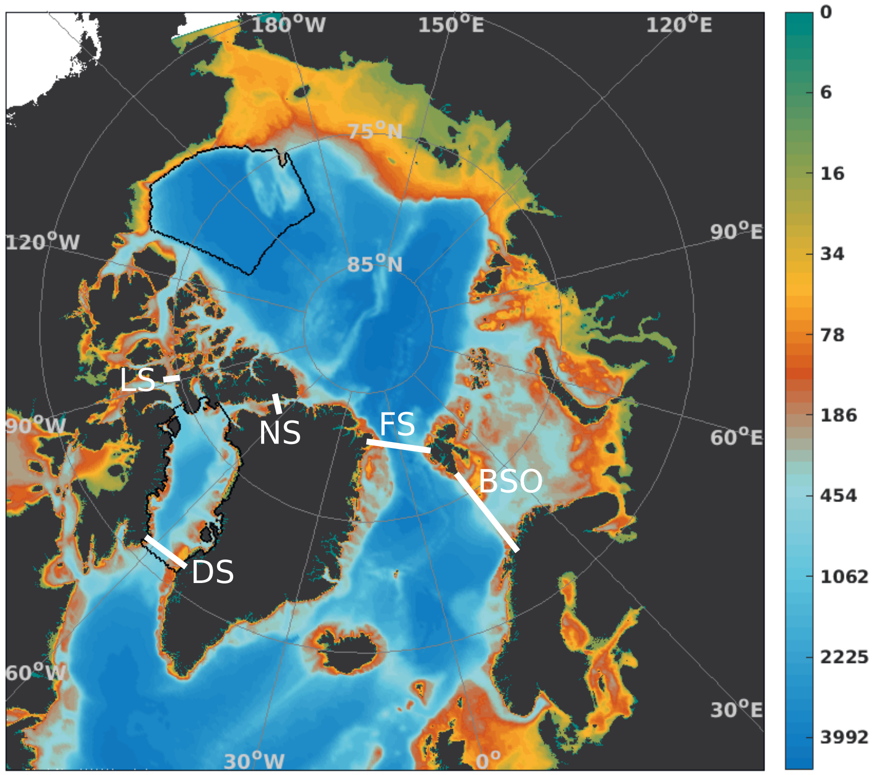

Figure 5.1: Map of the Arctic. The white lines represents the locations of the analyzed section out of the Arctic. LS: Lancaster Sound, DS: Davis Strait, NS: Nares Strait, FS: Fram Strait, BSO: Barents Sea Opening. The colormap indicates the model domain bathymetry in meters. Baffin Bay and Beaufort Gyre regions are shown by black contour.

the Bering Sea and in the Atlantic at 20°S. These boundaries are forced with data from the GLobal Ocean ReanalYSis 2 version 3 (GLORYS2v3; Masina et al. (2015)) for HIGH RESOLUTION and data from a global numerical experiment (ORCA025-K3415, from the Helmholtz Center for Ocean Research Kiel) for MIROC. Both versions possess 50 vertical layers, with a thickness increasing with depth. The bathymetry in the Arctic is derived from the 1 minute-arc global relief model of Earth's surface ETOPO1 (Amante and Eakins, 2009). 10 m winds, temperature and specific humidity, as well as short and long wave radiative fluxes are taken from the high temporal and spatial resolution atmospheric forcing from the Canadian Meteorological Centre's (CMC) Global Deterministic Prediction System (GDPS) ReForcasts (CGRF) (Smith et al., 2014) for HIGH RESOLUTION and from the climate model MIROC5 (Watanabe et al., 2010) for MIROC. Both datasets are used via bulk formulae (Large and Yeager, 2004). The model is initialized with ocean temperature, salinity and horizontal velocities from climatology field provided the Polar science center Hydrographic Climatology, version 3 (PHC3, Steele et al. (2001)).

Runoff is based on the inter-annual monthly 1°× 1° river discharge data from Dai et al. (2009), as well as Greenland meltwater (5 km × 5 km), provided by Bamber et al. (2012), and is carefully (volume conserved) remapped onto the model grid. Only the liquid part of the runoff is used. The river runoff dataset finishes in 2007 while the Greenland runoff finishes in 2010. After each date the previous year is repeated until the end of the experiment. The numerical experiment starts in January 1970 and finishes in December 2013. No restoring has been applied on any field. The output fields are averaged over 5-days.

The observations shown at Nares Strait are described in Münchow and Melling (2008) and Münchow (2016), and cover two periods from August 2004 to August 2005 and from August 2007 to August 2009. At West Lancaster Sound, the observations are described in Prinsenberg et al. (2009) and Peterson et al. (2012) and cover one period from August 1998 to August 2010. At Davis Strait, the observations are described in Curry et al. (2011) and Curry et al. (2014) and cover one period from 2004 to 2015 (described up to 2010 in the previous papers). The effect of tides on the transport have been removed from all datasets.

The power spectral density is computed by applying the Fast Fourier Transform on the detendred filtered volume and freshwater anomaly transports. We used a Hamming Filter with a total width of 5 (i.e., 30 days). This filtering is performed in order to filter out the short time scales on our transport series. This study is focused on changes over an extended time period. The relatively coarse (both temporal and spatial) resolution from the atmospheric forcing induces that the model response at short time scales (i.e. less than a month) is considered as noise and thus removed from the dataset. The frequency is computed using the whole available dataset, i.e., 3139 individual points. The section used to compute the transports and power spectral density are shown in Figure 5.1. The Sea Surface Height (SSH) gradient between the Beaufort Gyre and Baffin Bay has been calculated by averaging the SSH over the two regions highlighted in Figure 5.1

5.3 Results

5.3.1 Temporal domain

HIGH RESOLUTION has at Davis Strait an average volume (freshwater) transport of 1.32 Sv (81 mSv), which compares well with 1.63 Sv (94 mSv) from the observations (Cuny et al., 2005; Curry et al., 2014) (Figure 5.2a). The correlation with the observations is relatively high, with $r = 0.41$ ($r = 0.32$) for the volume (freshwater) transport. A more detailed evaluation of the quality of simulated Canadian Arctic Archipelago throughflow from this experiment is discussed in Chapter 4. The computational cost and the time needed to run a 50 years experiment with 1/12° resolution is prohibitive for our group. Thus in the rest of this paper we will use 1/4° resolution, which has results comparable to the 1/12° experiment for the present day. We note that 1/4 ° is a resolution close to the one used by recent climate models (Randall et al., 2007).

The transports from MIROC are shown in the Figure 5.2b to 5.2g. A summary of the

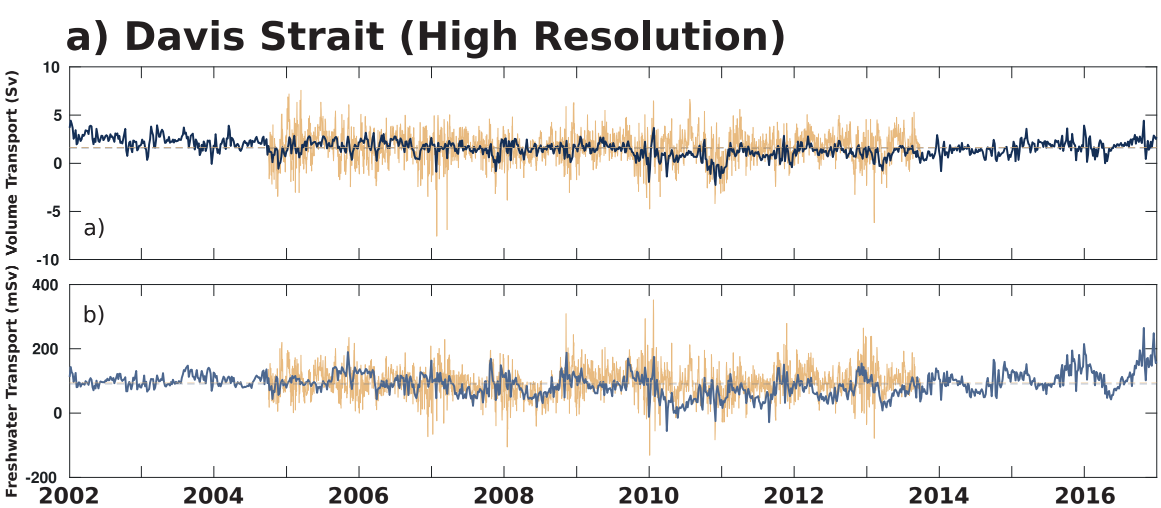

Figure 5.2: Volume (dark blue line) and freshwater (light blue line) transport for each considered section. The available observations are shown with orange lines. The dashed lines corresponds to the average over the whole available period.

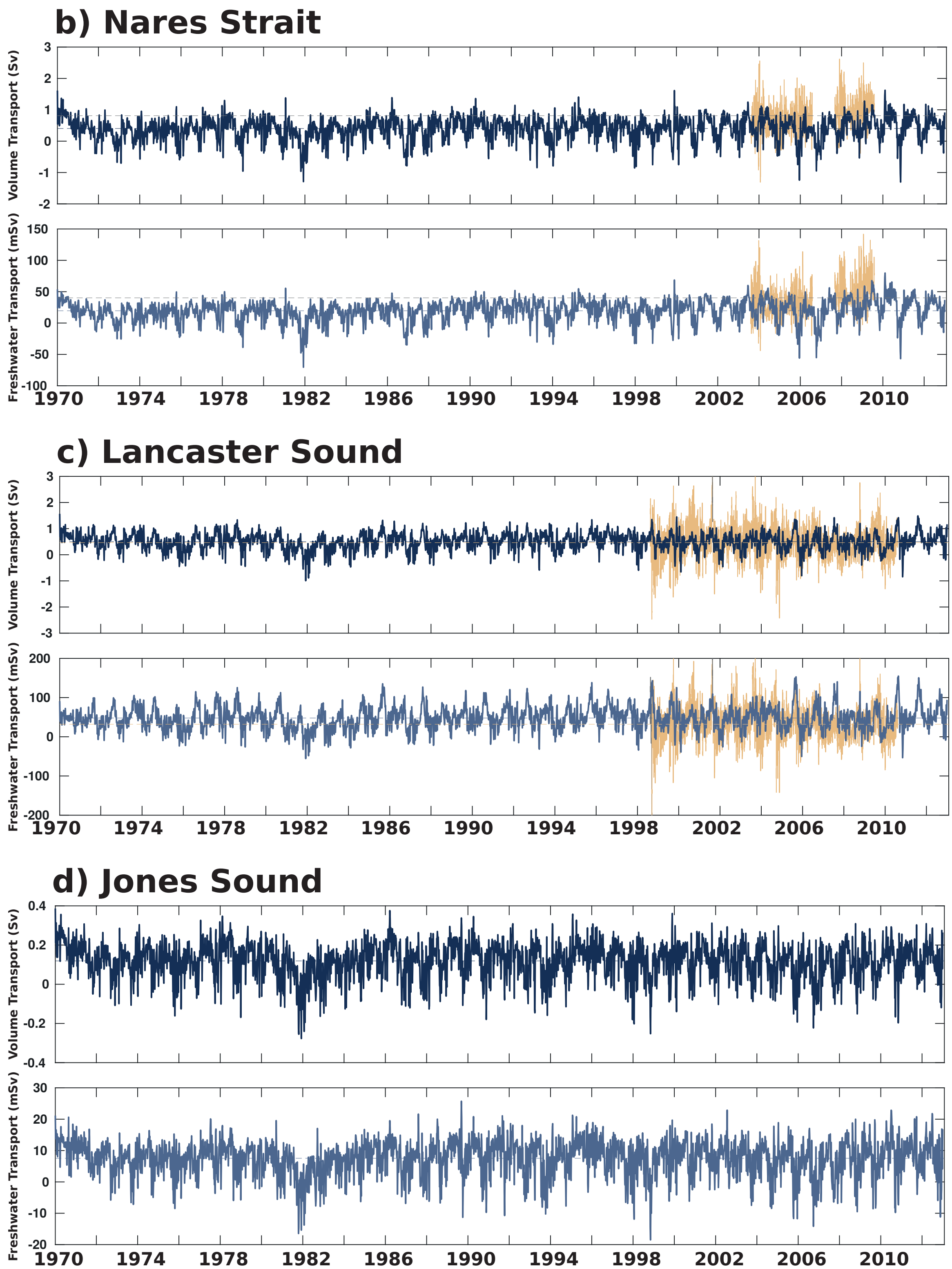
b) Nares Strait
Volume Transport (Sv)
Freshwater Transport (mSv)
c) Lancaster Sound
Volume Transport (Sv)
Freshwater Transport (mSv)
d) Jones Sound
Volume Transport (Sv)
Freshwater Transport (mSv)
1970
1974
1978
1982
1986
1990
1994
1998
2002
2006
2010

Figure 5.2

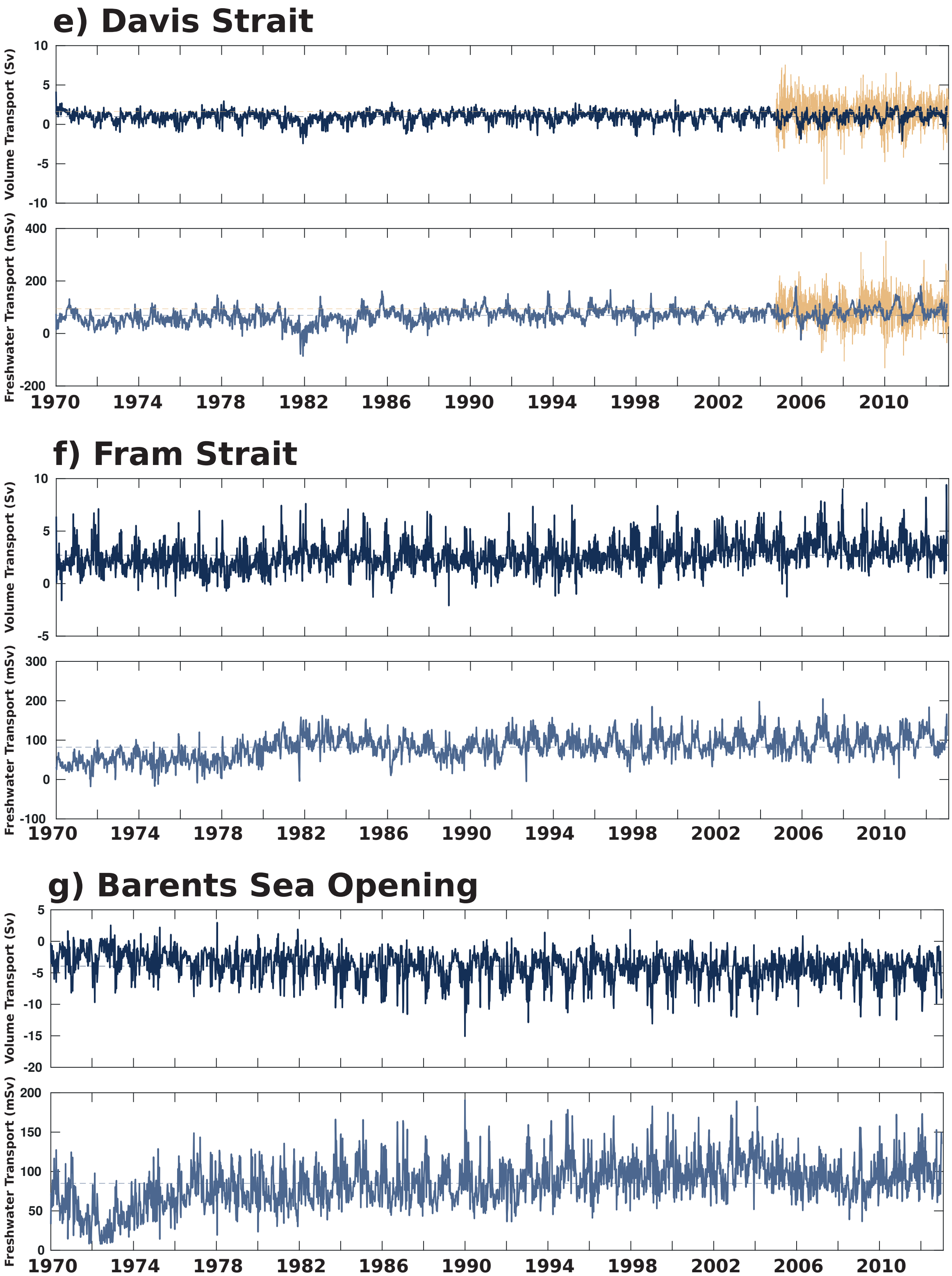
e) Davis Strait
Volume Transport (Sv)
Freshwater Transport (mSv)
f) Fram Strait
Volume Transport (Sv)
Freshwater Transport (mSv)
g) Barents Sea Opening
Volume Transport (Sv)
Freshwater Transport (mSv)
1970
1974
1978
1982
1986
1990
1994
1998
2002
2006
2010

Figure 5.2

Section Name	Volume Transport	Freshwater Transport	Source
Nares Strait			
1970-2013	0.40 ± 0.27	20 ± 14	This study
2002-2016	0.89	43	*Grivault et al. (2018)*
1958-2007	0.91	48	*Wekerle et al. (2013)*
1958-2004	1.4	77	*Wang et al. (2017)*
1988-2007	1.14	25	*Lu et al. (2014)*
1978-2013	0.81	-	*Zhang et al. (2016)*
1978-2013	**0.85**	**39**	*Münchow (2016)*
Lancaster Sound			
1970-2013	0.50 ± 0.25	48 ± 24	This study
2002-2016	0.58	44	*Grivault et al. (2018)*
1958-2007	0.86	71	*Wekerle et al. (2013)*
1988-2007	1.15	55	*Lu et al. (2014)*
1978-2013	0.71	-	*Zhang et al. (2016)*
1988-2010	**0.46 ± 0.09**	**33 ± 6**	*Peterson et al. (2012)*
Jones Sound			
1970-2013	0.12 ± 0.06	7 ± 4	This study
2002-2016	0	0	*Grivault et al. (2018)*
Davis Strait			
1970-2013	1.00 ± 0.73	81 ± 23	This study
2004-2010	**1.60 ± 0.20**	**93 ± 6**	*Curry et al. (2014)*
Fram Strait			
1970-2013	2.70 ± 0.92	82 ± 26	This study
1980-2005	1.7	-	*Rudels et al. (2008)*
1998-2011	**-**	**100 ± 23***	*Rabe et al. (2013)*
Barents Sea Opening			
1970-2013	-3.94 ± 1.60	85 ± 22	This study
1997-2006	-1.8	-	*Skagseth et al. (2008)*

Table 5.1: Summary of the Volume (in Sv) and freshwater (in mSv) transport. Numbers from observations are in bold. Positive means going out of the Arctic. *: contains only the outflow, with a reference salinity of 34.9. Variability is specified when available.

mean transport compared with other studies is shown in Table 5.1. From this point, if not stated otherwise, only MIROC will be discussed. Overall, the model underestimates the mean volume and freshwater transports through Nares Strait and Davis Strait with respect to other models and observations and overestimated the transports at Lancaster Sound, Jones Sound, Fram Strait and the Barents Sea Opening. However, the variability of the signal is within the uncertainty range of most of the other studies. Over the recent period, when we compare the monthly averaged modelled volume (freshwater) transport with the monthly averaged transports from available observations, we obtain correlation of about $r = 0.26$ ($r = 0.32$) at Lancaster Sound and $r = 0.28$ (not significant) at Davis Strait. The correlation at Nares Strait are not significant at the 95% level.

We note the absence in significance and the low correlations with observations. We

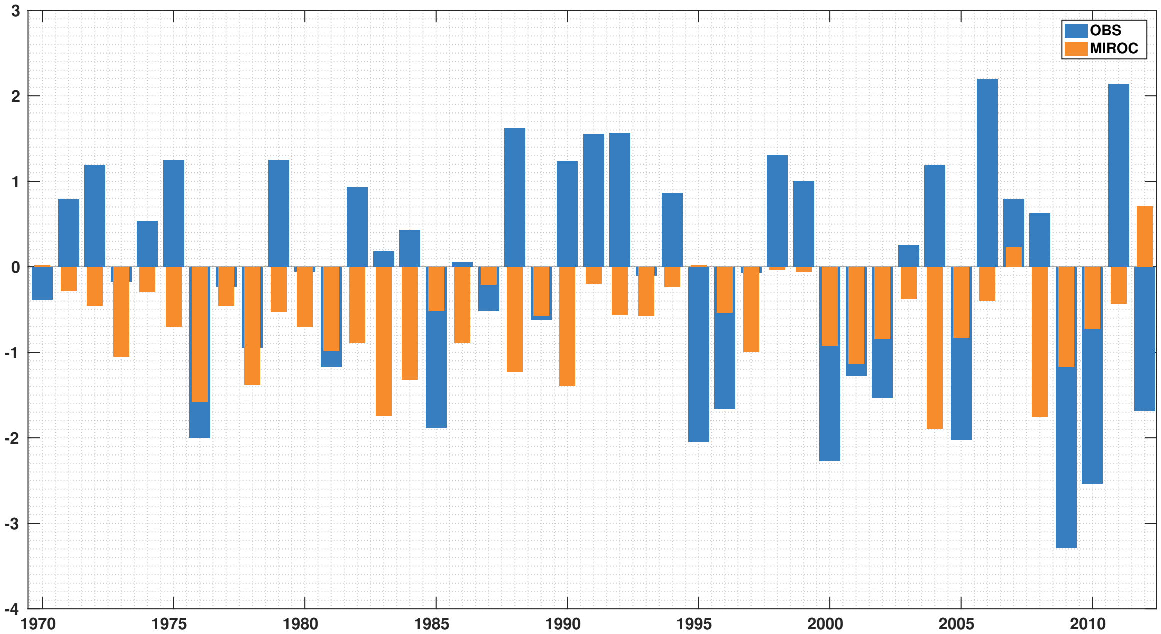

Figure 5.3: Arctic Oscillation Index from observations (blue bars) and from MIROC (orange bars).

attribute that to the low resolution (both temporal and spatial) of the atmospheric forcing used that does not permit us to resolve correctly short time scales in the transport, which impact significantly the quality of the correlation, as well as the larger variability in the model than in observation (see Table 5.1). However, this study is focused on the longer time scales. For this purpose, it is more important that the experiment does not show any significant numerical drift, which is the case in our experiment. The transport shows only a period of adjustment from the initial conditions during the first years. Then the model reaches a seasonal equilibrium.

The atmospheric forcing is locked in a positive AO, unlike in the observations where it switches back and forth (Figure 5.3). This can explain why the transport through Lancaster Sound and Jones Sounds is greater in MIROC than in the observations. An increase in the strength of the negative AO is usually associated with enhanced freshwater export through the CAA and a decrease in the Fram Strait export (e.g., 1981-1982, 1992-1998, Figure 5.2b, c, d, f). This is consistent with Wang et al. (2017) that also showed that the Arctic outflow goes preferably through the CAA during the negative phase of the AO.

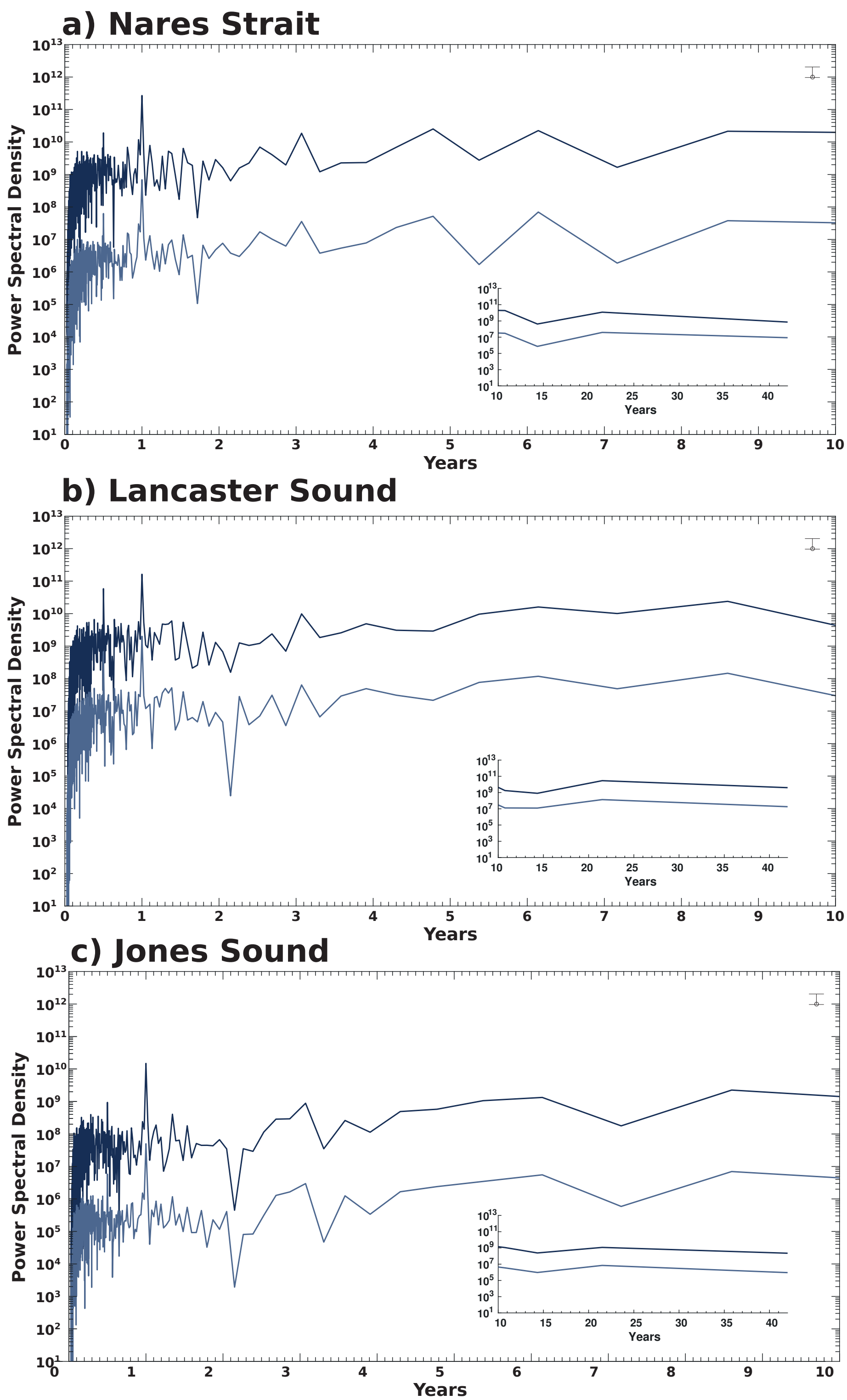

Figure 5.4: Power spectral density per frequency for the volume (dark blue) and freshwater (light blue) transport. The 95% confidence level is shown in the top right corner of each panel. Panel g (h) shows the power spectral density per frequency for the Arctic Oscillation and SSH gradient between the Beaufort Gyre and Baffin Bay (top panel) and for 1-10 years volume (freshwater) frequencies of each straits all together (bottom panel).

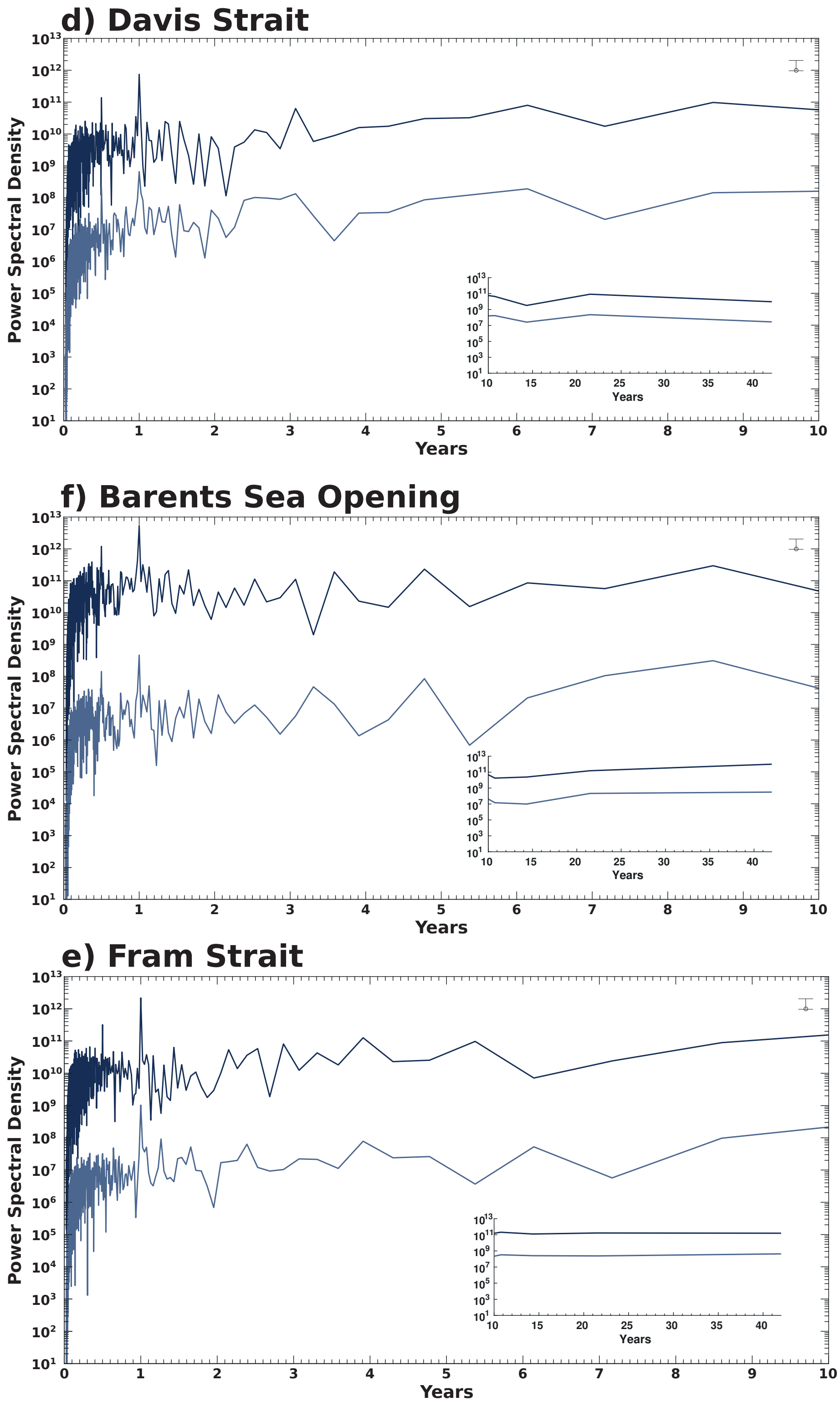
d) Davis Strait
f) Barents Sea Opening
e) Fram Strait
Power Spectral Density
Years

Figure 5.4

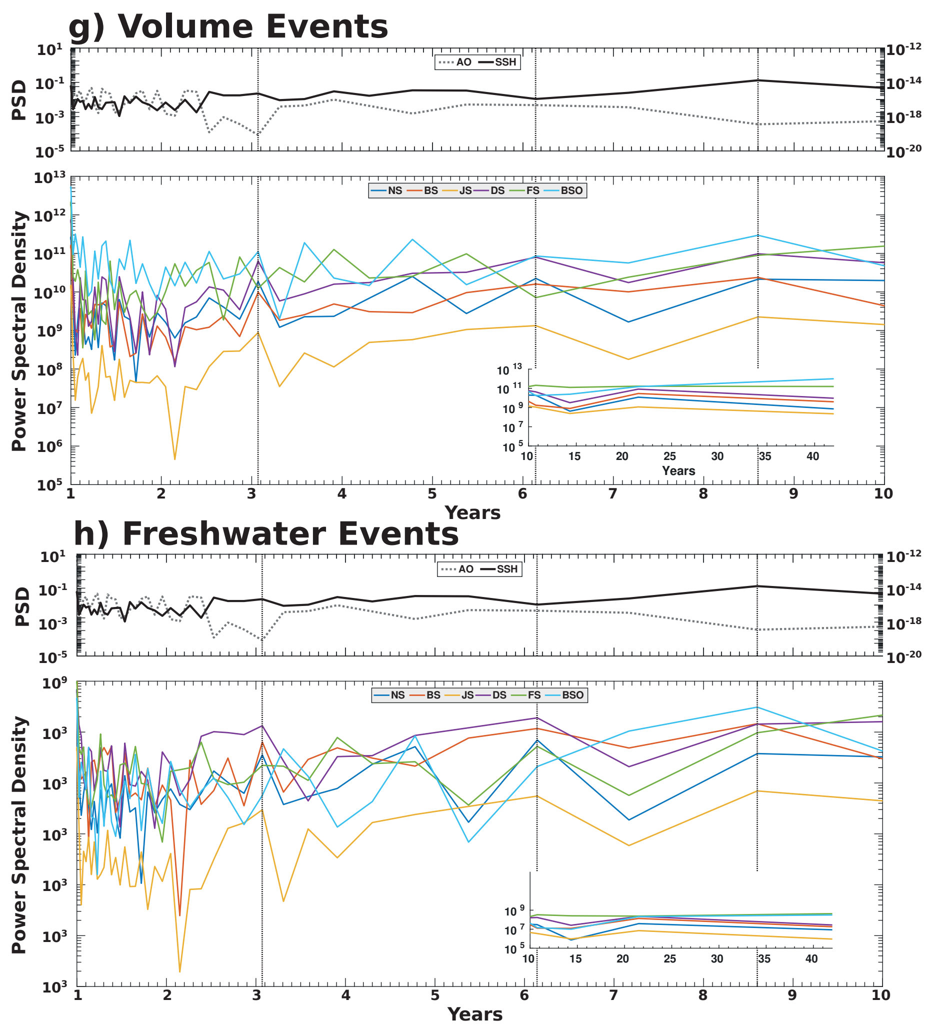

g) Volume Events
PSD
AO
SSH
Power Spectral Density
NS
BS
JS
DS
FS
BSO
Years
h) Freshwater Events
PSD
AO
SSH
Power Spectral Density
NS
BS
JS
DS
FS
BSO
Years

Figure 5.4

5.3.2 Frequency domain

Volume events

The transport in the frequency domain is shown in Figure 5.4. The volume events at each gate has a dominant spike of energy in the 1 year frequency band (i.e., the annual cycle). This frequency dominates by more than one order of magnitude the other frequencies. This shows that for all the straits, the most important frequency that acts on the volume transport is the annual cycle. A secondary spike is visible at 6 months frequency at all the gates, showing that the transport is strongly impacted by the seasonal conditions over the arctic, i.e., the sea-ice formation, melting, ice free periods, seasonal winds, or seasonal SSH gradients.

On timescales less than a year, the correlation between the straits in the CAA ($r > 0.75$) as well as on the Eurasian side ($r > 0.70$) are similarly high, and lower when comparing straits from each side together ($r \sim 0.62$) (Table 5.2a). This shows that on short time scales, we can not expect the same dynamics driving the flow through the gates of the CAA compared to the Eurasian Arctic. This is consistent with what we know of the Arctic outflow and how it is balanced between the CAA and the Eurasian side. The direct pathways out of the Arctic Ocean show a high correlation for each strait ($r > 0.70$), while the correlation for the less direct pathways (i.e., Nares Strait and Jones Sound) is lower ($r \sim 0.55$). At the opposite, the correlation with the SSH gradient between the Beaufort Gyre and Baffin Bay (see Figure 5.1 for the definition of both region) is stronger for Nares Strait and Jones Sound ($r \sim 0.53$) than for the more direct paths ($r \sim 0.30$). This is explained by the longer and less direct route the flows need to follow to reach these gates (i.e., around Ellesmere Island for Nares Strait and through the QEI for Jones Sound) which increase the response time of the transport to the atmospheric forcing and make it more sensitive to the large scale ocean dynamics.

On timescales between 1 and 10 years, most of the straits show a spike of energy in the 3, 5, 6 and 8.5 year bands . The magnitude of the 3 year frequency is similar to the 6-months cycle at Nares Strait, Jones Sound and Davis Strait and one order of magnitude less at Lancaster Sound. 6 and 8.5 years frequencies are one order of magnitude lower than the 6-month energy everywhere. Additional noticeable energy is contained in the 3.5 year cycle at the Barents Sea Opening, which appears in the 4 year band at Fram Strait. We note that the 5 years cycle energy happens in the 5.5 year band at Fram Strait, showing the same shift of 6 months in the frequency space, which is only present at Nares Strait on

a)	NS	LS	JS	DS	FS	BSO	AO	SSH
NS	**1**	**0.78**	**0.83**	**0.91**	**0.64**	**0.67**	**0.58**	**0.54**
LS	**0.81**	**1**	**0.76**	**0.95**	**0.79**	**0.73**	**0.89**	**0.26**
JS	**0.83**	**0.81**	**1**	**0.87**	**0.63**	**0.60**	**0.54**	**0.52**
DS	**0.84**	**0.86**	**0.80**	**1**	**0.75**	**0.72**	**0.78**	**0.39**
FS	**0.45**	**0.32**	**0.45**	**0.43**	**1**	**0.72**	**0.77**	**0.37**
BSO	**0.74**	**0.73**	**0.71**	**0.72**	**0.49**	**1**	**0.72**	**0.37**
AO	**0.72**	**0.94**	**0.72**	**0.79**	**0.28**	**0.72**	**1**	-
SSH	**0.44**	**0.18**	**0.41**	**0.33**	**0.73**	**0.34**	-	**1**

b)	NS	LS	JS	DS	FS	BSO	AO	SSH
NS	**1**	**0.67**	**0.77**	**0.86**	0.07	**0.40**	-0.25	**0.53**
LS	**0.67**	**1**	**0.89**	**0.92**	0.28	0.29	-0.23	**0.74**
JS	**0.76**	**0.84**	**1**	**0.93**	**0.34**	**0.34**	-0.27	**0.80**
DS	**0.69**	**0.63**	**0.75**	**1**	**0.21**	**0.35**	-0.22	**0.68**
FS	**0.34**	**0.42**	**0.36**	**0.39**	**1**	**0.07**	-0.26	**0.47**
BSO	**0.37**	**0.57**	**0.62**	0.30	**-0.44**	**1**	-0.14	**0.39**
AO	-0.27	**-0.19**	-0.30	-0.21	-0.21	-0.23	**1**	-
SSH	**0.38**	**0.67**	**0.72**	**0.40**	**0.49**	**0.91**	-	**1**

c)	NS	LS	JS	DS	FS	BSO	AO	SSH
NS	**1**	0.28	0.94	0.71	0.91	-0.53	0.32	-0.47
LS	0.71	**1**	0.59	0.87	0.08	-0.14	**0.95**	0.09
JS	0.93	0.90	**1**	0.90	0.77	-0.55	0.63	-0.41
DS	**0.98**	0.73	**0.95**	**1**	0.52	-0.38	0.86	-0.18
FS	-0.33	-0.53	-0.56	-0.48	**1**	-0.16	0.02	-0.15
BSO	0.82	0.35	0.08	0.07	0.54	**1**	-0.42	0.97
AO	0.69	**0.97**	0.90	0.75	-0.73	0.11	**1**	-
SSH	-0.19	0.04	-0.21	-0.33	0.75	0.94	-	**1**

Table 5.2: Correlation between each straits, Arctic Oscillation and SSH gradient and the volume (upper right) and freshwater (lower left) frequencies for a) 0-1 year period, b) 1-10 years period and c) 10+ years period. The correlation that are significant at the 95% level are shown in bold. NS: Nares Strait, LS: Lancaster Sound, JS: Jones Sound, DS: Davis Strait, FS: Fram Strait, BSO: Barents Sea Opening, AO: Arctic Oscillation, SSH: SSH gradient between the Beaufort Gyre and Baffin Bay.

the CAA route. The correlation between each strait (Table 5.2b) is significantly lower. The correlation between the volume transport events and the AO show a negative correlation ($r \sim -0.25$) that is not significant. However, the correlation with the large scale SSH gradient is significant and strong for the CAA route ($r > 0.68$, except at Nares Strait where $r = 0.53$) and is slightly less significant through the Eurasian route ($r \sim 0.40$). These results show that the atmospheric patterns have limited impact on long timescale events, with the transport mainly driven by the large scale oceanic state. This means that the change in the freshwater content inside the Beaufort Gyre (i.e., what drives the large scale SSH gradient) will most likely have a stronger impact on the volume fluxes out of the Arctic on these frequencies than the changes in the atmospheric patterns.

On timescales longer than 10 years, the CAA straits show a significant amount of energy contained in the 21 years cycle. The correlation between the transport and the AO events is high for the CAA ($0.63 < r < 0.95$, except at Nares Strait $r = 0.32$), but the correlation is significant only at Lancaster Sound. The Eurasian side shows no correlation at Fram Strait ($r = 0.02$) and a negative correlation at the Barents Sea Opening ($r = -0.42$). The correlation with the SSH gradient is usually negative and low ($r \sim -0.15$) to average ($r \sim -0.42$, Nares Strait and Jones Sound), except at Fram Strait ($r = 0.97$) and Lancaster Sound ($r = 0.09$). None of the correlations are significant. This absence of significance, can be explained by the limited number of points used for the correlation. Despite this, we note a clear average to high correlation with the AO, showing a potential importance on very long timescale events in the volume transport.

Freshwater events

The freshwater transport variability is similar to the volume transport with a few difference. First, the 6 months spike at Fram Strait is not present for freshwater (Figure 5.4e). This suggests that the sea-ice coverage over the Arctic does not impact the liquid freshwater transport at this gate. This could be explained by the fact that most of the freshwater transport is transported as solid sea-ice and not as liquid. At longer timescales, we observe much more variability in the 6 months to 2 years cycles (Figure 5.4), which is consistent with a stronger response to the atmospheric forcing. The correlations between the freshwater transport events and the AO events on timescales less than 1 year are higher than for the volume transport events ($r > 0.72$, up to $r = 0.94$ at Lancaster Sound). Despite being slightly higher, the low correlation at Fram Strait is also present with the freshwater events ($r = 0.28$) (Table 5.2a). The correlations between the freshwater events and the SSH gradient are lower (about 0.10 less). However, we note a strong correlation between Fram Strait freshwater events and the SSH ($r = 0.73$) showing that at this time scale the large scale ocean fields plays a significant role in the freshwater outflow by the Eurasian route.

On timescales between 1 and 10 years, the main frequencies present in the volume events are also present in the freshwater events (Figure 5.4h). The exceptions are the 2 to 3 years cycle at Davis Strait that is much more related to the SSH events (Figure 5.4h). In addition, some additional frequencies impact the freshwater transport but not the volume transport. This is the case of the 2.6 years cycle at Lancaster Sound, the 6 year cycle at Fram Strait and the Barents Sea Opening. The same happens with the 5.5 year cycle impacting the transport at Fram Strait, Nares Strait and the Barents Sea Opening or the whole 2 to 3 years band at the Barents Sea Opening and the 2.5 to 3 years band at Fram Strait. The correlation of the freshwater events with the AO events are usually slightly stronger (about -0.05 more) and it becomes significant at Lancaster Sound (Table 5.2b). The correlations with the SSH gradient are lower (about 0.05 to 0.15 less). This is expected considering that freshwater is mainly located in the upper layer of the ocean and this layer is the most impacted by the atmospheric forcing and less by the large scale ocean gradients. This also shows that the freshwater fluxes are going to be more likely impacted by the changes in the atmospheric patterns and the strength of the atmospheric events than by the large scale changes in the freshwater content of the Arctic Ocean and in particular, in the Beaufort Gyre.

The timescales greater than 10 years for the freshwater events are similar than the volume events with a 21 years cycle still strong for the same gates. We note that at the Barents Sea Opening presents a spike of energy in the volume frequency at the 21.5 cycle in the freshwater events but not in the volume events. A stronger correlation between the freshwater events and the AO is present at this timescale on the CAA (about 0.25 more). However, only Lancaster Sound has a significant correlation. The correlation with the SSH gradient is usually about half the correlation with the volume events. On the Eurasian side, Fram Strait shows a significantly stronger anti-correlation ($r = -0.71$), and a strong correlation with the SSH gradient ($r = 0.94$). At the Barents Sea Opening the correlation with the AO decreases and becomes positive ($r = 0.11$), while the correlation with the SSH gradient stays similar ($r = 0.94$). This shows that for these timescales, freshwater events through the Eurasian routes respond much strongly to the changes due to the atmospheric patterns and the oceanic state than the CAA route. This sensitivity is only something we see in the freshwater events and not in the volume events. We note that these correlations, despite showing promising difference in dynamics of each route, are not significant at the 95 % level and thus more investigation is required.

5.4 Conclusions

In this study, we use a numerical model to investigate the timescales associated with flux variability export at the Arctic Ocean gateways. We show that the most important frequency that acts on the transports is the annual cycle, with the 6-months frequency also strong for all straits except Fram Strait. In addition, the 3 years, 6 years, 8.5 and 21 year cycles are major frequencies impacting both the volume and freshwater events. The frequencies of the events are strongly linked to the Arctic Oscillation when short timescales are considered (i.e., less than 1 year) and largely related to the SSH gradient between the Beaufort Gyre and Baffin Bay on longer timescales (i.e., more than 1 year). Events in the freshwater export are similar to the volume events but show additional important frequencies (e.g., 2-3 years cycles at Davis Strait) or slightly different timing (e.g., events 6 months shorter). We show that the correlation with the Arctic Oscillation is stronger for the freshwater events than the volume events. The correlation with the SSH gradient is stronger for the volume events than the freshwater events. Finally, on timescales larger than 10 years, the CAA and the Eurasian routes react differently to the AO (CAA route: medium correlation; Eurasian route: none to medium correlation) and SSH gradient (CAA route: low to medium correlation; Eurasian route: low to strong correlation). However, the freshwater events are strongly correlated with both the AO and SSH gradient at these timescales.

We can find a parallel between the events out of the Arctic and what we currently know of the mechanisms behind the accumulation and release of freshwater inside of the Beaufort Gyre. At the current stage of the knowledge, the accumulation of freshwater in the Beaufort Gyre is wind driven (i.e., short timescale) and constrained by eddies (i.e., longer timescale) (Manucharyan and Spall, 2016). The absence of accumulation of freshwater inside of the Beaufort Gyre due to the absence of positive phase in the AO in our experiment prevents us observing any significant correlation between freshwater export and the dynamics of the Beaufort Gyre (seen in our study by the absence of significant correlation between AO and transport events). Could a better atmospheric forcing allow a more direct link between the timescales associated with accumulation / release periods of the Beaufort Gyre and the variability of the Arctic Ocean gateways? The phase lock is not surprising given an atmospheric forcing taken from a climate model, but will significantly impact the dynamics of the modelled Arctic Ocean.

This issue needs to be resolved before submitting this study for publication. In order to do this, we are currently running another 40 years experiment with a different atmospheric forcing (ERA-Interim, see Berrisford et al. (2011)) which is made from data reanalysis. This technique consists of running an atmospheric model with data assimilation to force the model to come back on a more realistic state instead of letting it freely evolve. The boundary forcing and initial conditions will be unchanged. Additionally, extending the experiment would be an improvement, improving the quality of the frequency analysis, due to the addition of more data. An addition of 10 years, for instance, would permit us to obtain more reliable results on the time scales between 1 and 10 years and will make the frequency from 10 to 20 years more robust. This could significantly improve the correlation, in particular the significance which should mathematically increase due to the addition of more data.

Bibliography

Amante, C. and Eakins, B. (2009). ETOPO1 1 arc-minute global relief model: Procedures, data sources and analysis. *NOAA Technical Memorandum NESDIS NGDC-24*.

Bamber, J., van den Broeke, M., Ettema, J., Lenaerts, J., and Rignot, E. (2012). Recent large increases in freshwater fluxes from greenland into the north atlantic. *Geophysical Research Letters*, 39(19):n/a–n/a.

Belkin, I. M., Levitus, S., Antonov, J., and Malmberg, S.-A. (1998). "great salinity anomalies" in the North Atlantic. *Progress in Oceanography*, 41(1):1–68.

Berrisford, P., Dee, D., Poli, P., Brugge, R., Fielding, M., Fuentes, M., Kållberg, P., Kobayashi, S., Uppala, S., and Simmons, A. (2011). The ERA-Interim archive version 2.0. Shinfield Park, Reading.

Blanke, B. and Delecluse, P. (1993). Variability of the Tropical Atlantic Ocean simulated by a general circulation model with two different mixed-layer physics. *Journal of Physical Oceanography*, 23(7):1363–1388.

Carmack, E. C., Yamamoto-Kawai, M., Haine, T. W. N., Bacon, S., Bluhm, B. A., Lique, C., Melling, H., Polyakov, I. V., Straneo, F., Timmermans, M.-L., and et al. (2016). Freshwater and its role in the Arctic marine system: Sources, disposition, storage, export, and physical and biogeochemical consequences in the arctic and global oceans. *Journal of Geophysical Research: Biogeosciences*, 121(3):675–717.

Cuny, J., Rhines, P. B., and Kwok, R. (2005). Davis Strait volume, freshwater and heat fluxes. *Deep Sea Research Part I: Oceanographic Research Papers*, 52(3):519–542.

Curry, B., Lee, C. M., and Petrie, B. (2011). Volume, freshwater, and heat fluxes through Davis Strait, 2004–05*. *Journal of Physical Oceanography*, 41(3):429–436.

Curry, B., Lee, C. M., Petrie, B., Moritz, R. E., and Kwok, R. (2014). Multiyear volume, liquid freshwater, and sea ice transports through Davis Strait, 2004–10*. *Journal of Physical Oceanography*, 44(4):1244–1266.

Dai, A., Qian, T., Trenberth, K. E., and Milliman, J. D. (2009). Changes in continental freshwater discharge from 1948 to 2004. *Journal of Climate*, 22(10):2773–2792.

Gelderoos, R., Straneo, F., and Katsman, C. (2012). Mechanisms behind the temporary shutdown of deep convection in the labrador sea: Lessons from the Great Salinity Anomaly years 1968-71. *Journal of Climate*, 25:6743–6755.

Grivault, N., Hu, X., and Myers, P. G. (2018). Impact of the surface stress on the volume and freshwater transport through the Canadian Arctic Archipelago from high resolution numerical modelling. *Journal of Geophysical Research: Oceans*.

Haine, T. W., Curry, B., Gerdes, R., Hansen, E., Karcher, M., Lee, C., Rudels, B., Spreen, G., de Steur, L., Stewart, K. D., and et al. (2015). Arctic freshwater export: Status, mechanisms, and prospects. *Global and Planetary Change*, 125:13–35.

Hu, X. and Myers, P. G. (2013). A Lagrangian view of Pacific water inflow pathways in the Arctic Ocean during model spin-up. *Ocean Modelling*, 71:66–80.

Hunke, E. C. (2001). Viscous–plastic sea ice dynamics with the EVP model: Linearization issues. *Journal of Computational Physics*, 170(1):18–38.

Jahn, A. and Holland, M. M. (2013). Implications of Arctic sea ice changes for north atlantic deep convection and the meridional overturning circulation in CCSM4-CMIP5 simulations. *Geophysical Research Letters*, 40(6):1206–1211.

Large, W. G. and Yeager, S. G. (2004). Diurnal to decadal global forcing for ocean and sea-ice models: the data sets and flux climatologies.

Lique, C., Holland, M. M., Dibike, Y. B., Lawrence, D. M., and Screen, J. A. (2016). Modeling the Arctic freshwater system and its integration in the global system: Lessons learned and future challenges. *Journal of Geophysical Research: Biogeosciences*, 121(3):540–566.

Lu, Y., Higginson, S., Nudds, S., Prinsenberg, S., and Garric, G. (2014). Model simulated volume fluxes through the Canadian Arctic Archipelago and Davis Strait: Linking monthly variations to forcing in different seasons. *Journal of Geophysical Research: Oceans*, 119(3):1927–1942.

Madec, G. (2008). Nemo ocean engine. *Note du Pole de modelisation*, 27:1288–1619.

Madec, G., Delecluse, P., Imbard, M., and Levy, C. (1998). OPA 8 ocean general circulation model - reference manual. Technical report, LODYC/IPSL Note 11.

Manucharyan, G. E. and Spall, M. A. (2016). Wind-driven freshwater buildup and release in the Beaufort Gyre constrained by mesoscale eddies. *Geophysical Research Letters*, 43(1):273–282.

Manucharyan, G. E., Spall, M. A., and Thompson, A. F. (2016). A theory of the wind-driven Beaufort Gyre variability. *Journal of Physical Oceanography*, 46(11):3263–3278.

Masina, S., Storto, A., Ferry, N., Valdivieso, M., Haines, K., Balmaseda, M., Zuo, H., Drevillon, M., and Parent, L. (2015). An ensemble of eddy-permitting global ocean reanalyses from the MyOcean project. *Climate Dynamics*, pages 1–29.

McPhee, M. G., Proshutinsky, A., Morison, J. H., Steele, M., and Alkire, M. B. (2009). Rapid change in freshwater content of the Arctic Ocean. *Geophysical Research Letters*, 36(10).

Morison, J., Kwok, R., Peralta-Ferriz, C., Alkire, M., Rigor, I., Andersen, R., and Steele, M. (2012). Changing Arctic Ocean freshwater pathways. *Nature*, 481(7379):66–70.

Münchow, A. (2016). Volume and freshwater flux observations from Nares Strait to the west of Greenland at daily time scales from 2003 to 2009. *Journal of Physical Oceanography*, 46(1):141–157.

Münchow, A. and Melling, H. (2008). Ocean current observations from Nares Strait to the west of Greenland: Interannual to tidal variability and forcing. *Journal of Marine Research*, 66(6):801–833.

Peterson, I., Hamilton, J., Prinsenberg, S., and Pettipas, R. (2012). Wind-forcing of volume transport through Lancaster Sound. *Journal of Geophysical Research: Oceans*, 117(C11):n/a–n/a.

Prinsenberg, S. and Bennett, E. (1989). Transport between peel sound and barrow strait in the Canadian Arctic. *Continental Shelf Research*, 9(5):427–444.

Prinsenberg, S., Hamilton, J., Peterson, I., and Pettipas, R. (2009). Observing and interpreting the seasonal variability of the oceanographic fluxes passing through Lancaster Sound of the Canadian Arctic Archipelago. In *Influence of Climate Change on the Changing Arctic and Sub-Arctic Conditions*, pages 125–143. Springer Netherlands.

Proshutinsky, A., Bourke, R. H., and McLaughlin, F. A. (2002). The role of the Beaufort Gyre in arctic climate variability: Seasonal to decadal climate scales. *Geophysical Research Letters*, 29(23):15–1–15–4.

Proshutinsky, A., Krishfield, R., Timmermans, M.-L., Toole, J., Carmack, E., McLaughlin, F., Williams, W. J., Zimmermann, S., Itoh, M., and Shimada, K. (2009). Beaufort Gyre freshwater reservoir: State and variability from observations. *Journal of Geophysical Research*, 114.

Rabe, B., Dodd, P. A., Hansen, E., Falck, E., Schauer, U., Mackensen, A., Beszczynska-Möller, A., Kattner, G., Rohling, E. J., and Cox, K. (2013). Liquid export of Arctic freshwater components through the Fram Strait 1998–2011. *Ocean Science*, 9(1):91–109.

Randall, D. A., Wood, R. A., Bony, S., Colman, R., Fichefet, T., Fyfe, J., Kattsov, V., Pitman, A., Shukla, J., Srinivasan, J., et al. (2007). Climate models and their evaluation. In *Climate change 2007: The physical science basis. Contribution of Working Group I to the Fourth Assessment Report of the IPCC (FAR)*, pages 589–662. Cambridge University Press.

Rudels, B., Marnela, M., and Eriksson, P. (2008). Constraints on estimating mass, heat and freshwater transports in the Arctic Ocean: An exercise. *Arctic–Subarctic Ocean Fluxes*, pages 315–341.

Serreze, M. C. and Barrett, A. P. (2011). Characteristics of the Beaufort Sea High. *Journal of Climate*, 24(1):159–182.

Serreze, M. C., Barrett, A. P., Slater, A. G., Woodgate, R. A., Aagaard, K., Lammers, R. B., Steele, M., Moritz, R., Meredith, M., and Lee, C. M. (2006). The large-scale freshwater cycle of the Arctic. *Journal of Geophysical Research*, 111(C11).

Skagseth, Ø., Furevik, T., Ingvaldsen, R., Loeng, H., Mork, K. A., Orvik, K. A., and Ozhigin, V. (2008). Volume and heat transports to the Arctic Ocean via the norwegian and barents seas. *Arctic–Subarctic Ocean Fluxes*, pages 45–64.

Smith, G. C., Roy, F., Mann, P., Dupont, F., Brasnett, B., Lemieux, J.-F., Laroche, S., and Bélair, S. (2014). A new atmospheric dataset for forcing ice-ocean models: Evaluation of reforecasts using the Canadian global deterministic prediction system. *Quarterly Journal of the Royal Meteorological Society*, 140(680):881–894.

Steele, M., Morley, R., and Ermold, W. (2001). PHC: A global ocean hydrography with a high-quality Arctic Ocean. *Journal of Climate*, 14(9):2079–2087.

Straneo, F. (2006). Heat and freshwater transport through the central Labrador Sea*. *Journal of Physical Oceanography*, 36(4):606–628.

Thompson, D. W. J. and Wallace, J. M. (1998). The Arctic Oscillation signature in the wintertime geopotential height and temperature fields. *Geophysical Research Letters*, 25(9):1297–1300.

Vancoppenolle, M., Fichefet, T., Goosse, H., Bouillon, S., Madec, G., and Maqueda, M. A. M. (2009). Simulating the mass balance and salinity of Arctic and Antarctic sea ice. 1. model description and validation. *Ocean Modelling*, 27(1–2):33–53.

Wang, Q., Ilicak, M., Gerdes, R., Drange, H., Aksenov, Y., Bailey, D. A., Bentsen, M., Biastoch, A., Bozec, A., Böning, C., Cassou, C., Chassignet, E., Coward, A. C., Curry, B., Danabasoglu, G., Danilov, S., Fernandez, E., Fogli, P. G., Fujii, Y., Griffies, S. M., Iovino, D., Jahn, A., Jung, T., Large, W. G., Lee, C., Lique, C., Lu, J., Masina, S., Nurser, A. G., Rabe, B., Roth, C., y Mélia, D. S., Samuels, B. L., Spence, P., Tsujino, H., Valcke, S., Voldoire, A., Wang, X., and Yeager, S. G. (2016). An assessment of the Arctic Ocean in a suite of interannual CORE-II simulations. part II: Liquid freshwater. *Ocean Modelling*, 99:86–109.

Wang, Z., Hamilton, J., and Su, J. (2017). Variations in freshwater pathways from the Arctic Ocean into the North Atlantic Ocean. *Progress in Oceanography*, 155:54–73.

Watanabe, M., Suzuki, T., O'ishi, R., Komuro, Y., Watanabe, S., Emori, S., Takemura, T., Chikira, M., Ogura, T., Sekiguchi, M., and et al. (2010). Improved climate simulation by MIROC5: Mean states, variability, and climate sensitivity. *Journal of Climate*, 23(23):6312–6335.

Wekerle, C., Wang, Q., Danilov, S., Jung, T., and Schröter, J. (2013). The Canadian Arctic Archipelago throughflow in a multiresolution global model: Model assessment and the driving mechanism of interannual variability. *Journal of Geophysical Research: Oceans*, 118(9):4525–4541.

Yang, J. (2009). Seasonal and interannual variability of downwelling in the Beaufort Sea. *Journal of Geophysical Research*, 114.

Yang, Q., Dixon, T. H., Myers, P. G., Bonin, J., Chambers, D., and van den Broeke, M. R. (2016). Recent increases in Arctic freshwater flux affects Labrador Sea convection and Atlantic overturning circulation. *Nature Communications*, 7:10525.

Zhang, Y., Chen, C., Beardsley, R. C., Gao, G., Lai, Z., Curry, B., Lee, C. M., Lin, H., Qi, J., and Xu, Q. (2016). Studies of the Canadian Arctic Archipelago water transport and its relationship to basin-local forcings: Results from AO-FVCOM. *Journal of Geophysical Research: Oceans*, 121(6):4392–4415.

Chapter 6

Conclusions

The Arctic environment is changing rapidly in response to the increase in the global temperature due to increasing anthropogenic greenhouse gas emissions. The most visible of changes is the dramatic decline in sea-ice coverage in the Arctic, but changes that are not as noticeable such as an increase in runoff from land and land ice, as well as a warming of the Arctic Ocean are also occurring. To improve our understanding of how the Arctic may respond to these changes, I used a numerical framework composed of an ocean and sea-ice coupled model to simulate the response of the Arctic system to the current and future changes.

I analyzed how the fluxes of volume and freshwater out of the Arctic are impacted and processes responsible. I focused on two key regions, Baffin Bay and the Canadian Arctic Archipelago, as well as the gates out of the Arctic (i.e., Lancaster Sound, Jones Sound, Nares Strait, Davis Strait, Fram Strait and the Barents Sea Opening). I showed that Baffin Bay has a strong response to the runoff from Greenland, the runoff having the potential to change the baroclinic gradient in the bay. This leads to an increase in warm inflow from the south, and leads to an increase of 53 % in the freshwater content in the bay and finally a decrease in the overall throughflow towards the northern Atlantic of about 75 %. In the Canadian Arctic Archipelago, I studied the relation between the surface stress and the variability of the volume and freshwater transport by analyzing the correlation and its variation based on sea-ice coverage and mobility (i.e., on the season). In particular, I highlighted how the sea-ice motion is driving too much transport through the Canadian Arctic Archipelago in ou model. Finally, I analyzed what time scales impact the volume and freshwater transports the most outside of the Arctic Ocean. I pinpointed the importance of long term measurements since most of the straits are significantly impacted by time-scales that are greater than 8 years. I also demonstrated the importance of the atmospheric pattern (i.e., the arctic oscillation) and large scale oceanic circulation (i.e., the SSH gradient between the Beaufort Gyre and Baffin Bay) on the events.

In the following section, I will explain in more detail how these findings answer the initial questions.

6.1 Main findings

6.1.1 Impact of enhanced Greenland melt on Baffin Bay dynamics

This study showed that Baffin Bay becomes fresher and warmer with time when runoff from Greenland is enhanced. In response to the freshening, the halosteric height increases, reducing the baroclinic gradient between the Arctic Ocean and Baffin Bay. As a consequence, the Arctic Water outflow that goes through Baffin Bay towards the North Atlantic is reduced and the West Greenland Current is strengthened, bringing in more warm, saline Atlantic derived water (i.e. West Greenland Irminger and Shelf waters). The volume of West Greenland Irminger Water starts to increase in the bay and a significant amount will eventually be trapped inside the cyclonic gyre. The increase in volume of Irminger and Shelf waters also lead to enhanced mixing with the underlying Transitional Water, leading to the formation of Irminger Water inside of Baffin Bay. The majority of the dynamical adjustment occurs before 1995, in response to freshwater input from runoff. After this date, the change in the halosteric height is minimum and the changes in the total steric height is mainly due to the increase in the mean temperature of the bay. The projection in the future showed that the steric height of the bay reaches an equilibrium in the 2050s, when the volume of the West Greenland Irminger and Shelf Waters stabilizes.

Our findings concerning Baffin Bay dynamics are consistent with several previous studies (e.g., Andresen et al. (2011); Holland et al. (2008)) and the changes I detected have been observed in the past (e.g., Myers and Ribergaard (2013); Zweng and Münchow (2006)). However, an increase has also been observed in the Arctic Water outflow (e.g., Münchow et al. (2015)) that I do not observe. I showed that the difference in the surface fluxes are small with both atmospheric forcings (less than 1%). However this forcing is coarse in both experiments. Could an improved atmospheric forcing increase the proportion of Arctic Water being exported? Moreover, the study was focused on the dynamics in Baffin Bay, but the transport out of the Arctic is a balance between the export through the Canadian route and through Fram Strait. I showed that the transport through Baffin Bay is reduced, but the transport through Fram Strait also has to be considered to get an overall picture of the Arctic outflow and the possible consequences for the Labrador Sea. Hence, a possible follow on is to extend this study using a more recent atmospheric forcing such as CGRF and extend the analysis to Fram Strait outflow.

6.1.2 Impact of surface stress in the Canadian Arctic Archipelago

The role of the surface stress on transport through the Canadian Arctic Archipelago has been analyzed. I showed that the surface stress is closely related to the sea-ice motion, especially in winter when the sea-ice coverage of the Arctic is larger. In particular, I showed that at West Lancaster Sound and Nares Strait, the mobility of sea-ice is one of the main drivers leading to an overestimation of the volume and freshwater transport in our numerical model. From a larger point of view, the flow through the Queen Elizabeth Islands is significantly impacted by changes in surface stress over the Beaufort Gyre and northern Baffin Bay, while changes in the local stress impacts other parts of the Canadian Arctic Archipelago more. Additionally, in winter, sea-ice motion significantly enhances the importance of the surface stress on the transports.

I showed the importance of the sea-ice in the transports and pathways through the Canadian Arctic Archipelago. However, could it be the only factor that drives the variability in this region? It has been shown that tides have a significant amplitude in the Canadian Arctic Archipelago (up to 2 m in Nares Strait; e.g., Luneva et al. (2015)) by increasing the mixing between water masses and by adding a tidal current. I thus suggest to improve our numerical experiment by adding tides and analyze how the pathways through the Canadian Arctic Archipelago is modified. I also showed that the sea-ice is too thick in our model (from 0.5 to 1.5 m, depending on the region). Could the inclusion of tides improve this aspect of the simulation? Finally, similar to the Baffin Bay dynamics study, I stayed focused on the role of surface stress over the Canadian Arctic Archipelago but, to understand all pathways out of the Arctic, an analysis of the dynamics of Fram Strait is required. Could the surface stress over the Eurasian Basin or over the Nordic Seas have an impact on Fram Strait dynamics?

6.1.3 Impact of frequencies of the transports

In this study, I explored the timescales associated with the volume and freshwater fluxes variability at the Arctic Ocean gateways. I highlighted the importance of annual cycle, the 6-months cycle, as well as longer timescales with the 3 years, 6 years, 8.5 years and 21 years cycles. I showed a strong relation between the Arctic Oscillation and the events at short timescales (i.e., less than 1 year) and a greater impact of the gradient between the Beaufort Gyre and Baffin Bay at longer timescales (i.e., more than 1 year). The freshwater frequencies are similar to the volume frequencies, but present additional important frequencies that vary in function of the considered gate. The freshwater frequencies are also more strongly related to the Arctic Oscillation than the volume frequencies, which is more strongly related to the SSH gradient. Finally, we showed a low to medium impact of the Arctic Oscillation and SSH gradient on the volume events on timescales more than 10 years. At the same timescales, the freshwater events are more strongly correlated with the Arctic Oscillation and SSH gradient.

I demonstrated the co-relationship between the Arctic Oscillation (i.e., atmospheric dynamics) and the SSH gradient between the Beaufort Gyre and Baffin Bay (i.e., oceanic dynamics). For doing that, I considered that these dynamics are fully independent. This is not true. Indeed, the atmosphere, and in particular the Arctic Oscillation, will drive more or less freshwater inside of the Beaufort Gyre (e.g., Manucharyan and Spall (2016); Manucharyan et al. (2016)), which will change the SSH over the Beaufort Gyre. Similarly Manucharyan and Spall (2016) showed that the amount of freshwater that can be extracted because of the atmosphere (i.e., via Ekman pumping) depends on the freshwater content in the Beaufort Gyre (i.e., strong cyclonic winds won't release more freshwater from the Beaufort Gyre if it's empty). Our study discussed this point but was not able to do a direct link between the frequency of the Beaufort Gyre oscillation and the variability at the Arctic Ocean gates. Can a more direct link be found?

6.2 Thesis summary

During the work realized during this Ph.D thesis, my aim was to improve the overall knowledge of the Arctic outflow towards the lower latitudes. I used a numerical framework and a set of numerical experiments forced with various datasets to perform sensitivity experiments and hindcast experiments in order to answer to our scientific questions. Therefore my main contribution to improve the overall knowledge of the Arctic system includes:

- Enhanced Greenland melt has the power to significantly impact Baffin Bay dynamics and, as a consequence, reduce the Arctic flow through the bay.
- The sea-ice motion has an significant impact on the transports through the Canadian Arctic Archipelago, especially on the freshwater transport.

- The main frequency acting on the Arctic outflow variability are up to 21 years. Short time scales (0-1 year) are strongly related to the Arctic Oscillation, intermediate timescales (1-10 years) are strongly related with SSH gradient.

Bibliography

Andresen, C. S., Straneo, F., Ribergaard, M. H., Bjørk, A. A., Andersen, T. J., Kuijpers, A., Nørgaard-Pedersen, N., Kjær, K. H., Schjøth, F., Weckström, K., and et al. (2011). Rapid response of Helheim Glacier in Greenland to climate variability over the past century. *Nature Geoscience*, 5(1):37–41.

Holland, D. M., Thomas, R. H., de Young, B., Ribergaard, M. H., and Lyberth, B. (2008). Acceleration of Jakobshavn Isbræ triggered by warm subsurface ocean waters. *Nature Geoscience*, 1(10):659–664.

Luneva, M. V., Aksenov, Y., Harle, J. D., and Holt, J. T. (2015). The effects of tides on the water mass mixing and sea ice in the Arctic Ocean. *Journal of Geophysical Research: Oceans*, 120(10):6669–6699.

Manucharyan, G. E. and Spall, M. A. (2016). Wind-driven freshwater buildup and release in the Beaufort Gyre constrained by mesoscale eddies. *Geophysical Research Letters*, 43(1):273–282.

Manucharyan, G. E., Spall, M. A., and Thompson, A. F. (2016). A theory of the wind-driven Beaufort Gyre variability. *Journal of Physical Oceanography*, 46(11):3263–3278.

Münchow, A., Falkner, K. K., and Melling, H. (2015). Baffin Island and West Greenland Current systems in northern Baffin Bay. *Progress in Oceanography*, 132:305–317.

Myers, P. G. and Ribergaard, M. H. (2013). Warming of the Polar Water layer in Disko Bay and potential impact on Jakobshavn Isbrae. *Journal of Physical Oceanography*, 43(12):2629–2640.

Zweng, M. M. and Münchow, A. (2006). Warming and freshening of Baffin Bay, 1916–2003. *Journal of Geophysical Research: Oceans*, 111(C7):n/a–n/a. C07016.

References

Aagaard, K. and Carmack, E. C. (1989). The role of sea ice and other fresh water in the Arctic circulation. *Journal of Geophysical Research*, 94(C10):14485.

Aagaard, K., Coachman, L., and Carmack, E. (1981). On the halocline of the Arctic Ocean. *Deep Sea Research Part A. Oceanographic Research Papers*, 28(6):529–545.

Aagaard, K., Swift, J., and Carmack, E. (1985). Thermohaline circulation in the Arctic Mediterranean seas. *Journal of Geophysical Research: Oceans*, 90(C3):4833–4846.

Adcroft, A., Hill, C., and Marshall, J. (1997). Representation of topography by Shaved Cells in a Height Coordinate Ocean Model. *Monthly Weather Review*, 125(9):2293–2315.

Agnew, T., Lambe, A., and Long, D. (2008). Estimating sea ice area flux across the Canadian Arctic Archipelago using enhanced AMSR-E. *Journal of Geophysical Research*, 113(C10).

Aksenov, Y., Bacon, S., Coward, A. C., and Holliday, N. P. (2010). Polar outflow from the Arctic Ocean: A high resolution model study. *Journal of Marine Systems*, 83(1-2):14–37.

Alvarez, A., Tintoré, J., Holloway, G., Eby, M., and Beckers, J. M. (1994). Effect of topographic stress on circulation in the western Mediterranean. *Journal of Geophysical Research*, 99(C8):16053.

Amante, C. and Eakins, B. (2009). ETOPO1 1 arc-minute global relief model: Procedures, data sources and analysis. *NOAA Technical Memorandum NESDIS NGDC-24*.

Andresen, C. S., Straneo, F., Ribergaard, M. H., Bjørk, A. A., Andersen, T. J., Kuijpers, A., Nørgaard-Pedersen, N., Kjær, K. H., Schjøth, F., Weckström, K., and et al. (2011). Rapid response of Helheim Glacier in Greenland to climate variability over the past century. *Nature Geoscience*, 5(1):37–41.

Antonov, J. I., Levitus, S., and Boyer, T. P. (2002). Steric sea level variations during 1957-1994: Importance of salinity. *Journal of Geophysical Research: Oceans*, 107(C12):SRF 14–1–SRF 14–8.

Bamber, J., van den Broeke, M., Ettema, J., Lenaerts, J., and Rignot, E. (2012). Recent large increases in freshwater fluxes from greenland into the north atlantic. *Geophysical Research Letters*, 39(19):n/a–n/a.

Barnier, B., Madec, G., Penduff, T., Molines, J.-M., Treguier, A.-M., Sommer, J. L., Beckmann, A., Biastoch, A., Böning, C., Dengg, J., Derval, C., Durand, E., Gulev, S., Remy, E., Talandier, C., Theetten, S., Maltrud, M., McClean, J., and Cuevas, B. D. (2006). Impact of partial steps and momentum advection schemes in a global ocean circulation model at eddy-permitting resolution. *Ocean Dynamics*, 56(5-6):543–567.

Belkin, I. M., Levitus, S., Antonov, J., and Malmberg, S.-A. (1998). “great salinity anomalies” in the North Atlantic. *Progress in Oceanography*, 41(1):1–68.

Berrisford, P., Dee, D., Poli, P., Brugge, R., Fielding, M., Fuentes, M., Kållberg, P., Kobayashi, S., Uppala, S., and Simmons, A. (2011). The ERA-Interim archive version 2.0. Shinfield Park, Reading.

Blanke, B. and Delecluse, P. (1993). Variability of the Tropical Atlantic Ocean simulated by a general circulation model with two different mixed-layer physics. *Journal of Physical Oceanography*, 23(7):1363–1388.

Carmack, E. C. (2007). The alpha/beta ocean distinction: A perspective on freshwater fluxes, convection, nutrients and productivity in high-latitude seas. *Deep Sea Research Part II: Topical Studies in Oceanography*, 54(23-26):2578–2598.

Carmack, E. C., Yamamoto-Kawai, M., Haine, T. W. N., Bacon, S., Bluhm, B. A., Lique, C., Melling, H., Polyakov, I. V., Straneo, F., Timmermans, M.-L., and et al. (2016). Freshwater and its role in the Arctic marine system: Sources, disposition, storage, export, and physical and biogeochemical consequences in the arctic and global oceans. *Journal of Geophysical Research: Biogeosciences*, 121(3):675–717.

Castro de la Guardia, L., Hu, X., and Myers, P. G. (2015). Potential positive feedback between greenland ice sheet melt and Baffin Bay heat content on the west Greenland shelf. *Geophysical Research Letters*, 42(12):4922–4930. 2015GL064626.

Coachman, L. K. and Aagaard, K. (1974). Physical oceanography of Arctic and subarctic seas. In *Marine geology and oceanography of the Arctic seas*, pages 1–72. Springer.

Comiso, J. C. (2000, updated 2015). Bootstrap sea ice concentration from Nimbus-7 SMMR and DMSP SSM/I, version 2 [2002 - 2016]. *NASA DAAC at National Snow and Ice Data Centre, Boulder, CO.*

Comiso, J. C. (2012). Large decadal decline of the Arctic multiyear ice cover. *Journal of Climate*, 25(4):1176–1193.

Comiso, J. C., Meier, W. N., and Gersten, R. (2017). Variability and trends in the Arctic sea ice cover: Results from different techniques. *Journal of Geophysical Research: Oceans*, 122(8):6883–6900.

Cuny, J., Rhines, P. B., and Kwok, R. (2005). Davis Strait volume, freshwater and heat fluxes. *Deep Sea Research Part I: Oceanographic Research Papers*, 52(3):519–542.

Curry, B., Lee, C. M., and Petrie, B. (2011). Volume, freshwater, and heat fluxes through Davis Strait, 2004–05*. *Journal of Physical Oceanography*, 41(3):429–436.

Curry, B., Lee, C. M., Petrie, B., Moritz, R. E., and Kwok, R. (2014). Multiyear volume, liquid freshwater, and sea ice transports through Davis Strait, 2004–10*. *Journal of Physical Oceanography*, 44(4):1244–1266.

Dai, A., Qian, T., Trenberth, K. E., and Milliman, J. D. (2009). Changes in continental freshwater discharge from 1948 to 2004. *Journal of Climate*, 22(10):2773–2792.

Dai, A. and Trenberth, K. E. (2002). Estimates of freshwater discharge from continents: Latitudinal and seasonal variations. *Journal of Hydrometeorology*, 3(6):660–687.

Dickson, R., Rudels, B., Dye, S., Karcher, M., Meincke, J., and Yashayaev, I. (2007). Current estimates of freshwater flux through Arctic and subarctic seas. *Progress in Oceanography*, 73(3-4):210–230.

Dickson, R. R., Meincke, J., Malmberg, S.-A., and Lee, A. J. (1988). The "Great Salinity Anomaly" in the northern North Atlantic 1968–1982. *Progress in Oceanography*, 20(2):103–151.

Diffenbaugh, N. S., Pal, J. S., Giorgi, F., and Gao, X. (2007). Heat stress intensification in the Mediterranean climate change hotspot. *Geophysical Research Letters*, 34(11).

Dumas, J. A., Flato, G. M., and Brown, R. D. (2006). Future projections of landfast ice thickness and duration in the Canadian Arctic. *Journal of Climate*, 19(20):5175–5189.

Fichefet, T. and Maqueda, M. A. M. (1997). Sensitivity of a global sea ice model to the treatment of ice thermodynamics and dynamics. *Journal of Geophysical Research: Oceans*, 102(C6):12609–12646.

Fissel, D., Lemon, D., and Birch, J. (1982). Major features of the summer near-surface circulation of western Baffin Bay, 1978 and 1979. *ARCTIC*, 35(1):180–200.

Galley, R. J., Else, B. G., Howell, S. E., Lukovich, J. V., and Barber, D. G. (2012). Landfast sea ice conditions in the Canadian Arctic: 1983 – 2009. *ARCTIC*, 65(2).

Ganachaud, A. and Wunsch, C. (2001). correction: Improved estimates of global ocean circulation, heat transport and mixing from hydrographic data. *Nature*, 410(6825):240–240.

Gelderoos, R., Straneo, F., and Katsman, C. (2012). Mechanisms behind the temporary shutdown of deep convection in the labrador sea: Lessons from the Great Salinity Anomaly years 1968-71. *Journal of Climate*, 25:6743–6755.

Gordon, C., Cooper, C., Senior, C. A., Banks, H., Gregory, J. M., Johns, T. C., Mitchell, J. F. B., and Wood, R. A. (2000). The simulation of SST, sea ice extents and ocean heat transports in a version of the Hadley Centre coupled model without flux adjustments. *Climate Dynamics*, 16(2-3):147–168.

Griffies, S. M. and Greatbatch, R. J. (2012). Physical processes that impact the evolution of global mean sea level in ocean climate models. *Ocean Modelling*, 51:37–72.

Grivault, N., Hu, X., and Myers, P. G. (2017). Evolution of Baffin Bay water masses and transports in a numerical sensitivity experiment under enhanced greenland melt. *Atmosphere-Ocean*, 55(3):169–194.

Grivault, N., Hu, X., and Myers, P. G. (2018). Impact of the surface stress on the volume and freshwater transport through the Canadian Arctic Archipelago from high resolution numerical modelling. *Journal of Geophysical Research: Oceans*.

Haas, C. and Howell, S. E. L. (2015). Ice thickness in the Northwest Passage. *Geophysical Research Letters*, 42(18):7673–7680.

Haine, T. W., Curry, B., Gerdes, R., Hansen, E., Karcher, M., Lee, C., Rudels, B., Spreen, G., de Steur, L., Stewart, K. D., and et al. (2015). Arctic freshwater export: Status, mechanisms, and prospects. *Global and Planetary Change*, 125:13–35.

Hall, M. M. and Bryden, H. L. (1982). Direct estimates and mechanisms of ocean heat transport. *Deep Sea Research Part A. Oceanographic Research Papers*, 29(3):339–359.

Hannah, C. G., Dupont, F., and Dunphy, M. (2009). Polynyas and tidal currents in the Canadian Arctic Archipelago. *ARCTIC*, 62(1).

Hartmann, D. L., Tank, A. M. K., Rusticucci, M., Alexander, L. V., Brönnimann, S., Charabi, Y. A. R., Dentener, F. J., Dlugokencky, E. J., Easterling, D. R., Kaplan, A., et al. (2013). Observations: atmosphere and surface. In *Climate Change 2013 the Physical Science Basis: Working Group I Contribution to the Fifth Assessment Report of the Intergovernmental Panel on Climate Change*. Cambridge University Press.

Hibler, W. D. (1979). A dynamic thermodynamic sea ice model. *Journal of Physical Oceanography*, 9(4):815–846.

Holland, D. M., Thomas, R. H., de Young, B., Ribergaard, M. H., and Lyberth, B. (2008a). Acceleration of Jakobshavn Isbræ triggered by warm subsurface ocean waters. *Nature Geoscience*, 1(10):659–664.

Holland, P. R., Jenkins, A., and Holland, D. M. (2008b). The response of ice shelf basal melting to variations in ocean temperature. *Journal of Climate*, 21(11):2558–2572.

Holloway, G. and Wang, Z. (2009). Representing eddy stress in an Arctic Ocean model. *Journal of Geophysical Research*, 114(C6).

Houssais, M.-N. and Herbaut, C. (2011). Atmospheric forcing on the Canadian Arctic Archipelago freshwater outflow and implications for the Labrador Sea variability. *Journal of Geophysical Research*, 116.

Howell, S. E., Tivy, A., Yackel, J. J., and McCourt, S. (2008). Multi-year sea-ice conditions in the western Canadian arctic archipelago region of the northwest passage: 1968–2006. *Atmosphere-Ocean*, 46(2):229–242.

Howell, S. E. L., Duguay, C. R., and Markus, T. (2009). Sea ice conditions and melt season duration variability within the Canadian Arctic Archipelago: 1979–2008. *Geophysical Research Letters*, 36(10).

Howell, S. E. L., Laliberté, F., Kwok, R., Derksen, C., and King, J. (2016). Landfast ice thickness in the Canadian Arctic Archipelago from observations and models. *The Cryosphere*, 10(4):1463–1475.

Howell, S. E. L., Wohlleben, T., Dabboor, M., Derksen, C., Komarov, A., and Pizzolato, L. (2013). Recent changes in the exchange of sea ice between the Arctic Ocean and the Canadian Arctic Archipelago. *Journal of Geophysical Research: Oceans*, 118(7):3595–3607.

Hu, X. and Myers, P. G. (2013). A Lagrangian view of Pacific water inflow pathways in the Arctic Ocean during model spin-up. *Ocean Modelling*, 71:66–80.

Hu, X. and Myers, P. G. (2014). Changes to the Canadian Arctic Archipelago sea ice and freshwater fluxes in the twenty-first century under the Intergovernmental Panel on Climate Change A1B climate scenario. *Atmosphere-Ocean*, 52(4):331–350.

Hu, X., Sun, J., Chan, T. O., and Myers, P. G. (2018). Thermodynamic and dynamic ice thickness contributions in the Canadian Arctic Archipelago in NEMO-LIM2 numerical simulations. *The Cryosphere*, 12(4):1233–1247.

Huang, R. X. (1999). Mixing and energetics of the oceanic thermohaline circulation*. *Journal of Physical Oceanography*, 29(4):727–746.

Hunke, E. C. (2001). Viscous–plastic sea ice dynamics with the EVP model: Linearization issues. *Journal of Computational Physics*, 170(1):18–38.

Hunke, E. C. and Dukowicz, J. K. (1997). An Elastic–Viscous–Plastic model for sea ice dynamics. *Journal of Physical Oceanography*, 27(9):1849–1867.

Jahn, A. and Holland, M. M. (2013). Implications of Arctic sea ice changes for north atlantic deep convection and the meridional overturning circulation in CCSM4-CMIP5 simulations. *Geophysical Research Letters*, 40(6):1206–1211.

Jahn, A., Tremblay, B., Mysak, L. A., and Newton, R. (2009). Effect of the large-scale atmospheric circulation on the variability of the Arctic Ocean freshwater export. *Climate Dynamics*, 34(2-3):201–222.

Killworth, P. D. (1983). Deep convection in the world ocean. *Reviews of Geophysics*, 21(1):1–26.

Kirtman, B., Power, S., Adedoyin, J., Boer, G., Bojariu, R., Camilloni, I., Doblas-Reyes, F., Fiore, A., Kimoto, M., Meehl, G., Prather, M., Sarr, A., Schär, C., Sutton, R., van Oldenborgh, G., Vecchi, G., and Wang, H. (2013). *Near-term Climate Change: Projections and Predictability*, book section 11, pages 953–1028. Cambridge University Press, Cambridge, United Kingdom and New York, NY, USA.

Kliem, N. and Greenberg, D. A. (2003). Diagnostic simulations of the summer circulation in the Canadian arctic archipelago. *Atmosphere-Ocean*, 41(4):273–289.

Kwok, R. (2006). Exchange of sea ice between the Arctic Ocean and the Canadian Arctic Archipelago. *Geophysical Research Letters*, 33(16).

Kwok, R. and Rothrock, D. A. (2009). Decline in Arctic sea ice thickness from submarine and ICESat records: 1958-2008. *Geophysical Research Letters*, 36(15):n/a–n/a.

Landerer, F. W., Jungclaus, J. H., and Marotzke, J. (2007). Regional dynamic and steric sea level change in response to the IPCC-A1B scenario. *Journal of Physical Oceanography*, 37(2):296–312.

Large, W. B. (2006). *Surface Fluxes for Practitioners of Global Ocean Data Assimilation*. Springer.

Large, W. G., McWilliams, J. C., and Doney, S. C. (1994). Oceanic vertical mixing: A review and a model with a nonlocal boundary layer parameterization. *Reviews of Geophysics*, 32(4):363.

Large, W. G. and Yeager, S. G. (2004). Diurnal to decadal global forcing for ocean and sea-ice models: the data sets and flux climatologies.

Large, W. G. and Yeager, S. G. (2009). The global climatology of an interannually varying air–sea flux data set. *Climate Dynamics*, 33(2):341–364.

Laxon, S. W., Giles, K. A., Ridout, A. L., Wingham, D. J., Willatt, R., Cullen, R., Kwok, R., Schweiger, A., Zhang, J., Haas, C., Hendricks, S., Krishfield, R., Kurtz, N., Farrell, S., and Davidson, M. (2013). CryoSat-2 estimates of arctic sea ice thickness and volume. *Geophysical Research Letters*, 40(4):732–737.

Lindsay, R. and Schweiger, A. J. (2013, updated 2017). Unified sea ice thickness climate data record, 1947 onward, version 1. [ICESat1-G and CryoSat-AWI]. *Boulder, Colorado USA. NSIDC: National Snow and Ice Data Center.*

Lique, C., Holland, M. M., Dibike, Y. B., Lawrence, D. M., and Screen, J. A. (2016). Modeling the Arctic freshwater system and its integration in the global system: Lessons learned and future challenges. *Journal of Geophysical Research: Biogeosciences*, 121(3):540–566.

Lu, Y., Higginson, S., Nudds, S., Prinsenberg, S., and Garric, G. (2014). Model simulated volume fluxes through the Canadian Arctic Archipelago and Davis Strait: Linking monthly variations to forcing in different seasons. *Journal of Geophysical Research: Oceans*, 119(3):1927–1942.

Luneva, M. V., Aksenov, Y., Harle, J. D., and Holt, J. T. (2015). The effects of tides on the water mass mixing and sea ice in the Arctic Ocean. *Journal of Geophysical Research: Oceans*, 120(10):6669–6699.

Madec, G. (2008). Nemo ocean engine. *Note du Pole de modelisation*, 27:1288–1619.

Madec, G., Delecluse, P., Imbard, M., and Levy, C. (1998). OPA 8 ocean general circulation model - reference manual. Technical report, LODYC/IPSL Note 11.

Madec, G. and Imbard, M. (1996). A global ocean mesh to overcome the North Pole singularity. *Climate Dynamics*, 12(6):381–388.

Mann, M. E. and Emanuel, K. A. (2006). Atlantic hurricane trends linked to climate change. *Eos, Transactions American Geophysical Union*, 87(24):233.

Manucharyan, G. E. and Spall, M. A. (2016). Wind-driven freshwater buildup and release in the Beaufort Gyre constrained by mesoscale eddies. *Geophysical Research Letters*, 43(1):273–282.

Manucharyan, G. E., Spall, M. A., and Thompson, A. F. (2016). A theory of the wind-driven Beaufort Gyre variability. *Journal of Physical Oceanography*, 46(11):3263–3278.

Marshall, J. and Schott, F. (1999). Open-ocean convection: Observations, theory, and models. *Reviews of Geophysics*, 37(1):1–64.

Masina, S., Storto, A., Ferry, N., Valdivieso, M., Haines, K., Balmaseda, M., Zuo, H., Drevillon, M., and Parent, L. (2015). An ensemble of eddy-permitting global ocean reanalyses from the MyOcean project. *Climate Dynamics*, pages 1–29.

McGeehan, T. and Maslowski, W. (2012). Evaluation and control mechanisms of volume and freshwater export through the Canadian Arctic Archipelago in a high-resolution pan-Arctic ice-ocean model. *Journal of Geophysical Research: Oceans*, 117(C8):n/a–n/a.

McPhee, M. G., Proshutinsky, A., Morison, J. H., Steele, M., and Alkire, M. B. (2009). Rapid change in freshwater content of the Arctic Ocean. *Geophysical Research Letters*, 36(10).

Melling, H. (2002). Sea ice of the northern Canadian Arctic Archipelago. *Journal of Geophysical Research*, 107(C11).

Melling, H., Agnew, T. A., Falkner, K. K., Greenberg, D. A., Lee, C. M., Münchow, A., Petrie, B., Prinsenberg, S. J., Samelson, R. M., and Woodgate, R. A. (2008). *Fresh-Water Fluxes via Pacific and Arctic Outflows Across the Canadian Polar Shelf*, pages 193–247. Springer Netherlands.

Mesinger, F. and Arakawa, A. (1976). Numerical methods used in atmospheric models. -1.

Morison, J., Aagaard, K., and Steele, M. (2000). Recent environmental changes in the Arctic: A review. *ARCTIC*, 53(4).

Morison, J., Kwok, R., Peralta-Ferriz, C., Alkire, M., Rigor, I., Andersen, R., and Steele, M. (2012). Changing Arctic Ocean freshwater pathways. *Nature*, 481(7379):66–70.

Münchow, A. (2016). Volume and freshwater flux observations from Nares Strait to the west of Greenland at daily time scales from 2003 to 2009. *Journal of Physical Oceanography*, 46(1):141–157.

Münchow, A., Falkner, K. K., and Melling, H. (2007). Spatial continuity of measured seawater and tracer fluxes through Nares Strait, a dynamically wide channel bordering the Canadian Archipelago. *Journal of Marine Research*, 65(6):759–788.

Münchow, A., Falkner, K. K., and Melling, H. (2015). Baffin Island and West Greenland Current systems in northern Baffin Bay. *Progress in Oceanography*, 132:305–317.

Münchow, A. and Melling, H. (2008). Ocean current observations from Nares Strait to the west of Greenland: Interannual to tidal variability and forcing. *Journal of Marine Research*, 66(6):801–833.

Murray, R. J. (1996). Explicit generation of orthogonal grids for ocean models. *Journal of Computational Physics*, 126(2):251–273.

Myers, P. G. and Ribergaard, M. H. (2013). Warming of the Polar Water layer in Disko Bay and potential impact on Jakobshavn Isbrae. *Journal of Physical Oceanography*, 43(12):2629–2640.

Nakicenovic, N., Alcamo, J., Grubler, A., Riahi, K., Roehrl, R., Rogner, H.-H., and Victor, N. (2000). *Special report on emissions scenarios (SRES), a special report of Working Group III of the intergovernmental panel on climate change*. Cambridge University Press.

Nummelin, A., Ilicak, M., Li, C., and Smedsrud, L. H. (2016). Consequences of future increased Arctic runoff on Arctic Ocean stratification, circulation, and sea ice cover. *Journal of Geophysical Research: Oceans*, 121(1):617–637.

Palut, M. P. J. and Canziani, O. F. (2007). *Contribution of working group II to the fourth assessment report of the intergovernmental panel on climate change*. Cambridge University Press.

Parkinson, C. L. (2014). Global sea ice coverage from satellite data: Annual cycle and 35-yr trends. *Journal of Climate*, 27(24):9377–9382.

Parkinson, C. L. and Cavalieri, D. J. (2008). Arctic sea ice variability and trends, 1979–2006. *Journal of Geophysical Research: Oceans*, 113(C7):n/a–n/a. C07003.

Parkinson, C. L. and Comiso, J. C. (2013). On the 2012 record low Arctic sea ice cover: Combined impact of preconditioning and an august storm. *Geophysical Research Letters*, 40(7):1356–1361.

Peterson, I., Hamilton, J., Prinsenberg, S., and Pettipas, R. (2012). Wind-forcing of volume transport through Lancaster Sound. *Journal of Geophysical Research: Oceans*, 117(C11):n/a–n/a.

Pickart, R. S., Spall, M. A., Ribergaard, M. H., Moore, G., and Milliff, R. F. (2003). Deep convection in the Irminger Sea forced by the Greenland tip jet. *Nature*, 424(6945):152.

Prinsenberg, S. and Bennett, E. (1987). Mixing and transports in Barrow Strait, the central part of the Northwest passage. *Continental Shelf Research*, 7(8):913–935.

Prinsenberg, S. and Bennett, E. (1989). Transport between peel sound and barrow strait in the Canadian Arctic. *Continental Shelf Research*, 9(5):427–444.

Prinsenberg, S., Hamilton, J., Peterson, I., and Pettipas, R. (2009). Observing and interpreting the seasonal variability of the oceanographic fluxes passing through Lancaster Sound of the Canadian Arctic Archipelago. In *Influence of Climate Change on the Changing Arctic and Sub-Arctic Conditions*, pages 125–143. Springer Netherlands.

Proshutinsky, A., Bourke, R. H., and McLaughlin, F. A. (2002). The role of the Beaufort Gyre in arctic climate variability: Seasonal to decadal climate scales. *Geophysical Research Letters*, 29(23):15–1–15–4.

Proshutinsky, A., Krishfield, R., Timmermans, M.-L., Toole, J., Carmack, E., McLaughlin, F., Williams, W. J., Zimmermann, S., Itoh, M., and Shimada, K. (2009). Beaufort Gyre freshwater reservoir: State and variability from observations. *Journal of Geophysical Research*, 114.

Rabe, B., Dodd, P. A., Hansen, E., Falck, E., Schauer, U., Mackensen, A., Beszczynska-Möller, A., Kattner, G., Rohling, E. J., and Cox, K. (2013). Liquid export of Arctic freshwater components through the Fram Strait 1998–2011. *Ocean Science*, 9(1):91–109.

Rahmstorf, S., Box, J. E., Feulner, G., Mann, M. E., Robinson, A., Rutherford, S., and Schaffernicht, E. J. (2015). Exceptional twentieth-century slowdown in Atlantic Ocean overturning circulation. *Nature Climate Change*, 5:475.

Randall, D. A., Wood, R. A., Bony, S., Colman, R., Fichefet, T., Fyfe, J., Kattsov, V., Pitman, A., Shukla, J., Srinivasan, J., et al. (2007). Climate models and their evaluation. In *Climate change 2007: The physical science basis. Contribution of Working Group I to the Fourth Assessment Report of the IPCC (FAR)*, pages 589–662. Cambridge University Press.

Reynolds, O. (1895). On the dynamical theory of incompressible viscous fluids and the determination of the criterion. *Philosophical Transactions of the Royal Society of London A: Mathematical, Physical and Engineering Sciences*, 186:123–164.

Rhein, M., Kieke, D., Hüttl-Kabus, S., Roessler, A., Mertens, C., Meissner, R., Klein, B., Böning, C. W., and Yashayaev, I. (2011). Deep water formation, the subpolar gyre, and the meridional overturning circulation in the subpolar North Atlantic. *Deep Sea Research Part II: Topical Studies in Oceanography*, 58(17-18):1819–1832.

Rudels, B. (2001). Arctic Basin circulation. *Encyclopedia of Ocean Sciences*, pages 177–187.

Rudels, B. (2015). Arctic Ocean circulation, processes and water masses: A description of observations and ideas with focus on the period prior to the International Polar Year 2007–2009. *Progress in Oceanography*, 132:22–67.

Rudels, B., Marnela, M., and Eriksson, P. (2008). Constraints on estimating mass, heat and freshwater transports in the Arctic Ocean: An exercise. *Arctic–Subarctic Ocean Fluxes*, pages 315–341.

Ryan, P. A. and Münchow, A. (2017). Sea ice draft observations in Nares Strait from 2003 to 2012. *Journal of Geophysical Research: Oceans*, 122(4):3057–3080.

Screen, J. A. and Simmonds, I. (2010). The central role of diminishing sea ice in recent Arctic temperature amplification. *Nature*, 464(7293):1334–1337.

Serreze, M. C. and Barrett, A. P. (2011). Characteristics of the Beaufort Sea High. *Journal of Climate*, 24(1):159–182.

Serreze, M. C., Barrett, A. P., Slater, A. G., Woodgate, R. A., Aagaard, K., Lammers, R. B., Steele, M., Moritz, R., Meredith, M., and Lee, C. M. (2006). The large-scale freshwater cycle of the Arctic. *Journal of Geophysical Research*, 111(C11).

Shroyer, E. L., Samelson, R. M., Padman, L., and Münchow, A. (2015). Modeled ocean circulation in Nares Strait and its dependence on landfast-ice cover. *Journal of Geophysical Research: Oceans*, 120(12):7934–7959.

Skagseth, Ø., Furevik, T., Ingvaldsen, R., Loeng, H., Mork, K. A., Orvik, K. A., and Ozhigin, V. (2008). Volume and heat transports to the Arctic Ocean via the norwegian and barents seas. *Arctic–Subarctic Ocean Fluxes*, pages 45–64.

Smith, G. C., Roy, F., Mann, P., Dupont, F., Brasnett, B., Lemieux, J.-F., Laroche, S., and Bélair, S. (2014). A new atmospheric dataset for forcing ice-ocean models: Evaluation of reforecasts using the Canadian global deterministic prediction system. *Quarterly Journal of the Royal Meteorological Society*, 140(680):881–894.

Sou, T. and Flato, G. (2009). Sea ice in the Canadian Arctic Archipelago: Modeling the past (1950–2004) and the future (2041–60). *Journal of Climate*, 22(8):2181–2198.

Spence, C. and Burke, A. (2008). Estimates of Canadian Arctic Archipelago runoff from observed hydrometric data. *Journal of Hydrology*, 362(3-4):247–259.

Steele, M. and Ermold, W. (2007). Steric sea level change in the Northern Seas. *Journal of Climate*, 20(3):403–417.

Steele, M., Morley, R., and Ermold, W. (2001). PHC: A global ocean hydrography with a high-quality Arctic Ocean. *Journal of Climate*, 14(9):2079–2087.

Steele, M., Zhang, J., and Ermold, W. (2010). Mechanisms of summertime upper Arctic Ocean warming and the effect on sea ice melt. *Journal of Geophysical Research*, 115(C11).

Stirling, I. (1980). The biological importance of polynyas in the Canadian Arctic. *ARCTIC*, 33(2).

Stommel, H. (1961). Thermohaline convection with two stable regimes of flow. *Tellus*, 13(2):224–230.

Straneo, F. (2006). Heat and freshwater transport through the central Labrador Sea*. *Journal of Physical Oceanography*, 36(4):606–628.

Stroeve, J., Holland, M. M., Meier, W., Scambos, T., and Serreze, M. (2007). Arctic sea ice decline: Faster than forecast. *Geophysical Research Letters*, 34(9).

Talley, L. D., Pickard, G. L., Emery, W. J., and Switft, J. H. (2011). Arctic Ocean and Nordic Seas.

Tang, C. C., Ross, C. K., Yao, T., Petrie, B., DeTracey, B. M., and Dunlap, E. (2004). The circulation, water masses and sea-ice of Baffin Bay. *Progress in Oceanography*, 63(4):183–228.

Terwisscha van Scheltinga, A. D., Myers, P. G., and Pietrzak, J. D. (2010). A finite element sea ice model of the Canadian Arctic Archipelago. *Ocean Dynamics*, 60(6):1539–1558.

Thompson, D. W. J. and Wallace, J. M. (1998). The Arctic Oscillation signature in the wintertime geopotential height and temperature fields. *Geophysical Research Letters*, 25(9):1297–1300.

Thorndike, A. S. (1986). Kinematics of sea ice. *The Geophysics of Sea Ice*, pages 489–549.

Timofeyev, V. (1962). The movement of Atlantic Water and heat into the Arctic basin. *Deep Sea Research and Oceanographic Abstracts*, 9(7-10):358–361.

Trenberth, K. E. and Caron, J. M. (2001). Estimates of meridional atmosphere and ocean heat transports. *Journal of Climate*, 14(16):3433–3443.

Vancoppenolle, M., Fichefet, T., Goosse, H., Bouillon, S., Madec, G., and Maqueda, M. A. M. (2009). Simulating the mass balance and salinity of Arctic and Antarctic sea ice. 1. model description and validation. *Ocean Modelling*, 27(1–2):33–53.

Vellinga, M. and Wood, R. A. (2002). Global climatic impacts of a collapse of the Atlantic thermohaline circulation. *Climatic Change*, 54(3):251–267.

Wallace, J. M. (2007). North atlantic oscillatiodannular mode: Two paradigms-one phenomenon. *Quarterly Journal of the Royal Meteorological Society*, 126(564):791–805.

Walsh, J. E. (2014). Intensified warming of the Arctic: Causes and impacts on middle latitudes. *Global and Planetary Change*, 117:52–63.

Wang, J., Kim, H.-M., and Chang, E. K. M. (2017a). Changes in Northern Hemisphere winter storm tracks under the background of Arctic Amplification. *Journal of Climate*, 30(10):3705–3724.

Wang, Q., Ilicak, M., Gerdes, R., Drange, H., Aksenov, Y., Bailey, D. A., Bentsen, M., Biastoch, A., Bozec, A., Böning, C., Cassou, C., Chassignet, E., Coward, A. C., Curry, B., Danabasoglu, G., Danilov, S., Fernandez, E., Fogli, P. G., Fujii, Y., Griffies, S. M., Iovino, D., Jahn, A., Jung, T., Large, W. G., Lee, C., Lique, C., Lu, J., Masina, S., Nurser, A. G., Rabe, B., Roth, C., y Mélia, D. S., Samuels, B. L., Spence, P., Tsujino, H., Valcke, S., Voldoire, A., Wang, X., and Yeager, S. G. (2016). An assessment of the Arctic Ocean in a suite of interannual CORE-II simulations. part II: Liquid freshwater. *Ocean Modelling*, 99:86–109.

Wang, Q., Myers, P. G., Hu, X., and Bush, A. B. (2012). Flow constraints on pathways through the Canadian Arctic Archipelago. *Atmosphere-Ocean*, 50(3):373–385.

Wang, Z., Hamilton, J., and Su, J. (2017b). Variations in freshwater pathways from the Arctic Ocean into the North Atlantic Ocean. *Progress in Oceanography*, 155:54–73.

Watanabe, M., Suzuki, T., O'ishi, R., Komuro, Y., Watanabe, S., Emori, S., Takemura, T., Chikira, M., Ogura, T., Sekiguchi, M., and et al. (2010). Improved climate simulation by MIROC5: Mean states, variability, and climate sensitivity. *Journal of Climate*, 23(23):6312–6335.

Watanabe, S., Hajima, T., Sudo, K., Nagashima, T., Takemura, T., Okajima, H., Nozawa, T., Kawase, H., Abe, M., Yokohata, T., and et al. (2011). MIROC-ESM 2010: model description and basic results of CMIP5-20C3M experiments. *Geoscientific Model Development*, 4(4):845–872.

Wekerle, C., Wang, Q., Danilov, S., Jung, T., and Schröter, J. (2013). The Canadian Arctic Archipelago throughflow in a multiresolution global model: Model assessment and the driving mechanism of interannual variability. *Journal of Geophysical Research: Oceans*, 118(9):4525–4541.

Yang, J. (2009). Seasonal and interannual variability of downwelling in the Beaufort Sea. *Journal of Geophysical Research*, 114.

Yang, Q., Dixon, T. H., Myers, P. G., Bonin, J., Chambers, D., and van den Broeke, M. R. (2016). Recent increases in Arctic freshwater flux affects Labrador Sea convection and Atlantic overturning circulation. *Nature Communications*, 7:10525.

Zalesak, S. T. (1979). Fully multidimensional flux-corrected transport algorithms for fluids. *Journal of Computational Physics*, 31(3):335–362.

Zhang, Y., Chen, C., Beardsley, R. C., Gao, G., Lai, Z., Curry, B., Lee, C. M., Lin, H., Qi, J., and Xu, Q. (2016). Studies of the Canadian Arctic Archipelago water transport and its relationship to basin-local forcings: Results from AO-FVCOM. *Journal of Geophysical Research: Oceans*, 121(6):4392–4415.

Zweng, M. M. and Münchow, A. (2006). Warming and freshening of Baffin Bay, 1916–2003. *Journal of Geophysical Research: Oceans*, 111(C7):n/a–n/a. C07016.